Synthesis and Functionalization of 1D, 2D Germanium-based Nanostructures

by

Haoyang Yu

A thesis submitted in partial fulfillment of the requirements for the degree of

Doctor of Philosophy

Department of Chemistry

University of Alberta

© Haoyang Yu, 2020

Abstract

The synthesis of germanium nanomaterials with well-defined surface chemistry is of considerable interest, not only because of general scientific curiosity but also because of their vast potential applications in optoelectronics, energy storage, and the semiconductor industry. Covalently bonded organic monolayers(MLs) play important roles in defining the solution processability, ambient stability, and electronic properties of two-dimensional (2D) materials, such as germanium nanosheets (GeNSs).

In Chapter 2, we report a straightforward preparative route that yields hydride-terminated germanium nanosheet (H-GeNS) monolayers via sonochemical exfoliation of hydride-terminated germanane flakes (HGe-flakes) derived from crystalline $CaGe_2$. We subsequently show in Chapter 3 that these freestanding H-GeNSs are functionalized readily by a radical-initiated and thermal-induced hydrogermylation reaction. Furthermore, we demonstrate that, upon functionalization, the crystal structure of the GeNSs remains intact, and the introduction of organic moieties to the GeNS surfaces imparts improved thermal stability and solvent compatibility.

In Chapter 4, we extend the scope of surface linkages to Si—Ge bonding and present the first demonstration of heteronuclear dehydrocoupling of organosilanes to hydride-terminated GeNSs by deintercalation and exfoliation of $CaGe_2$. We further exploit this new surface reactivity and demonstrate the preparation of directly bonded silicon quantum dot-Ge nanosheet hybrids.

Polygermanes, which contain Ge—Ge backbones are soluble semiconductors with applications in different fields. In Chapter 5, we prepare a stable form of polydihydrogermane with $–(GeH_2)–$ repeating units, rigorously characterize its

structure, chemical environment, absorption features, and thermal stability, and compare it with unstable polydihydrogermane prepared by a traditional method. We also show that these materials can be applied as a template for ligand substitution via a hydrogermylation reaction (e.g. using 1-dodecene). This facile one-step reaction using Ge–H as the synthetic handle can be utilized to synthesize a variety of functional polygermanes.

Preface

Chapter 1 provides a brief introduction to the basic principles of silicon- and germanium-based nanostructures and polymers syntheses and pathways of surface group functionalization or ligand substitution. The concept of Zintl phase and the exfoliation of layered materials also is covered briefly. Chapter 2 introduces a convenient method to prepare a layered $CaGe_2$ precursor and a subsequent topotactic transformation into germanane flakes. Chapter 3 describes the formation of Ge—C bonds on the Ge nanosheets surface via a thermally-induced and radically-initiated hydrogermylation reaction. Chapter 4 studies the dehydrogenative coupling reaction between Ge—H and Si—H bonds donated from Ge nanosheets and organosilanes or silicon quantum dots. Chapter 5 introduces the preparation of polygermanes via deintercalation of Zintl phase CaGe using water and HCl and evaluated their thermal stability and ligand substitution via a hydrogermylation reaction. Chapter 6 summarizes the thesis and proposes several directions for future research.

A portion of Chapter 2 is based on the publication "Yu, H.; Helbich, T.; Scherf, L. M.; Chen, J.; Cui, K.; Fässler, T. F.; Rieger, B.; Veinot, J. G. C. Radical-Initiated and Thermally Induced Hydrogermylation of Alkenes on the Surfaces of Germanium Nanosheets. *Chemistry of Materials*. **2018**, *30* (7), 2274–2280." This is an Alberta/Technical University of Munich International Graduate School for Hybrid Functional Materials (ATUMS) project between the Technical University of Munich (TUM) and the University of Alberta (UofA). Dr. Lavinia Scherf (TUM) synthesized the precursor $CaGe_2$ in the Fässler lab. Dr. Tobias Helbich (TUM) and I explored the deintercalation reaction of $CaGe_2$, exfoliation, and purification process. Prof. Thomas Fässler (TUM), Prof. Bernhard Rieger (TUM), and Prof. Jonathan Veinot were the supervisory authors and were involved with the concept formation and manuscript

composition.

A portion of Chapter 3 is based on the publication "Yu, H.; Helbich, T.; Scherf, L. M.; Chen, J.; Cui, K.; Fässler, T. F.; Rieger, B.; Veinot, J. G. C. Radical-Initiated and Thermally Induced Hydrogermylation of Alkenes on the Surfaces of Germanium Nanosheets. *Chemistry of Materials*. **2018**, *30* (7), 2274–2280." This is an ATUMS project between TUM and UofA. I was responsible for the data acquisition and analysis as well as the manuscript composition. Initial reaction conditions were explored with Dr. Tobias Helbich. The simulation of Ge nanosheets stacking-dependent electron diffraction was assisted by Dr. Jian Chen from the National Research Council of Canada (NRC Canada). Dr. Kai Cui, from NRC Canada, assisted in obtaining transmission electron microscopy images and electron energy loss spectroscopy line scans. Prof. Thomas Fässler, Prof. Bernhard Rieger, and Prof. Jonathan Veinot were the supervisory authors and were involved with the concept formation and manuscript composition.

Chapter 4 is based on the publication "Yu, H.; Thiessen A. N.; Hossain, M. A.; Kloberg, J. M; Rieger, B.; Veinot, G. C. J. Thermally-Induced Dehydrogenative Coupling of Organosilanes and H-terminated Silicon Quantum Dots onto Germanane Surfaces. *Chemistry of Materials*. **2020**. *32* (11), 4536–4543" This is an ATUMS project between TUM and UofA. I was responsible for the concept formation, precursor synthesis, data acquisition and analysis, as well as the manuscript composition. Alyxandra Thiessen provided the Si quantum dots at different sizes for hybrid synthesis. Md Asjad Hossain and Marc Julian Kloberg (TUM) were involved with the concept formation of the project as well as the optimization of the reaction conditions. Prof. Bernhard Rieger and Prof. Jonathan Veinot were the supervisory authors and were involved with the concept formation and manuscript composition.

Chapter 5 also is written as an article. I was responsible for the concept

formation, precursor synthesis, data acquisition and analysis, figure preparation, as well as the manuscript composition. Chuyi Ni, in his first-year graduate research, assisted in the precursor synthesis, data acquisition, and building of crystal structure models under my supervision. Alyxandra Thiessen carried out powered X-ray diffraction measurements of the samples at the Canadian Light Source. Prof. Jonathan Veinot was the supervisory author and were involved with the concept formation and manuscript composition.

All the Zintl precursors, except the first batch of $CaGe_2$, were synthesized in the Mar Lab, Department of Chemistry, UofA. All Raman spectroscopy was carried out in the McDermott lab located in the Nanotechnology Research Centre, UofA.

Acknowledgements

When I look back, it is hard to believe that I have spent more than ten years in Canada since pursuing my undergraduate studies. In the past five years of my Ph.D. studies, working on challenging but interesting projects, operating multi-million instruments, collaborating with international partners, working at the TUM in Germany, attending international conferences, I feel a sense of fulfillment I have never had before. All the wonderful moments would not have happened without my wonderful family, supportive supervisor, and friends.

Mom and Dad, we have been separated by the Pacific Ocean most of the time since I started my studies in Canada, but you have never complained about it. You were always supportive of any decisions that I made. I know that today you are as happy as I am, if not more. Mom, you could have been pursuing a higher education degree when I was little, but instead, you chose to concentrate all your attention on me since then. Dad, I know that we do not have a lot of conversations, like fathers and sons (I guess), but I know I am the one you are most proud of. I love you three thousand and one times.

There were so many people in the university who helped me a lot with my research. First of all, I would like to thank my supervisor, Prof. Jonathan Veinot, for his mentorship throughout the five-year graduate process. Jon, you always stand by our side and have faith in us. When I face any challenges, I do not hesitate to tell you my honest feeling, and we chat more like friends than mentor and student, as you really are. You can always discover the highlights in me, even when sometimes I do not realize it. You are very generous to us, supporting us, and even “pushing” us in a good way to learn and to experience outside the lab, which I found extremely useful. Also, I really admire your rigorous attitude towards science, which changed my view

of data analysis. I enjoyed the time we spent struggling with the first nanosheet project together and was surprised that you could always come up with “crazy” ideas.

I would like to thank the members of the Veinot team from 2015 onwards. First of all, Leah Veinot, you have been spent so much effort on us in the ATUMS program. I am so glad and honored to be a member of the ATUMS family, where all my research and collaborations started. This thesis would not exist without you! I would also like to thank my office mates, Drs. Christopher Jay Robidillo and Alyxandra N. Thiessen. Chris and Alyx, you are such awesome friends! We started our research almost the same time and have many happy and sad memories together. It is interesting that when we were discussing science, we looked as though we were quarrelling with one another’s view. But, after that, we instantly became reconciled like relaxed electrons. I think this is the best status, as friends or quantum dots. I would like to thank Drs. Maryam Aghajamali, Regina Sinelnikov, and Morteza Javadi, who were the first members of the Veinot group to mentor me when I started my research. Thank you for all the useful advice and things you taught me.

A big thank to the previous and current group members, Dr. Lida Hadidi, Dr. Christina Gonzalez, Austin Toresdahl, Dr. Tapas Purkait, Kelsey Deutsch, Dr. Rhett Clark, Dr. Md Hosnay Mobarok, Dr. Muhammad Amirul Islam, Dr. John Washington, Md Asjad Hossain, Dr. Philipp Kitschke, Subha Jana, Xiyu (Zach) Zhang, Dr. Angélique Faramus, Mckenzie Oliver, Lydia Fialka, Sarah Milliken, Yingjie (Jay) He, Dr. Jonathan Hiltz, Dr. Nduka Ikpo, I Teng (Emily) Cheong, Kevin O'Connor, Riley Hooper, Ziqi (Amber) Li, Chuyi (Martin) Ni, and many others! Thank you for your input and help through the most stressful times of my Ph.D. life, the 502 presentation and the candidacy. I was very lucky to have all of you.

I would like to thank the ATUMS family members Dr. Tobias Helbich, Marc Kloberg, Dr. Arzu Angi, and Dr. Réka Csiki for the help when I was conducting

research in Germany. Tobi, I just feel lucky to have met you in my first year. You have a passion for everything, and it seems like there is nothing you cannot solve. You and Marc definitely played the centre role in this thesis; I miss the fun times when we were in Canada and Germany. I would like to thank Prof. Martin Stutzmann, Prof. Thomas Fässler, Prof. Bernhard Rieger, and their teams, as well as my amazing friends in Germany for their great hospitality.

I have also recognized the generous continued support from my supervisory committee members, Prof. Arthur Mar and Prof. Mark McDermott, and faculty members in the Department of Chemistry, Prof. Jillian Buriak, Prof. Vladimir Michaelis, and Prof. Eric Rivard. Thank you for providing me with unfailing support and continuous encouragement throughout my years of study. I want to thank Prof. Raymond E. Schaak for taking the time to be my external examiner. I am also grateful to the useful instrumentation trainings and discussions from Peng Li, Dr. Dimitre Karpuzov, Dr. Shihong Xu, Dr. Anqiang he, Shiau-Yin Wu, Wayne Moffat, Jennifer Jones, Dr. Nathan Gerein, Greg Popowich, Dr. Abishek Iyer, Casey Rusin, and Stephanie Bozic. There were also so many support staff who helped me a lot with characterization. Dr. Michael Fleischauer, Dr. Kai Cui, Dr. Jian Chen, Dr. Aaron Hryciw, Danielle Covelli, Dr. Ramaswami Sammynaiken, Minh Tang Duc Hoang, Jing Zheng, and Dr. Nancy Zhang are some of the names whose help I appreciate. Also, a colossal thank you, Dr. Anna Jordan, for polishing this thesis and making it look exquisite. Thank you.

Finally, and most importantly, I would like to thank my fiancée Dr. Minjia Hu. We met in our first year and, because of you, my Ph.D. life could never have been this vibrant. We have been to mountains and oceans, seen auroras and stars, and ice-climbed, while trusting our lives with each other. You are always supporting and encouraging, making this dissertation possible. I’m your lobster.

Contents

List of Figures

List of Tables

List of Symbols

Symbol	Meaning
β_{gem}	Geminal orbital interaction
β_{prim}	Primary orbital interaction
β_{vin}	Vicinal orbital interaction
I	XPS signal intensity
ρ	Atomic density
λ_i	Attenuation length of element i
λ	Wavelength
d	Thickness
θ	take-off angle
n	Number of layers
SF	Element sensitivity factor

List of Abbreviations

Abbreviation	Meaning
0D	Zero-dimension
1D	One-dimension
2D	Two-dimension
3D	Three-dimension
4-DDB	4-decylbenzene diazonium tetrafluoroborate
AFM	Atomic force microscopy
AIBN	Azobisisobutyronitrile
Ar	Aryl
a.u.	Arbitral unit
BE	Binding energy
C12E7	Dodecylheptaglycol
c-Ge	Crystalline germanium
CPS	Cyclopentasilane
CPU	Central Processing Units
CTAB	Cetyl trimethylammonium bromide
DHC	Dehydrocoupling
DI	Deionized
DRA	Diffuse reflective absorption
EDX	Energy dispersive X-ray spectroscopy
EELS	Electron energy loss spectroscopy
EL	Electroluminescence
FET(s)	Field effect transistor(s)
FIB	Focus ion beam

FFT	Fast Fourier transfer
FTIR	Fourier transfer infrared spectroscopy
FWHM	Full width at half maximum
HAADF-STEM	High-angle annular dark-field scanning transmission electron microscopy
h-BN	Hexagonal boron nitride
HDMS	Hexamethyldisilazane
HIM	Helium ion microscopy
H-GeNS(s)	Hydride-terminated germanium nanosheet(s)
HOMO	Highest occupied molecular orbital
HRTEM	High-resolution transmission electron microscopy
HSQ	Hydrogen silsesquioxane
H-SiQD(s)	Hydride-terminated silicon quantum dot(s)
IC	Integrated circuits
LUMO	Lowest unoccupied molecular orbital
LIB	Lithium ion battery
mAm	mAmetrine
MCF-7	Michigan Cancer Foundation-7
MIBK	Methyl isobutyl ketone
ML	Monolayer
NS(s)	Nanosheet(s)
NP(s)	Nanoparticle(s)
NMP	N-Methyl-2-pyrrolidone
PL	Photoluminescence
p-Si	Porous silicon
PTFE	Polytetrafluoroethylene

pXRD	Powder X-ray diffraction
PX	Paraoxon
QD(s)	Quantum dot(s)
rpm	Revolutions per minute
RT	Room temperature
SAED	Selected area electron diffraction
SEM	Scanning electron microscopy
STM	Scanning tunneling microscopy
TEM	Transmission electron microscopy
TGA	Thermogravimetric analysis
THF	Tetrahydrofuran
TMDs	Transition metal dichalcogenide(s)
UHV	Ultra-high vacuum
UV	Ultra-violet
vdW	van der Waals
VLS	Vapour-liquid-solid
XP	X-ray photoemission
XPS	X-ray photoemission spectroscopy

Chapter 1

Introduction – The Nano World is "Big"

Silicon and germanium are the basic materials that have been utilized to develop transistors, integrated circuits (IC), and charged coupled devices, which contribute to the fundamentals of the semiconductor industry. Their importance has been highlighted by the Nobel Prizes in Physics in 1956, 2000, and 2009. Over the past seven decades, the size of the commercial transistor has been shrunk into the sub -10 nm node, with each modern central processing unit (CPU) containing billions of transistors.

One of the challenges of developing even smaller transistors is that interesting shape and size-dependent properties, which are different from those observed for molecular or bulk systems, became apparent.[1] The study of materials with nanoscopic dimensions is growing rapidly and continues to accelerate because of a deeper understanding and a wider range of applications. Surface plasmon resonance observed in noble metal nanostructures has been applied for signal enhancement,[2] sensors,[3] and cancer treatments.[4] Quantum confinement of electrons in semiconductor nanomaterials leads to an increase on band gap and results in size-dependent strong photoluminescence (PL)/electroluminescence (EL), making quantum dots ideal for display, sensor, and imaging applications.[5–8] Materials with low dimensions, such as graphene, hexagon boron nitride (h-BN), and transition metal dichalcogenides (TMDs), are typical examples of 2-dimensional (2D) conducting, insulating, and semiconducting materials, showing layered dependent properties.[9–12]

1.1 Si/Ge Nanostructures

Silicon and germanium-based nanostructures have attracted considerable attention due to their size-tunable band gap, limited toxicity, and wide range of applications, such as in catalysis,[13] water remediation,[14] photodetectors,[15] field-effect transistors (FETs),[16,17] solar cells,[18–20] lithium-ion batteries,[21] bio-imaging,[8,22] and sensing.[23,24] Different silicon and germanium nanostructures have been synthesized successfully; a few examples are shown in Figure 1.1.

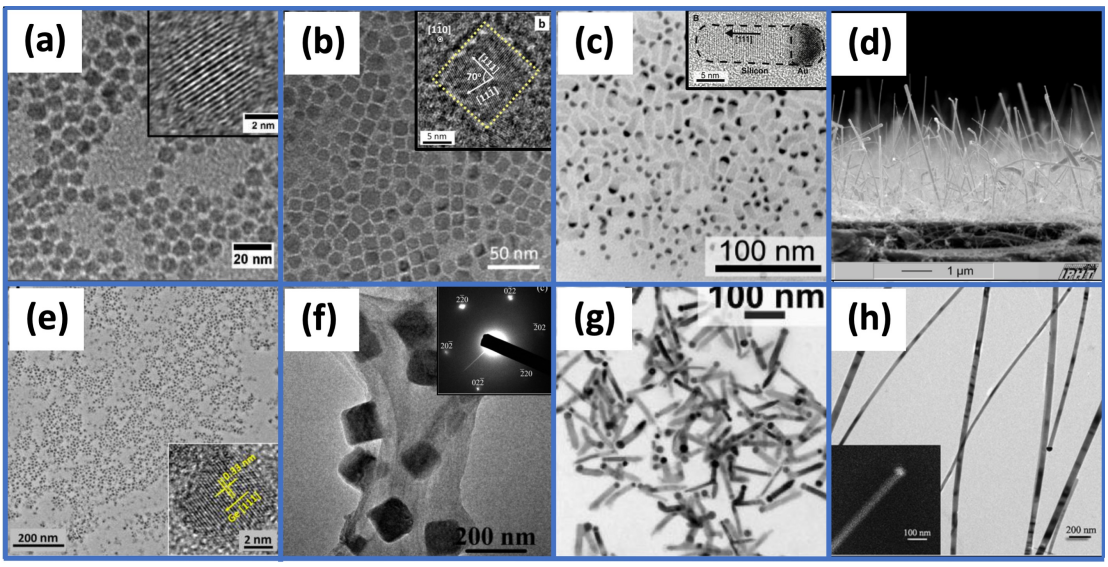

Figure 1.1. Transmission electron microscopy and scanning electron microscopy images of (a-d) silicon and (e-g) germanium nanostructures, (a,e) spherical nanocrystal, (b,f) nanocubes, (c,g) nanorods, (d,h) nanowires. (a) Reprinted with permission from ref 25. Copyright 2017 American Chemical Society. (b) Reprinted with permission from ref 26. Copyright 2012 American Chemical Society. (c) Reprinted with permission from ref 27. Copyright 2009 American Chemical Society. (d) Reprinted with permission from ref 19. Copyright 2008 IOP Publishing Ltd. (e) Reprinted with permission from ref 28. Copyright 2017 American Chemical Society. (f) Reprinted with permission from ref 29. Copyright 2005 American Chemical Society. (g) Reprinted with permission from ref 30. Copyright 2011 American Chemical Society. (h) Reprinted with permission from ref 31. Copyright The Royal Society of Chemistry 2008.

To synthesize Si/Ge quantum dots (0D, QDs), four general strategies have been predominant in the literature: mechanochemical ball milling of bulk

crystals,[32–36] metathesis reactions involving Zintl salts (such as NaSi,[37] NaGe,[38] Mg_2Si[39]), hydride reduction of Si/Ge halides,[37,38,40,41] and thermal disproportion reaction of Si/Ge-rich precursors.[6,25,28,42–44] In the Veinot Lab, hydrogen silsesquioxane ($H_8Si_8O_{12}$, HSQ) was utilized as a precursor for the size and shape-controlled synthesis of Si QDs.[25] Thermal processing of polymeric HSQ at 1100 °C under a slightly reducing atmosphere (95 % N_2/5% H_2) produced Si QDs (d = 3 nm) embedded in a silica (SiO_2) matrix. The Si QDs were liberated from the SiO_2 matrix through HF etching (Figure 1.2) to produce spherical H-SiQDs that displayed size-dependent photoluminescence (PL); details will be discussed in Chapter 4.

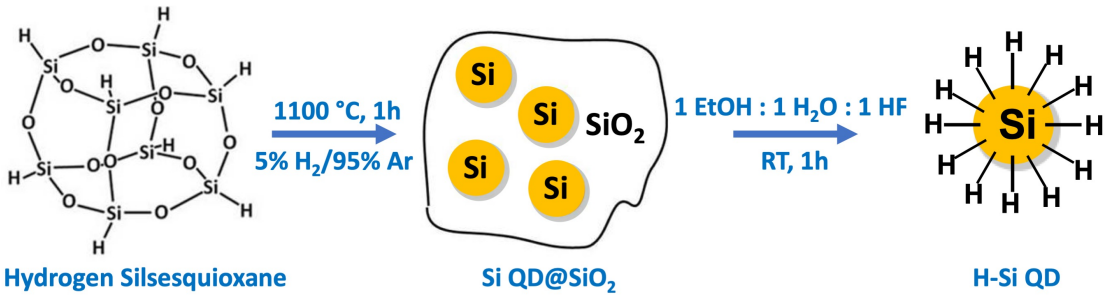

Figure 1.2. Solid-state synthesis of 3 nm hydride-terminated Si QDs using HSQ as a precursor. QD size can be tuned by heating profile and etching condition.

The shape control is, in general, challenging for 0D Si/Ge QDs. Unlike the colloidal synthesis of metal nanoparticles, where the growth rate can be tuned by surfactants or through the dynamic etching of reactive facets during synthesis, the Si/Ge QDs synthesis often requires high temperatures or high boiling point solvents. When applying colloidal synthesis, Vaughn and co-workers prepared crystalline Ge nanocubes using hexamethyldisilazane (HDMS) and tri-n-octylphosphine as cosurfactant during GeI_4 reduction.[45] Similarly, Ge nanocubes also were synthesized successfully using dodecylheptaglycol (C12E7) as the single surfactant in the

reduction of $GeCl_4$ and $PhGeCl_3$.[29] With rigorous temperature control, cubic and ordered cuboctahedra shaped Si QDs were reported using HSQ as a precursor.[26,46] Silicon and germanium nanorods and nanowires as 1-dimensional (1D) structures are synthesized almost exclusively through methods similar to vapour–liquid–solid (VLS) growing,[27,30,31,45,47,48] template synthesis,[49,50] and lithography techniques.[50,51]

From the work outlined herein, it is clear that the morphologies of Si/Ge nanostructures have advanced significantly. Efficient methods for material preparation bearing a variety of reactive surfaces will lead to a better understanding of the fundamental properties and future applications.

1. 1. 1 Layered Si/Ge

Since the exfoliation of graphene using Scotch® tape, 2-dimensional (2D) van der Waals (vdW) materials have attracted attention due to their unique layered dependent mechanical, electronic, thermal, and optical properties.[52–55] Silicon and germanium are two of the few elements that have 2D structures by themselves, named silicene and germanene, respectively. These atomically thin slightly buckled honeycomb structure exhibit a Dirac cone in their band structures, which, similar to graphene, predicts high carrier mobilities (Figure 1.3a).[56]

High-quality silicene and germanene can be synthesized by various deposition methods on well-organized substrates (Figure 1.3). Multiple groups studied the formation of silicene on an Ag substrate with (110), (001), and (111) orientation and obtained strip, ribbon, and sheet morphologies, respectively.[57–60] Other substrates, such as ZrB_2,[61] ZrC,[62] MoS_2,[63] and Ir (111)[64], also were reported with successful synthesis. Similarly, germanene sheets can grow epitaxially on Ag (111),[65] Au (111),[66] or Pt (111)[67] and have a morphology characterized by scanning tunneling microscopy (STM). Unfortunately, these sheets are sensitive under ambient conditions using these methods. Only Tao and co-workers have fabricated monolayer silicene-based FETs

with a protecting layer. The carrier mobility of their FET was reported as ~100 cm^2/Vs when operating at room temperature.[68]

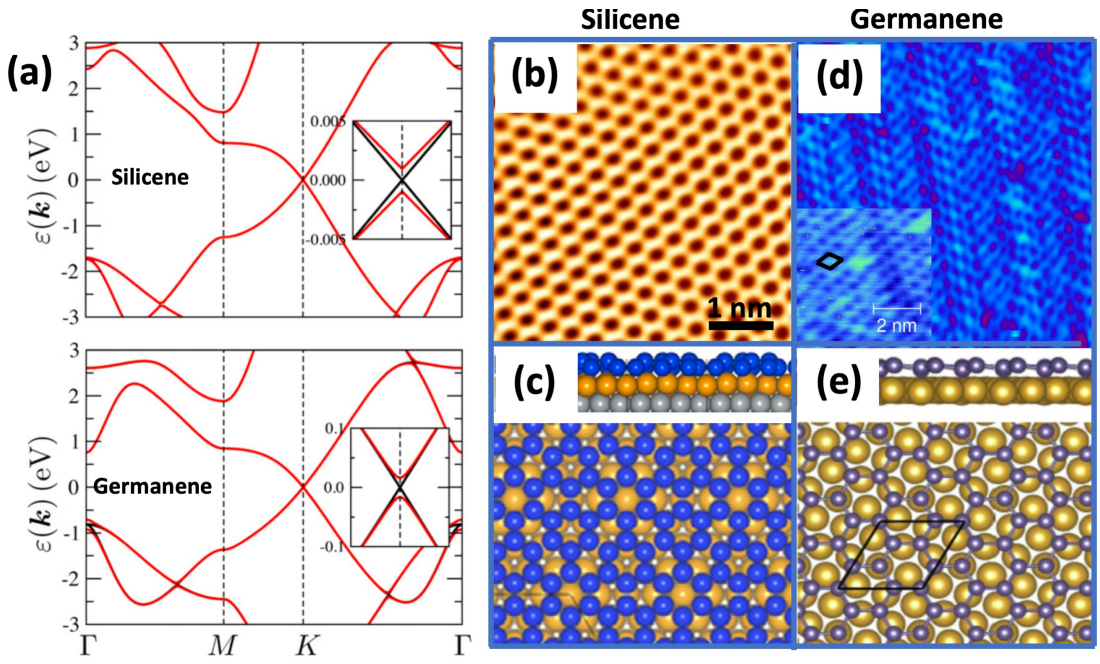

Figure 1.3. (a) Band structure of silicene and germanene, (b) scanning tunneling microscopy (STM) scan of silicene on Ag (111) substrate, and (c) structure model. (d) Scanning tunneling microscopy scan of germanene on Au (111) substrate and (e) structure model. (a) Reprinted with permission from ref 56. Copyright 2013 IOP Publishing Ltd. (b, c) Reprinted with permission from ref 59. Copyright 2012 IOP Publishing Ltd. (d, e) Reprinted with permission from ref 66. Copyright 2014 IOP Publishing Ltd.

Fully hydrogenated silicene and germanene are Si and Ge analogues of graphane. They are named silicane and germanane and have a general formula of (Si_6H_6) and (Ge_6H_6), respectively. These structures can be synthesized by hydrogenation of silicene or germanene at an elevated temperature in a hydrogen atmosphere,[69] but it is more convenient to prepare them via topotactic deintercalation from layered precursors, such as $CaSi_2$ and $CaGe_2$; details will be discussed in Chapter 2. Gram-scale synthesis of silicane/germanane has been achieved by the solid-state synthesis of $CaSi_2/CaGe_2$ granules[70–73], and wafer-size silicane/germanane

has been reported by epitaxial growth on Si/Ge substrates.[74–76] With the benefit of scalable production, these materials have been applied to FET,[77–79] photodetectors,[77] and lithium-ion battery (LIB) anode material (Figure 1.4).[80]

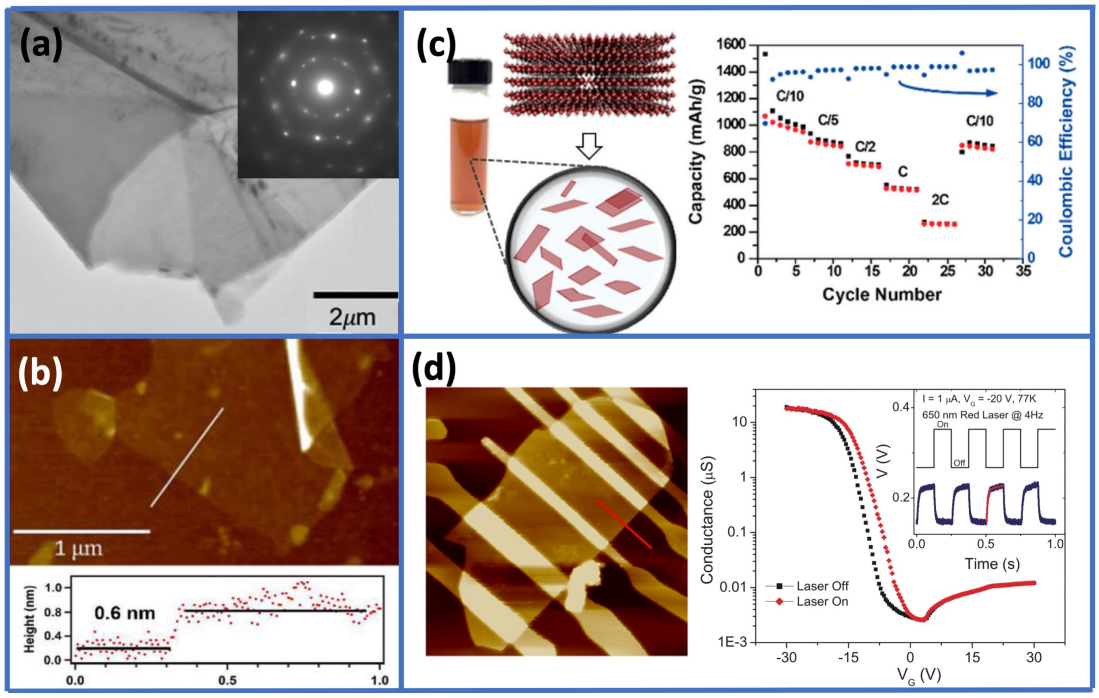

Figure 1.4. (a) TEM image and electron diffraction of germanane, (b) atomic force microscopy scan of germanane, (c) exfoliated germanane as an anode material in LIB, (d) germanane-based photodetector. (a) Reprinted with permission from ref 81. Copyright The Royal Society of Chemistry 2019. (b) Reprinted with permission from ref 70. Copyright 2013 American Chemical Society. (c) Reprinted with permission from ref 80. Copyright 2017 American Chemical Society. (d) Reprinted with permission from ref 77. Copyright 2017 IOP Publishing Ltd.

By simply changing the composition of the precursor to $CaSi_{2x}Ge_{2-2x}$, nanosheets (NSs) with a different Si:Ge ratio can be prepared and exhibit tunable bandgaps. Similarly, introducing dopants such as As, Ga, and Al during synthesis leads to doped germanane, with an increase in conductivity of at least three orders of magnitude without disturbing the layered structure.[82] Despite the available applications of germanane and silicane sheets, their structures are identical to hydride-terminated Si/Ge (111) surfaces and are prone to oxidation after long term exposure at ambient

conditions.

In 2013, Bianco and co-workers performed a systematic study on the thermal stability of germanane (Figure 1.5).[70] In general, the Ge–Ge framework is disturbed when the annealing temperature rises above 100 °C, indicated by the diminishing Ge–Ge vibration and the reduced optical band gap from 1.59 eV to 1.1 eV. After annealing at 150 °C, the interlayer distance was reduced, as indicated by the larger 2θ value in XRD. At higher temperatures, the layered morphology completely vanished, and the dehydrogenative reaction was observed in the thermogravimetric analysis (TGA). These materials need to be stabilized further via surface functionalization, which will be discussed in Section 1. 2. 2.

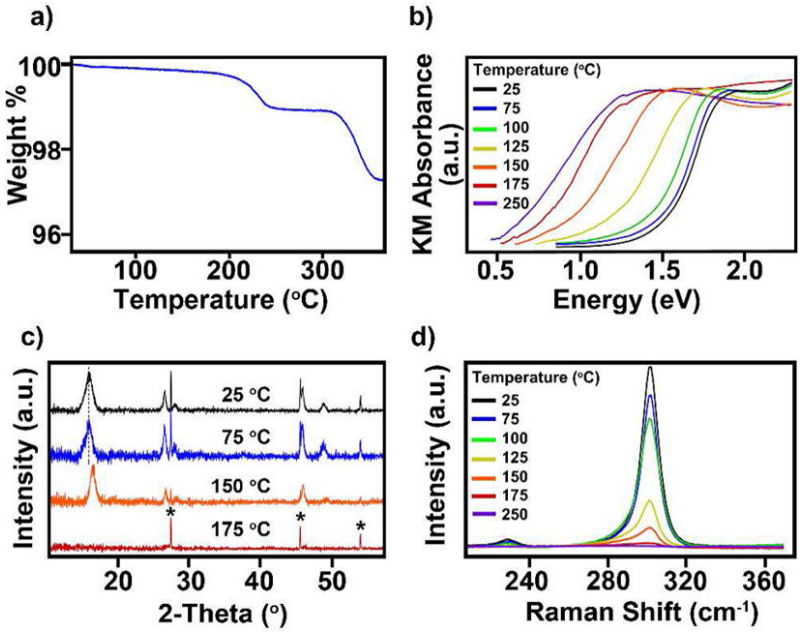

Figure 1.5. (a) TGA analysis of germanane. (b) DRA spectra, (c) XRD patterns, and (d) Raman spectra of Ge_6H_6 measured after thermal annealing. The starred peaks in (c) correspond to the Ge standard. Reprinted with permission from ref 70. Copyright 2013 American Chemical Society.

1. 1. 2 Polysilanes and Polygermanes

Catenated polysilanes and polygermanes, which contain single element–element

bonds, can be considered as 1D nanostructures. Although structurally identical to alkanes, they exhibit delocalized electrons across the entire backbone; this is known as σ-delocalization.[83–85] This σ-delocalization makes them semiconducting in cases where their HOMO-LUMO gaps are dominated mainly by the element–element backbone, leading to interesting optical properties. This is due to three primary orbital interactions, geminal (β_{gem}), primary (β_{prim}), or vicinal (β_{vin}), along the polymer backbone (Figure 1.6).[86] This leads to a tunable bandgap by tailoring their bond lengths and angles through side-group substitution or by introducing tensile strains.[85,87–89] In fact, it has been proposed that in longer chains, the existence of a gauche or gauche-like conformation will decouple the interaction between segments partially and result in different optical HOMO-LUMO gaps.[90]

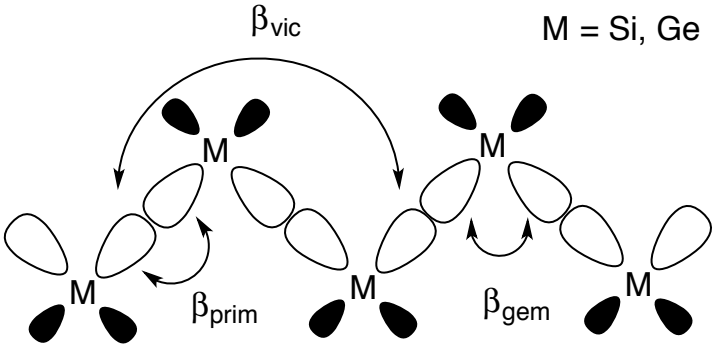

Figure 1.6. Orbital interactions along a polygermane/polysilane backbone.

Since the first synthesis of poly(diphenylsilane) in the 1920s by Kipping and Sands using a Wurtz-type coupling reaction,[91] a wide variety of simple and functional polysilanes have been prepared and reviewed.[92–96] The most commonly applied methods are (a) sodium-mediated Wurtz-type coupling, (b) homogenous dehydrocoupling reaction using a transition metal (i.e., Cp_2ZrCl_2/2 *n*-BuLi, Wilkinson's catalyst), (c) ring-opening polymerization, and (d) electrochemical reduction (conditions summarized in Table 1.1) Other approaches, such as anionic

polymerization of masked disilanes (prepared by reacting dichlorosilanes with a diphenyl anion radical), and post-functionalization on -H, -Cl or -OEt substituted polysilanes also have been developed.

Table 1.1. Experimental Approaches to Polysilane Synthesis

Technique	Variations	Monomer	Polymer	Substituents	Other Reagents	Solvent	T/ °C
Wurtz	Na-based reduction	R_2SiCl_2	$(R_2Si)_n$	alkyl, aryl	Na	Toluene, THF	110
	KC_8-based reduction	R_2SiCl_2	$(R_2Si)_n$	ether functions	KC_8	THF	60
Dehydro-coupling	Early TM-cat[a]	$ArSiH_3$	(ArSiH)	Phenyl or other aryl and 3H	Group 4 metallocene catalyst	None	RT
	Late TM-cat[a]	$RSiH_3$, $RSiH_2$	$(RSiH)_n$ $(R_2Si)_n$	Aryl or alkyl	Rh, Ni, Pd, Pt catalyst	Toluene or neat	Heat
Ring-opening	Anionic or cationic	$(SiR_2)_4$	$(R_2Si)_n$	Smaller is better	RCuLiX	THF	–78
	Photochemical	Si_4Cl_8	$(Cl_2Si)_n$	Cl	None	None	RT
Electro-chemical	Divided or undivided cell	R_2SiCl_2	$(R_2Si)_n$	Aryl, alkyl, vinyl	Mg electrodes, electrolyte, complexing agent	THF or DME	RT

[a]TM-cat: transition metal catalyst.

Compared to polysilanes synthesis, the diversity of prepared polygermanes is relatively limited due to the availability of the dichlorogermanes and cyclogermanes starting materials required for a Wurtz-type or electrochemical reaction and ring-opening polymerization, respectively. Wurtz-type polymerization often has been performed in toluene under reflux with molten sodium as the reducing agent (mechanism shown in Figure 1.7). The organic side chains that can withstand these very harsh conditions are usually the alkyl and aryl groups.

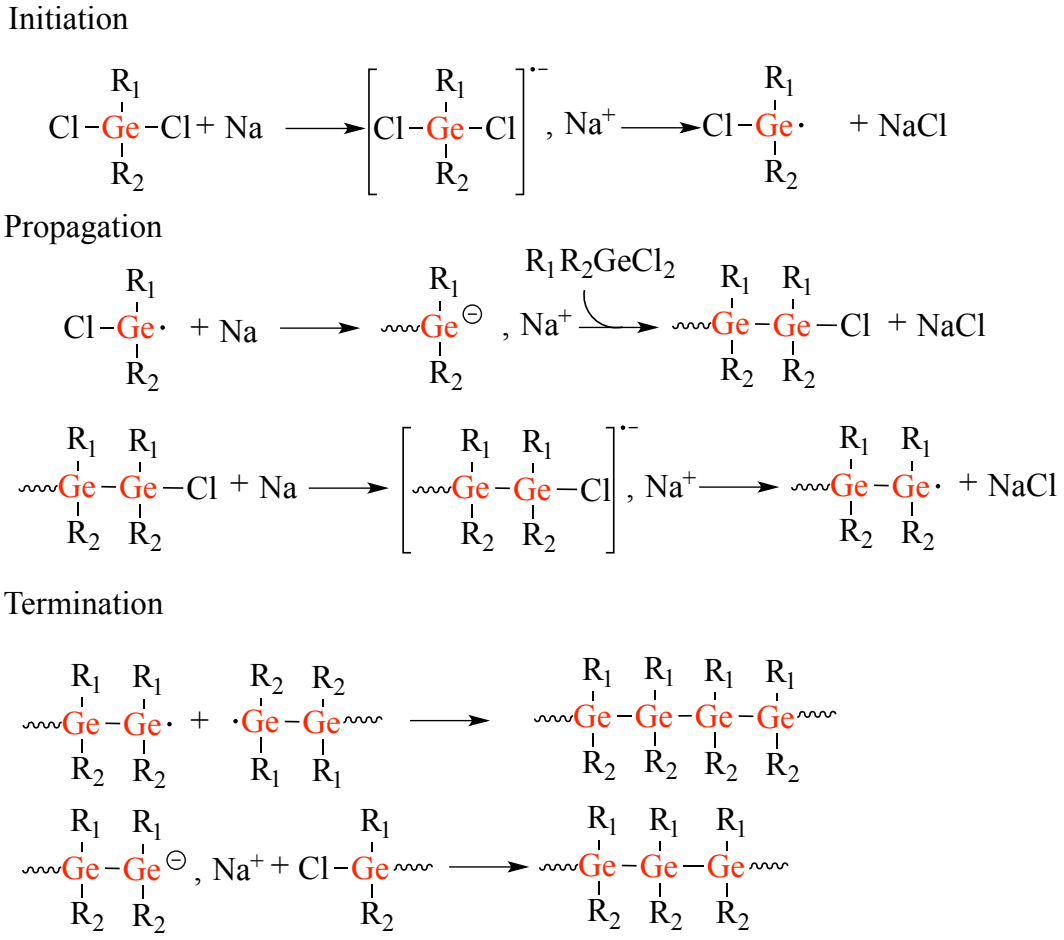

Figure 1.7. Proposed mechanism for linear polygermane formation by a Wurtz-type reduction. Ge is labeled red to guide the eye.

Polygermanes prepared via an electrochemical reduction method are usually similar to those synthesized by a Wurtz-type reduction. The polygermanes that were recovered achieved modest molecular weights, but this method is not as efficient as in polysilane synthesis.[88,97] The plausible mechanism proposed by Okano et al. is summarized in Figure 1.8.[98]

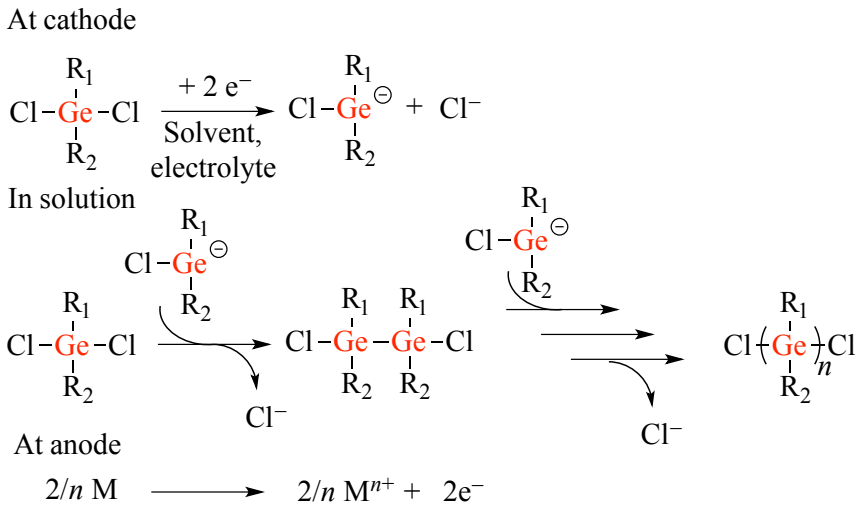

Figure 1.8. Proposed mechanism for linear polygermane formation by electrochemical reduction. Ge is labeled red to guide the eye.

It is reported that the versatile dehydrocoupling reaction in polysilane preparation cannot be applied to the synthesis of high molecular weight polygermanes,[99,100] which further eliminates the selections of digermane monomers. Harrod and co-workers reported the dehydrocoupling of Ph_2GeH_2 in the presence of Cp_2TiCl_2 catalyst, and only the H-[Ph_2Ge]$_4$-H oligomer was formed.[100] When dehydrocoupling primary $PhGeH_3$ using Cp_2ZrCl_2/2 *n*-BuLi catalyst, Choi and Tanaka prepared modest molecular weight polymers (<1000 Da) with a partial network structure.[101] Instead, demethanative coupling of dimethyl- or trimethyl-containing germanes using $Ru(PMe_3)_4Me_2$ catalyst was quite effective (as low as 0.01 mol%).[83,102,103] The proposed mechanism (Figure 1.9) involves Ge—C bond cleavage, Ge—Ge bond formation, and the elimination of CH_4.

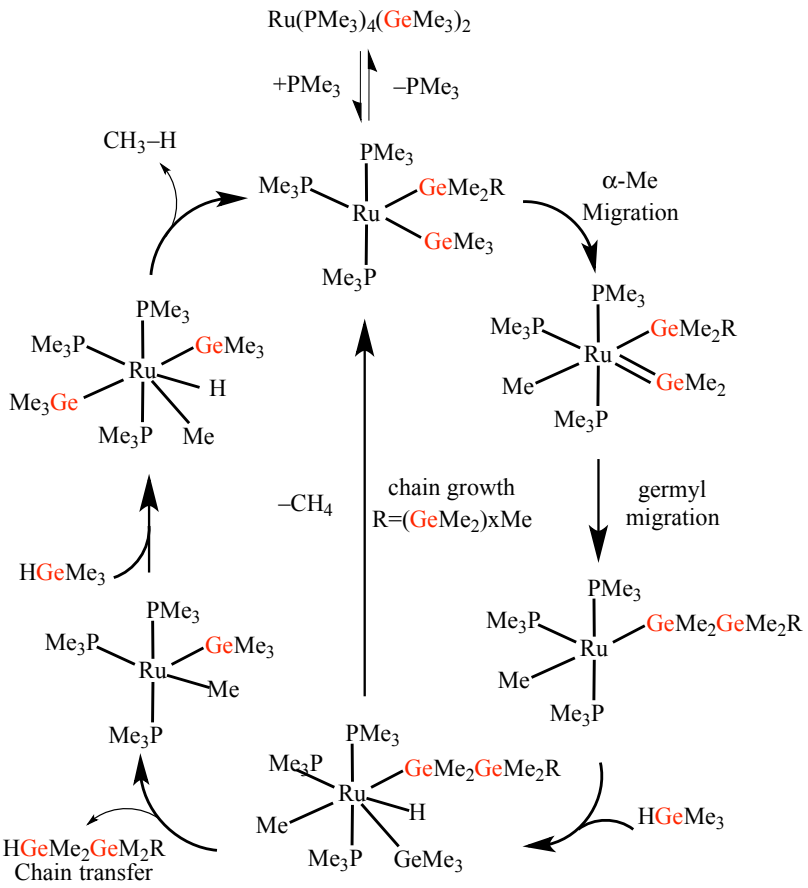

Figure 1.9. Proposed mechanism for linear polygermane formation by demethanative coupling. Ge is labeled red to guide the eye.

While the direct syntheses of polysilanes and polygermanes have been studied extensively, these routes often present limitations to substituent functionalities, and post-polymerization functionalization is required. Since Si—X or Ge—X (X = Cl, Br, I) bonds cannot survive in the Wurtz-type or electrochemical reduction. Hydride termination, naturally present in dehydrocoupling methods to synthesize polysilane ($RSiH_3$ monomer) or demethanative coupling synthesized polygermanes ($(Me)_2RGeH$ monomer), becomes one of the most promising synthetic handles for modification. The simplest polysilanes and polygermanes contain only Si/Ge and H; they are poly(dihydrosilane) $–[SiH_2]_n–$ and poly(dihydrogermane) $–[GeH_2]_n–$, respectively. Poly(dihydrosilane) was synthesized using cyclopentasilane (CPS: Si_5H_{10}) via

ring-opening polymerization, and it is applied as a precursor to form hydrogenated amorphous silicon thin films.[104–106] The germanium analog of CPS is, however, not known. By applying chemical vapour deposition using GeH_4 as a monomer, small segments of hydrogermanes were detected by mass spectrometry; therefore, it is not practical for post functionalization.[107] Surprisingly, poly(dihydrogermane) can be prepared using the solid-state synthesized precursor CaGe, and their topotactic deintercalation under acid environment lead to a pale yellow material with high molecular weight.[108,109] Unfortunately, poly(dihydrogermane) prepared by this method is photodegradable and cause explosive decomposition when dry at an ambient environment. The preparation of a safe method to handle high-quality poly(dihydrogermane) precursors is urgent.

1. 2 Covalent Functionalization on Si/Ge Surface

The eminent physicist Wolfgang Pauli used to say, "God made the bulk; surface was invented by the devil". Pauli explained that the diabolical characteristic of the surface was due to the simple fact that a solid surface shares its border with the external world. As a result, the properties of surface atoms are very different from those in the adjacent bulk media. This is especially true for nanostructures because of their massive surface ratio. Silicon quantum dots with same sizes but different surface group terminations can exhibit different PL colours across the visible spectrum (Figure 1.10a).[110–112] Upon treating with functional groups, the surface energy of nanostructures can be tuned, resulting in hydrophobic or hydrophilic surfaces,[113] which is vital in bio-imaging applications[114] (Figure 1.10b,f). Surface functionalization is acting also as an excellent template for hybrid material synthesis.

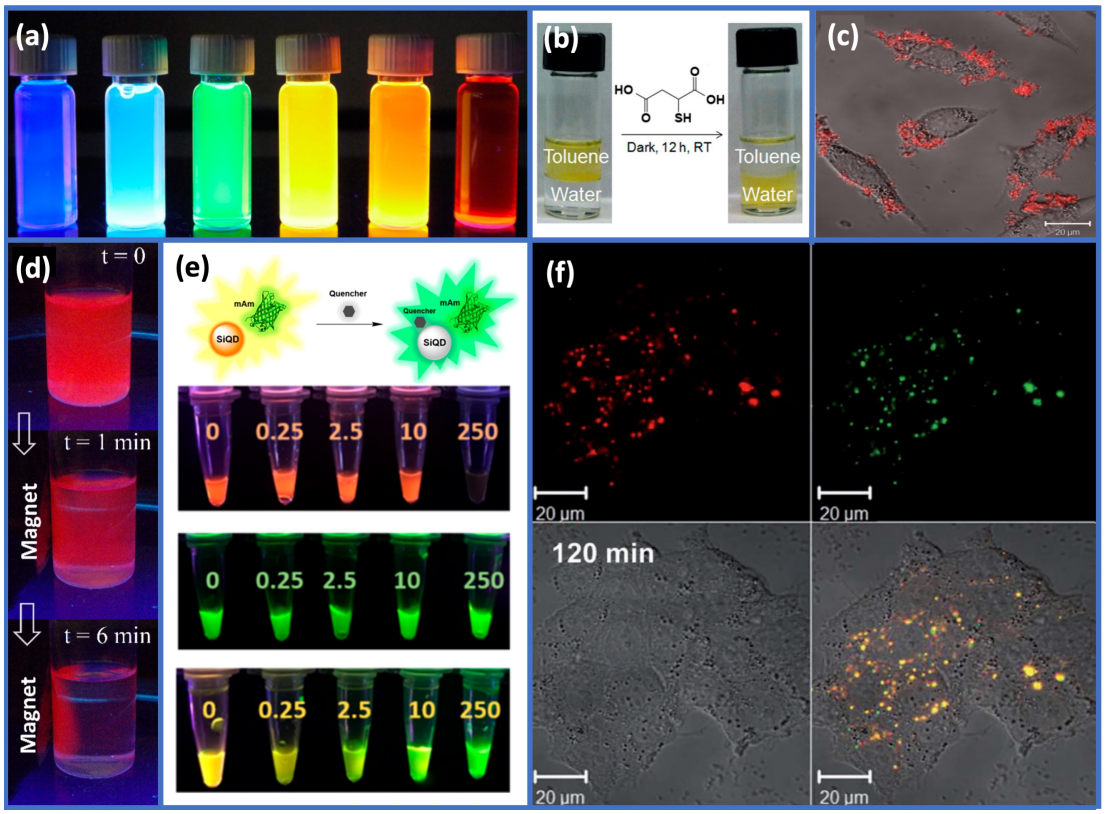

Figure 1.10. (a) Photograph of 3-4 nm Si QDs functionalized with various surface groups dispersed in toluene, under UV illumination: blue, dodecylamine; blue-green, acetal; green, diphenylamine; yellow, trioctylphosphine oxide; orange, dodecyl (air); red, dodecyl (inert). (b) Solubilization of Ge/CdS core-shell QDs in water via thiol ligand exchange. (c) Confocal microscopy images of MCF-7 cells incubated with chitosan capped Ge QDs, which was functionalized further with doxorubicin and conjugated with folic acid. (d) Photograph of a water suspension of Si-amide-Fe_3O_4 NPs under UV light and permanent magnet. (e) Photograph of (top) Si QDs, (middle) mAmetrine (mAm), and (bottom) combined Si QDs and mAm with increasing micromolar concentrations of PX under UV illumination. (f) Fluorescence microscopy images of Qu-Ge NPs and colocalization of Qu-GeNPs (red) and lysosomes (green) in MCF-7 cells. (a, b) Reprinted with permission from ref 113, ref 115. Copyright 2014 American Chemical Society. (c) Reprinted with permission from ref 116. Crown Copyright 2013 Published by Elsevier B.V. (d) Reprinted with permission from ref 117. Copyright 2016 Materials Research Society. (e) Reprinted with permission from ref 118. Copyright 2019 American Chemical Society. (f) Reprinted with permission from ref 114. Copyright 2014 Wiley-VCH Verlag GmbH & Co.

Pei-hui Yang and co-workers prepared multifunction water-dispersible Ge QDs (Figure 1.10c) by capping with chitosan, loaded with doxorubicin (a classic drug for cancer treatment), and then conjugated with folic acid for targeting purposes.[116] When

Si QDs are linked covalently to Fe_3O_4 nanoparticles, these hybrid structures exhibit both PL and magnetic properties (Figure 1.10d).[117] When the surface of these nanostructures are bonded to specific functional groups, their luminance will be quenched, making them a good candidate for sensing applications, such as the detection of explosives[24] or neuro-agents (Figure 1.10e).[118]

1. 2. 1 On Wafer Surface

Before discussing the functionalization of the Si/Ge nanostructures, it is worth reviewing the established methods to functionalize the Si/Ge (111) bulk. The (111) orientation is the plane with the densest Si/Ge atoms on the surface (Figure 1.11) and the most observed reflection in Si/Ge QDs.[26,41,119,120] The topmost (111) surfaces consisting of a puckered, honeycomb arrangement is also structurally identical to Si/Ge in the silicane/germanane layers.[70,121,122]

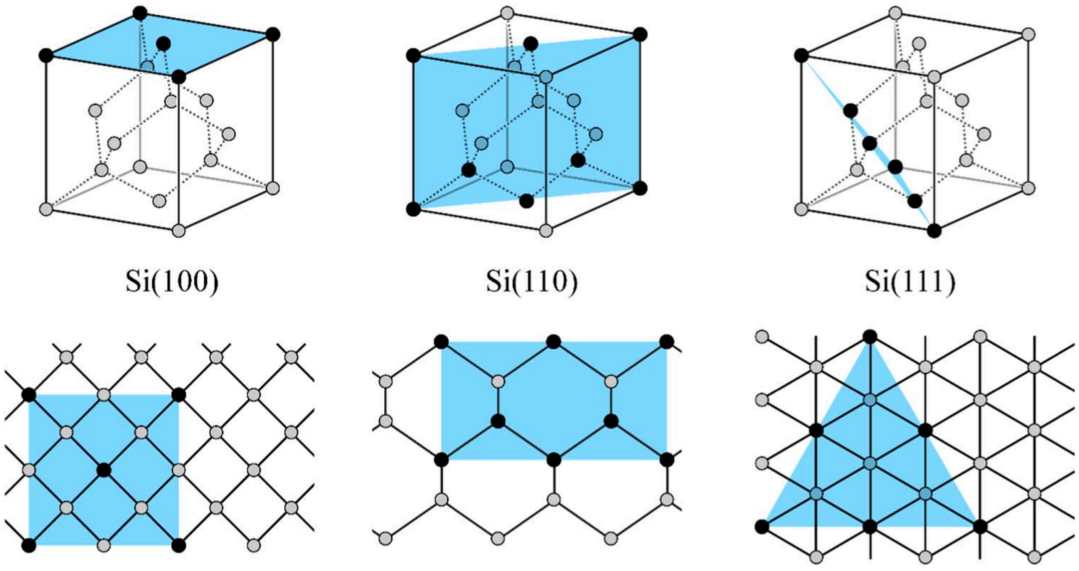

Figure 1.11. Unit cells of Si(100), Si(110), and Si(111) (upper part), and view along the different directions of the diamond cubic lattice (lower part). The black marked silicon atoms belong to a particular plane. Reprinted with permission from ref 123. Copyright 1998 IEEE.

Due to their wide use in microelectronic applications, single-crystal Si and Ge wafers with a selected orientation are commercially available. Upon exposure to air, these crystals are oxidized readily to form a thin oxide layer that can be removed chemically with fluoride ion[124,125] or thermally under UHV conditions (not covered in this thesis).[126,127] Additionally, the surface of GeO_2 is much less stable than that of SiO_2 and is readily washed away in water or acids.[122] After fluoride-based etching, freshly etched hydride-terminated Si and Ge surfaces are good candidates for direct functionalization, or as the surface reactive precursors for halide-terminated surfaces before further functionalization (a few general methods are summarized in Figure 1.12).

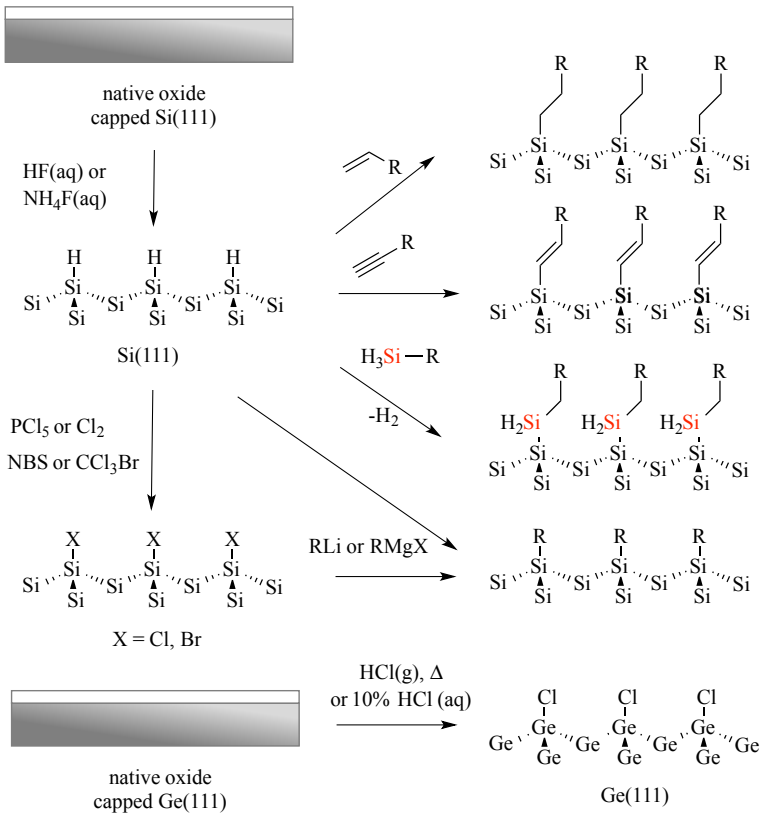

Figure 1.12. Reaction path to prepare hydride- and halide-terminated Si/Ge surfaces and products of Si/Ge–R functionalization. NBS: N-bromosuccinimide.

Hydrosilylation/Hydrogermylation has been known in the molecular organosilicon/organogermanium literature for decades for convenient Si—C/Ge—C bond formation. It involves the insertion of an unsaturated bond into a Si—C or Ge—C group, such as alkynes and alkenes.[126] The first example of hydrosilylation on Si(111)–H surface was carried out in 1993.[128] Insertion of alkenes in the presence of diacyl peroxide as a radical initiator yielded a high-quality monolayer and demonstrated excellent stability in boiled solvents, water, base, or in HF solution.[129] The study of hydrosilylation/hydrogermylation on a bulk surface then divided into a few major categories: radical-based, surface photoemission-driven, exciton-driven, and plasmon-assisted. Radical initiation is one of the commonly applied methods. It was proposed that the key intermediate is the surface silyl radical or the germanium equivalent (also known as the dangling bond), represented by ≡Si• or ≡Ge•, respectively. These radicals can be formed by initiators (such as diacyl peroxide, [128] 4-nitro or bromobenzene diazonium salt,[130] heating,[131] including microwave irradiation), [132,133] UV light,[134,135] and gas-phase generation[136] (Figure 1.13).

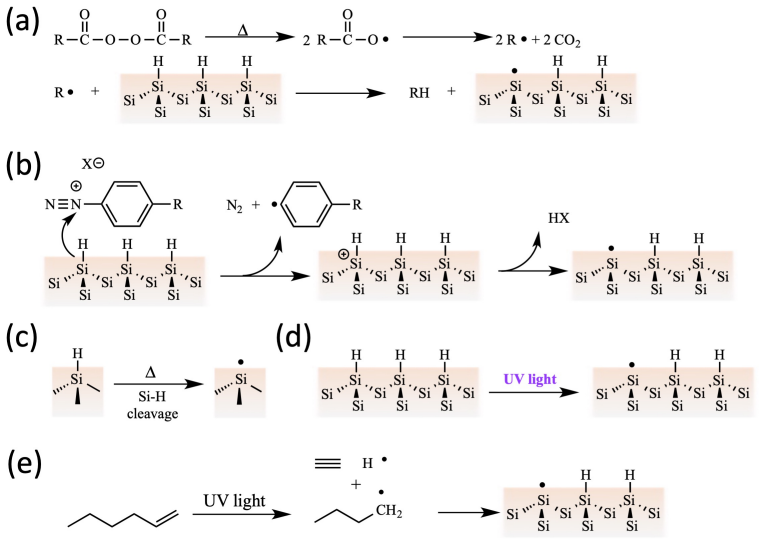

Figure 1.13. Routes for silyl radical formation: (a) diacyl peroxide radical-initiator, (b) diazonium salt, (c) thermal heating, (d) UV irradiation, and (e) gas phase decomposition.

The formed dangling bond can react extremely rapidly with olefins, forming a carbon-based radical, which can abstract hydrogen from a neighbouring Si—H/Ge—H group, and propagation will form a uniformly functionalized surface (Figure 1.14).[137,138]

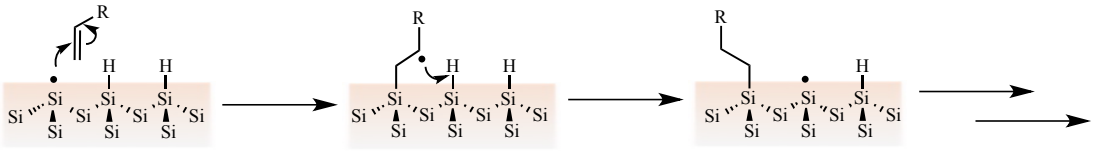

Figure 1.14. Reaction of a surface silyl radical with an alkene.

For photoemission-driven hydrosilylation, silicon has a work function of ~4.7 eV, and UV light with 254-nm wavelength possesses sufficient energy to eject an electron directly from the conductive band, leading to the positively charged silicon surface.[134] Then, it is attacked by the π-electron from the alkene, leading to the formation of the Si—C bond. When using white light, although the energy is not sufficient to eject an electron, an electron/hole pair, or exciton, is formed upon absorption of a photon.[139,140] The hole weakens the surface Si—Si bond, which then is attacked by the alkene, and the positive charge remains in the silicon. On flat silicon, the exciton-based hydrosilylation is, however, takes significantly longer than on a porous surface or nanoparticles due to a slight difference in the reaction mechanism.[135,141] Interestingly, the reactivity of white light hydrosilylation on flat silicon can be enhanced with the presence of gold NPs.[142] It is explained by gold NPs operating as "photon collectors" or enhanced electric fields that assist in exciton dissociation.[143,144]

As briefly covered in Table 1.1, dehydrogenative coupling is a common method for polysilane synthesis via the disproportionation reaction between Si—H bonds to form Si—Si and H—H bonds. In 2006, Li and Buriak presented the

reactivity on flat and porous silicon with primary silanes using the early transition metal catalyst Cp_2TiCl_2 and Cp_2ZrCl_2/2 *n*-BuLi.[125] Contrary to the molecular system, only monolayer coverage is obtained on the Si wafer surface due to steric hindrance.

Another major methodology to functionalize Si/Ge(111) surfaces is by Grignard and organolithium chemistry. It involves the forming of Si/Ge-halogen bonds on the (111) surface, which can be achieved via PCl_5 treatment of an H-terminated Si surface[145,146] (e.g., 20–60 min at 80–100 °C using benzoyl peroxide as a radical initiator), Cl_2 under a 300 W tungsten lamp for 2 min,[147,148] or exposure of an oxidized Ge (111) surface with 10 % aqueous HCl for 10 min.[149,150] Subsequently, the halide surface can react with an alkyllithium or Grignard reagent at 80 °C, yielding LiX or MgX_2 and an alkyl group bound to the silicon surface through a Si-C linkage that is stable at ambient conditions for at least a month.[146,151–153]

1. 2. 2 On Nanostructured Surface

1. 2. 2. 1 Porous Si/Ge

Porous silicon and germanium are bulk substrates with nanosized pores and apparent quantum-confinement effects (i.e., PL). They are fabricated mainly by electrochemical etching of a single crystal (100) wafer in HF or HCl (for germanium), and pore sizes are varied by the applied current density.[154–156] Thermally-induced hydrosilylation/hydrogermylation of alkenes and alkynes has been applied to Si—H/Ge—H surfaces.[156–158] Auger depth profile shows consistent carbon incorporation throughout the pores. Interestingly, additional to the adventitious initiation mechanism (Figure 1.14), the authors also proposed that the residual fluoride from etching will attach to the surface silicon, which would transfer a hydride to the double bond to give the carbanion, or the double bond will attack a surface silicon atom to form a pentavalent silicon, followed by hydride transfer to the carbocation (Figure 1.15).[158]

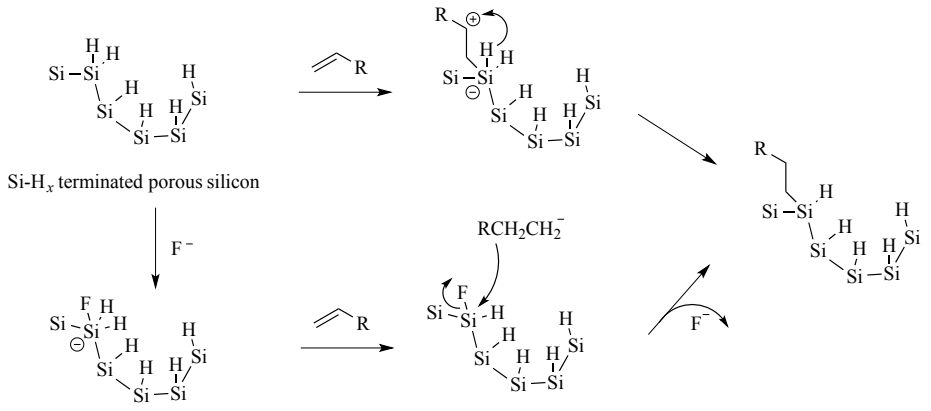

Figure 1.15. Two alternative mechanisms to the radical-based mechanism proposed for thermal hydrosilylation on hydride-terminated porous Si.

Metal complex-mediated hydrosilylation/hydrogermylation of alkenes and alkynes has been applied to hydride-terminated porous Si/Ge.[159,160] A late transition metal complex was reported extremely effective with soluble molecular silanes[161] but can be problematic on the porous surface due to metal deposition or surface oxidation, which quenches the PL.[162] Lewis acid-mediated hydrosilylation/hydrogermylation using $EtAlCl_2$ was found to be effective (ca. 28% coverage when alkyl terminated) and soluble in non-polar solvents.[163]

While photochemical hydrosilylation with white light is a slow process on the flat surface (>10 h),[139] hydrosilylation reaction is induced on the porous surface at room temperature in minutes.[135,141] It is proposed that it is driven by long-lived excitons in porous silicon and nanoparticles that are generated in-situ, as opposed to Si—H cleavage under UV light. As shown in Figure 1.16, electron/hole pairs are formed upon absorption of photons in the nanocrystalline matrix and the photogenerated holes interacted with alkenes, forming Si—C bonds. Then, the silyl-substituted carbocation can be neutralized with a neighbouring H and the electron derived from the original exciton. The reaction rate can be improved further with the addition of electron acceptors, such as CBr_4, CCl_4, C_2Cl_6.[164]

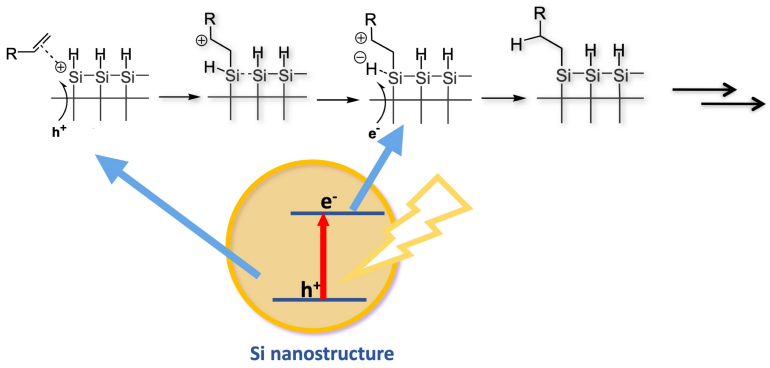

Figure 1.16. Mechanism for the exciton-mediated hydrosilylation on porous silicon and silicon nanoparticles.

Because this reaction is photoinduced, photopatterning can be achieved by applying photomasks with a feature resolution of less than 33 μm (Figure 1.17).[135,141] The authors noticed that the alkyl-functionalized silicon could survive in boiling KOH solution, while the PL of H-terminated area is completely quenched.

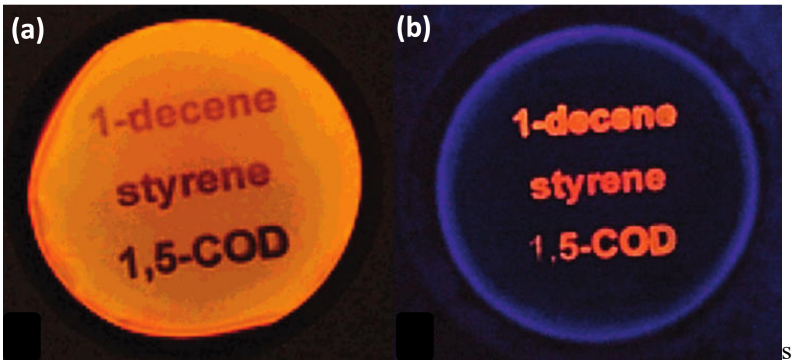

Figure 1.17. Photographs of porous silicon samples photoluminescing under UV irradiation. (a) The words are the areas reacted with these same reagents via a masking procedure. The reacted areas are slightly red shifted and darkened as compared to the PL of the unreacted regions of the sample. (b) The same sample development using boiling pH 12 $KOH_{(aq)}$ solution. Reprinted with permission from ref 141. Copyright 2001 American Chemical Society.

Furthermore, other reactivities that are not observed in the flat surface or molecular silanes were reported on the porous surface. In 2016, Sailor and co-workers

reported the dehydrogenative coupling of primary silanes onto the hydride-terminated porous surface under gentle heat at 80 °C.[165] After surface modification, the PL of the porous surface is not quenched, while the contact angle remains unchanged after 5 days, indicating uniform passivation. The authors also introduced the functional silanes with perfluoro-, alkenyl-, and halide- termination that indicated good post-functionalization potential. The addition of organolithium[166,167] and Grignard reagents[168] to hydride-terminated porous silicon was found to proceed efficiently at room temperature without electronic bias. The mechanism proposed for silicon–carbon formation involves the attack of a weak Si—Si bond by the carbanion nucleophile; the resulting silyl anions on the porous silicon surface can react further, offering the possibility to form mixed surfaces.

1. 2. 2. 2 Si/Ge QDs

Despite the relatively short history of silicon and germanium quantum dot synthesis and functionalization, their interesting optical and electronic properties have attracted enormous attention. Almost all variants of functionalization on the bulk surface and molecular system mentioned above have been applied to the surfaces of QDs. These include but not limited to radical-based,[22,25,26,169–173] transition metal-mediated,[174,175] Lewis acid-catalyzed,[176,177] photochemical[178,179] hydrosilylation, dehydrogenative coupling reactions with[180] or without catalyst,[165] and organolithium reagents[181,182] for silicon-based QDs, and radical-based,[28,183] Lewis-acid catalyzed[28] hydrogermylation and thermally-induced dehydrogenative coupling reactions[44] for germanium-based QDs. These methods are summarized in Figure 1.18.

It is worth mentioning that while thermal thiolation passivation is challenging on a Si QD surface,[184] it is one of the common methods to protect germanium via simply heating at 80 °C,[185] lower than thermally induced hydrogermylation temperature. Furthermore, Ge QDs prepared by many synthetic routes, such as

reduction of $GeCl_4$ using organoalkali and alkali metal reagents, metathesis reactions of germanium Zintl salts, and thermal decomposition of organogermanes, are usually already alkyl- or halide- terminated when the Ge—X bonds are functionalized with organolithium or Grignard reagents.[186]

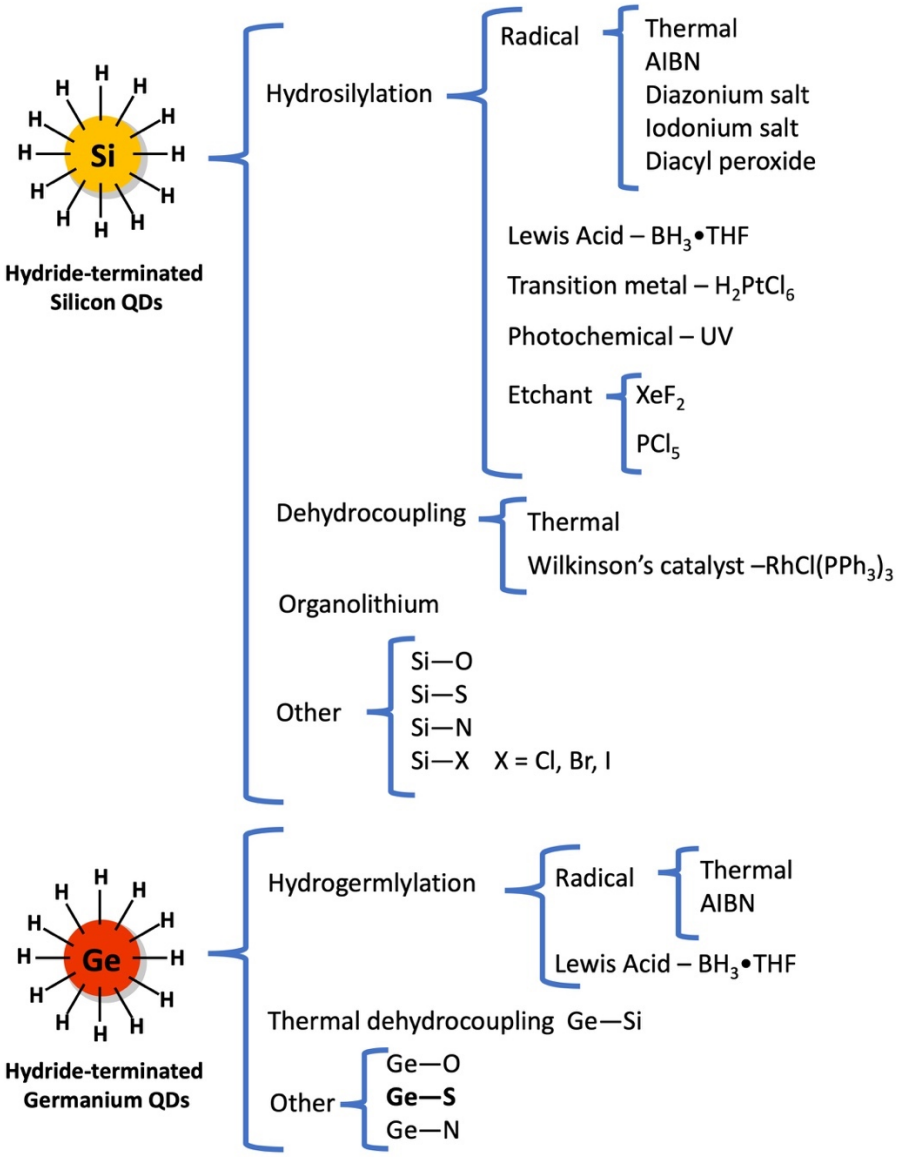

Figure 1.18. Summary of the synthetic pathway of hydride-terminated Si and Ge QDs.

Surprisingly, another category of hydrosilylation that has not been developed yet on bulk surface or not applicable for silane monomers, has been studied in the Veinot lab.[13,187] XeF_2 and PCl_5 are known etchants that cleave Si—Si α bonds.[123,168] When they are exposed to Si surfaces at room temperature, large quantities of fluorine radicals (F•) or chlorine radicals (Cl•) are generated, which rapidly strip off surface Si atoms and leave dangling bonds (≡Si•). Then, the dangling bonds can follow the adventitious hydrosilylation pathway (Figure 1.19). The major advantages of these methods are room temperature, fast reaction (30–60 s, XeF_2 initiated) with high ligand-surface coverage, and bright PL.

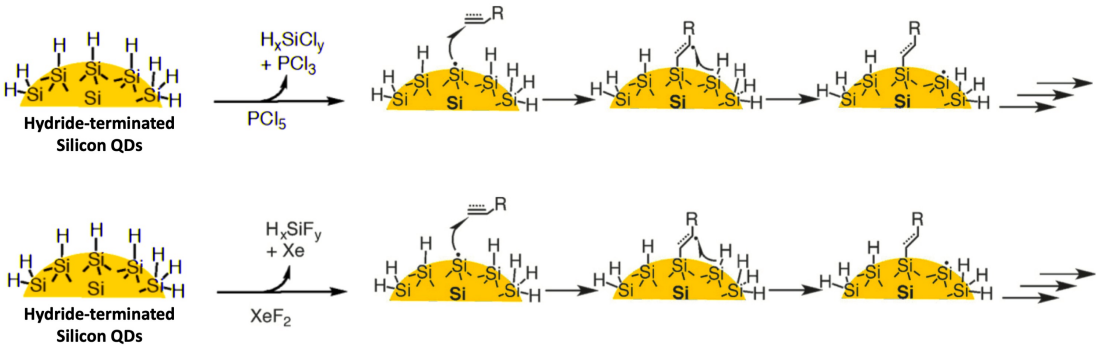

Figure 1.19. Proposed mechanism for etchant-based hydrosilylation. (top) XeF_2 and (bottom) PCl_5.

While alkyl-terminated functionalizations were utilized for surface protection and for introducing functionality, heteroatoms bonded on silicon QDs have a direct impact on the overall band structure. It was noticed first on the slightly oxidized dodecyl passivated Si QDs that the PL colour changes from red to orange.[110,188,189] Dasog et al. have studied the impact of ligand substitution from N-bonded, O-bonded Si QDs and functionalization from halide (-Cl, -Br, -I) terminated Si QDs.[110,111,190] The observation on PL shift is explained by different exciton recombination mechanisms.[112] A PL lifetime study suggests that the alkyl-terminated or slightly oxidized QDs are dominated by the band gap transition from the emission core, where

alkanes have a negligible interface. The blue-emitting alkylamine- functionalized emission is originating from a surface-state-influence. The synthesis path of a few heteroatoms bonded Si QDs examples is summarized in Figure 1.20, with an actual photograph of samples shown in Figure 1.10a.

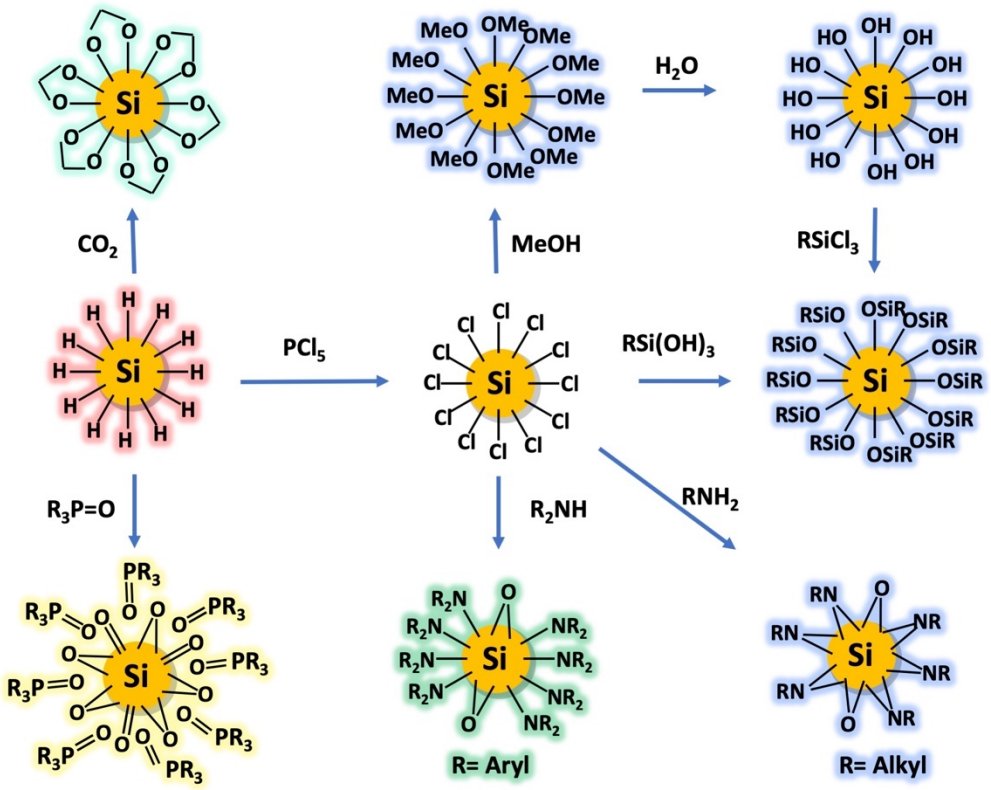

Figure 1.20. Synthesis pathway for heteroatom bonded Si QDs. The PL colour is indicated in the background.

From the work outlined herein, it is clear that these colloidal Si/Ge QDs are amenable to exciting opportunities for both pure and applied research.

1. 2. 2. 3 2D Si/Ge

For the 2D structure that only arose over the past decade, the preliminary results on layered Si/Ge already suggest tantalizing differences from all other Si/Ge nanostructures. First principles simulations predict that the electron mobility of

germanane is five times larger than that of bulk germanium (18000 vs 3900 cm^2/Vs).[191,192] Upon simple thermal annealing of germanane layers in an Ar environment, their resistivity is reduced gradually from >10 MΩ at room temperature to 3 Ω (1.6×10^{-7} Ω•m) upon annealing at 210 °C, which is comparable to that of graphene (1×10^{-8} Ω•m).[193,194] Silicane or surface-functionalized Si NSs emit bright lime green colour[195] PL due to a larger indirect (2.94 eV) or direct band (3.14 eV),[196] compared to Si QDs (ca. 2.1 eV, 3 nm).[181]

As a novel category of materials, the surface functionalization methods are still under development. So far, radical-based (diazonium and iodonium salts, AIBN and thermal),[72,79,195,197] transition metal-catalyzed (H_2PtCl_6•$6H_2O$) [198] and Lewis acid catalyzed[199] (including BH_3•$S(CH_3)_2$, BF_3, $B(C_6F_5)_3$ and $Al(C_6F_5)_3$) hydrosilylation have been reported on silicane surfaces. We recently reported the only hydrogermylation reaction on a germanane surface using thermal heating and AIBN as a radical initiator; this will be discussed in Chapter 3.[200] We also observed reactivity via Lewis acid (BH_3•THF) or etchant (XeF_2) hydrogermylation methods. Similar to hydride- terminated porous silicon surface, Grignard reagents can react with silicane sheets directly at 70 °C for 2 days to yield phenyl-terminated Si NSs that luminesce at 3.0 eV.[201] While organoamines show limited reactivity on hydride-terminated Si(111), they can be accomplished on a silicane surface via direct reaction at 60 °C for 12–24 h, yielding both Si-NHR and Si-(NR)-Si, similar to those on a Si QD surface.[202,203] We also attempted these reactions and noticed successful amination and thiolation on a germanane surface via direct reaction at ≤ 80 °C for 15 h; these reactivities will be the basis of future studies.

Topotactic transformation of a layered Si and Ge precursor (i.e., $CaSi_2$ and $CaGe_2$) with organohalides is a unique category for the direct synthesis of functionalized sheets which is conceptionally consistent to the deintercalation of

$CaGe_2$ with concentrated HCl to yield hydride-termination. In 1961, Bonitz found that $CaSi_2$ can react with different Cl sources ($FeCl_3$, S_2Cl_2, $SbCl_3$, PCl_5, Cl_2) at 60–140 °C to form a layered silicene (Si_6) structure.[204] Xu and co-workers applied a similar method to react $CaSi_2$ with I_2 in acetonitrile and reported the synthesis of multilayer silicene, which can be exfoliated further into monolayers and assembled as an anode material in LIB (Figure 1.21).[205] In 2019, Nakano and co-workers reacted $CaSi_2$ with neat benzyl bromide at 150 °C to yield a yellow benzyl-modified silicane (Figure 1.22). The authors also observed photogeneration under irradiation of UV-vis light (λ > 240 nm and > 420 nm) and no decay of performance after dispersing the sheets in aqueous solution for a week.[206]

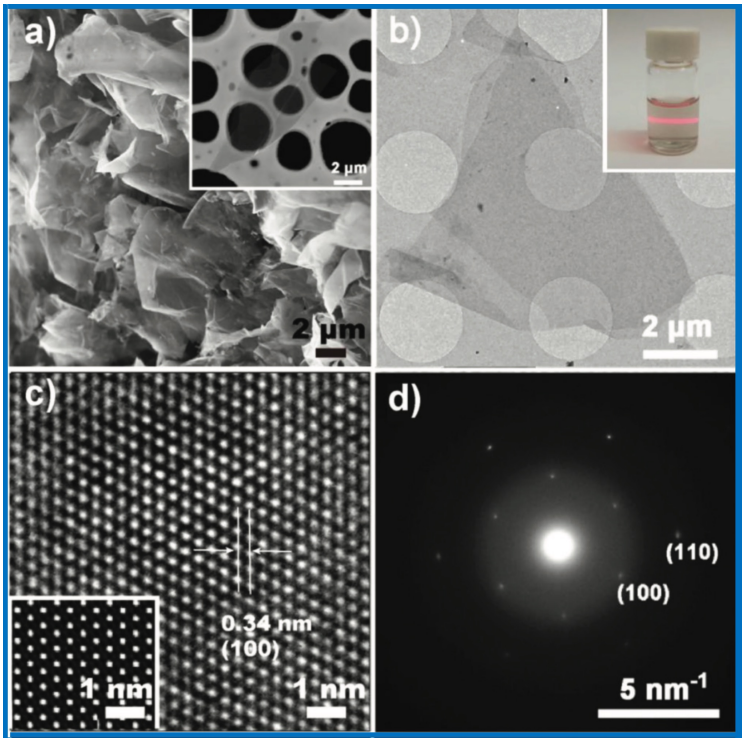

Figure 1.21. (a) SEM images of silicene nanosheets and a single silicene sheet (inset), respectively. (b) TEM image of silicene sheets with the inset showing the photograph of a stable dispersion of silicene in NMP (5 µg mL^{-1}). (c) HRTEM image of silicene matching with AA stacking model. (d) SAED pattern of a silicene sheet. Reprinted with permission from ref 205. Copyright 2018 WILEY-VCH Verlag GmbH & Co.

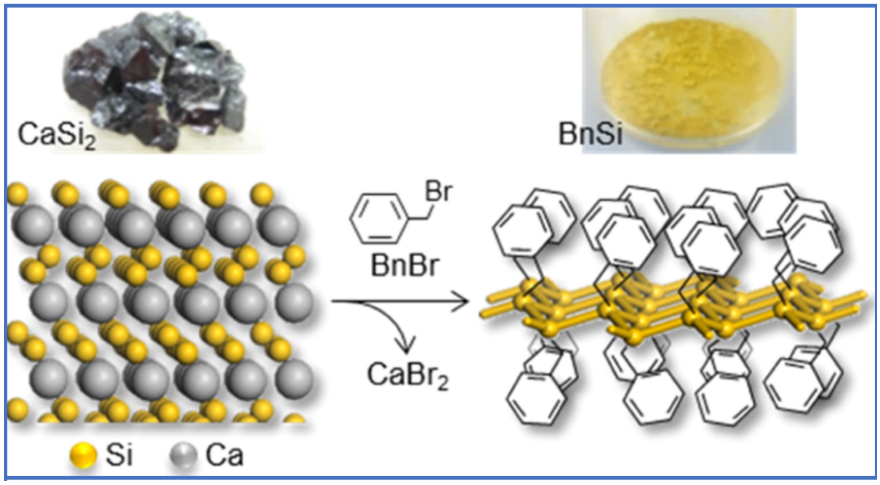

Figure 1.22. The synthesis of benzyl-modified silicane from $CaSi_2$. Reprinted with permission from ref 206. Copyright 2019 American Chemical Society.

The topotactic transformation of $CaGe_2$ is surprisingly more developed compared to $CaSi_2$. In 2014 and 2016, Jiang et al. prepared methyl-terminated germanane sheets by two methods via reacting CH_3I with $CaGe_2$ at room temperature, with >95% surface coverage, which they attributed this to the small methyl group.[207,208] The insertion of a methyl group will not disturb the crystal structure, and layer spacing was calculated as 0.86 nm in $GeCH_3$ compared to that of 0.55 nm in GeH (Figure 1.23a). Red PL with an average of hundreds of picoseconds was observed under UV illumination, and they attributed it to the adsorption of water molecules between interlayer spaces.[209]

This method can be extended to larger sized organo-iodides with the trade-off of week-long reaction times and lower surface coverage (<30 %). To date, heptyl-terminated germanane has been synthesized using this method.[210] Pumera and co-workers prepared iodinated germanane (GeI) by reacting $CaGe_2$ with ICl in acetonitrile and, subsequently, functionalized it with Grignard reagents. There is no doubt that a deeper understanding of these 2D nanostructures is still needed for fundamental and applied applications.

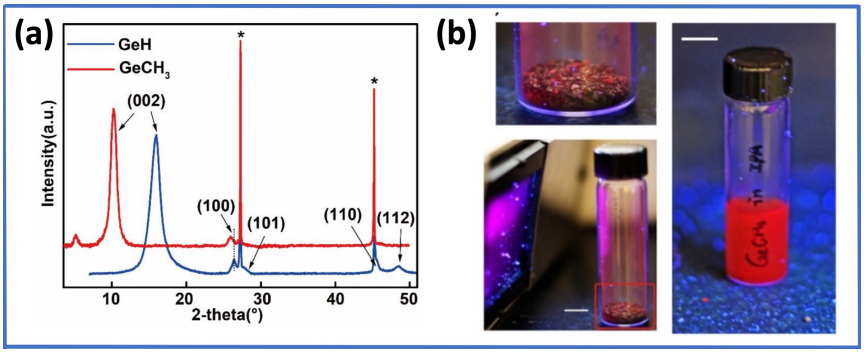

Figure 1.23. (a) pXRD patterns of GeH (blue) and $GeCH_3$ (red), (b) $GeCH_3$ shows red PL under UV light. Reprinted with permission from ref 207. Copyright 2014 Macmillan Publishers Limited.

1. 2. 3 On Si—Si/Ge—Ge Backbone

There is only very limited literature on the postpolymerization functionalization of existing polysilanes and polygermanes. The functionalization was achieved mainly via replacement of aryl groups with halogen by saturating a benzene solution of the polymer with hydrogen halide (HCl, HBr) in AlX_3 catalyst[92,93] or by reacting existing Si—H bonds (usually polymerized by a dehydrocoupling reaction) with unsaturated groups via hydrosilylation.[211] The development of new stable and scalable base polysilanes and polygermanes is under urge demand.

1. 3 Zintl Phases

The term Zintl phases originally was used to recognize the pioneering chemist Eduard Zintl for his contributions in the field of solid-state inorganic compounds.[212–215] They were defined as a subgroup of intermetallic phases where the anions (or the anionic cluster) are formally valence satisfied. These compounds are made up of electropositive group 1 or 2 elements, which donate their electrons to the electronegative group 13, 14, 15, or 16 elements, which use those electrons to form a number of bonds such that each element has a filled shell. The group of Zintl phases is expanding continuously from binary to ternary phases, and transition metals and

rare earth elements also are included in some cases. Zintl electron counting or the Zintl–Klemm concept is a powerful guideline to make new compounds and materials. In many cases, the structural subunits in Zintl phases lead themselves to topotactic reactions, where a metastable intermediate has a crystallographic relationship to the precursor. In Zintl phases NaSi, KSi, KGe, CsSi, and CsGe, or $SrGe_2$, $BaSi_2$, and $BaGe_2$, each Si and Ge atom has a formal charge of (–1) that leads to three coordination and forms isolated tetrahedron clusters $[Si_4]^{4-}$ or $[Ge_4]^{4-}$. Interestingly, this same formal charge and coordination also can arrange the Si and Ge atoms into a layered or 3D network, as observed in $CaSi_2$, $CaGe_2$, or $SrSi_2$. The anions in the Zintl phases also may share a fractional formal charge, such as (-3.33) in Ca_5Si_3 and Ba_5Si_3. This is because the unit cell contains Si_2 dumbbells and isolated Si atoms that have formal charges of (-2) and (-4), respectively. In samples of $Na_{12}Ge_{17}$, two types of clusters, $[Ge_4]^{4-}$ and $[Ge_9]^{4-}$, are observed in the unit cell, where Ge has (0) and (–1) formal charges in the $[Ge_9]^{4-}$ cage. More complicated structures, such as Li_7Ge_{12}, also can be prepared (Figure 1.24).

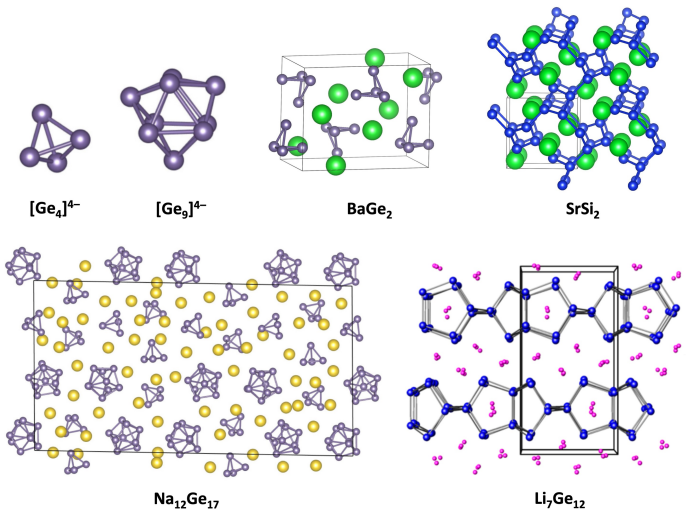

Figure 1.24. Isolated $[Ge_4]^{4-}$ and $[Ge_9]^{4-}$ and crystal structures of $BaGe_2$, $SrSi_2$, $Na_{12}Ge_{17}$, Li_7Ge_{12}. Adapted with permission from ref 214. Copyright 2019 by the authors. Structure of Li_7Ge_{12}, adapted with permission from ref 216. Copyright 2014 American Chemical Society.

The pure phase of isolated $[Ge_9]^{4-}$ cluster was prepared in K_4Ge_9 by Fässler and co-workers and has been applied as a soluble Ge source in the template formation of inverse opal structures (Figure 1.25).[217,218] The Zintl phases are also precursors in the synthesis of Si and Ge QDs, as introduced above. Nanoporous Ge or $Ge_{1-x}Si_x$ were prepared from dissolving solid K_2Ge_9 or $K_4Ge_5Si_4$ in ethylenediamine and mixing with cetyltrimethylammonium bromide (CTAB) surfactant.[219,220] Hexagonal mesoporous Ge can be prepared from Mg_2Ge and $GeCl_4$.[221]

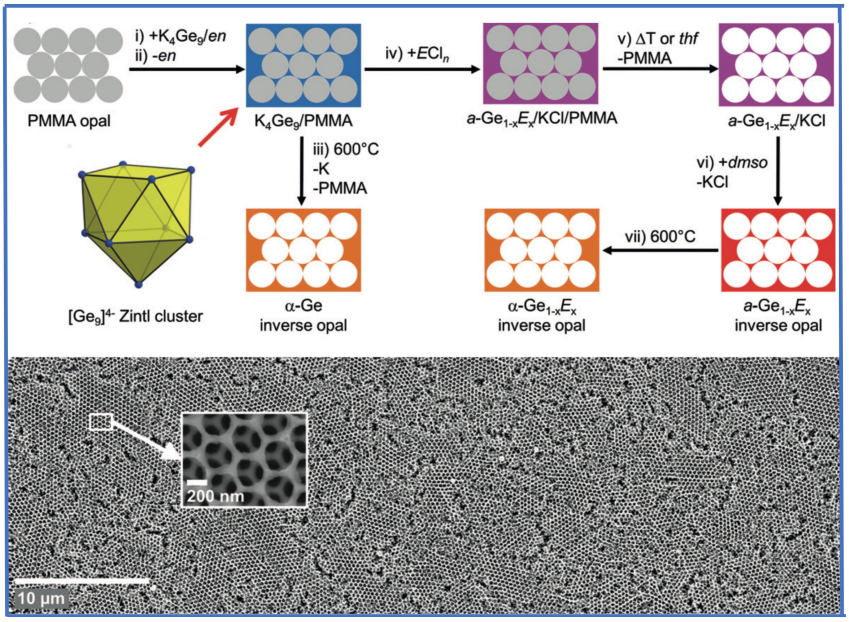

Figure 1.25. (Top) Fabrication of Ge inverse opals by controlled oxidation of $[Ge_9]^{4-}$ Zintl clusters. (Bottom) SEM image of Ge inverse opal with the magnified area indicated. Reprinted with permission from ref 218. Copyright 2016 Wiley-VCH Verlag GmbH & Co.

1. 3. 1 Ca–Ge System

The thermodynamic properties of the Ca–Ge system are very limited because of the volatility of elemental calcium. The phase diagram was incomplete until 2002 when Palenzona et al. updated the Ca_7Ge_6 intermetallic phase (Figure 1.26 dash line).[222]

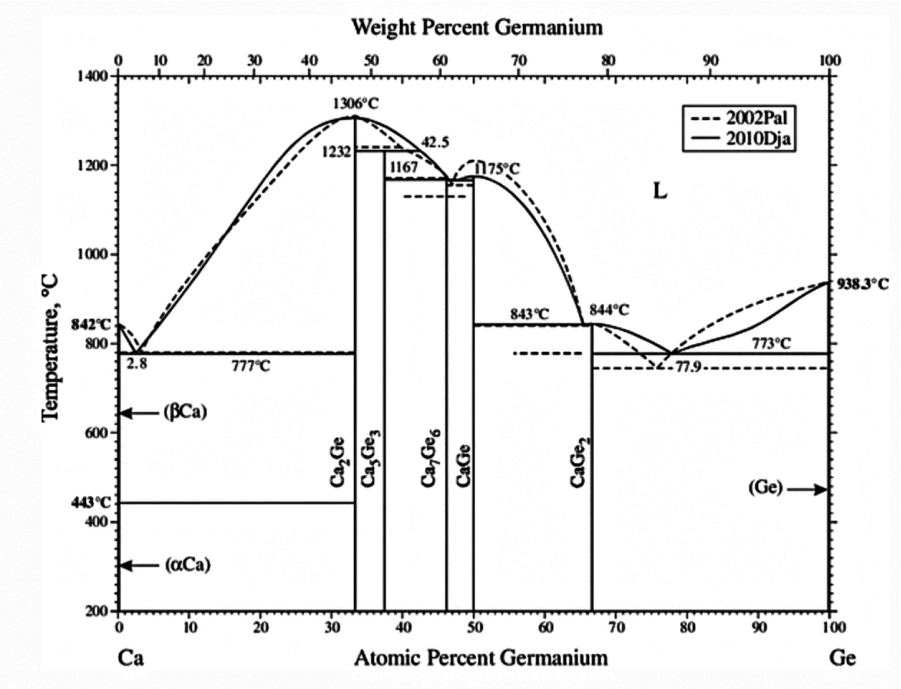

Figure 1.26. Ca—Ge phase diagram, dash line: Palenzona, solid line: Djaballah. Reprinted with permission from ref 223. Copyright 2013 ASM International.

Based on his work, Djaballah reported the new thermodynamic modeled phase diagram.[223,224] There are in total four intermetallic compounds: Ca_2Ge, Ca_7Ge_6, CaGe, and $CaGe_2$. Three other compounds are observed only at low temperatures, with unknown composition: $Ca_{33}Ge$, Ca_7Ge and Ca_5Ge_3. The crystal structures of all compounds except $Ca_{33}Ge$ are shown in Figure 1.27.

$Ca_{33}Ge$ and Ca_7Ge are phases having a high content of electropositive element that does not obey the Zintl–Klemm concept, as Cl atoms are cubic close-packed with superstructures imposed by the Ge atoms.[215] Ca_2Ge is the first intermetallic phase with the highest melting temperature of the system. All the Ge atoms in the unit cell are four coordinated with Ca atoms, leading to isolated anions with limited potential as a precursor. Similarly, compound Ca_5Ge_3 only contains Ge_2 dumbbells and isolated Ge atoms, which would potentially form germane (GeH_4) and digermane (Ge_2H_6) gas after acid deintercalation.

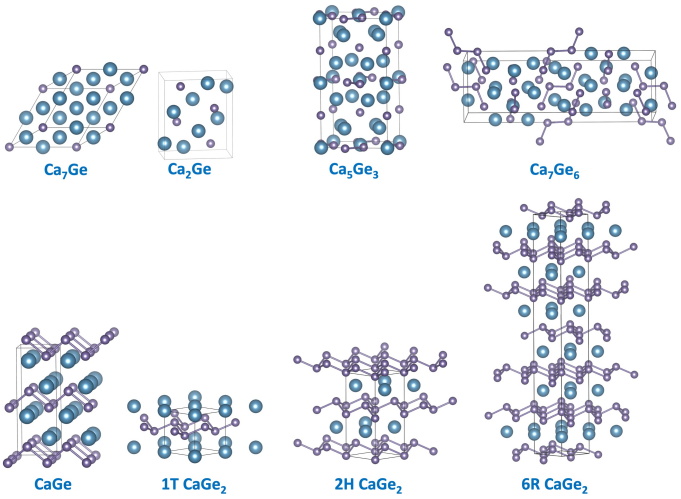

Figure 1.27. The crystal structure of Ca–Ge Zintl salts with indicated unit cell and extended structures of CaGe and $CaGe_2$ present for a clear view of interlayer structures. 1T $CaGe_2$ is not reported experimentally.

The compound Ca_7Ge_6 is crystalline, in the form of large platelets separated by voids, for which the equilibrium in these alloys was difficult to reach after 15 attempts by Palenzona et al.[222] During the synthesis of compound CaGe, we noticed the presence of a small Ca_7Ge_6 impurity when at.5% excess Ca was loaded in the arc furnace and characterized by powder X-ray diffraction (pXRD, Figure 1.28). Upon acid/water treatment, they decompose into molecular oligogermanes that can be isolated via centrifugation easily.

The equiatomic composition CaGe can be prepared by congruently melting Ca and Ge together.[225] The Ge subunits are arranged into planar zig-zag chains that are structurally equivalent to the preferred *anti* conformation in the Ge—Ge polygermane backbone. These zig-zag chains are aligned parallelly to form a "layered" morphology, where an interlayer space is separated by two layers of Ca atoms. The last intermetallic compound is $CaGe_2$, where four polytypes (2H, 3R, 4H, and 6R) have been reported, all containing germanene layers stabilized by Ca cations.[71,226–229]

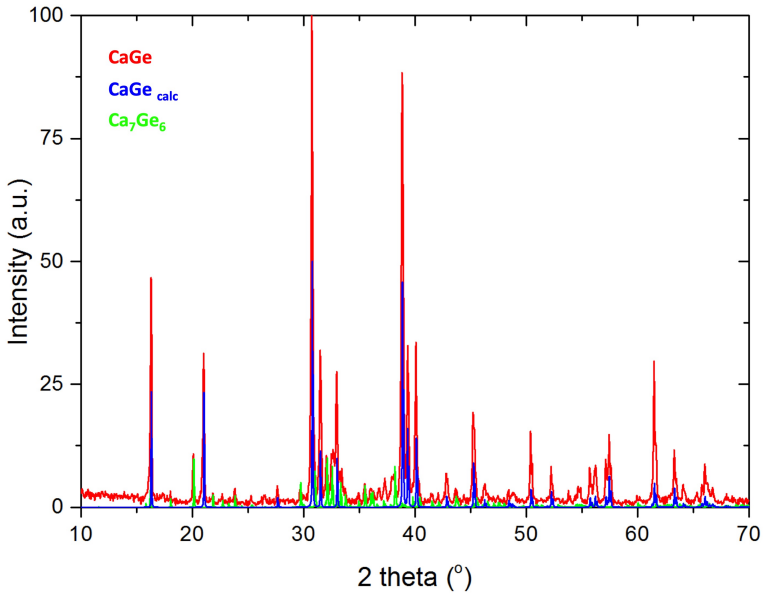

Figure 1.28. Powder X-ray diffraction pattern of (red) as synthesized CaGe, (blue) calculated pattern, and (green) calculated Ca_7Ge_6 pattern (λ = 1.5406 Å).

The 2H and 4H polytypes have a hexagonal crystal system with two and four layers of germanene stacked in the AB and AA'BC order, respectively. The 3R and 6R polytypes have a trigonal rhombohedral crystal system, with three and six layers of germanene stacked in the ABC and AA'BB'CC' order, respectively. The computed structure of 1T polytype is shown in Figure 1.27, which has germanene layers in an AA-type of stacking that have not been characterized experimentally. However, this type of Ge layer stacking was observed in 1T $EuGe_2$.[228]

1. 3. 2 Exfoliation of Layered Materials

After the topotactic transformation of Zintl precursor $CaGe_2$ and CaGe using acid or organohalides, the resulting germananes or polygermanes are still intact as bulk material and need to be exfoliated into individual layers or strands in order to maximize the surface area for further functionalization or to increase their potential catalytic reactivity. Additionally, the electron wave function extends in three

dimensions in a layered crystal that could be constrained to adopt a 2D wave function, thus modifying the electronic band structure.[230] In 2004, Geim and Nocosolov showed the exfoliation of graphite into graphene sheets using Scotch® tape.[52,53] Similarly, the van der Waals force between germanane layers are in the similar order as graphite, and the exfoliation is achieved using the same technique.[70] While this mechanical exfoliation remains the source of the highest quality and resulted in some major advances, it suffers from extremely low yield, with monolayers needed to be selected from multilayers. One possible solution is the exfoliation of layered compounds in liquids to give a large quantity of freestanding nanosheets. Recently, Nakamura and Nakano[231] rationally studied the sonochemical exfoliation efficiency of germanane powders in 35 solvents (Figure 1.29, Table 1.2) and their dispersibility after one day of standing.

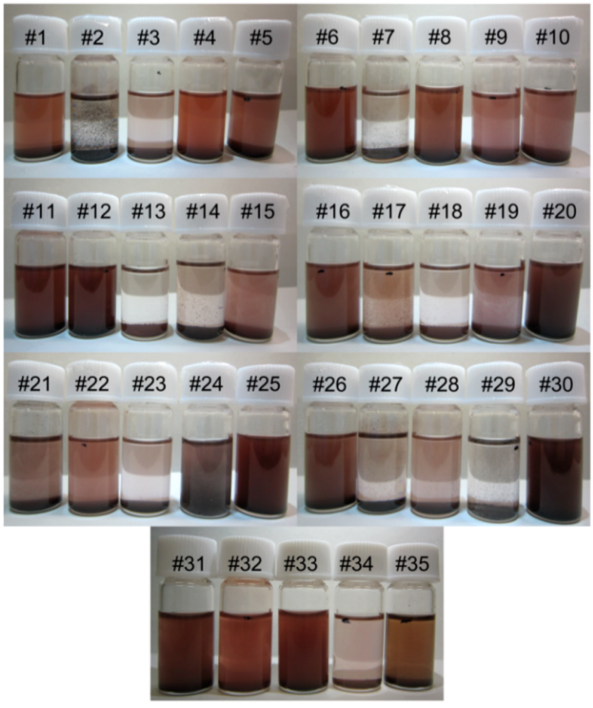

Figure 1.29. Photographs of germanane dispersions in probe liquids #1−35. Reprinted with permission from ref 231. Copyright 2018 American Chemical Society.

The probed solvents are summarized in Table 1.2. It is worth noting that these dispersibilities are a good guideline for hydride-terminated Ge NSs. Surface functionalized Ge NSs with designated ligands often show significant improvement in solvent dispersibility.

Table 1.2. Selected Liquids #1−35 for Germanane Dispersibility Tests

no.	Liquid name	no.	Liquid name	no.	Liquid name
1	Acetone	13	Acetonitrile	25	2-Butanol
2	Toluene	14	Tetrachloroethylene	26	n-Butyl Acetate
3	2-Propanol	15	Acetic Acid	27	Carbon Disulfide
4	Methyl Ethyl Ketone	16	Ethanol	28	Diether Ether
5	N-Methyl-2-pyrrolidone	17	Cyclopentanone	29	1,3-Butanediol
6	Dimethyl Formamide	18	Ethyl Acetate	30	Cyclohexylchloride
7	Hexane	19	Formic Acid	31	Dimethyl Sulfoxide
8	Formamide	20	Ethylene Glycol	32	1,3-Dioxolane
9	1,4-Dioxane	21	Tetrahydronaphthalene	33	Caprolactone
10	Propylene Carbonate	22	Chloroform	34	Methylene Dichloride
11	o-Dichlorobenzene	23	Methylal	35	1-Bromonaphthalene
12	Benzyl Alcohol	24	Cyclohexanol		

1. 4 The Scope of This Thesis

The underlying hypotheses of this work are Zintl phases will provide convenient precursors for the preparation of 1D and 2D germanium nanostructures and that their surface chemistry can be tailored using solution methods. Chapter 2 concentrates on the attempts to synthesize the high purity layered precursor $CaGe_2$ and its topotactic transformation into fully hydride-terminated germanane flakes. In Chapter 3 and 4, the germanane flakes were exfoliated in liquid phase and functionalized simultaneously into Ge NSs with different functionality.

In Chapter 3, two of the radical-based hydrogermylation reactions, thermally

or radical-initiator are introduced, both show improved solvent dispersibility and thermal stability compare to hydride-terminated Ge NSs. The crystal structures of Ge networks were intact after functionalization and show layer stacking dependent electron diffraction patterns. For the Ge NSs prepared at higher temperature, the solution appears as a dark colour with a lower bandgap. A ligand-sheet-ligand model is derived from the overlayer model for surface coverage estimation.

In Chapter 4, the surface of hydride-terminated Ge NSs was reacted directly with Si—H bonds via a thermal dehydrogenative coupling reaction. This reaction is mild, where both primary hydridosilanes ($H_3SiC_{18}H_{37}$, $H_3Si(CH_2)_2(CF_2)_6CF_3$), and tertiary hydridosilanes ($HSi(Me)(C_{18}H_{37})$, $HSi(CH_{17})_3$) can be modified on to the Ge NSs surface. The reactivity was explored further with hydride-terminated Si QDs at average diameters of 3–64 nm. The successful reaction was monitored as the quenching of PL, and the synthesized hybrid material was evaluated directly under electron microscopy.

Chapter 5 focuses on the synthesis of poly(dihydrogermane) from precursor CaGe by two topotactic transformation reactions using HCl or water. The resulting compounds exhibit a substantial difference in stability and optical band gap. The Ge—H bonds on the Ge—Ge backbone were modified further via hydrogermylation reactions.

Finally, Chapter 6 summarizes the findings made in Chapters 2–6 and provides a brief outlook for the methodologies and materials synthesized in this Thesis.

Chapter 2

Synthesis and Characterization of Germanane[1]

The preparation and applications of van der Waals materials has become an area of intense investigation because exfoliation of layered precursors can yield new materials with properties that differ substantially from their bulk material equivalents.[55,230,232,233] The prototypical van der Waals material is graphene; it exhibits tremendously high carrier mobility compared to graphite and is among the strongest materials known.[53,55,234] While the preparation and derivatization as well as physical and chemical properties of graphene have been studied widely, investigations of sheet materials of carbon's heavier periodic congeners (i.e., silicon and germanium) are far less prevalent.[70,232]

Doubtless, the limited number of studies of nanosheets of heavier Group 14 elements is partly because there is no naturally occurring layered allotrope of silicon or germanium with a graphite-like structure. Epitaxially grown 2D elemental Si (silicene) and Ge (germanene) can be achieved only on metallic surfaces in ultrahigh vacuum conditions[66,67,235] and must be encapsulated to survive in the ambient environment.[68] The search for a suitable layered precursor for Si sheets saw Wöhler deintercalate layered calcium disilicide ($CaSi_2$).[236] Stutzmann and co-workers extended this Ca-deintercalation methodology to prepare hydride-terminated germanane $(Ge_6H_6)_n$ from layered calcium digermanide ($CaGe_2$).[71,227] Goldberger and co-workers revisited this approach and mechanically exfoliated hydride-terminated

* Portions of this Chapter have been copied and/or adapted from the following publication: Yu, H.; Helbich, T.; Scherf, L. M.; Chen, J.; Cui, K.; Fässler, T. F.; Rieger, B.; Veinot, J. G. C. Radical-Initiated and Thermally Induced Hydrogermylation of Alkenes on the Surfaces of Germanium Nanosheets. *Chemistry of Materirals*. **2018**, *30* (7), 2274–2280.

Ge nanosheets (H-GeNSs) as single- and few-layer sheets via Scotch Tape® and polydimethylsiloxane lift-off.[70] H-GeNSs prepared in this way possess a buckled honeycomb structure, with surfaces crystallographically identical to Ge (111) oriented wafers.[66,237,238]

This Chapter will focus on the preparation of $CaGe_2$ precursor via an alternative heating method for fast production and its deintercalation into germanane flakes (Figure 2.1), with detailed characterization and comparison to the germanane materials prepared in the previous methods.

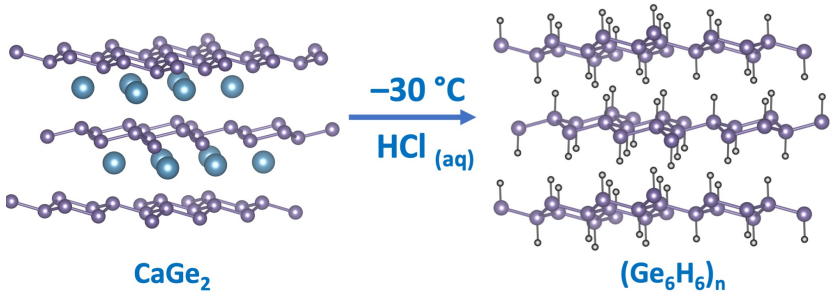

Figure 2.1. Schematic illustration of germanane $(Ge_6H_6)_n$ synthesis.

2.1 Material Synthesis

2. 1. 1 Material

All reagents were purchased from *Sigma-Aldrich* and used without further purification, unless otherwise stated. All solvents, except acetone, were dried using an Innovative Technology, Inc. Grubbs-type solvent purification system. Anhydrous ethanol was dried over molecular sieves (3 Å), degassed via three freeze-pump-thaw cycles using an argon-charged double manifold. All solvents and liquid reagents were degassed via three freeze-pump-thaw cycles using an argon-charged double manifold and stored in a MBraun glove box with nitrogen working gas.

2. 1. 2 Synthesis of $CaGe_2$

A stoichiometric mixture of calcium (granular, Sigma, 99.0 %) and germanium (Sigma, 99.999 %) was pressed to a pellet and subsequently melted in an arc furnace installed in an argon-filled glove box (MBraun, H_2O and O_2 levels < 0.1 ppm). It also is noticed that an arc furnace in an ambient condition produces $CaGe_2$ in adequate quality after the chamber has been evacuated and backfilled with argon for three cycles (Figure 2.2). Since calcium has a high vapour pressure compared to germanium, the granulated calcium needs to be sandwiched between germanium powder during the pellet press. Direct exposure to a high temperature will result in the evaporation of calcium and leave elemental germanium in the sample. To ensure effective homogenization, the resulting silver metallic regulus was melted upon simultaneous heating from the top and bottom in the arc furnace, ground thoroughly in an agate mortar, pressed again to a pellet, melted from both sides in the arc furnace, and ground into a powder again.[239]

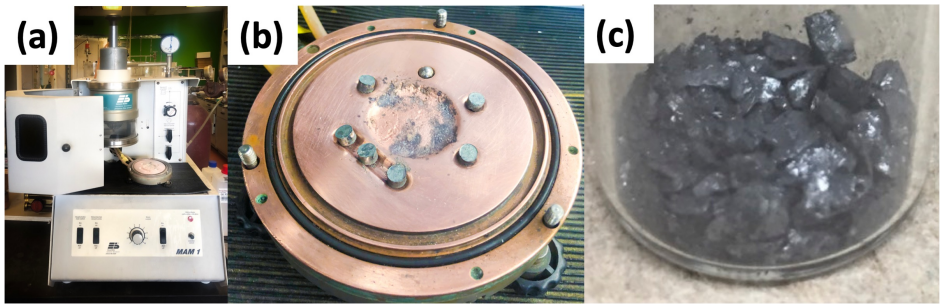

Figure 2.2. Photographs of (a) arc furnace, model Compact Arc Melter MAM-1, (b) calcium and germanium pressed into a pellet, and (c) the as prepared $CaGe_2$ granular.

2. 1. 3 Synthesis of Germanane $(Ge_6H_6)_n$

A standard Schlenk flask was charged with 100 mL of concentrated HCl, cooled down to -30 °C in a low-temperature freezer before reaction, and fine powdered

$CaGe_2$ (1.00 g) was added. The mixture was maintained at -30 °C for at least seven days and shaken 10 times per day at regular intervals.[70] Then, the reaction mixture was filtered using a glass frit under argon (Figure 2.3). The obtained shiny metallic flakes were washed three times, first with ice-cold water and then three times with anhydrous ethanol, followed by drying under the vacuum on the Schlenk line.

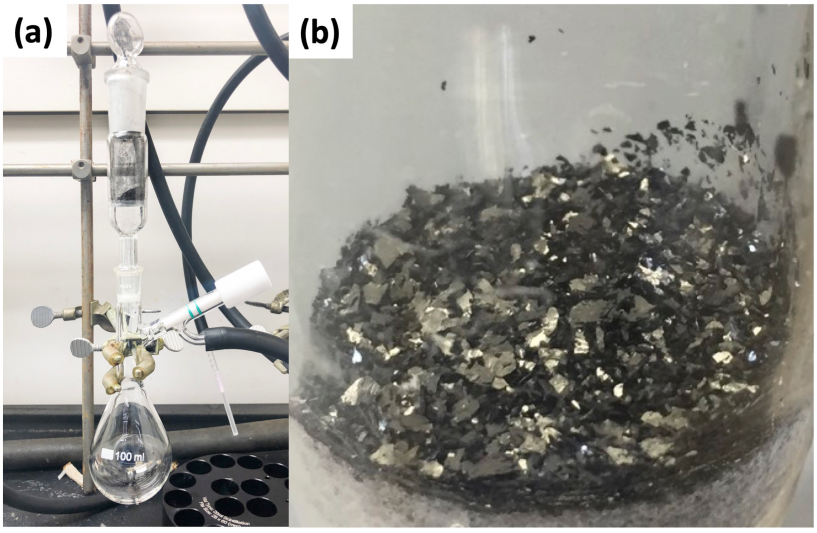

Figure 2.3. Photographs of (a) purification and drying apparatus and (b) dried $(Ge_6H_6)_n$ flakes in a glass frit.

2. 2 Material Characterization

2. 2. 1 Fourier Transformed Infrared (FT-IR) Spectroscopy

FT-IR Spectra were acquired using a Thermo Nicolet Magna 750 IR Spectrometer. Samples were prepared by drop coating a toluene dispersion of the material of choice onto an electronic-grade Si-wafer (N-type, 100 surface, 100 mm thickness and 10 ohm·cm resistivity) and dried under a nitrogen atmosphere.

2. 2. 2 Electron Microscopy

Bright-field transmission electron microscopy (TEM) images were acquired using a Hitachi- 9500 or JEOL JEM-ARM200CF S/TEM electron microscope at accelerating voltages of 300 kV or 200 kV, respectively. HRTEM images obtained from a Hitachi-9500 were processed using Gatan Digital Micrograph software (Version 3.22.1461.0). TEM samples were prepared by depositing a drop of GeNS suspension in toluene onto a holey/lacey carbon-coated copper grid (Electron Microscopy Inc.) The grid was kept in a vacuum chamber for at least 24 h prior to data collection.

Scanning electron microscopy (SEM) images were obtained from Zeiss Sigma 300 VP-FESEM (equipped with a Bruker energy dispersive X-ray spectroscope) at an accelerating voltage of 20 kV. SEM samples were prepared by depositing $CaGe_2$ or germanane powder onto a carbon tape mounted on an aluminum stub. Non-conductive samples were coated further with graphite using a thermal evaporator.

2. 2. 3 X-ray Photoelectron Spectroscopy (XPS)

XPS was performed using a Kratos Axis Ultra instrument operating in energy spectrum mode at 210 W. Samples were prepared by depositing a suspension of the material of choice onto a copper foil substrate, followed by drying in air. Prior to the analysis, the Ge (111) wafer reference was cleaned by immersing in 30% v/v H_2O_2 for 90 s, followed by 10 min etching in 10% v/v HF. The base and operating chamber pressure were maintained at 10^{-7} Pa. A monochromatic Al K source (λ = 8.34Å) was used to irradiate the samples, and the spectra were obtained with an electron take-off angle of 90°. CasaXPS software (VAMAS) was used to interpret high-resolution spectra. All spectra were calibrated internally to the C1s emission (284.8 eV). After calibration, a Shirley-type background was applied to remove most of the extrinsic loss of structure.

2. 2. 4 Powder X-ray Diffraction (XRD)

PXRD data were collected using an Inel MPD MultiPurpose Diffractometer equipped with a CPS 120 curved position sensitive X-ray detector and Cu Kα (8.047 KeV energy) source or a Stoe STADI P diffractometer equipped with a Ge(111) monochromator for Cu Kα radiation (λ = 1.54056 Å) and a Dectris MYTHEN DCS 1K solid-state detector. The $CaGe_2$ was ground in an agate mortar, filled into 0.3 mm glass capillaries, and then sealed. The sample was measured within a 2θ-range of 5–87.5° (PSD steps, 1.5°; time/step,15 s). The H-Ge powders were deposited on an amorphous silica holder.

2. 3 Results and Discussion

Compared to the previously reported $CaGe_2$ precursor synthesis, either through depositing element calcium onto a Ge wafer at an elevated temperature[71,78,227] or by sealing Ca/CaH_2 and Ge in a quartz tube under a vacuum environment, with a 2–6 days heating profile in a conventional tube furnace,[70,222] the use of a compact size arc furnace in this method significantly reduces the synthesis time to within an hour while producing ca. 2.2 g of high-quality $CaGe_2$. Calcium ions were deintercalated topotactically from crystalline $CaGe_2$ to afford hydride-terminated germanane flakes (HGe-flakes).[70] Exposure of $CaGe_2$ to cold (i.e., –30 °C) concentrated HCl for one week caused the characteristic gray appearance of $CaGe_2$ to become black with a shiny metallic luster (Figure 2.3).

2. 3. 1 Structural Characterization

Scanning electron microscopy (Figure 2.4a) shows a clear layered morphology of $CaGe_2$. After deintercalation, as shown in Figure 2.4b, fissures across the flakes were formed parallelly due to the insertion of hydrogen into the Ge layers, extending

interlayer distance and relaxing the strains.

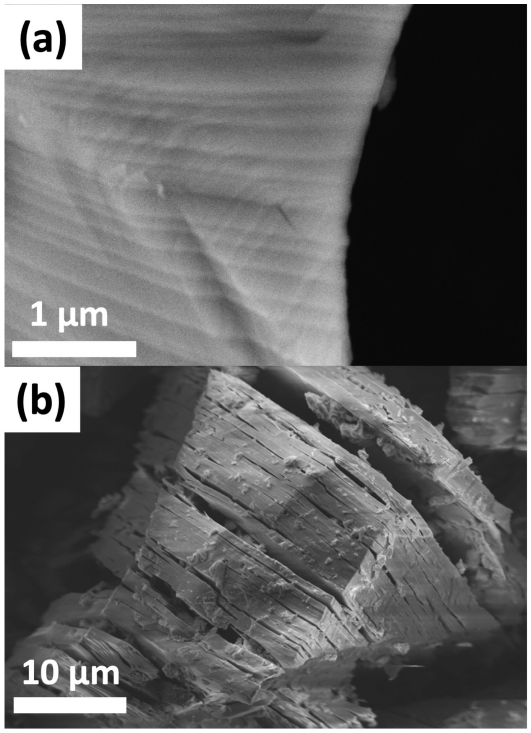

Figure 2.4. Scanning electron microscopy images of (a) $CaGe_2$ and (b) $(Ge_6H_6)_n$.

Powder X-ray diffraction (XRD) confirmed that the synthesized $CaGe_2$ was highly crystalline, and the pattern can be indexed to a *6R* unit cell where the Ge layers stacked in an AA'BB'CC' form (Figure 2.5).[228] After deintercalation, the germanane flakes contains the same *6R* unit cell, with a = 3.99 Å and $c/6$ = 5.50 Å; these are slightly smaller in a (4.01 Å) but with a larger spacing in the c direction (5.10 Å) compared to that of $CaGe_2$. These observations indicate that the germanane flakes are composed of $(Ge_6H_6)_n$ layers, and the interlayer spacing increases as a result of Ge–H bonds. Compared to the commonly synthesized and relatively stable *2H* polytype, the *6R* unit cell is one of the polytypes that is unstable at ambient conditions due to the slightly larger interlayer spacing in the c axis.[71,228] On the other hand, this approach exploits the comparatively weak interlayer interactions (i.e., 72 meV per Ge atom)

within germanane flakes, which are dominated by van der Waals forces and are of the same order of magnitude as that of graphite (i.e., 53.5 meV per C atom).[240,241] Individual $(Ge_6H_6)_n$ nanosheets (H-GeNSs) could be prepared easily via sonication of bulker flakes in an appropriate organic solvent (e.g., toluene).

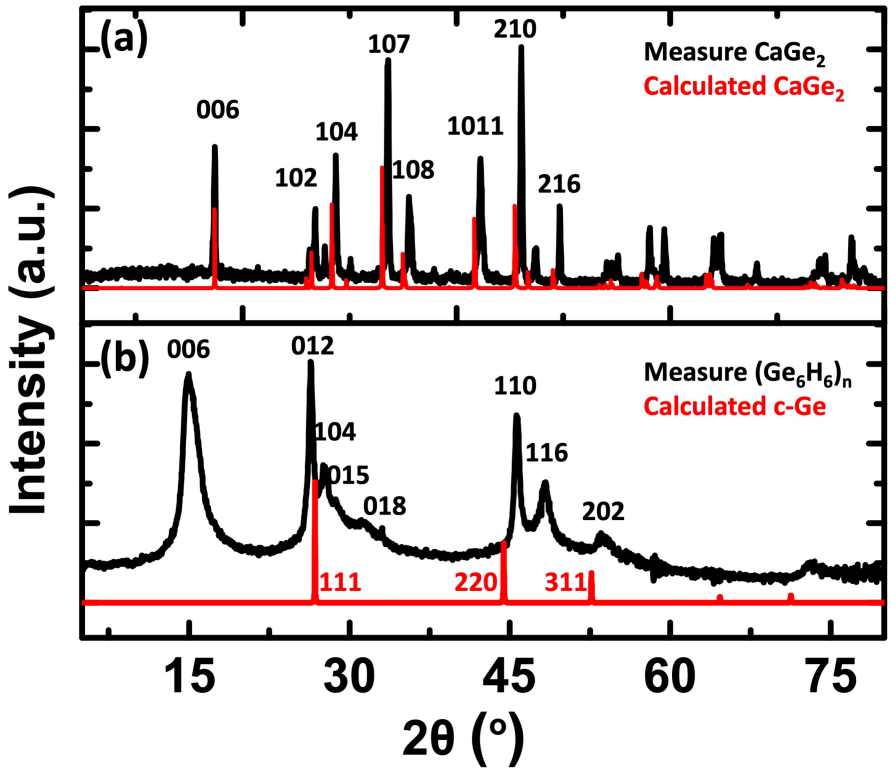

Figure 2.5. XRD patterns of (a) $CaGe_2$ compared with calculated values and (b) $(Ge_6H_6)_n$ powders compared to Ge powders with diamond lattice. The $(Ge_6H_6)_n$ of the regularly stacked sheets can be indexed by a *6R* $CaGe_2$ unit cell with a = 3.99 Å and c = 33.0 Å, with no elemental Ge impurity.

The degree of exfoliation impacts the physical appearance of the resulting H-GeNSs. After a 5 min ultrasonication, the black germanane flakes break up to yield a pink suspension (Figure 2.6); this suspension becomes deep red after a 3 h sonication.

After exfoliation, these freshly prepared sheets were screened under bright-field transmission electron microscopy immediately; the loose stacking of each

monolayer can be observed with a contrast comparable to the thin lacey carbon support (Figure 2.7). Further electron diffraction analysis reveals that the monolayers have a hexagonal symmetry, assuming a viewing from the [0001] zone axis, and the inner pattern can be assigned as a $(10\bar{1}0)$ plane, while the outer pattern is $(11\bar{2}0)$ planes, with lattice constants of 0.34 nm and 0.20 nm, respectively.

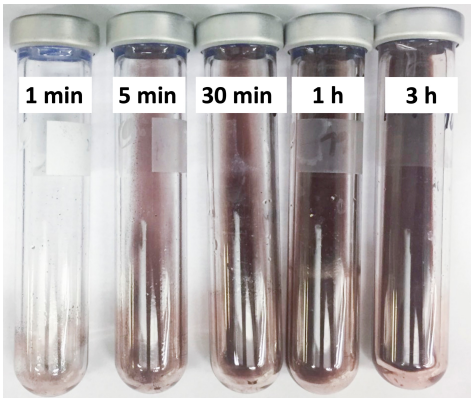

Figure 2.6. Photograph of $(Ge_6H_6)_n$ in toluene with different sonication times.

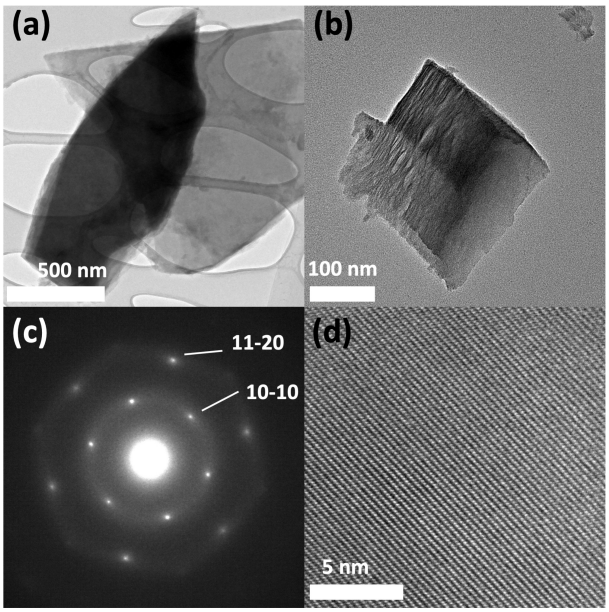

Figure 2.7. Transmission electron microscopy images of H–Ge NSs. (a, b) low magnification, (c) electron diffraction pattern, and (d) high resolution.

2. 3. 2 Compositional Characterization

Surface hydride-termination of $(Ge_6H_6)_n$ flakes was confirmed using FTIR spectroscopy, which shows characteristic Ge–H stretching and bending vibrations at 2001 and 830 cm^{-1}, respectively (Figure 2.8). Additional O–H stretching and bending vibrations at ~3370 and 1630 cm^{-1} can be assigned to water adsorbed between these layers.[200,242]

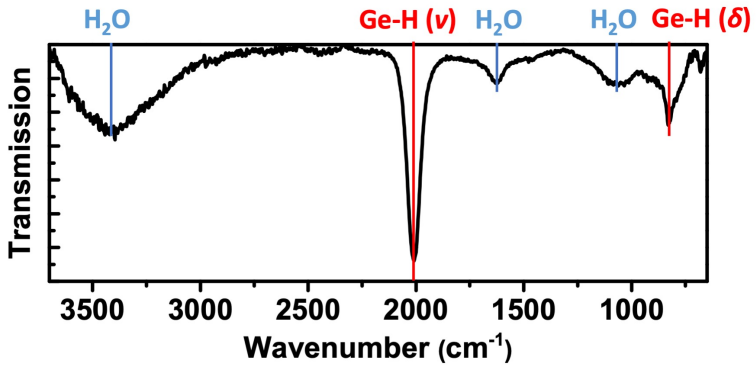

Figure 2.8. FTIR spectrum of $(Ge_6H_6)_n$ flakes.

Comparing the Raman spectra of crystalline Ge(111), germanane flakes, and exfoliated H–Ge NSs provides insight into the Ge–Ge bond energy (Figure 2.9). The present germanane flakes show a Ge-Ge feature at 287 cm^{-1} that is broader than that of the Ge(111) wafer and is shifted to lower energy. These observations are expected because of the incorporation of hydrogen and loss of the long-range structure of crystalline Ge(111). Germanane flakes and exfoliated H–Ge NSs exhibit comparably broad Ge-Ge features at approximately the same Raman shift (i.e., 289 cm^{-1}). We attribute this observation to the H-GeNSs reassembling upon drying during sample preparation.

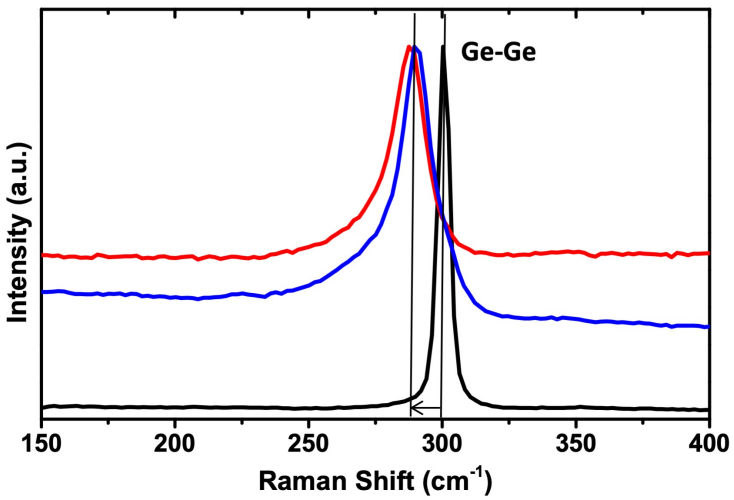

Figure 2.9. FTIR spectra of (black) elemental Ge powder, (blue) $(Ge_6H_6)_n$ flakes and (red) H-GeNSs.

Elemental composition of $CaGe_2$ and germanane flakes was confirmed by energy dispersive X-ray spectroscopy (EDX, Figure 2.10) and X-ray photoelectron spectroscopy (XPS, Figure 2.11). The EDX result of $CaGe_2$ indicates an average of 1:1.96 atomic ratio and the presence of trace O (<2 at%). After deintercalation, due to the limit of EDX technique that H cannot be detected, Ge is the only element noticed where the O level is even lower than the substrate conductive double-sided tape.

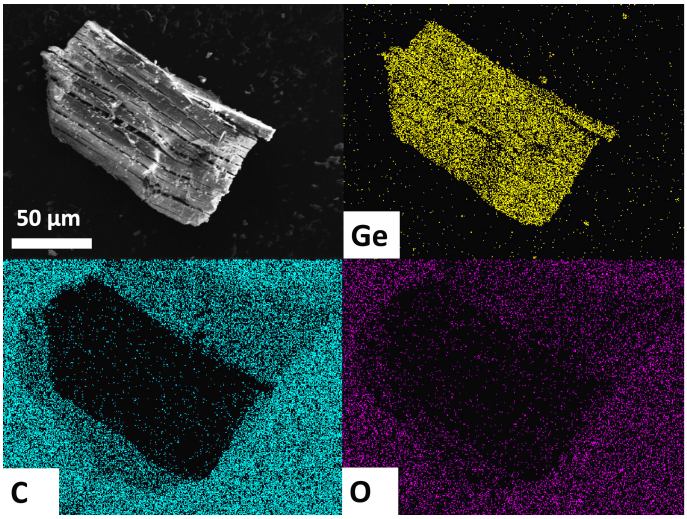

Figure 2.10. SEM image of $(Ge_6H_6)_n$ flakes with Ge, C, and O elemental mapping.

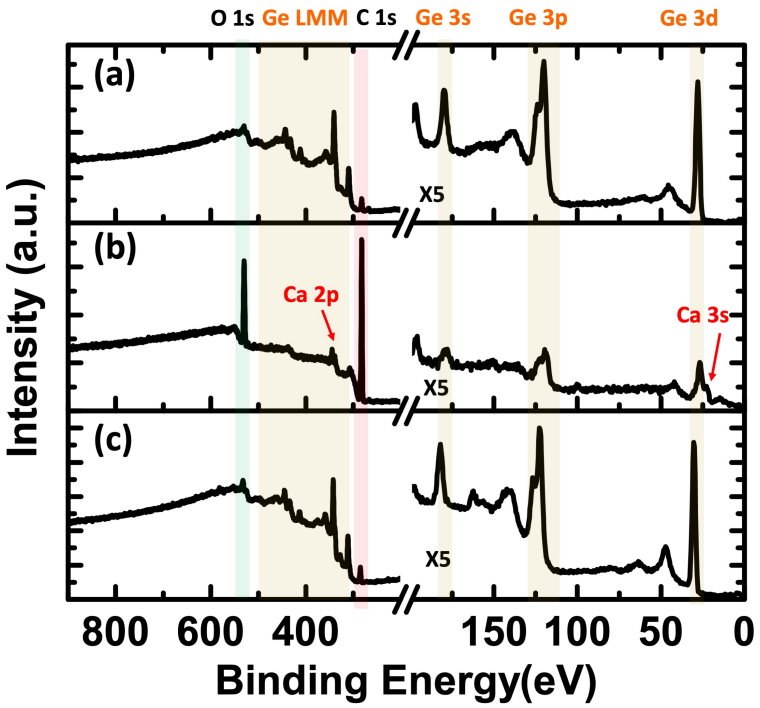

Figure 2.11. Survey X-ray photoelectron spectroscopy of clean (a) Ge (111) wafer, (b) $CaGe_2$ and (c) germanane flakes.

Consistent with the EDX results, the survey XP spectra of $CaGe_2$, germanane flakes, and a freshly etched clean Ge (111) wafer as reference indicate almost identical spectra between the germanane and the Ge wafer. Additional Ca 2p and 3s emissions can be observed in $CaGe_2$, and strong O 1s and C 1s emissions are contributed mainly from the substrate conductive double-sided tape.

The high-resolution XP spectrum gives insight into the oxidation state of Ge atoms on the $CaGe_2$ and germanane flake surface (i.e., within the top 10 nm, Figure 2.12). All spectra were calibrated to adventitious carbon at a binding energy (BE) of 284.8 eV.[243] A negatively charged Ge-layer stabilized by Ca ions in $CaGe_2$ is evidenced by a Ge $3d_{5/2}$ BE of 28.4 eV that appears at lower energy than the Ge emission for the Ge (111) standard (i.e., 29.4 eV). The BE of the Ge $3d_{5/2}$ feature in the spectrum of germanane flakes that appears at 29.8 eV is at a slightly higher

energy than that of the Ge standard. We attribute this shift to the influence of the hydrogens that bonded to the GeNS surfaces.

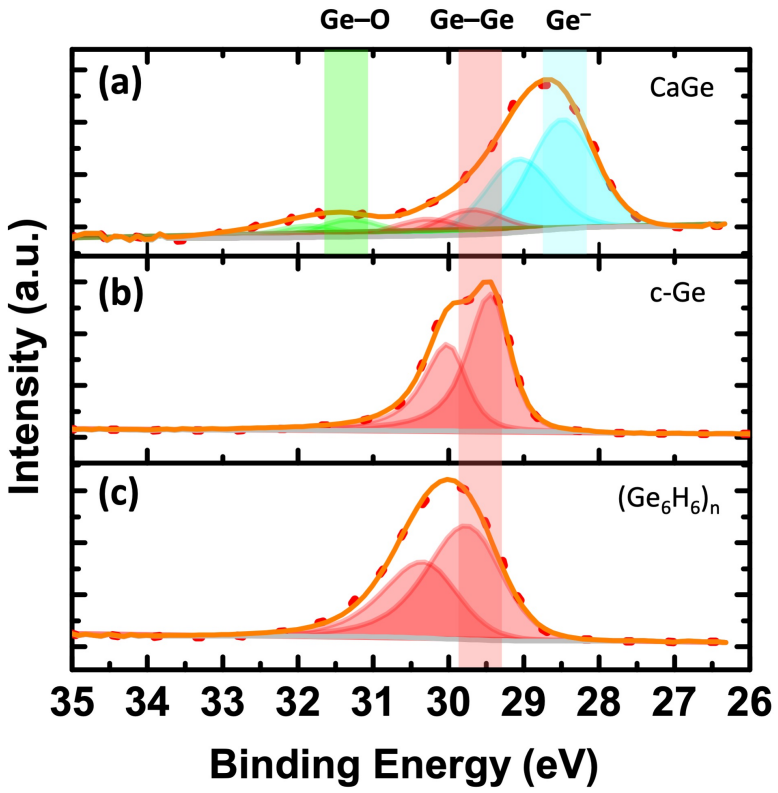

Figure 2.12. High-resolution XPS of Ge 3d region: (a) clean Ge (111) wafer, (b) $CaGe_2$ and (c) germanane flakes. The deconvolution of each oxidation state has been fit to the Ge $3d_{5/2}$ and $3d_{3/2}$ spin−orbit pairs in the same colour set.

In addition, features associated with surface oxidation of $CaGe_2$ were noted in the high resolution XPS of C 1s, Ca 2p, and O 1s regions (Figure 2.13). While Ca remains in a (+2) state in $CaGe_2$ and potential oxidized products, the O 1s reveals the presence of a Ca–O emission, suggesting the potential oxidized product is $Ca(OH)_2$. However, from the presence of CO_3 emission observed in the C 1s and O 1s spectra, the possibility of $CaCO_3$ cannot be eliminated.[244]

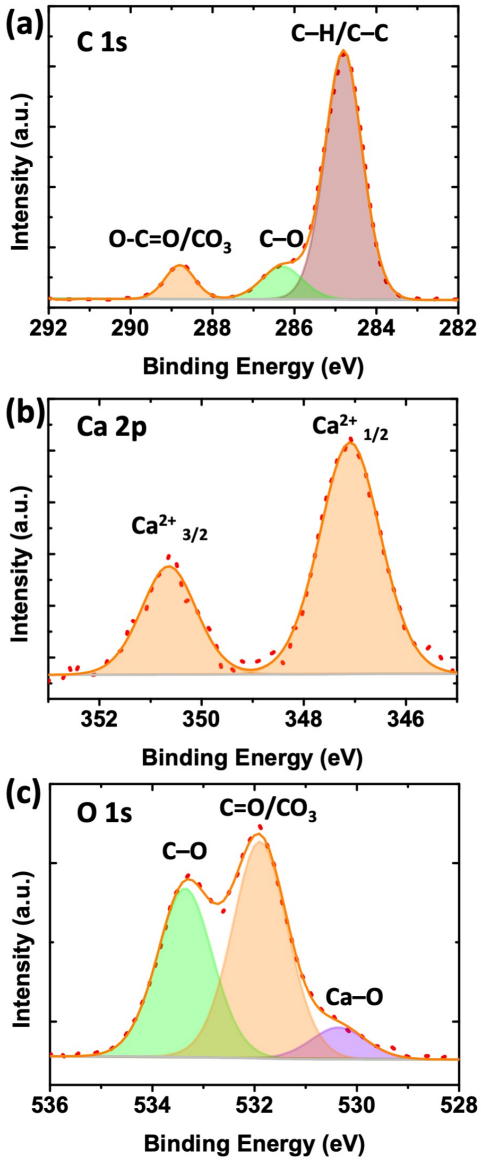

Figure 2.13. High-resolution XPS of $CaGe_2$, (a) C 1s region, (b) Ca 2p region, and (c) O 1s region.

2. 4 Summary and Outlook

In this Chapter, we developed a very fast gram-scale synthesis method for high quality $CaGe_2$ granular that can be deintercalated topotactically using concentrated HCl and yield germanane flakes with large grain size. The structure of $CaGe_2$ precursor and germanane flakes can be indexed as a *6R* unit cell, confirmed with

pXRD. After deintercalation, the germanane flakes have each germanium bonded to three other germanium atoms, and one hydrogen with the presence of trace oxygen. The XPS survey spectrum of $(Ge_6H_6)n$ is identical to the freshly HF etched hydride-terminated Ge (111) wafer. Additionally, these germanane flakes can be exfoliated easily into hydride-terminated nanosheets, with a hexagonal lattice observed by electron diffraction, which is individual layers with Ge–H bonds on the surface. These bonds can be regarded as a synthetic handle for further surface group substitution.

Chapter 3

Germanium Nanosheets Surface Functionalization: Hydrogermylation Reaction[2]

3. 1 Ge-C Bond Formation

Exfoliated H–Ge NSs oxidize when exposed to ambient conditions. This behaviour is similar to that of hydride-terminated Ge (111) wafer surfaces[126,245,246] as well as germanene.[66,67] The introduction of covalently bonded layers onto the surfaces of Ge NSs is of particular interest because of the expected chemical stability and solvent/medium compatibility they will impart. In addition, modifying the molecular layer presents an opportunity to tailor material properties predictably (e.g., conductivity, processability, optical response, assembly).[28,72,124,126,198,201,202,239,247]

To date, only a few solution routes have been reported that afford functionalized Ge NSs. Goldberger and coauthors prepared surface protected Ge NSs by topotactically reacting layered $CaGe_2$ with small iodoalkanes (e.g., R-I; R= $–CH_3$, $–CH_2OCH_3$, $–CH_2CH=CH_2$, etc.).[207,208,210] While the materials produced by this approach exhibited improved ambient and thermal stability, the scope (i.e., length, reactivity, electronic properties, etc.) of the surface functionality is very limited; more importantly, it is not immediately clear how more complex surface functionalities could be introduced using this approach.

We and others have demonstrated various hydrosilylation protocols that afford

---

* Portions of this Chapter have been copied and/or adapted from the following publication: Yu, H.; Helbich, T.; Scherf, L. M.; Chen, J.; Cui, K.; Fässler, T. F.; Rieger, B.; Veinot, J. G. C. Radical-Initiated and Thermally Induced Hydrogermylation of Alkenes on the Surfaces of Germanium Nanosheets. *Chemistry of Materirals*. **2018**, *30* (7), 2274–2280.

convenient methods for modifying hydride-terminated silicon (111) surfaces,[126] silicon nanoparticles[171,176,248] and silicane.[198,239] There also have been a few reports of hydrogermylation on Ge substrates and nanomaterials.[28,124,126]

In this Chapter, we studied the first demonstration of radical-initiated and thermally-induced hydrogermylation on H–Ge NSs (Figure 3.1) as well as detailed structural and compositional characterization of the resulting functionalized materials.

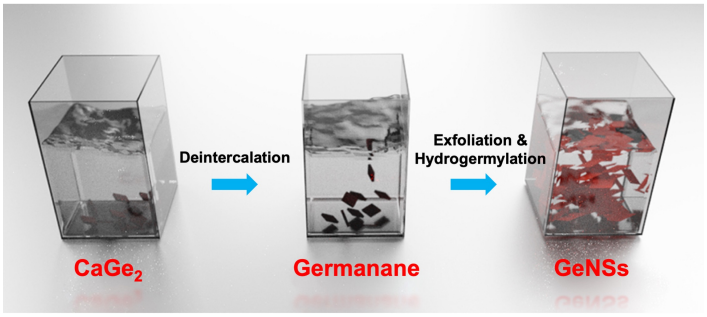

Figure 3.1. Schematic illustration of surface-functionalized Ge NSs preparation.

3. 2 Materials and Methods

3. 2. 1 Materials

All reagents were purchased from *Sigma-Aldrich* and used without further purification unless otherwise stated. All solvents, except acetone, were dried using an Innovative Technology, Inc. Grubbs-type solvent purification system. Acetone was dried over molecular sieves (3 Å), degassed via three freeze-pump-thaw cycles using an argon-charged double manifold. All solvents and liquid reagents were degassed via three freeze-pump-thaw cycles using an argon-charged double manifold and stored in a MBraun glove box with nitrogen working gas. The synthesis of precursors $CaGe_2$ and germanane flakes are described in Chapter 2.

3. 2. 2 Radical-initiated Hydrogermylation

In a nitrogen-charged glove box, germanane flakes (5 mg) were transferred into a dry 5 mL Biotage® microwave tube. Dry degassed toluene (2 mL), AIBN (10 mg), and 1-dodecene (1 mL, 5 mmol) were added, and the tube was sealed. The reaction mixture was ultrasonicated in a bath sonicator (Fisher Scientific FS30) for three hours, after which it was heated to and maintained at 65 °C and stirred for 12 h. The resulting red suspension was transferred to a PTFE centrifuge tube, methanol (40 mL) was added, and the mixture was centrifuged (12,000 rpm for 10 min) to yield a deep red pellet. The solid was redispersed in a minimal amount of toluene (2 mL). Methanol (40 mL) was added, and the mixture was centrifuged (12,000 rpm for 10 min). This suspension/precipitation procedure was repeated twice, after which the dodecyl-Ge NSs were freeze-dried from benzene and finally dispersed in toluene.

3. 2. 3 Thermally-induced Hydrogermylation

In a nitrogen-charged glovebox, germanane flakes (5 mg) were transferred into a dry 5 mL Biotage® microwave tube, 1-dodecene (2 mL, 9 mmol) was added, and the tube was sealed. Next, the reaction mixture was ultrasonicated in a bath sonicator (Fisher Scientific FS30) for three h, after which it was heated to and maintained at 190 °C for 12 h. On completion of the reaction, the dark brown mixture was transferred to a PTFE centrifuge tube, methanol (40 mL) was added, and the mixture was centrifuged (12,000 rpm for 10 min). The solid was redispersed in a minimal amount of toluene (2 mL). Methanol (40 mL) was added, and the mixture was centrifuged (12,000 rpm for 10 min). This suspension/precipitation procedure was repeated twice, after which the dodecyl-Ge NSs were freeze-dried from benzene and finally dispersed in toluene.

3. 3 Material Characterization

3. 3. 1 Fourier Transformed Infrared (FT-IR) Spectroscopy

FT-IR Spectra were acquired using a Thermo Nicolet Magna 750 IR Spectrometer. Samples were prepared by drop- coating a toluene dispersion of the material of choice onto an electronic- grade Si-wafer (N-type, 100 surface, 100 mm thickness, and 10 ohm·cm resistivity) and dried under a nitrogen atmosphere.

3. 3. 2 Transmission Electron Microscopy (TEM)

Bright-field transmission electron microscopy (TEM) images were acquired using a Hitachi- 9500 or JEOL JEM-ARM200CF S/TEM electron microscope at accelerating voltages of 300 kV or 200 kV, respectively. HRTEM images obtained from a Hitachi-9500 were processed using Gatan Digital Micrograph software (Version 3.22.1461.0). HRTEM images were enhanced with commercial software HREM-Filters Pro/Lite v.2.5.1 equipped in Gatan Digital Micrograph. The CrystalKitX was employed for the selected area electron diffraction (SEAD) pattern simulation. The crystallographic data using for the simulation is from Cultrara et al. [228] TEM samples were prepared by depositing a drop of GeNS suspensions in toluene onto a holey/lacey carbon-coated copper grid (Electron Microscopy Inc.)The grid was kept in a vacuum chamber for at least 24 h prior to data collection.

3. 3. 3 Atomic Force Microscopy (AFM)

AFM was performed using a Bruker Dimension Edge^{TM} system with NanoDrive version 8.02 software. The tapping mode cantilever was purchased from Bruker (Resonance frequency: 300 kHz, force constant 42 N/m). Thin films of Ge NSs (5 mg of exfoliated sheets in 2 mL of toluene) were spin coated (90 s, 1000 rpm) onto

a Si (111) wafer substrate that had been cleaned using a standard Piranha protocol.

3. 3. 4 X-ray Photoelectron Spectroscopy (XPS)

XPS was performed using a Kratos Axis Ultra instrument operating in energy spectrum mode at 210 W. Samples were prepared by depositing a suspension of the material of choice onto a copper foil substrate, followed by drying in air. Prior to the analysis, the Ge (111) wafer reference was cleaned by immersing in 30% v/v H_2O_2 for 90 s, followed by 10 min etching in 10% v/v HF. The base and operating chamber pressure were maintained at 10^{-7} Pa. A monochromatic Al K source (λ = 8.34Å) was used to irradiate the samples, and the spectra were obtained with an electron take-off angle of 90°. CasaXPS software (VAMAS) was used to interpret high-resolution spectra. All spectra were calibrated internally to the C1s emission (284.8 eV). After calibration, a Shirley-type background was applied to remove most of the extrinsic loss of structure.

3. 3. 5 Thermogravimetric Analysis (TGA)

TGA was performed using a Mettler Toledo Star TGA/DSC system. The sample was placed in a Pt pan and heated under a nitrogen atmosphere from 35 to 700 °C at a rate of 10 °C/min.

3. 3. 6 Powder X-ray Diffraction (XRD)

PXRD data were collected using an Inel MPD MultiPurpose Diffractometer equipped with a CPS 120 curved position sensitive X-ray detector and Cu Kα (8.047 KeV energy) source or Stoe STADI P diffractometer equipped with a Ge(111) monochromator for Cu Kα radiation (λ = 1.54056 Å) and a Dectris MYTHEN DCS 1K solid-state detector. The $CaGe_2$ was ground in an agate mortar and filled into 0.3 mm glass capillaries and sealed. The sample was measured within a 2θ-range of

5–87.5° (PSD steps, 1.5°; time/step,15 s). The H-Ge powders were deposited on an amorphous silica holder.

3. 3. 7 Diffuse Reflective Absorption (DRA)

Diffuse reflective analysis was performed using a Cary 5000 UV-Vis-NIR, with a diffuse reflectance integrating sphere attachment. The detector and grading filter were changed at 900 nm.

3. 3. 8 Raman Spectroscopy

Raman spectroscopy was performed using a Renishaw inVia Raman microscope equipped with a 643 nm laser operating at a power of 3.98 mW on the sample. Samples were prepared by mounting the suspension on 100 nm thick gold-coated glass.

3. 4 Results and Discussion

Azobisisobutyronitrile (AIBN) radical-initiated hydrogermylation has been exploited previously for the derivatization of hydride-terminated germanium nanocrystals;[18] in this context, similar conditions were applied here to the functionalization of exfoliated H–Ge NSs. AIBN activated surface modification of H–Ge NSs with 1-dodecene in degassed toluene heated to 60 °C was completed after 12 h. At these temperatures, no obvious surface modification was observed when the reaction mixture is heated in the absence of AIBN (i.e., there is no thermal activation of hydrogermylation). Thermally-induced hydrogermylation also has been demonstrated for Ge surfaces and nanosystems.[48,124,126] Here, we extend this approach to the alkyl-termination of H–Ge NSs upon heating exfoliated germanane flakes in neat 1-dodecene to 190 °C in an inert atmosphere. This procedure caused the initially deep red suspension to turn brown-gray after 2 h (Figure 3.2).

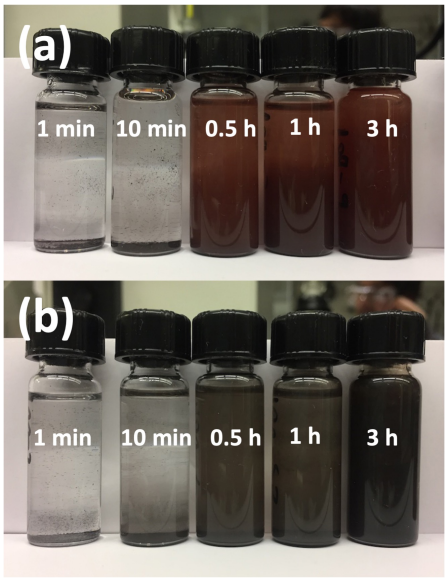

Figure 3.2. Photographs of dodecyl-Ge NSs at the indicated sonication time prepared by (a) thermally induced method and (b) radical-initiated method.

Sonochemical exfoliation renders materials with a broad size distribution, which can be narrowed through preferential precipitation at different centrifugation speeds. As shown in Figure 3.3, after functionalization, non-fully exfoliated flakes precipitate down immediately, and the remaining suspension can be separated into “big” and “small” nanosheets at low (3,000 rpm) and high speed (12,000 rpm) centrifugation, respectively. From SEM images, both "small" and "big" size nanosheets have a layered morphology with the layers distinguishable.

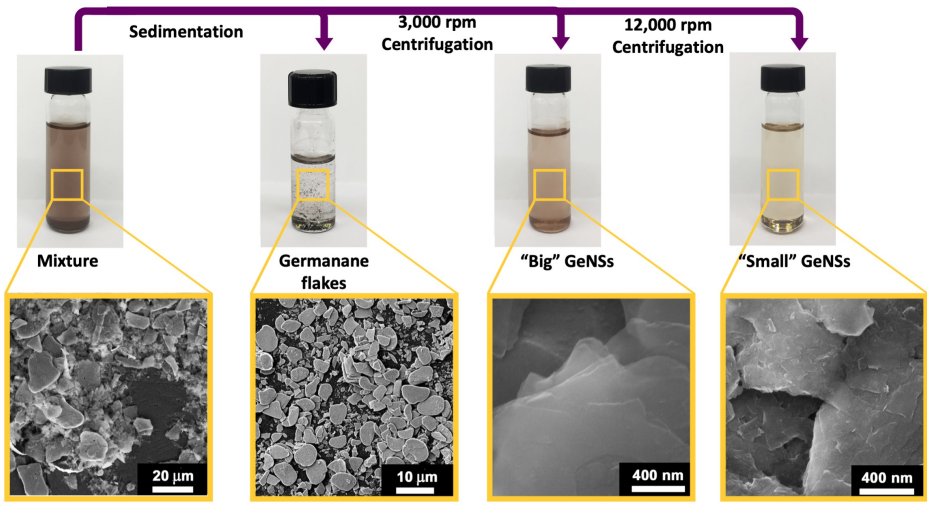

Figure 3.3. Photography and SEM images of hydrogermylation reaction purification at different stages. The suspensions are diluted for display purpose.

3. 4. 1 Structural Characterization

After surface functionalization, the Ge NSs lose their long-range order due to their freestanding nature in solution. Instead, select area electron diffraction (SAED) patterns were obtained from dodecyl-Ge NSs prepared via radical-initiated hydrogermylation (Figure 3.4). It can be indexed readily to a simple hexagonal unit cell with a = 3.98 Å and calculated d-spacings of 0.344 and 0.198 nm for the $(10\bar{1}0)$ and $(11\bar{2}0)$ planes, respectively, assuming a [0001] zone axis. These data are consistent with reports of hydride- and methyl-terminated nanosheets.[27] We also note a stronger diffraction intensity for the inner $(10\bar{1}0)$ plane when compared to that of the outer $(11\bar{2}0)$ plane (see Figures 3.4a and c); this observation differs from the prediction of the dynamically simulated electron diffraction for AB- and ABC-type germanane stacking (Figure 3.5) performed using available 2H or 6R germanane cell parameters, respectively.[228] However, the experimental diffraction intensities we observe mirror those of mechanically exfoliated germanane monolayers[70] as well as graphene structures (e.g., graphene, fluorographene).[249,250]

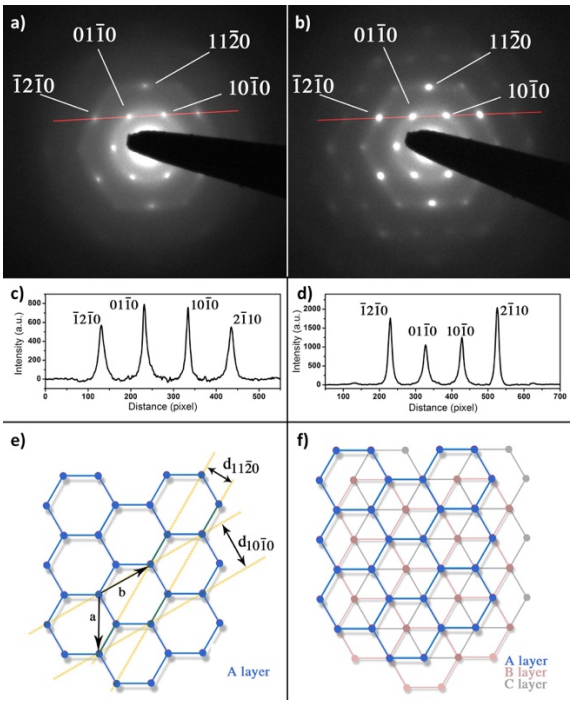

Figure 3.4. Selected electron diffraction patterns of dodecyl- Ge NSs (AIBN method) along the [0001] zone (a,b), line profile (c,d), and corresponding models (e,f): fully (left) and partially exfoliated nanosheets (right).

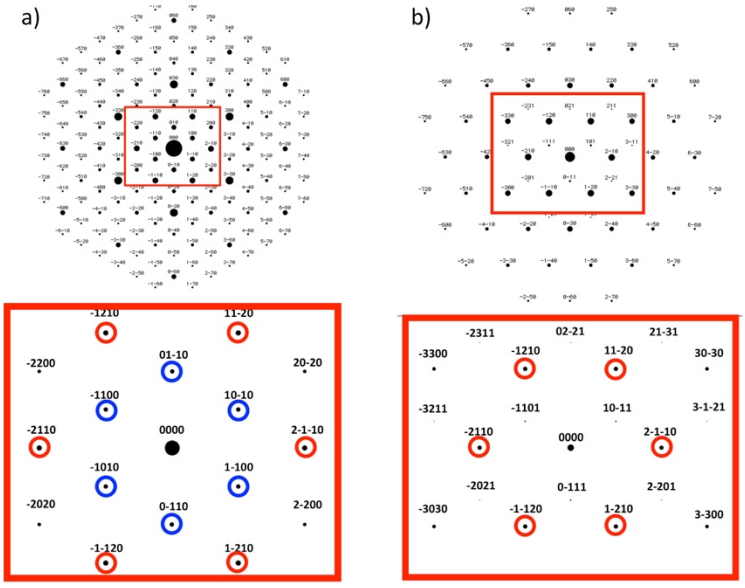

Figure 3.5. Electron diffraction pattern simulation results for non-fully exfoliated Ge NSs using a) 2H and b) 6R unit cell parameters. The diffraction patterns shown in the red boxes are enlarged by changing the camera height during the simulation.

In contrast, a line profile analysis of the SAED of partially exfoliated Ge NSs (i.e., multilayer structures) prepared using radical-initiated hydrogermylation (Figures 3.4b and d) show a diffraction intensity profile that is in good agreement with simulated AB stacking; of important note, while we can conclude that these assemblies are not monolayers, we cannot discount the possibility of these multilayer structures being a mixture of AB and ABC stacking.

Bright-field transmission (TEM) electron microscopy imaging of the present dodecyl-terminated Ge NSs indicates that they are randomly shaped thin sheets. For Ge NSs prepared via thermally-induced functionalization, lattice fringes were measured directly using high-resolution TEM (Figure 3.6). It is important to note that the long-chain alkyl groups on the GeNS surfaces can occlude high-resolution imaging and lead to blurring of lattice fringes; this is not the case for graphene, where no pendant surface groups are present. Consistent with the present SAED for dodecyl-terminated Ge NSs prepared using radical-induced reactions, the HRTEM analyses afforded lattice spacings of 0.34 nm for $(10\bar{1}0)$ planes when evaluating the edges of the GeNS assemblies, showing distinct contrast compared to the surrounding vacuum (Figure 3.6f). Further supporting the conclusion that freestanding Ge NSs were prepared using the present methods, we note incremental increases in thickness contrast in TEM imaging and the same lattice structure away from NS edges (Figure 3.6g). Unfortunately, direct imaging of the lattice fringes in some stacks is not possible. Presumably, visualization is precluded by the presence of long alkyl chains that separate the layers by ~6 nm (AFM analysis). In some cases, we observe lattice fringes for the thermally modified NSs that do not correspond to the $(10\bar{1}0)$ spacing (Figures 3.6d and e). Evaluation of these regions shows a *d*-spacing of 0.20 nm that can correspond to the $(11\bar{2}0)$ plane of isolated and/or stacked nanosheets (Figure 3.6); this is similar to what has been reported for graphene and multilayer silicenes.[205,251]

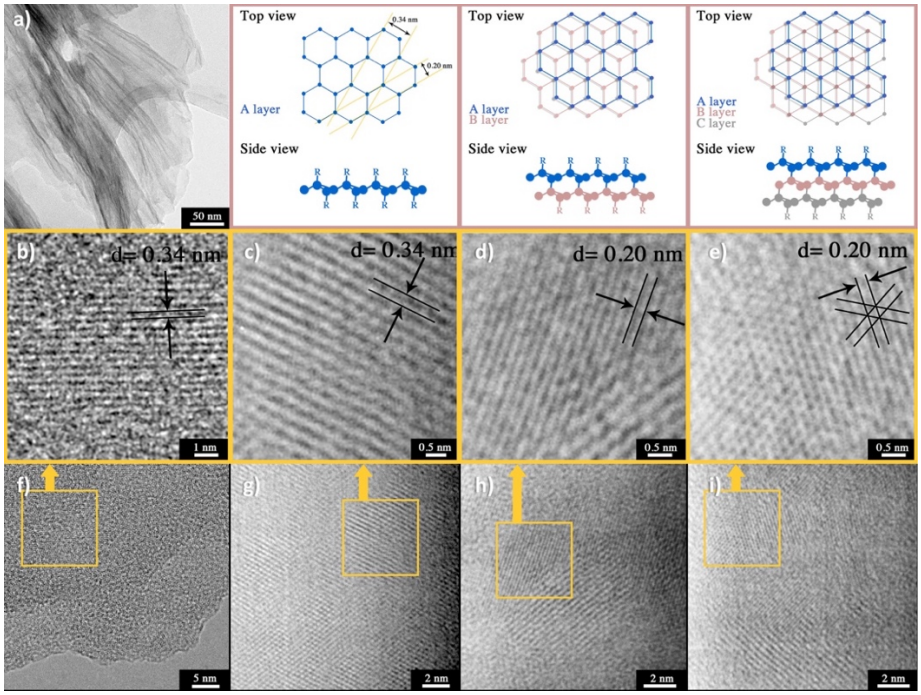

Figure 3.6. Top: (a) Brightfield TEM and models for Ge nanosheet stacking; Middle: (b-e) magnified regions of the HRTEM images, shown in (f-i), respectively; Bottom: HRTEM images of thermally modified dodecyl-terminated Ge NSs measured at different locations; f) edge of Ge NSs; g) center of Ge NSs; h, j) partially stacked Ge NSs.

It is difficult to separate the contributions of isolated and stacked nanosheets to this observation, and multilayers cannot be discounted. However, SAED modelling and data indicate that detection of the $(11\bar{2}0)$ reflection is more likely in multilayer assemblies. In addition, we expect that for cases where NS stacking is observed, visualization of lattice planes in the HRTEM suggests that there is a limited separation between Ge layers. We propose that in these isolated regions, the Ge NSs have linked together through Ge–Ge bonds arising from dehydrocoupling reactions. This proposal is supported further by reports of dehydrogenation reactions taking place at elevated temperatures (190 °C).[70] This reactivity is described in Chapter 4.

Atomic force microscopy (AFM) shows the thicknesses of the sheets prepared using radical-initiated hydrogermylation to be 4.5 nm (Figure 3.7); this is comparable to surface-modified silicane NSs[198,239] and substantially thicker (i.e., ~8x) than

hydride-terminated Ge NSs reported elsewhere.[70] On the contrary, for Ge NSs prepared via thermally-induced functionalization, the measured layer thickness is ca. 6 nm, suggesting that the sheets might not be covered by a monolayer of ligand but oligomers. The details are discussed in Section 3. 4. 3.

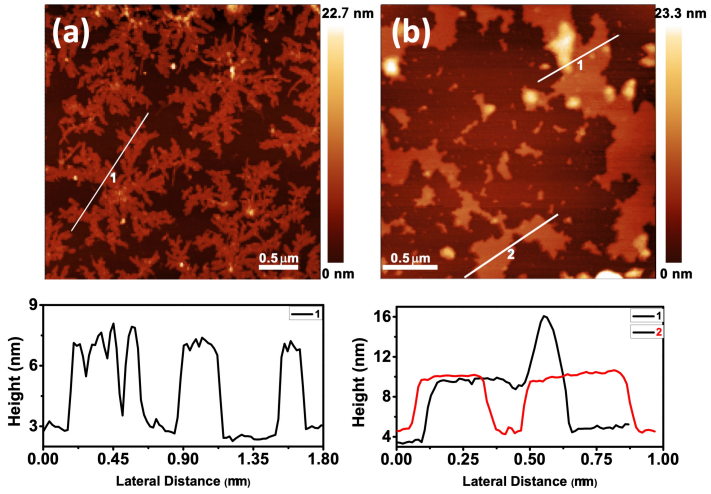

Figure 3.7. AFM imaging (top) and height profiles (bottom) of dodecyl-terminated Ge NSs deposited on clean silicon (111) substrates obtained using (a) radical-initiated and (b) thermally-induced methods.

3. 4. 2 Compositional Characterization

Consistent with alkyl derivatization, the FTIR spectrum (Figure 3.8) of the dodecyl-functionalized NSs (i.e., dodecyl-Ge NSs) shows the concomitant appearance of $\nu(C{-}H)_{asym}$ features at 2852 cm^{-1} and loss of $\nu(Ge{-}H)$ at 2001 cm^{-1} and $\nu(C{=}C)$ at 3078 cm^{-1}.[18] We also note that the adsorbed water $\nu(O{-}H)$ feature at 3400 cm^{-1} in the spectrum of germanane is diminished substantially in the spectrum of dodecyl-Ge NSs. We propose that this is because the outer layers of the Ge-H flakes are oxidized and are removed during purification due to their limited compatibility with non-polar media. The FTIR spectra of the recovered product are similar to those of functionalized Ge NSs prepared using radical-initiated reactions.

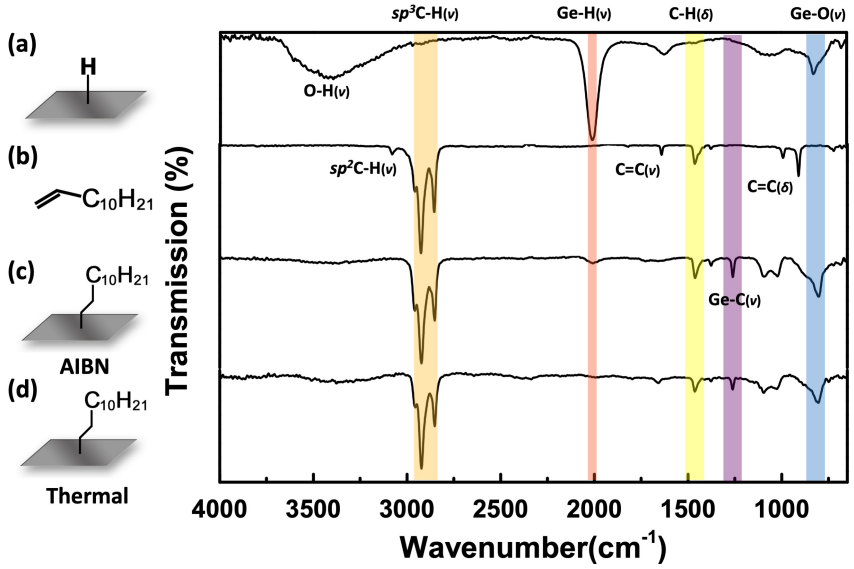

Figure 3.8. FTIR spectra of (a) germanane, (b) neat 1-dodecene, dodeceyl-terminated Ge NSs prepared by (c) thermally-induced hydrogermylation, and (d) radical-initiated hydrogermylation.

Comparing the Raman spectra of crystalline germanane and dodecyl functionalized GeNS prepared using thermal- and radical-initiated methods provides insight into the functionalization processes (Figure 3.9).

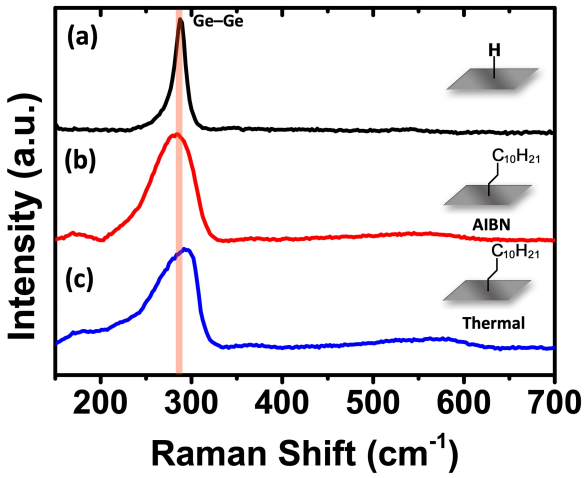

Figure 3.9. Raman spectra of (a) germanane, and dodeceyl-terminated Ge NSs prepared by (b) thermally-induced hydrogermylation, and (c) radical-initiated hydrogermylation.

The combination of the introduction of dodecyl groups to the GeNS surfaces and the

corresponding loss of the underlying structural support of the germanane flake assembly may be expected to introduce tensile strain into the bonding network of the individual Ge NSs; this results in further broadening of the Ge–Ge optical phonon. Similar observations (i.e., Raman shift broadening) have been noted for MoS_2 and WS_2 systems.[252]

Survey XP spectra were measured for functionalized for Ge NSs prepared by both hydrogermylation methods and have been used to compare with that of germanane flakes (Figure 3.10). All three spectra indicate the presence of Ge and trace O, while the functionalized NSs show a high C 1s emission compared to germanane, suggesting the materials are carbon-rich. Small Cu emissions are collected because these solutions were drop-cast on a clean Cu substrate.

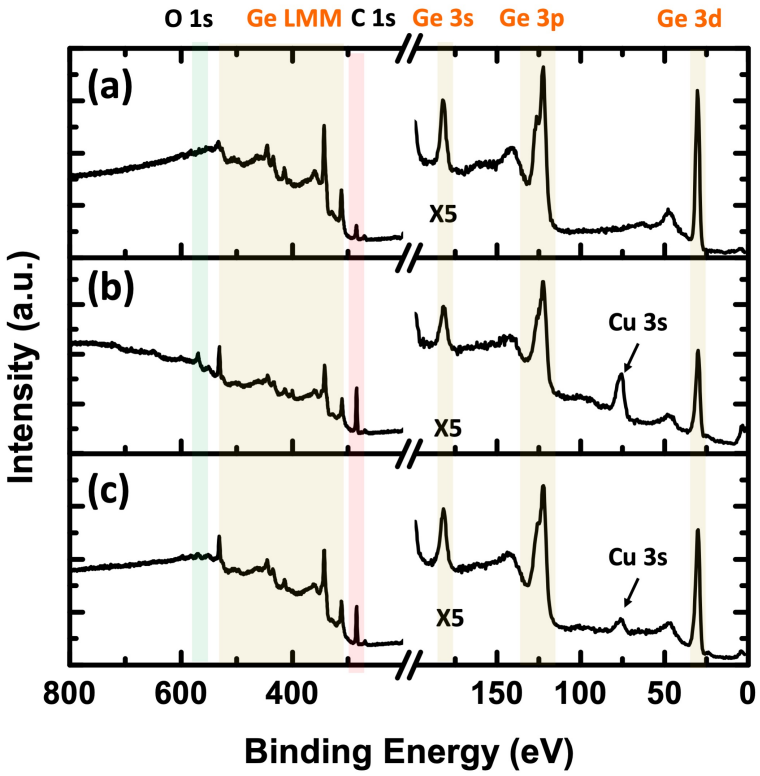

Figure 3.10. Survey X-ray photoelectron spectra of (a) germanane, dodeceyl-terminated Ge NSs prepared by (b) thermally-induced hydrogermylation, and (c) radical-initiated hydrogermylation.

High-resolution XP spectra of germanane flakes as well as dodecyl-terminated Ge NSs prepared by both methods were obtained (Figure 3.11). All spectra were calibrated to adventitious carbon at a binding energy (BE) of 284.8 eV.[243] The binding energy (BE) of the Ge $3d_{5/2}$ feature in the spectrum of dodecyl-Ge NSs prepared using radical-initiated reactions appears at 29.7 eV; this feature appears at similar energy to that observed for germanane flakes (29.8 eV) and slightly higher energy than that of the Ge standard (29.4 eV). We attribute this shift to the influence of hydrogen and carbon that are bonded to the GeNS surfaces. There are also high energy shoulders on the Ge spectral features of the dodecyl-Ge NSs that we have fitted to Ge^{2+} (31.2 eV) and Ge^{4+} (32.4 eV) and attribute to GeO_x arising from trace oxidation.[48,245]

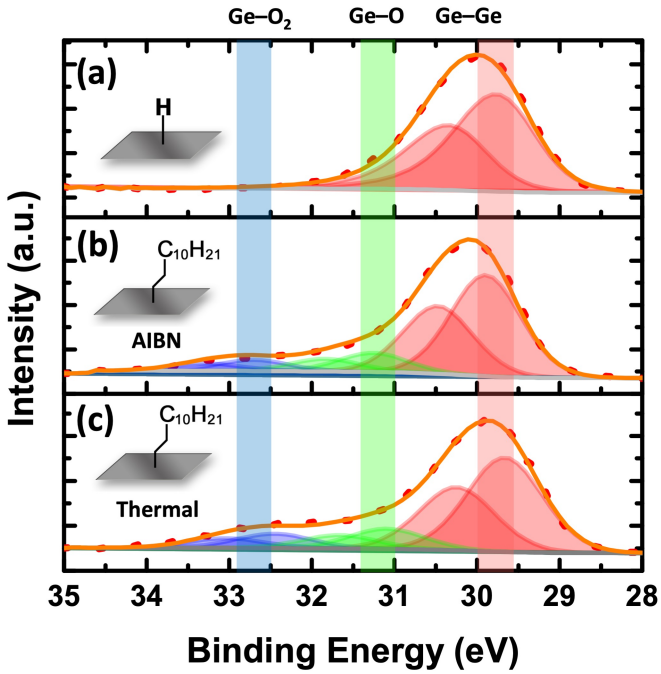

Figure 3.11. High resolution XP spectra of the Ge 3d spectra region of (a) germanane, and dodecyl-terminated Ge NSs prepared by (b) thermally-induced hydrogermylation, and (c) radical-initiated hydrogermylation. The deconvolution of each oxidation state has been fitted to the Ge $3d_{5/2}$ and $3d_{3/2}$ spin-orbit pairs in the same colour set.

3. 4. 3 Surface Coverage Estimation

The C 1s and Ge 3d regions of the high-resolution XP spectra of the present dodecyl-Ge NSs were evaluated to estimate the fractional dodecyl monolayer coverage resulting from hydrogermylation reactions. For a monolayer passivated flat surface (i.e. Si wafer), the thickness of the carbon overlayer can be calculated using the overlayer model described in the literature:[153,253,254]

$$\left(\frac{I_{Ov}}{I_{Ge}}\right)\left(\frac{SF_{Ge}}{SF_{Ov}}\right)\left(\frac{\rho_{Ge}}{\rho_{Ov}}\right)=\left(\frac{1-e^{-d_{Ov}/(\lambda_{Ov}\cos\theta)}}{e^{-d_{Ov}/(\lambda_{Ge}\cos\theta)}}\right) \qquad (3.1)$$

where I is the peak intensity, ρ is the atomic volume density, SF is the sensitivity factor, d_{Ov} is the overlayer thickness, λ is the photoelectron escape length, and θ is the photoelectron take-off angle determined by the surface orientation relative to the analyzer. The subscript Ov signifies an overlayer component; the subscript Ge signifies a Ge component. The take-off angle (θ) is 0° for this work, and atomic volume density is assumed identical where each Ge atom is bonded to one alkyl chain and three other Ge atoms, giving Equation 3.2:

$$\left(\frac{I_{Ov}}{I_{Ge}}\right)\left(\frac{SF_{Ge}}{SF_{Ov}}\right)=\left(\frac{1-e^{-d_{Ov}/\lambda_{Ov}}}{e^{-d_{Ov}/\lambda_{Ge}}}\right) \qquad (3.2)$$

We have applied a ligand-sheet-ligand model of the functionalized GeNS, in which both sides (top and bottom) are functionalized (Figure 3.12).

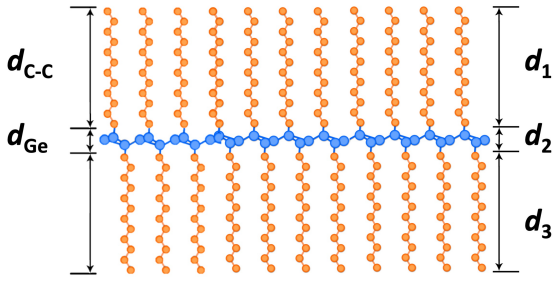

Figure 3.12. An illustration of ligand-sheet-ligand model.

For these structures, photoelectrons generated from the dodecyl ligands bonded to both nanosheet surfaces and the GeNS itself can be used to estimate the fractional coverage. This approach relies on the following assumptions: 1) the dodecyl-Ge NSs are deposited uniformly on the XPS substrate, 2) carbon appearing in the XP spectrum arises only from the dodecyl functionalities (i.e., there is negligible adventitious carbon) and all emission intensity at 284.8 eV arises from surface tethered dodecyl ligands, 3) the number of edge-bonded ligands is negligible, and 4) each Ge atom is bonded to three other Ge atoms and one alkyl chain (i.e., same atomic volume density).

This model describes a nanosheet that is bonded covalently to two overlayers at both sides, where the thickness of each carbon overlayer can be determined using Equation 3.3:

$$\left(\frac{I_{C-C}}{I_{Ge}}\right)\left(\frac{SF_{Ge}}{SF_{C-C}}\right)=\frac{\left(1-e^{-d_{C-C}/\lambda_{C-C}}\right)\left(1+e^{-\left(d_{C-C}+d_{Ge}\right)/\lambda_{C-C}}\right)}{\left(1-e^{-d_{Ge}/\lambda_{Ge}}\right)\left(e^{-d_{C-C}/\lambda_{Ge}}\right)} \qquad (3.3)$$

In Equation 3.3, $(1-e^{-d_{C-C}/\lambda_{C-C}})$ describes the signal generated in the $d_{C\text{-}C}$ layer, $(1+e^{-(d_{C-C}+d_{Ge})/\lambda_{C-C}})$ describes the signal collected from the $d_1(n = 1)$ and d_2 layers, while $(1-e^{-d_{Ge}/\lambda_{Ge}})$ describes the signal generated from the d_{Ge} layer, and $(e^{-d_{C-C}/\lambda_{Ge}})$ describes the signal collected from d_2 layer. While Equation 3.3 describes the relationship between carbon and germanium intensities collected from a single Ge NSs (n = 1), the thickness of the dodecyl-terminated Ge NSs was determined to be 4.4 nm using tapping mode AFM; in this context, the majority (>99%) of the photoelectrons detected originated from the top three GeNS layers (n = 3). The thickness of the dodecyl ligands bonded to the Ge NSs can be estimated using the following equation:

$$\left(\frac{I_{C-C}}{I_{Ge}}\right)\left(\frac{SF_{Ge}}{SF_{C-C}}\right)=\frac{\left(1-e^{-\frac{d_{C-C}}{\lambda_{C-C}}}\right)\left(\sum_{m=1}^{n}e^{-\frac{(2m-1)\bullet d_{C-C}+m\bullet d_{Ge}}{\lambda_{C-C}}}+\sum_{m=0}^{n-1}e^{-\frac{(2m)\bullet d_{C-C}+m\bullet d_{Ge}}{\lambda_{C-C}}}\right)}{\left(1-e^{-\frac{d_{Ge}}{\lambda_{Ge}}}\right)\left(\sum_{m=0}^{n-1}e^{-\frac{(2m+1)\bullet d_{C-C}+m\bullet d_{Ge}}{\lambda_{Ge}}}\right)} \quad (3.4)$$

where: I_{C-C} and I_{Ge} are the integrated intensities of the photoemission peaks from surface tethered alkyl functionalities and Ge NSs, respectively; SF_{C-C} and SF_{Ge} are the instrument sensitivity factors for the C 1s (0.278) and Ge 3d (0.536) photoemission signals, respectively; d_{C-C} and d_{Ge} are the thicknesses of the ligand and Ge layers, respectively;[253] λ_{C-C} and λ_{Ge} are the attenuation lengths of C 1s (3.6 nm) and Ge 3d photoelectrons (2.9 nm),[255] respectively.

We performed a series of iterative calculations using Equation 3.4. For these calculations, the number of dodecyl-GeNS (n) layers was defined as n = 10 to ensure that the maximum photoemission intensity was considered. The relationship between monolayer coverage, obtained by dividing d_{C-C} by the fully extended chain length of 1-dodecane (1.8 nm), and d_{Ge} was plotted (Figure 3.13).[165] The thickness of each Ge layer was defined as 0.6 nm. Based upon this model, the ligand coverage on dodecyl-Ge NSs prepared via radical initiated reactions was determined to be 0.55 ML (at d_{Ge} = 0.6 nm). This is in excellent agreement with accepted literature values (i.e., 0.5 ML) for the substitution limit for long-chain alkyl groups on flat Ge/Si (111) surfaces[152,153,256,257] and lower than that for Ge nanoparticles (0.62 ML), for which surface curvature is expected to play a role.[19] For dodecyl-functionalized Ge NSs using thermally-induced hydrogermylation reactions, the coverage (1.03 ML) was found to be more than double the accepted limit on flat Ge (111). This is comparable with observations for thermally-induced hydrosilylation on Si (111) surfaces.[127,153,254,258,259] Alkyl chain propagation also has been reported for silyl radicals in the case of thermal hydrosilylation on the Si NP surface.[171] AFM analysis

of these Ge NSs sheets shows that they are substantially thicker than NSs modified using radial-initiated reactions. These observations suggest that the thermally modified dodecyl-Ge NSs may be covered by oligomers. The oligomerization of unsaturated ligands can result in even higher surface coverage on curved Ge nanoparticle surfaces when conditions similar to those described here are employed.[28]

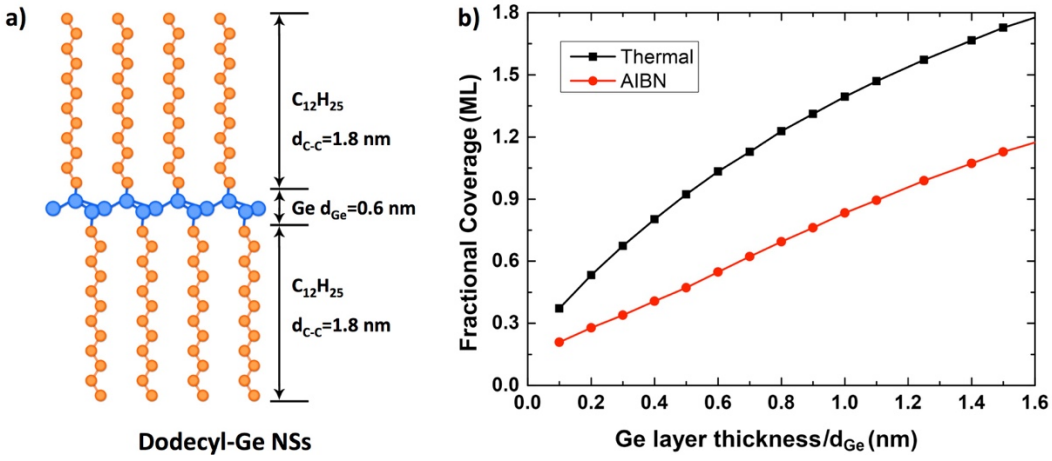

Figure 3.13. (a) Ideal model for dodecyl-terminated Ge NSs (n = 1). (b) Calculated fractional monolayer ligand coverage determined using Equation 1 for indicated Ge layer thicknesses of d_{Ge} using XPS, for dodecyl-terminated Ge NSs prepared from thermal (black) and AIBN initiated (red) hydrogermylation.

3. 4. 4 Optical Bandgap and Thermal Stability

The introduction of functionalization induced tensile strain in the GeNS structure is evidenced further by a shift in the optical band gap determined using diffuse reflectance absorption (DRA; Figure 3.14). We note that the band gap narrows moving from germanane (1.7 eV) to radical prepared dodecyl-Ge NSs (1.5 eV) to thermally prepared dodecyl-GeNS (1.1 eV). Previous reports of Ge NSs suggest longer bonded alkyl surface groups induce greater tensile strain, leading to band gap narrowing.[3210] This is consistent with our observations (vide infra, AFM, XPS, TGA) that Ge NSs functionalized via radical-initiated reactions bear molecular monolayers,

while those modified using thermal methods possess surface bonded oligomers.

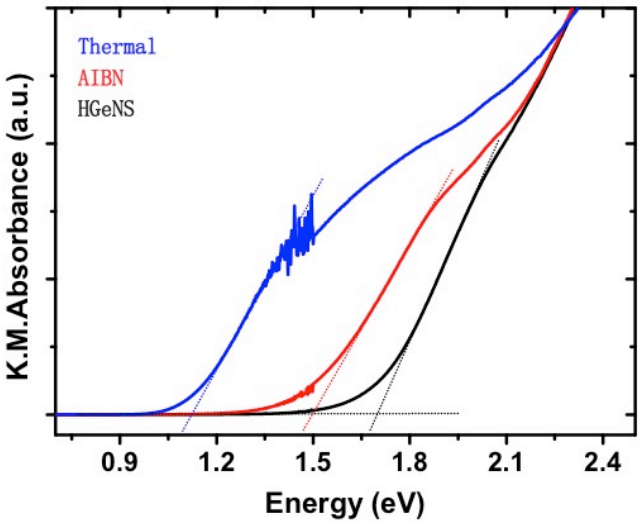

Figure 3.14. Diffuse reflectance spectroscopy of germanane flakes (black), radical-induced functionalized (red), and thermally-induced functionalized (blue) dodecyl-Ge NSs.

The thermal stability of dodecyl-GeNS was investigated using thermogravimetric analysis (TGA). Evaluation of germanane (Figure 3.15) shows two mass loss events that previously have been attributed to dehydrogenation at 190 °C and chlorine-loss starting from 300–350 °C.[70] In contrast, dodecyl-Ge NSs show no detectable mass loss associated with hydrogen release; this is consistent with the presented surface functionalization. The loss of the dodecyl functionalities resulting from cleavage of Ge–C surface bonds on Ge NSs begins spanning the 365 to 470 °C and at 475 °C for samples prepared via radical- and thermally activated hydrogermylation, respectively. While the origin of the different thermal responses of the dodecyl-Ge NSs is the subject of the ongoing investigation, it could be attributed to differences in their surface chemistry noted in the AFM and XPS analyses outlined above.

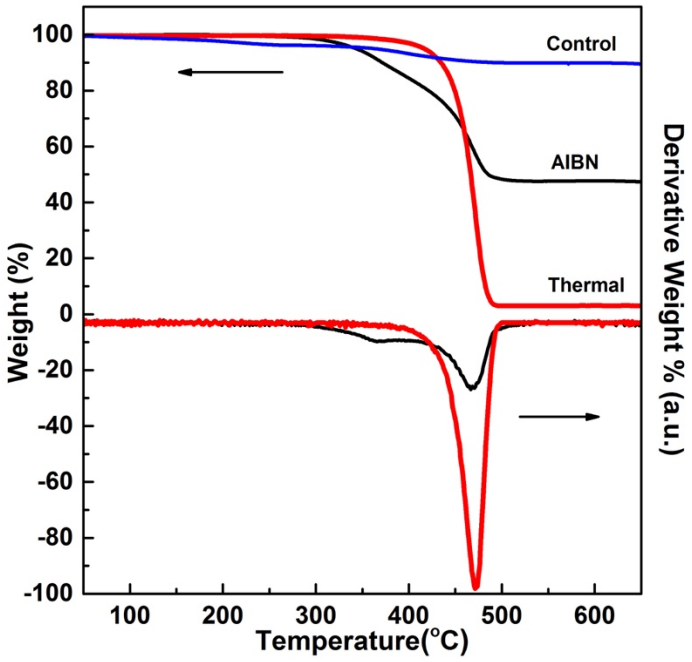

Figure 3.15. Thermogravimetric analysis (TGA) (top, left axis) and Derivative Thermogravimetric (DTG) (bottom, right axis) of Ge NSs functionalized through AIBN (black) and thermal-induced (red) methods, respectively. The TGA profile of H-terminated GeNS is provided for comparison (blue).

3. 4. 5 Exfoliation Efficiency

The efficiency of sonochemical exfoliation is investigated by treating the reaction mixture at different sonication times, in toluene or neat 1-dodecene, and heated at a target temperature and time. Aside from the colour change observed in the optical photos (Figure 3.3), TGA results of these NSs also indicate the importance of the sonication time and purification process (Figure 3.16). When the nanosheets are not fully exfoliated, the ligand, such as 1-dodecene, is too bulky to diffuse into the $(Ge_6H_6)_n$ layers, which is consistent with topotactic deintercalation of $CaGe_2$ with bulkier organoiodines.[210] As a result, a low %mass drop was observed in cases with short sonication time.

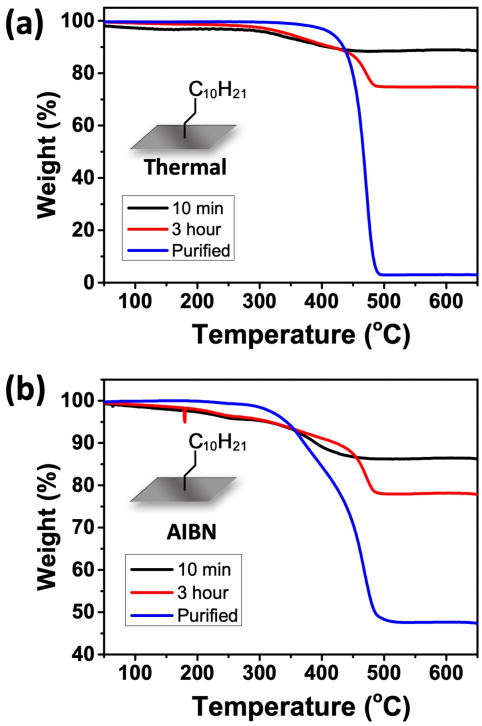

Figure 3.16. TGA of dodecyl-Ge NSs at the indicated sonication time prepared by (a) thermally induced method and (b) radical-initiated method.

Additionally, the diffuse limit of bulk ligand was confirmed directly by an electron energy loss spectrum (EELS) line scan across the few-layer Ge NSs that have been surface modified with 1-dodecene (Figure 3.17).

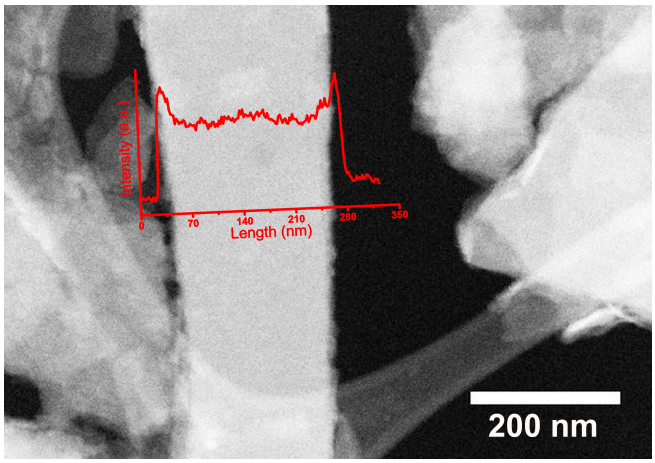

Figure 3.17. Electron energy loss spectrum line scan of dodecyl-functionalized few-layer Ge NSs.

Compared to the vacuum background, the Ge NSs show large electron counts,, with energy loss corresponding to the carbon K line, where the value maximizes at close to the edges of sheets (ca. 15 nm). This observation strongly suggests the success of the hydrogermylation reaction and confirmed the importance of layer exfoliation.

3. 5 Summary and Outlook

In conclusion, radical-initiated and thermally-induced hydrogermylation reactions were employed to modify hydride-terminated Ge NSs. Both hydrogermylation reactions are rapid and afford surface modification. Radical initiated reactions provide monolayer coverage, while thermally activated processes lead to surface oligomerization. As a result, functionalized nanosheets exhibited thicknesses of ~4.5 to 5.5 nm depending upon the functionalization method employed. In all cases, the Ge atoms are arranged in a buckled simple hexagonal unit cell. In addition, the band gap of the GeNS decreases with surface functionalization and the surface group chain length (i.e., surface group oligomerization). Finally, the thermal stability of functionalized GeNS was increased to 470 °C, which is expected to facilitate ready processing (e.g., blending and extrusion) with functional polymers.

Chapter 4

Germanium Nanosheets Surface Functionalization: Dehydrocoupling Reaction[3]

4. 1 Ge-Si Bond Formation

A key parameter that can impact nanomaterial properties dramatically is surface functionality;[126] it influences material stability and processability, while simultaneously providing a convenient approach for tailoring optical and electronic response. We[200] and others[207,208,210,260] have reported surface modification of germanane nanosheets (Ge NSs). However, these studies have been limited largely to cases in which surface groups are tethered through covalent Ge−C bonds.

Dehydrogenative coupling (DHC; Equation 4.1) reactions have been applied widely in organic syntheses as well as in materials chemistry.[180,125,165,261–263] Transition-metal-promoted DHC has been demonstrated for organosilanes as well as Si-based materials (e.g., nanoparticles, bulk surfaces),[125,180] and catalyst-free thermally-induced DHC involving Si-based systems also has been reported.[165] In contrast, reports of DHC reactions involving Ge-based materials remain largely unknown.

$$\equiv Ge{-}H + \equiv Si{-}H \rightarrow \equiv Ge{-}Si\equiv + H_2 \qquad (4.1)$$

Herein, we report a study into using thermally-induced DHC reactions to modify GeNS surfaces (Figure 4.1) and demonstrate that these reactions afford

[*] Portions of this Chapter have been reproduced and/or adapted from the following publication: Yu, H.; Thiessen A. N.; Hossain, M. A.; Kloberg, J. M; Rieger, B.; Veinot, G. C. J. Thermally-Induced Dehydrogenative Coupling of Organosilanes and H-terminated Silicon Quantum Dots onto Germanane Surfaces. Chemistry of Materials. 2020, 32 (11), 4536-4543.

convenient attachment of organosilanes, as well as other Si–H bonds containing nanomaterials (e.g., nanoparticles).

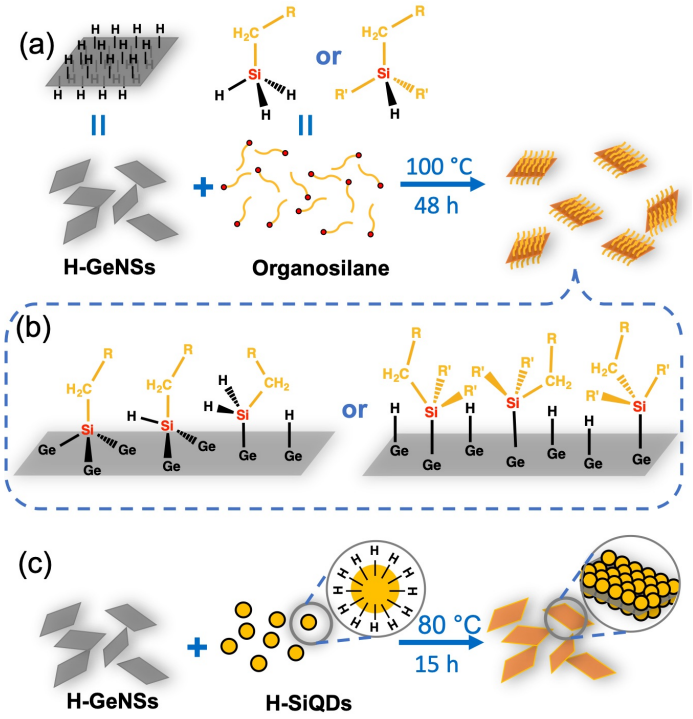

Figure 4.1. (a) Heteronuclear dehydrocoupling of organosilanes on the surfaces of germanane nanosheets. (b) Possible surface bonding modes of attachment of primary (left) and tertiary alkylsilanes. (c) Heteronuclear dehydrocoupling of H-SiQDs on the surfaces of germanane nanosheets.

4. 2 Materials and Methods

4. 2. 1 Materials

All reagents were purchased from *Sigma-Aldrich* and *Gelest Inc* and used without further purification, unless otherwise stated. All solvents were dried using an Innovative Technology, Inc. Grubbs-type solvent purification system. $CaGe_2$ and HGe-flakes were synthesized with the same methods as in the Chapter 2.

4. 2. 2 Dehydrocoupling Between Organosilanes and H-GeNSs

In a nitrogen-filled glove box, HGe-flakes (5 mg, 0.06 mmol Ge-H groups) were transferred into a dry 5 mL Biotage® microwave tube. Dry degassed toluene (5 mL) and silanes (0.8 mmol) were added, and the tube was sealed. Subsequently, the reaction mixture was ultrasonicated in a bath sonicator (Fisher Scientific FS30) for 3 h, after which it was heated to and maintained at 100 °C and stirred for 48 h. The resulting red suspension was transferred to a PTFE centrifuge tube, methanol (40 mL) was added, and the mixture was centrifuged (12,000 rpm for 10 min) to yield a deep red pellet. The solid was redispersed in 2 mL of toluene. Methanol (40 mL) was added, and the mixture was centrifuged (12,000 rpm for 10 min). This suspension/precipitation procedure was repeated twice, after which the silane-Ge NSs were freeze-dried from benzene and finally dispersed in toluene.

4. 2. 3 Synthesis of 3-nm Si QDs in SiO_2 Matrix Composite

The synthesis of hydride-terminated silicon quantum dots (Si QDs) was followed by the method developed in the Veinot lab. In a typical synthesis, hydrogen silsesquioxane (ca. 4 g) was placed in a quartz reaction boat, transferred to a Lindberg Blue tube furnace, and heated from ambient to a peak processing temperature of 1100 °C at 18 °C min^{-1} in a slightly reducing atmosphere (5% H_2/95% Ar). The sample was maintained at the peak processing temperature for 1 h. Upon cooling to room temperature, the resulting amber solid was ground into a fine brown powder using a two-step process. First, the solid was crushed using an agate mortar and pestle to remove large particles. Further grinding was achieved using a Burrell wrist-action shaker upon shaking with high-purity silica beads for 5 h. The resulting SiQD/SiO_2 composite powders were liberated from the SiQD/SiO_2 composites using HF etching.

4. 2. 4 Synthesis of 8-nm Si QDs in SiO_2 Matrix Composite

The synthesis of hydride-terminated silicon quantum dots (Si QDs) was followed by the method developed in the Veinot lab. In a typical synthesis, hydrogen silsesquioxane (ca. 4 g) was placed in a quartz reaction boat, transferred to a Lindberg Blue tube furnace, and heated from ambient to a peak processing temperature of 1200 °C at 20 °C min^{-1} in a slightly reducing atmosphere (5% H_2/95% Ar). The sample was maintained at the peak processing temperature for 1 h. Upon cooling to room temperature, the resulting amber solid was ground into a fine brown powder using a two-step process. First, the solid was crushed using an agate mortar and pestle to remove large particles. Further grinding was achieved using a Burrell wrist-action shaker upon shaking with high-purity silica beads for 5 h. The resulting SiQD/SiO_2 composite powders were liberated from the SiQD/SiO_2 composites using HF etching.

4. 2. 5 Synthesis of 64-nm Si QDs in SiO_2 Matrix Composite

The synthesis of hydride-terminated silicon quantum dots (Si QDs) was followed by the method developed in the Veinot lab. In a typical synthesis, hydrogen silsesquioxane (ca. 4 g) was placed in a quartz reaction boat, transferred to a Lindberg Blue tube furnace, and heated from ambient to a peak processing temperature of 1500 °C at 25 °C min^{-1} in a slightly reducing atmosphere (5% H_2/95% Ar). The sample was maintained at the peak processing temperature for 1 h. Upon cooling to room temperature, the resulting amber solid was ground into a fine brown powder using a two-step process. First, the solid was crushed using an agate mortar and pestle to remove large particles. Further grinding was achieved using a Burrell wrist-action shaker upon shaking with high-purity silica beads for 5 h. The resulting SiQD/SiO_2 composite powders were liberated from the SiQD/SiO_2 composites using HF etching.

4. 2. 6 Synthesis of Hydride-terminated Si QDs

First, 0.2 g of the ground SiQD/SiO_2 composite was transferred to a PTFE beaker equipped with a Teflon-coated stir bar. Then, ethanol (3 mL) and water (3 mL) were added under mechanical stirring to form a brown suspension, followed by 3 mL of 49 % HF aqueous solution. (**Caution! HF must be handled with extreme care.**) After etching for 1 h in subdued light, the suspension appeared orange/yellow. Subsequently, hydride-terminated Si QDs were extracted from the aqueous layer into ca. 30 mL of toluene by multiple (i.e., 3 × 10 mL) extractions. The SiQD toluene suspension was transferred to test tubes, and the Si QDs were isolated by centrifugation at 3000 rpm. The resulting Si QDs were freeze-dried from benzene and stored in a nitrogen-filled glove box for future functionalization.

4. 2. 7 Dehydrocoupling of Si QDs and H–Ge NSs

In a nitrogen-charged glove box, HGe-flakes (10 mg, 0.12 mmol Ge-H) were transferred into a dry 25 mL Biotage® microwave tube. Dry degassed toluene (10 mL), and Si QDs (50 mg, 0.45 mmol Si-H) were added, and the tube was sealed. Next, the reaction mixture was ultrasonicated in a bath sonicator (Fisher Scientific FS30) for 3 h, after which it was heated to and maintained at 80 °C (Sample 1) and 70 °C (Sample 2), respectively, and stirred for 15 h. Afterwards, 1-dodecene (2 mL, 9.0 mmol) was added by syringe, and the reaction mixture was heated and stirred at 130 °C for 15 h. The resulting yellow-brown suspension was transferred to a PTFE centrifuge tube, toluene (40 mL) was added, and the mixture was centrifuged (5,000 rpm for 30 min) to yield a deep brown pellet. The solid was redispersed in toluene (40 mL). This suspension/precipitation procedure was repeated twice, after which the dodecyl protected Si QDs/Ge NSs hybrids were freeze-dried from benzene and finally dispersed in toluene.

4. 3 Material Characterization

4. 3. 1 Fourier Transformed Infrared (FT-IR) Spectroscopy

FT-IR Spectra were acquired using a Thermo Nicolet Magna 750 IR Spectrometer. Samples were prepared by drop coating a toluene dispersion of the material of choice onto an electronic- grade Si-wafer (N-type, 100 surface, 100 mm thickness and 10 ohm·cm resistivity) and dried under a nitrogen atmosphere.

4. 3. 2 Electron Microscopy (TEM)

Bright-field transmission electron microscopy (TEM) images were taken with a JEOL JEM-ARM200CF S/TEM electron microscope at an accelerating voltage of 200 kV. The HRTEM images were processed using Gatan Digital Micrograph software (Version 2.02.800.0). TEM samples were prepared by depositing a droplet of diluted functionalized Ge NSs suspensions in toluene onto a holey/lacey carbon-coated copper grid (obtained from Electron Microscopy Inc.). The grid was kept in a vacuum chamber for at least 24 h prior to data collection.

Scanning electron microscopy (SEM) images were obtained from Zeiss Sigma 300 VP-FESEM (equipped with a Bruker energy dispersive X-ray spectroscope) at an accelerating voltage of 20 kV. SEM samples were prepared by depositing a droplet of concentrated functionalized Ge NSs suspensions (ca. 1 mg/mL) in toluene onto an aluminum stub. For GeH flakes and thick samples, powders of samples were coated on conductive double side tape supported by an aluminum stub. Non-conductive samples were coated further with graphite using a thermal evaporator.

4. 3. 3 X-ray Photoelectron Spectroscopy (XPS)

XPS was performed using a Kratos Axis Ultra instrument operating in energy spectrum mode at 210 W. Samples were prepared by depositing a suspension of the

material of choice onto a copper foil substrate, followed by drying in air. Prior to analysis, the Ge (111) wafer reference was cleaned by immersing in 30% v/v H_2O_2 for 90 s, followed by 10 min etching in 10% v/v HF. The base and operating chamber pressure were maintained at 10^{-7} Pa. A monochromatic Al K source (λ = 8.34Å) was used to irradiate the samples, and the spectra were obtained with an electron take-off angle of 90°. CasaXPS software (VAMAS) was used to interpret high-resolution spectra. All spectra were calibrated internally to the C1s emission (284.8 eV). After calibration, a Shirley-type background was applied to remove most of the extrinsic loss structure.

4. 3. 4 Diffuse Reflective Analysis

Diffuse reflective analysis was performed using a Cary 5000 UV-Vis-NIR, with a diffuse reflectance integrating sphere attachment. The detector and grading filter were changed at 900 nm.

4. 3. 5 Raman Spectroscopy

Raman spectroscopy was performed using a Renishaw inVia Raman microscope equipped with a 643 nm laser operating at a power of 3.98 mW on the sample. Samples were prepared by mounting the suspension on 100 nm thick gold-coated glass.

4. 4 Results and Discussion

4. 4. 1 Organosilane Functionalized Germanium Nanosheets

Germanane flakes (HGe-flakes) used throughout the presented investigation were prepared as described in Chapter 2.[200] Briefly, $CaGe_2$ was synthesized via arc melting of a stoichiometric mixture of the constituent metals (i.e., Ca and Ge). Then, it was

exposed to concentrated HCl at –30 °C for one week to deintercalate Ca^{2+} ions. The resulting HGe-flakes were exfoliated with 3 h sonication to yield freestanding H-GeNSs and maximize the accessibility of their surfaces. Subsequently, an excess of the Si-H bearing reagent of choice was added, and the resulting deep red suspension was mixed thoroughly and heated to 100 °C in a nitrogen atmosphere for 48 h. These conditions were chosen, based upon prescreening (Figure 4.2) of products prepared at defined reaction temperatures and times for characteristic functional groups (e.g., Ge−H, Si−H, Si−O−Si, etc.).

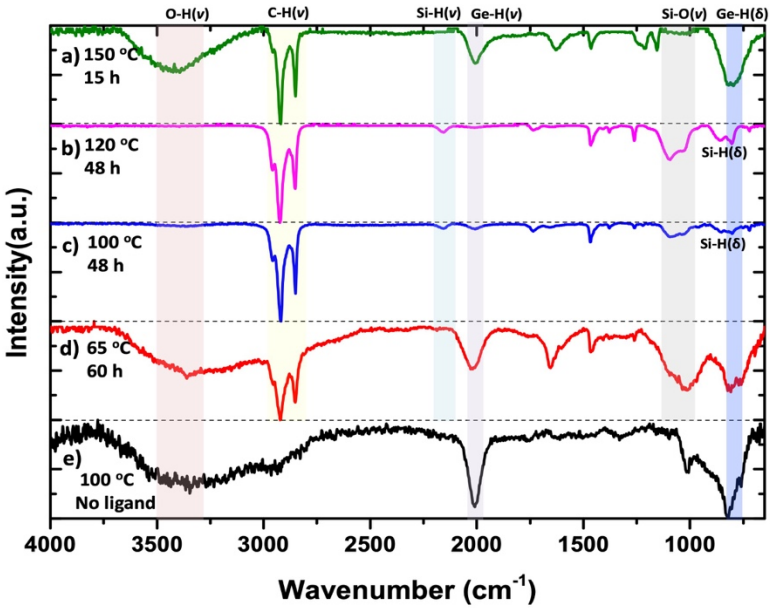

Figure 4.2. FTIR spectra of products obtained from indicated reaction conditions between octadecylsilane and germanane nanosheets. Products of reactions performed at 100 °C or 120 °C (blue and magenta traces, respectively) show a diminished Ge-H feature (ca. 2000 cm^{-1}), consistent with effective surface functionalization after 48 h. Reaction products obtained from higher reaction temperatures and shorter reaction times (150 °C, 15 h; green trace) did not provide effective functionalization, as evidenced by the presence of features arising from oxygen-containing species. Reactions performed at lower temperatures for longer times (i.e., 65 °C, 60 h; red trace) provide materials exhibiting intense Si-O-Si stretching and Ge-H features consistent with a mixture of oxidized silanes with non-functionalized GeH NSs.

The organo-functionalized R-Ge NSs remain suspended in toluene for weeks and resist oxidation in wet ethanol for days, as evidenced by its characteristic red colour. This is consistent with functionalization and in direct contrast to the behaviour exhibited by H-GeNSs that settle from suspension rapidly.

FTIR spectroscopy provides insight into GeNS surface chemistry. Spectra of all functionalized NSs investigated here show the expected features associated with the target surface groups (Figure 4.3). Further supporting functionalization, we note that residual Ge−H features at ca. 830 and 2001 cm^{-1} in functionalized systems are diminished in intensity when compared to equivalent spectral features of the parent H-Ge flakes. Features associated with O−H stretching and bending at ca. 3420 and 1633 cm^{-1}, respectively, that are manifested in the H-Ge flakes spectrum also are diminished dramatically following the reaction, consistent with functionalization.[242]

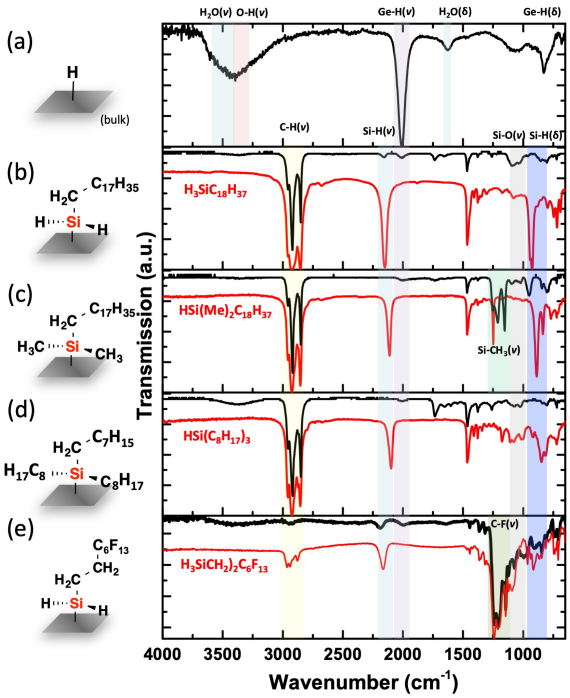

Figure 4.3. FTIR spectra of (a) H-Ge flakes, (b-e) neat organosilanes (red) and organosilane-terminated Ge NSs (in black); the silanes are (b) octadecylsilane, (c) dimethyloctadecylsilane, (d) trioctylsilane and (e) (tridecafluoro-1,1,2,2-tetrahydrooctyl)silane.

This is in agreement with the present functionalized Ge NSs possessing very limited amounts of surface oxidation (See XPS; vide infra) and in direct contrast to what has been reported previously for DHC modified porous-Si surfaces.[165]

Closer inspection of the IR spectra of dimethyloctadecylsilane and trioctylsilane modified Ge NSs provides additional insight into the surface structure. Upon reacting with H-GeNSs, all Si−H associated spectral features from these silanes possess a single Si−H bond disappear. In addition, the characteristic ν(Si−CH_3) observed at 1249 cm^{-1} in the spectrum of neat dimethyloctadecylsilane splits into three peaks after GeNS surface attachment. This observation suggests that vibrations within the surface bonded dimethyloctadecylsilyl moiety are more restricted as a result of the underlying GeNS. Finally, contrary to what is observed for GeNS surfaces modified with primary silanes, ν(Si−O) bands at 1020 and 1070 cm^{-1} show intensity comparable to parent silanes.

Raman spectroscopy probes the internal (i.e., Ge-Ge) bonding of the Ge NSs. Unfortunately, due to the lack of long-range ordering, the Ge−Si stretching is not observed at ca. 400 cm^{-1}.[264–266] However, in all cases, a Ge−Ge stretching feature is noted. For HGe-flakes this feature appears at slightly lower energy (i.e., 288 vs. 300 cm^{-1}) than for bulk crystalline Ge (i.e., c-$Ge_{(bulk)}$; Figure 4.4 blue trace); it also shows minor tailing to lower energy that has previously been attributed to increased amorphous content (i.e., structural disorder).[210] After attachment of surface groups via DHC, the Ge−Ge feature blue-shifts slightly to 292 cm^{-1}. Given that surface bonded Si is less electronegative than H moieties, this observation is expected because surface-bonded Si will impart a smaller inductive influence on Ge−Ge bond strength that the H it replaces. We also note that increasing steric bulk surrounding the Si (i.e., dimethyloctadecylsilane-terminated Ge NSs) provides additional tailing/broadening of the Ge−Ge feature. The exact origin of this observation is

unclear. However, similar observations have been noted for "bulkier" surface groups introduced using other approaches.[120]

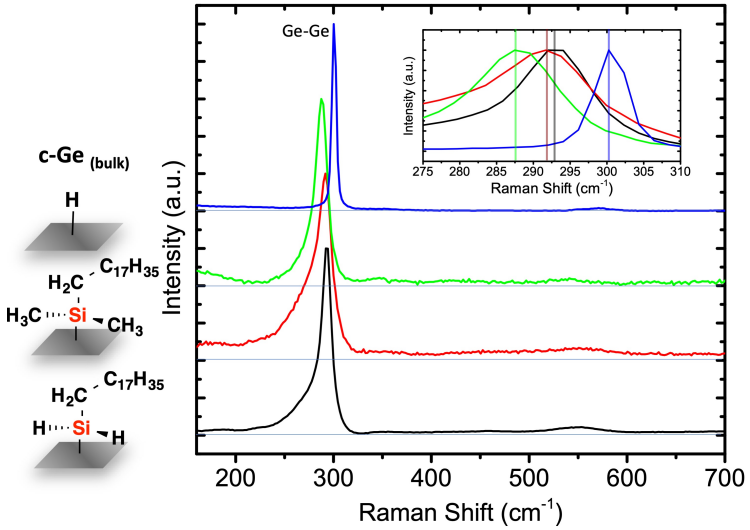

Figure 4.4. Raman spectra of crystalline germanium powder (blue), H-Ge flakes (green), dimethyloctadecylsilane-terminated Ge NSs (red), and octadecylsilane-terminated Ge NSs (black). Inset: highlighting the shifts of Ge-Ge vibration.

The survey XPS results of (tridecafluoro-1,1,2,2-tetrahydrooctyl)silane, dimethyloctadecylsilane, and octadecylsilane functionalized Ge NSs were compared to a Ge (111) reference, and all show intense Ge emissions (Figure 4.5). After surface modification, additional Si emissions and an increase in the C 1s signal were observed, indicating the presence of organsilanes. Furthermore, strong F 1s and KLL auger electrons were detected from the fluorine-rich (tridecafluoro-1,1,2,2-tetrahydrooctyl)silane functionlized GNSs.

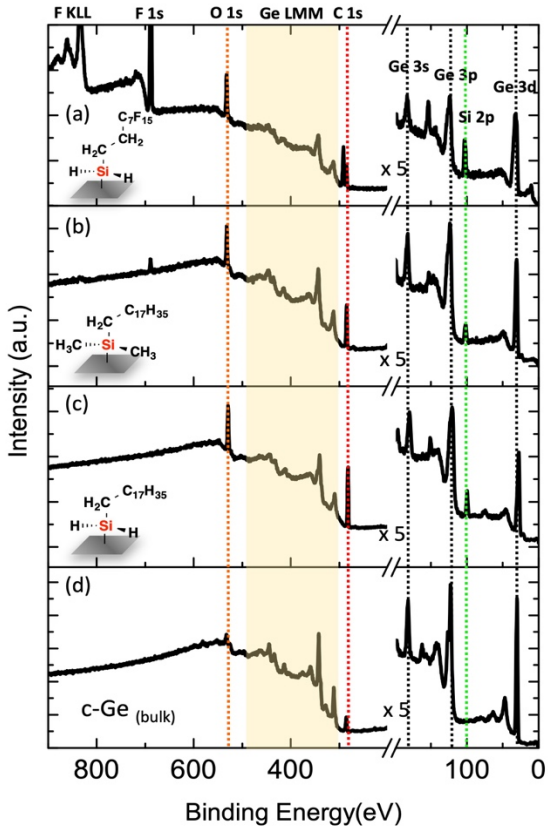

Figure 4.5. Survey X-ray photoelectron spectra of (a-c) organosilane functionalized Ge NSs and (d) clean Ge (111) wafer; the silanes are (a) (tridecafluoro-1,1,2,2- tetrahydrooctyl)silane, (b) dimethyloctadecylsilane and (c) octadecylsilane.

X-ray photoelectron spectroscopy (XPS) allows probing of the composition as well as oxidation states of constituent elements in the presented Ge NSs (Figure 4.6). All spectra were calibrated to adventitious carbon at a binding energy (BE) of 284.8 eV.[120,243] We also have provided a spectrum acquired from an intrinsic Ge (111) wafer for comparison that shows a characteristic Ge(0) emission at 29.45 eV. This emission is fitted readily to the $3d_{5/2}$ and $3d_{3/2}$ spin-orbit couple and is well defined (i.e., the $3d_{3/2}$ component is obvious as a high BE shoulder), consistent with a long-range ordered structure of crystalline Ge.

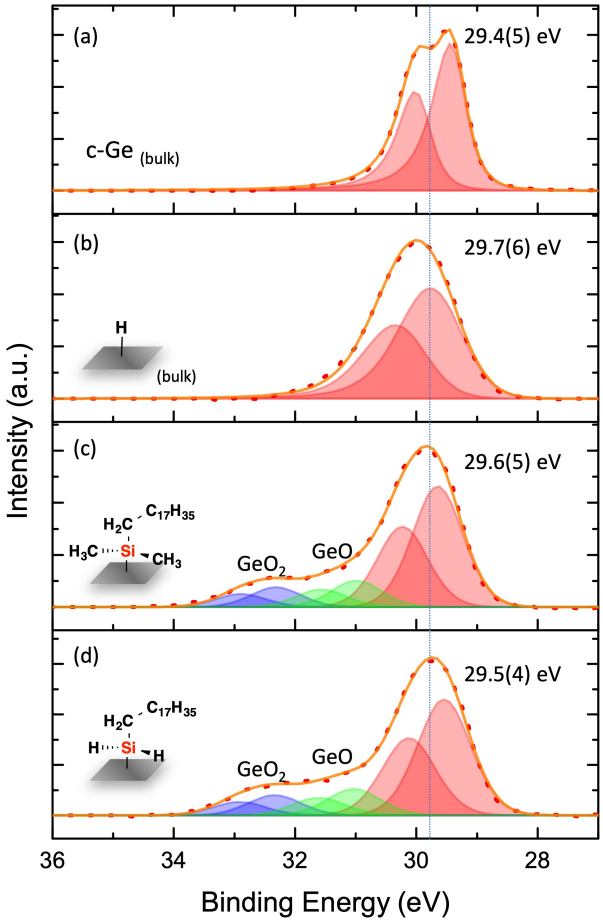

Figure 4.6. High-resolution XP spectra of Ge 3d region for (a) Ge (111) wafer, (b) precursor H-Ge flakes, (c) dimethyloctadecylsilane-terminated Ge NSs, and (d) octadecylsilane-terminated Ge NSs. The deconvolution of each Ge species has been fit to the Ge $3d_{5/2}$ and $3d_{3/2}$ spin-orbit pairs in the same colour set.

The XP spectra of all Ge NSs feature emissions that are attributed readily to the Ge framework, however, their breadth (i.e., full-width-at-half-maximum; FWHM) is greater than that observed for the crystalline Ge (111) wafer standard. This observation is expected and has been attributed previously to a considerable number of atoms in materials with different sizes and orientations, which lead to a distribution of binding energies and symmetric broadening that is Lorentzian in nature.[120] Following DHC surface modification, high-energy shoulders appear on the Ge emission that are confidently attributed to trace oxidation that occurs during material

processing. We also note that the center of the Ge $3d_{5/2}$ emission shifts to lower BE (ca. 0.1 to 0.2 eV) because surface bonded H atoms are replaced by less electronegative Si atoms.

Unfortunately, while the integrity of NS Ge–Ge framework can be confirmed post DHC functionalization, any detailed evaluation of the Ge 3d spectral region for (tridecafluoro-1,1,2,2-tetrahydrooctyl)silane functionalized Ge NSs is precluded by overlap with the F 2s photoelectron emission Figure 4.7).[267]

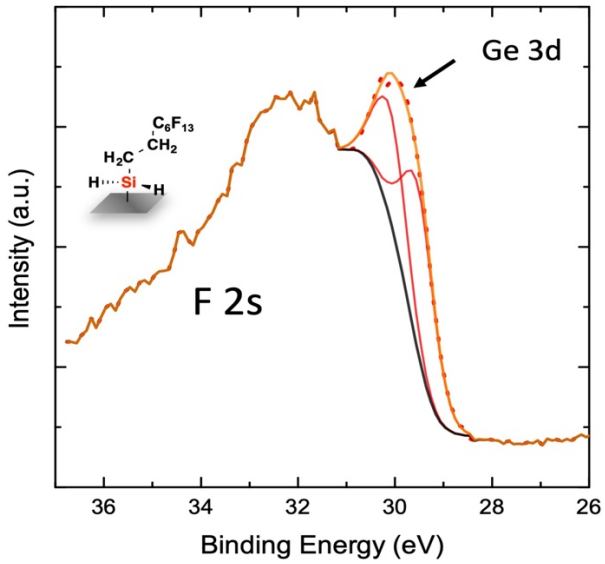

Figure 4.7. High-resolution XP spectrum of Ge 3d region of (tridecafluoro- 1,1,2,2-tetrahydrooctyl) silane-terminated Ge NSs. The Ge 3d and F 2s emissions overlap, preventing detailed analysis.

It is also possible to probe the presence of surface-bonded Si atoms. The high-resolution Si 2p spectra (Figure 4.8) of all functionalized sheets show the presence of organosilicon species at ca. 102.1 eV, consistent with DHC surface modification.[268,269] We also note trace higher oxidation state Si in the XP spectra at 103.5 eV, consistent with very limited (i.e., <10%) oxidation. From the integration of the Si and Ge spectral regions, surface coverages are estimated to be 22% and 35% for dimethyloctadecylsilane- and octadecylsilane-terminated Ge NSs, respectively.

Again, similar evaluation surface coverage for tridecafluoro-1,1,2,2-tetrahydrooctyl)-silane functionalized Ge NSs is limited by the overlap of the Ge 3d and F 2s emissions.

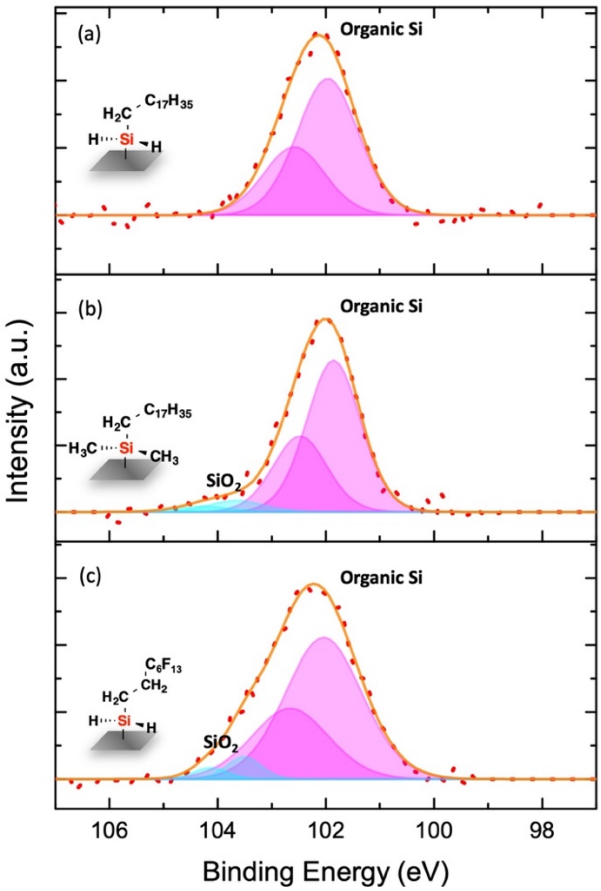

Figure 4.8. High resolution XP spectra of of Si 2p region organosilane functionalized Ge NSs, the silanes are (a) octadecylsilane, (b) dimethyloctadecylsilane and (c) (tridecafluoro-1,1,2,2-tetrahydrooctyl)silane.

Deconvolution of the high-resolution C 1s spectra (Figure 4.9) provides further evidence of the surface bonded organosilane ligands presence. The degree of contamination from instrument chamber adventitious carbon was estimated by deconvoluting the C 1s region for a clean Ge (111) wafer and H-Ge flakes. As expected, octadecylsilane and dimethyloctadecylsilane functionalized Ge NSs show a

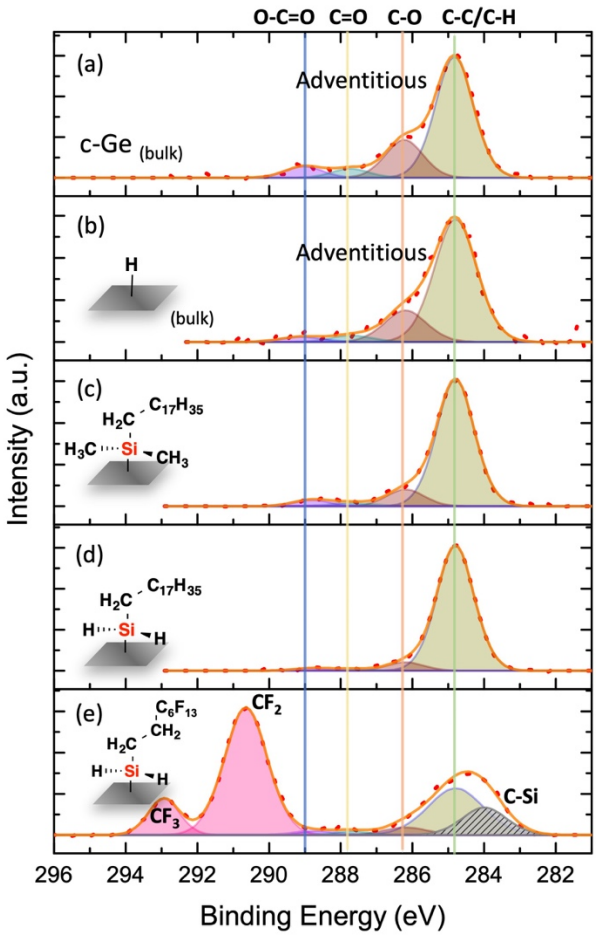

Figure 4.9. Hign resolution XP spectra of C1s regions of (a) clean Ge (111) wafer (b) H-Ge flakes, (c-e) organosilane functionalized Ge NSs, the silanes are (c) octadecylsilane, (d) dimethyloctadecylsilane and (e) (tridecafluoro-1,1,2,2- tetrahydrooctyl)silane, (a) and (b) were used to evaluate advititious carbon level.

more intense emission centered at 284.8 eV that is attributable to hydrocarbons containing alkyl chains (i.e., surface groups). For (tridecafluoro-1,1,2,2-tetrahydrooctyl)silane functionalized Ge NSs, we also note new spectral features in the C 1s region at 291.6 eV and 293.1 eV originated from $-\underline{C}F_2-$ and $-\underline{C}F_3$ respectively, that are accompanied by the appearance of an F1s emission at 688.3 eV (Figure 4.10).

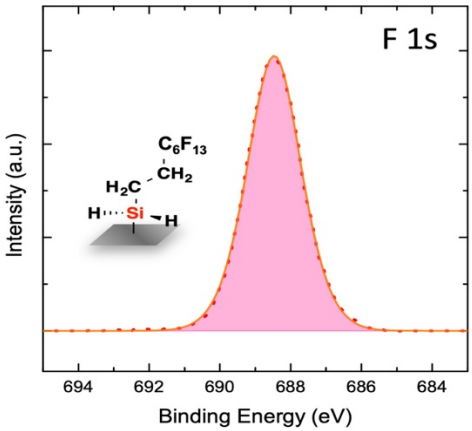

Figure 4.10. High resolution XP spectrum of F 1s region of (tridecafluoro-1,1,2,2-tetrahydrooctyl) silane-terminated Ge NSs

Diffuse-reflectance spectra (Figure 4.11) obtained for H-terminated Ge NSs and dodecyl-Ge NSs, both heated to 130 °C, as well as Samples 1 and 2 (vide infra) show that the optical band gaps of these materials are dominated by Ge NSs. Furthermore, functionalization (with alkyl functionalities or Si QDs) has a negligible impact on this property.

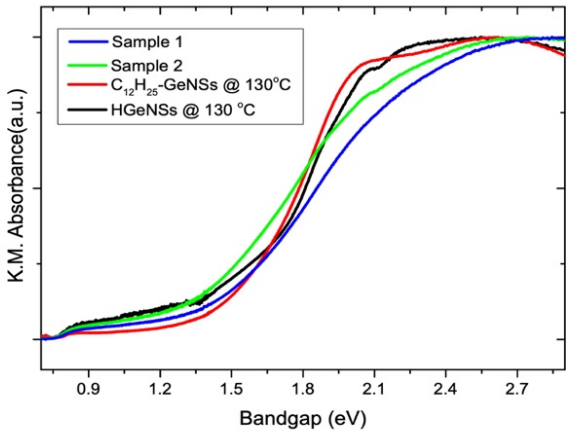

Figure 4.11. Diffuse reflectance spectra for **(blue)** Sample 1: H−Ge NSs reacted with H−Si QDs at 80 °C and dodecyl-functionalized at 130 °C, **(green)** Sample 2: H-GeNSs reacted with H−Si QDs at 70 °C and dodecyl- functionalized at 130 °C, **(red)** dodecyl- functionalized Ge NSs at 130 °C, and **(black)** H−Ge NSs heated at 130 °C.

Bright-field transmission electron microscopy (TEM) imaging of functionalized Ge NSs shows randomly shaped thin structures (Figures 4.12 to 14). Lattice fringes measured directly afford separations of 0.32 nm, consistent with the $(10\bar{1}0)$ plane of GeNS;[70,76] however, discerning these features is challenging for individual NSs bearing long-chain organosilane moieties.[200] Complicating this analysis, the freestanding NSs can stack randomly further occluding this measurement.

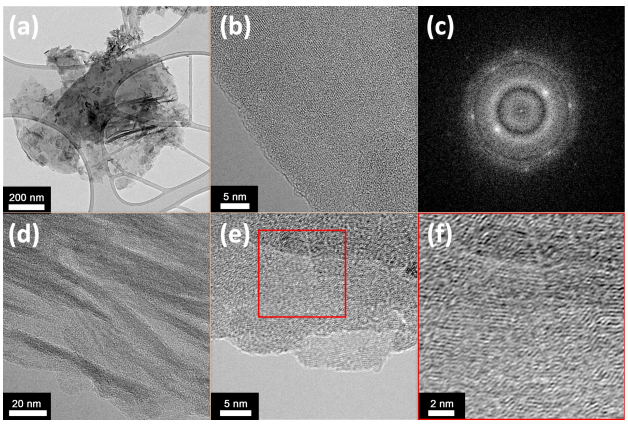

Figure 4.12. TEM images of octadecylsilane-terminated Ge NSs, (a) low magnification overview, (b) high magnification, (c) fast Fourier transform (FFT) of (b), (d) edge of randomly folded Ge NSs, (e) randomly stacked Ge NSs, and (f) the magnified area in (e).

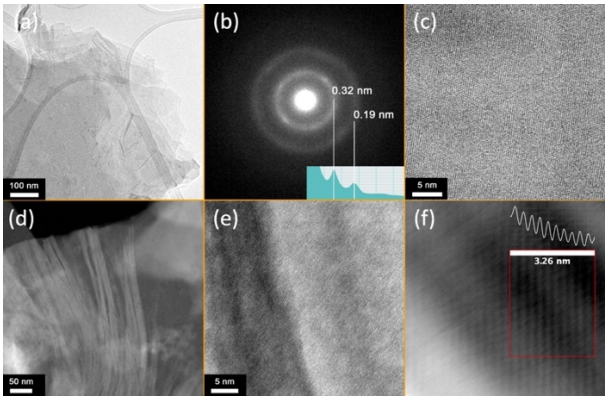

Figure 4.13. (S)TEM images of trioctylsilane-functionalized Ge NSs, (a) bright-field low magnification, (b) SAED pattern at low-magnification (inset: radially integrated signal), (c) higher magnification, and (d-f) dark-field scanning images.

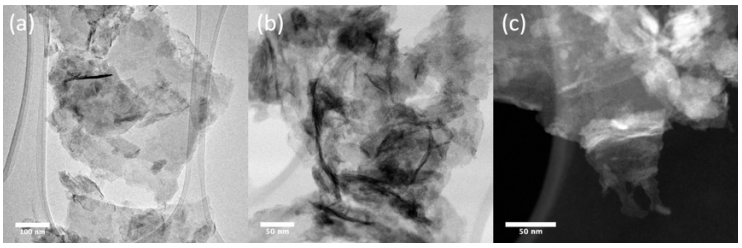

Figure 4.14. (a, b) bright-field TEM images and (c) dark-field STEM image of (tridecafluoro-1,1,2,2,-tetrahydrooctyl)silane-functionalized Ge NSs.

Energy dispersive X-ray mapping of organosilanes functionalized sheets were measured under high angle annular dark-field (HAADF) scanning mode (Figure 4.15). Regions with high-contrast in HAADF images consisted primarily of Ge, as evidenced by spatial overlapping with Ge Kα mapping. For octadecylsilane functionalized Ge NSs, despite the trace Si and the strong carbon background generated from the clean holey carbon grid, the Si and C Kα mapping overlap with regions of high Ge content. For (tridecafluoro-1,1,2,2-tetrahydrooctyl)silane functionalized Ge NSs, additional F Kα signal was detected.

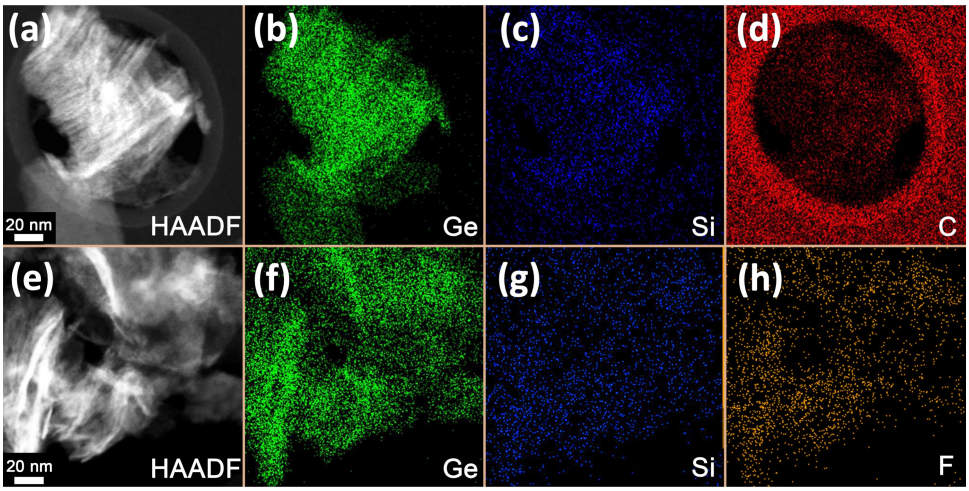

Figure 4.15. (a-d) HAADF-STEM images with elemental mapping of octadecylsilane-terminated Ge NSs and (e-h) (tridecafluoro-1,1,2,2-tetrahydrooctyl)silane-terminated Ge NSs.

4. 4. 2 Silicon Quantum Dot–Germanium Nanosheets Hybrids

To explore the utility of DHC surface reactions further, we investigated reactions of luminescent H-terminated silicon quantum dots (H-SiQDs) of predefined size (d_{TEM} = 3 nm) with H-GeNSs. Our goal was to link 0D and 2D Group 14 nanomaterials via Ge-Si bonds to prepare SiQD-GeNS hybrids (Figure 4.16). While the primary focus of the present study was to demonstrate reactivity, one can envision that these materials could lead to the development of heretofore unknown applications that derive their utility from a combination of the high electron mobility of germanium with the optical and/or chemical response of nanosilicon (e.g., advanced battery electrodes, photoresponsive materials, etc.).

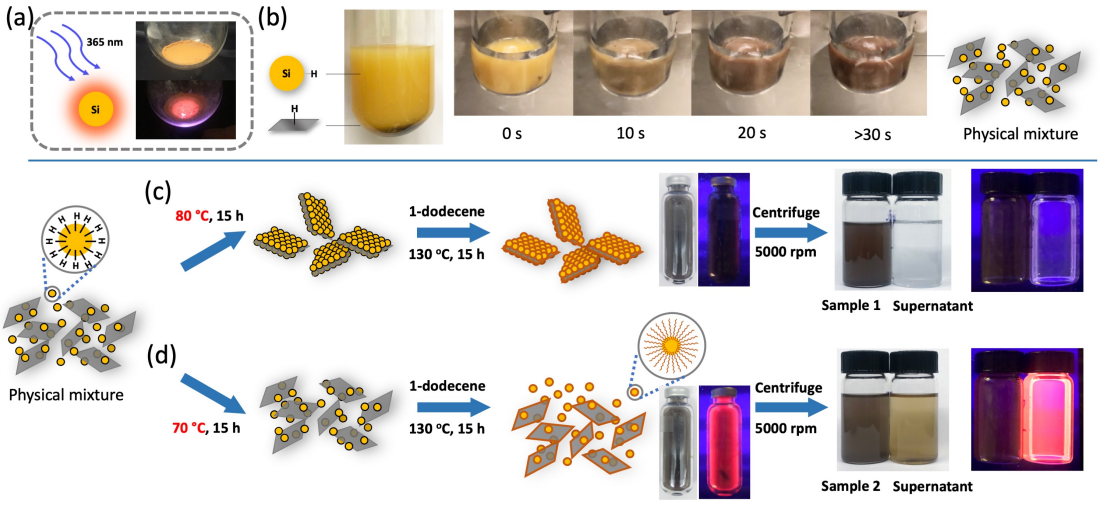

Figure 4.16. Preparation of SiQD-GeNS hybrids. (a) Photoluminescence of H-terminated 3 nm diameter Si QDs under UV-illumination (365 nm). (b) Visual appearance of a physical mixture of Si QDs and GeNS after indicated sonication times. (c, d) Dehydrocoupling protocols showing the visual appearance and photoluminescence at indicated stages upon exposure to UV illumination (365 nm).

H-SiQDs were synthesized following a well-established method developed in the Veinot laboratory (See: Supporting Information).[25,120] Subsequently, they were combined and sonicated with H-GeNSs under an inert atmosphere (Figure 4.16b). Weak photoluminescence arising from the H-SiQDs is detected visually upon exposure to a handheld UV lamp (365 nm). The mixture was divided into two identical aliquots (Figures 4.16c and d); one was heated to 80 °C (the threshold temperature for DHC to proceed; Sample 1) and the other 70 °C (Sample 2). After

heating for 15 h, no photoluminescence was detected visually from Sample 1, while the emission from Sample 2 remained, albeit at a qualitatively diminished intensity. The observations for Sample 1 are consistent with direct SiQD-GeNS bonding when samples are heated to appropriate temperatures (i.e., 80 °C). The diminished intensity observed for Sample #2 was attributed reasonably to scattering; however, the possibility of some limited DHC cannot be neglected completely.

Separation of physical mixtures of Ge NSs and Si QDs is difficult even when the two components are not bonded. However, differences in material solvent compatibility do allow for differential settling (i.e., functionalized GeNS and SiQD/GeNS hybrids settle from suspensions more readily than functionalized Si QDs). In addition, Si QDs functionalized via hydrosilylation are intensely luminescent and readily detected.[112] In this regard, 1-dodecene was added to both samples, and the mixtures were heated to 130 °C in an inert atmosphere for 15 h. While one might expect DHC reactions to proceed under these conditions, we have observed that solid–solid reactions involving Si QDs and Ge NSs are slow. As such, hydrosilylation and hydrogermylation reactions involving 1-dodecene are expected to dominate, and the remaining H-terminated surfaces of Si QDs and Ge NSs will be passivated.

Centrifuging Samples 1 and 2 provided dark red/purple solids. However, the resulting supernatants differed qualitatively. The colourless supernatant obtained from Sample 1 (Figure 4.16c) showed no visible photoluminescence upon exposure to UV excitation. In contrast, the supernatant from Sample 2 was pale yellow and exhibited intense UV exposure-induced photoemission characteristic of Si QDs (Figure 4.16d). These observations are consistent with the vast majority of Si QDs in Sample 1 being bonded to Ge NSs via Si−Ge linkages (i.e., DHC proceeded). While the specific origin of the absence/loss of SiQD luminescence is unknown, we can discount the

influence of a straightforward internal filter effect in which Ge NSs are simply masked excitation of Si QDs. If this were the case, no SiQD luminescence would be observed for a physical mixture of Ge NSs and functionalized Si QDs (Figure 4.16d).

The quenching of SiQD PL in Sample 1 is the subject of an ongoing investigation in our labs, and we postulate that, because Ge NSs are likely a direct band gap semiconductor and their band gap is smaller than that of Si QDs,[70] photoexcited carriers within the Si QDs are transferred to the bonded germanane nanosheets. This process can be viewed reasonably as a charge transfer process that has been invoked previously for SiQD PL and exploited in sensors.[24,270] In contrast, in Sample 2, DHC did not proceed, and the majority of Si QDs are freestanding. As such, the behaviour of the isolated supernatant is qualitatively similar to what has been noted for Si QDs functionalized with alkyl-terminated surfaces via thermally-induced hydrosilylation reactions.[25]

Transmission electron microscopy and EDX mapping of the present SiQD-GeNS hybrids are consistent with the conclusions drawn from our qualitative evaluation of their PL behaviour noted above. Figure 4.17 shows imaging and EDX mapping of the precipitate obtained from Sample 1; Si QDs maintain their crystallinity, are consistently associated with/on GeNS, and there is no evidence of freestanding Si QDs on the TEM grid. In contrast, Figure 4.18 shows bright-field TEM imaging in which Si QDs are distributed on the grid (i.e., everywhere) with no obvious preference toward having an association with Ge NSs, supporting Sample 2 being a physical (i.e., non-bonded) mixture of Si QDs and Ge NSs.

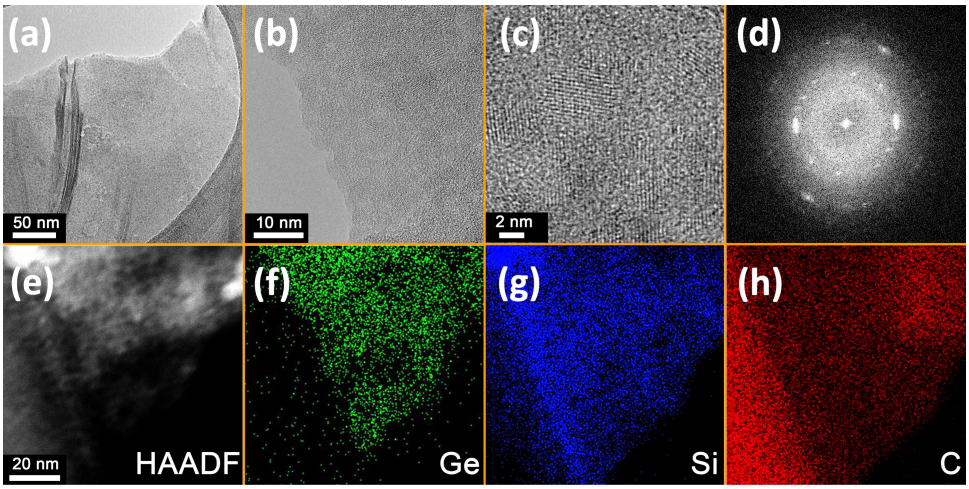

Figure 4.17. 3-nm diameter SiQD-GeNS hybrids; (a, b) bright-field TEM images, (c) high-resolution image, (d)FFT pattern of (c), and (e-h) HAADF-STEM with elemental mapping.

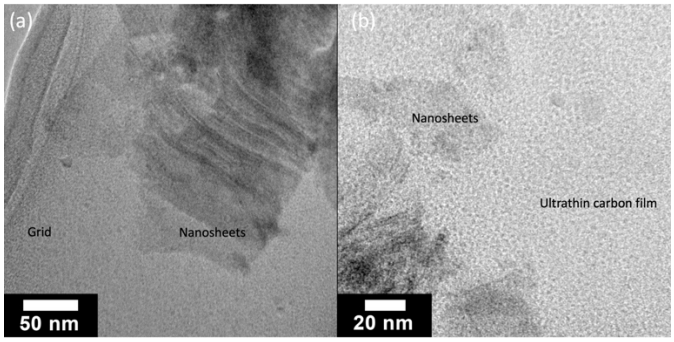

Figure 4.18. Bright-field TEM images of a physical mixture of Si QDs and Ge NSs, Si QDs are dark dots observed on Ge NSs as well as on (a) support grid and (b) ultrathin carbon film.

Finally, Si QDs-Ge NSs hybrids with larger sized Si QDs (i.e. 8 nm and 64 nm) were prepared and confirmed under TEMs (Figure 4.19). Consistent with 3 nm hybrids, individual Si QDs were observed on the carbon film only in rare areas, suggesting effective DHC reactions and purification. At a larger size, crystallinity lattice from HRTEM is contributed mainly from Si QDs due to high coverage. In a particular area with fewer Si QDs (Figure 4.19c), the lattice of both underlying sheets and particles were observed, which again suggests that the Ge-Ge framework is retained after the dehydrocoupling reaction. When the size of nanocrystals is

significantly large (i.e. 64 nm), Ge NSs are no longer acting as a substrate to host particles but rather wrap Si QDs due to their difference in size.

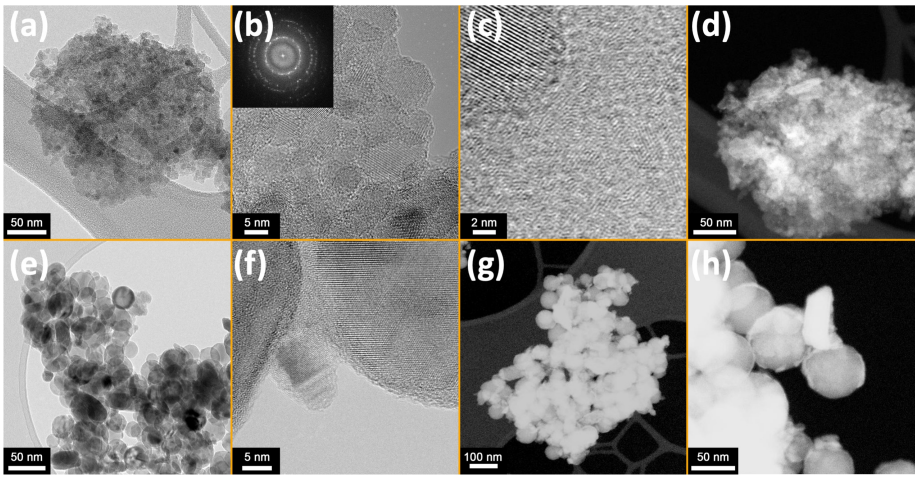

Figure 4.19. TEM images of (a-d) 8-nm sized Si QDs-Ge NSs hybrids, (a) low magnification, (b,c) high magnification at different locations, and (d) in dark field mode; (e-h) 64-nm sized Si QDs-Ge NSs hybrids, (a) low magnification, (b) high magnification, and dark field images at (g) low magnification, (h) high magnification.

4. 5 Summary and Outlook

In summary, we have presented that thermally-induced heteronuclear dehydrocoupling provides a convenient approach to tailoring the surface chemistry of Ge NSs. This represents the first demonstration of the introduction of moieties on Ge surfaces that are linked via Ge−Si bonds. Furthermore, we demonstrated the preparation of a 0D/2D hybrid material comprised of covalently linked Si QDs and Ge NSs that was effectively modified via concurrent hydrogermylation/silylation reactions.

Chapter 5

Poly(dihydrogermane): Synthesis, Stability, and Side Group Substitution

5.1 The Family of Catenated Polygermanes

As described in Chapter 1, catenated polysilanes and polygermanes exhibit unique optical and electrical properties, such as non-linear optical properties[271] and photo-induced electron transfer.[272] Currently, known linear polygermanes are synthesized commonly by using diorganodichlorogermane precursors via Wurtz-type coupling[85,271,273,274] and electroreductive synthesis.[88,97,98] Alternatively, the demethanative coupling of $HGeMe_3$ catalyzed by a Ru complex also was reported with high yield.[103,275] While these reactions offer polygermanes with relatively high molecular weight, the substituents are limited by the availability of dimethyl- or dihalide- germane precursors. On the other hand, reacting Grignard or organolithium reagents with germanium diiodide generally yield short-chain oligogermanes.[85,273,275] We and others have demonstrated various hydrogermylation protocols that afford convenient methods for substituted Ge—H bonds with unsaturated groups on Ge substrates,[124] nanostructures,[28] and layered polygermanes.[200]

The catenated poly(dihydrogermanes), with a formula of $[GeH_2]_n$, which provides Ge–H reactive sites, has been synthesized previously by a topochemical deintercalation reaction of Zintl phase CaGe in cold acids.[108,109] The $[GeH_2]_n$ prepared by this method is a yellow solid with high molecular weight that can, however, cause explosive decomposition to Ge when dry; this significantly limited its processability and scalability. However, since the previous work was done in the early era when most of the material characterization was not available, including powder X-ray

diffraction with synchrotron radiation source, transmission electron microscopy (TEM), Raman spectroscopy, X-ray photoelectron spectroscopy (XPS), absorption spectroscopy, and thermogravimetric analysis (TGA), the structure and properties of these materials remain largely unknown. Furthermore, we also prepared $[GeH_2]_n$ using an alternative method that is safer to handle, and the production is scalable.

In this Chapter, we studied the preparation of high-quality gram-scale $[GeH_2]_n$ using a two-step deintercalation reaction from CaGe and compared its morphology, bonding environment, level of disorder, optical band, and thermal decomposition with traditionally simple acid deintercalated $[GeH_2]_n$. We have shown the $[GeH_2]_n$ prepared by the new method has a more ordered linear fabric morphology, stronger Ge—Ge bond strength, and a larger interstrand distance, which lead to better stability than traditionally prepared $[GeH_2]_n$. Finally, we performed a hydrogermylation reaction on both types of $[GeH_2]_n$ with 1-dodecene that yielded free-standing $[Ge(C_{12}H_{25})_2]_n$, and we noticed interesting patterns upon drying on TEM grids.

5.2 Material and Synthesis

5. 2. 1 Materials

All reagents were purchased from Sigma-Aldrich and Gelest Inc and used without further purification, unless otherwise stated. All solvents were dried using an Innovative Technology, Inc. Grubbs-type solvent purification system.

5. 2. 2 Synthesis of CaGe

A stoichiometric mixture of calcium (Sigma, 99.0%) and germanium (Sigma, 99.999%) was pressed into a pellet and then melted together from both sides in an arc furnace. The resulting product was evaluated using X-ray powder diffraction and X-ray photoelectron spectroscopy.

5. 2. 3 Synthesis of $[GeH_2]_n$

Method 1. In a typical reaction, 2.00 g (17.8 mmol) of freshly ground CaGe fine powders were loaded into an argon-filled Schlenk flask. Then, a mixture of 30 mL distilled acetonitrile and 0.960 mL (53.4 mmol) deionized water was added to the flask and kept for 24 h at room temperature without disturbing. The orange-red reaction mixture was separated by 3000 rpm centrifugation for five min, then washed five times with ice-cold 1:5 v/v concentrated hydrochloride in anhydrous ethanol and three times with anhydrous ethanol; each time, the mixture was separated by 3000 rpm centrifugation for five min. The final yellow-orange powders were dried in vacuum on the Schlenk line. The resulting $[GeH_2]_n$ was covered with aluminum foil and stored in a freezer located in a nitrogen-filled glove box, until further use.

Method 2. In a typical reaction, 0.25 g (2.2 mmol) of freshly prepared CaGe granular was loaded into a Schlenk flask filled with 30 mL of concentrated HCl cooled to –30 °C in a low-temperature freezer. (Caution! Do not use ground fine powder) The granular submerged and broke into pieces in 1–2 min, and the mixture was maintained at –30 °C for 30 min. Then, the bright yellow coloured mixture was centrifuged at 3000 rpm for five min and washed three times with anhydrous ethanol, followed by three times with dry toluene; each was separated by 3000 rpm centrifugation for five min. The final $[GeH_2]_n$ (ca. 0.15 g, 2.0 mmol) was stored in dry toluene (15 mL) with a standard freeze-pump-thaw procedure in a Schlenk flask, covered with aluminum foil, and stored in a –30 °C freezer until further use.

5. 2. 4 Synthesis of $[Ge(C_{12}H_{25})_2]_n$

A mixture of $[GeH_2]_n$ (10 mg, 0.13 mmol Ge-H_2), dry degassed toluene (10 mL), and 1-dodecene (2.0 mL, 2.6 mmol) was loaded into a 25 mL Biotage® microwave tube in a nitrogen-filled glove box or by cannular transfer from a Schlenk flask, and then

the tube was sealed. The reaction mixture was ultrasonicated in a bath sonicator (Fisher Scientific FS30) for three h, after which it was heated to and maintained at 150 °C and stirred for 15 h. The resulting yellow-orange suspension was transferred to a PTFE centrifuge tube, anhydrous ethanol (40 mL) was added as an anti-solvent, and the mixture was centrifuged (13,000 rpm for 30 min) to yield a deep orange pellet. The solid was re-suspended in a minimum amount of toluene (ca. 1 mL). This suspension procedure was repeated twice, after which the $[Ge(C_{12}H_{25})_2]_n$ was freeze-dried from benzene and finally dispersed in toluene.

5. 3 Material Characterization

5. 3. 1 Fourier Transformed Infrared (FTIR) Spectroscopy

FT-IR Spectroscopic analyses were performed using a Thermo Nicolet Magna 750 IR Spectrometer. Samples for FT-IR analysis were prepared by drop coating a toluene dispersion of the functionalized Ge NSs of choice onto an electronic-grade Si-wafer (N-type, 100 surface, 100 mm thickness and 10 ohm-cm resistivity) and dried under nitrogen atmosphere.

5. 3. 2 Electron Microscopy

Bright-field transmission electron microscopy (TEM) images were taken with a JEOL JEM-ARM200CF S/TEM electron microscope at an accelerating voltage of 200 kV. The HRTEM images were processed using Gatan Digital Micrograph software (Version 3.4.1). TEM samples were prepared by depositing a droplet of a diluted suspension in toluene onto a holey or ultra-thin carbon-coated copper grid (obtained from Electron Microscopy Inc.). The grid was kept in a vacuum chamber for at least 24 h prior to data collection.

5. 3. 3 X-ray Photoelectron Spectroscopy (XPS)

XPS analyses were performed using a Kratos Axis Ultra instrument operating in energy spectrum mode at 210 W. The base and operating chamber pressure were maintained at 10^{-7} Pa. A monochromatic Al Kα source (λ = 8.34 Å) was used to irradiate the samples, and the spectra were obtained with an electron take-off angle of 90°. CasaXPS software (VAMAS) was used to interpret high-resolution spectra. All spectra were calibrated internally to the C 1s emission (284.8 eV). After calibration, a Shirley-type background was applied to remove most of the extrinsic loss of structure. The Ge (111) wafer reference was cleaned by immersing in 30% v/v H_2O_2 for 90 s, followed by 10 min etching in 10% v/v HF.

5. 3. 4 Powder X-ray Diffraction (XRD) Analysis

Powder diffraction data was collected at the Canadian Light Source using the CMCF beamline. Samples were loaded in polyimide Katpons, with an inner diameter of 0.300 mm and an outer diameter of 0.350 mm. The samples were loaded into the set up using a magnetic sample holder in transmission mode. Powder data was collected using a Rayonix MX300HE 2D detector, with a detector distance of 150 mm. The beam energy was set to 18 keV, with a spot size of 150 microns. The synchrotron radiation wavelength was calibrated using a LaB_6 standard and was found to be 0.68745 Å. The powder data was integrated using GSAS-II with the LaB_6 calibration to identify the integration area and radiation wavelength. The background from the empty Kapton also was subtracted prior to integration.

5. 3. 5 Raman Spectroscopy

Raman spectroscopy was performed using a Renishaw in*Via* Raman microscope equipped with a 632 nm diode laser operating at a power of 3.98 mW on the sample. Samples were prepared by mounting the powders on a glass slide. At least three spots

were measured for each sample, with an integration of five scans on each spot, with a laser power of 1–5%. To induce $[GeH_2]_n$ prepared by Method 1, a power of 50–100% is applied.

5. 3. 6 Diffuse Reflective Analysis

Diffuse reflective analysis was performed using a Cary 5000 UV-Vis-NIR, with a diffuse reflectance integrating sphere attachment. The detector and grading filter were changed at 900 nm.

5. 4 Result and Discussion

5. 4. 1 Structural Characterization

Poly(dihydrogermane) was prepared by two methods through deintercalation using a Zintl phase precursor CaGe (details are provided in Section 5. 2. 2). Briefly, CaGe was synthesized first by pressing stoichiometric ratios of Ca and Ge into a pellet and then melting them together from both sides in an arc-furnace. The synthesized CaGe is highly crystalline and has its structure confirmed via powder X-ray diffraction (pXRD, Figure 5.1f). CaGe can react with water rapidly at ambient conditions, as evidenced by its colour change from dark gray with a lustre to dark lime in a few minutes and, eventually, to deep orange after several days (Figure 5.1c). A similar observation has been noticed by Vogg and co-workers in the deintercalation of $CaGe_2$ using water to form the $[Ca(OH)_2GeH]_n$ structure.[71] Based on this, we optimized the $[GeH_2]_n$ synthesis condition by mixing fine powders of CaGe and water in a 1:3 molar ratio for 24 h, with acetonitrile used as a solvent, and then washed and centrifuged them with ice-cold 1:5 v/v HCl/EtOH five times (Method 1, Figure 5.1a).

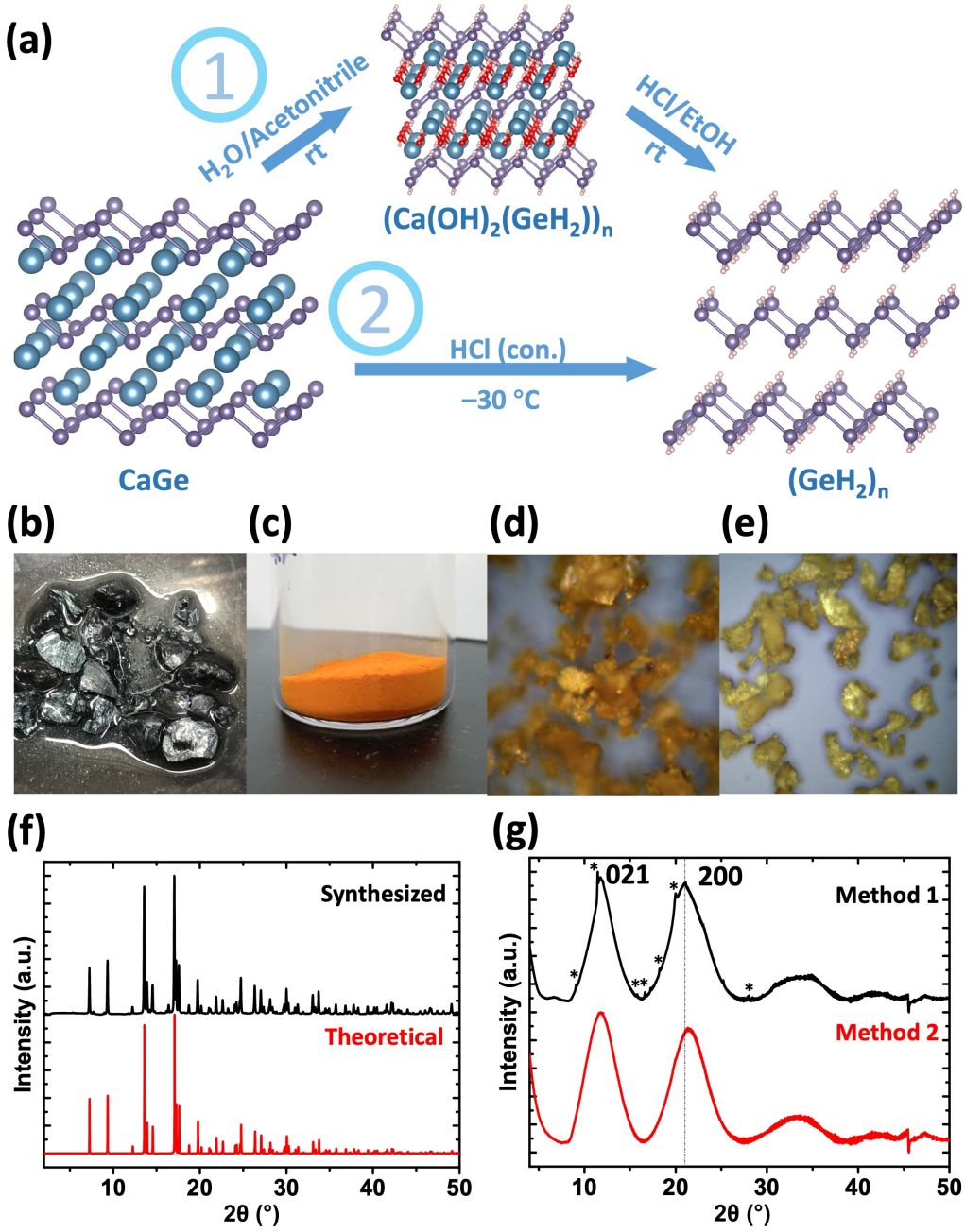

Figure 5.1. (a) Schematic illustration of $[GeH_2]_n$ synthesis from CaGe by Method 1 and 2. Photograph of (b) CaGe, (c) $(Ca(OH)_2GeH_2)_n$, (d) $[GeH_2]_n$ (Method 1), (e) $[GeH_2]_n$ (Method 2). Powder XRD pattern of (f) CaGe and (g) $[GeH_2]_n$ by two methods, λ = 0.68745 Å, * trace $CaOCaCl_2{\cdot}3H_2O$.

$[GeH_2]_n$ also can be prepared directly by reacting CaGe with cold (–30 °C) concentrated HCl, similar to its $CaGe_2$ counterpart (Method 2, Figure 5.1a).[108,225] This reaction is, however, extremely exothermic and violent and should be prepared only

on a small scale (≤0.3 g of CaGe granular). The deintercalation reaction is so fast that the granular will break into pieces after 1–2 min, and the reaction is complete in 30 min, compared to several days for the deintercalation of $CaGe_2$.[200,228] PXRD analysis confirmed that both types of $[GeH_2]_n$ have quite broad peaks (Figure 5.1g), indicating short-range crystallinity (i.e., nanostructured). The first two peaks can be indexed as (021) and (200), assuming the same orthorhombic unit cell, where the (021) plane value is close to the (111) plane in diamond lattice Ge and the (200) plane is half of the distance between the $[GeH_2]_n$ strands in the same layer (Figure 5.2).

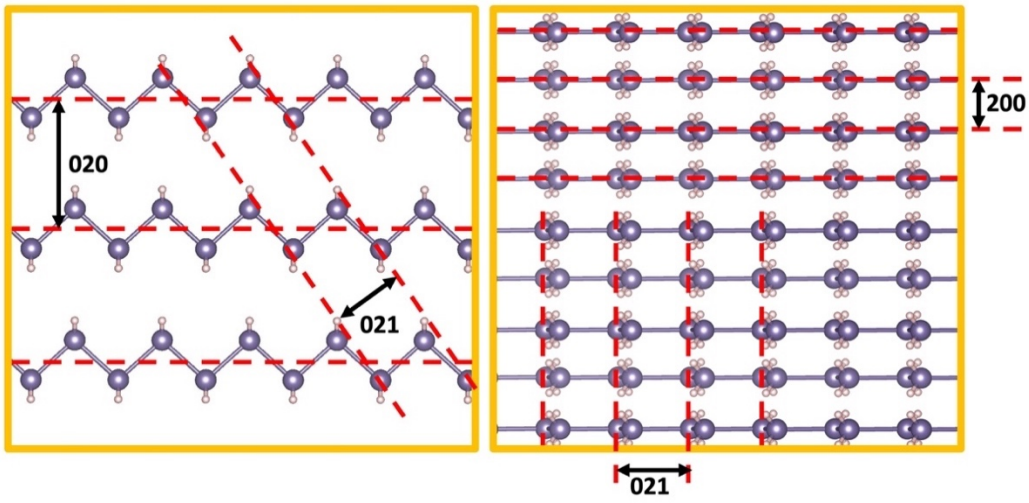

Figure 5.2. Schematic illustration of (020), (200), and (021) reflection.

These values were calculated to be 3.35 Å (021) and 1.87 Å (200) for $[GeH_2]_n$, by Method 1 and 3.28 Å (021) and 1.84 Å (200) by Method 2. While the (021) plane for $[GeH_2]_n$ by both methods is in close proximity to bulk Ge (111) (3.324 Å), the (200) plane shrinks significantly compared to the parent CaGe (2.288 Å),[222,225] which suggests that the $[GeH_2]_n$ strands are closer by ca. 20% upon the removal of Ca atoms (Figure 5.3).

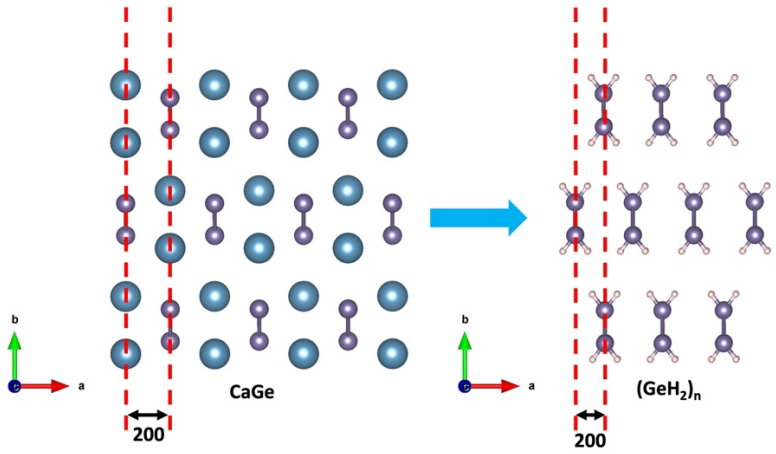

Figure 5.3. Schematic illustration of the (200) reflection from (left) CaGe and (right) $[GeH_2]_n$.

We believe that this dramatic change will disturb the packing of the $[GeH_2]_n$ strands on the b axis, resulting in the missing of a (020) reflection. This is supported by the pXRD analysis of the orange intermediate $(Ca(OH)_2GeH_2)_n$, where $Ca(OH)_2$ only formed and diffused locally and the (020) plane was observed (5.47 Å, Figure 5.4).

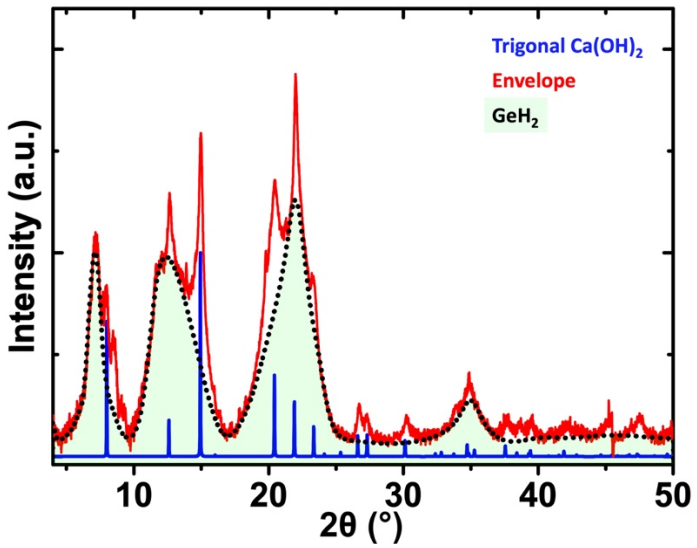

Figure 5.4. (red) Envelope of powder X-ray diffraction of $(Ca(OH)_2GeH_2)_n$ using an X-ray source with λ = 0.68745 Å: (blue) calculated pattern from single-crystal trigonal $Ca(OH)_2$ and (black dot) deconvoluted area suggested scattering generated from $[GeH_2]_n$.

Two morphologies, a closely packed linear assembly or some random agglomeration, were confirmed using transmission electron microscopy in $[GeH_2]_n$ prepared by Method 1 (Figure 5.5 a-c). The fabric structure was retained after deintercalation and packed closer due to the merging of multiple $[GeH_2]_n$ strands. The random morphology is the free-standing form of $[GeH_2]_n$ that was exfoliated from the structure agglomerates via van der Waals forces and forms a random agglomeration during the preparation of the TEM sample. Because of a more violent deintercalation reaction, $[GeH_2]_n$ prepared by Method 2 primarily obtained a random agglomeration form.

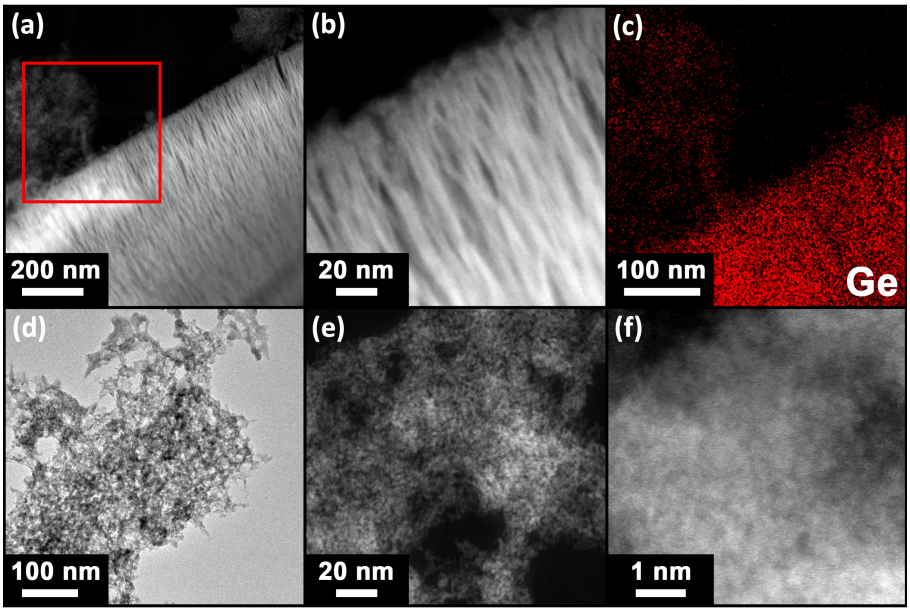

Figure 5.5. (a-c) TEM analysis of $[GeH_2]_n$ prepared by Method 1: (a) low magnification image and (b) high magnification HAADF-STEM images, (c) EDX mapping of Ge Kα at an area selected in (a); (d-f) TEM analysis of $[GeH_2]_n$ prepared by Method 2: (d) low magnification TEM image, (e) high magnification, and (f) atomic resolution HAADF-STEM images.

5. 4. 2 Compositional Characterization

Energy dispersive X-ray (EDX) mapping indicates that both morphologies have a strong Ge signal and spectrum (Figure 5.6), absence of Ca, negligible O, and a trace

amount of Cl (ca. 2.5%). The trace Cl is observed in the deintercalation of $CaGe_2$,[70] which can be explained by the Ge–O being etched by HCl.[108,109]

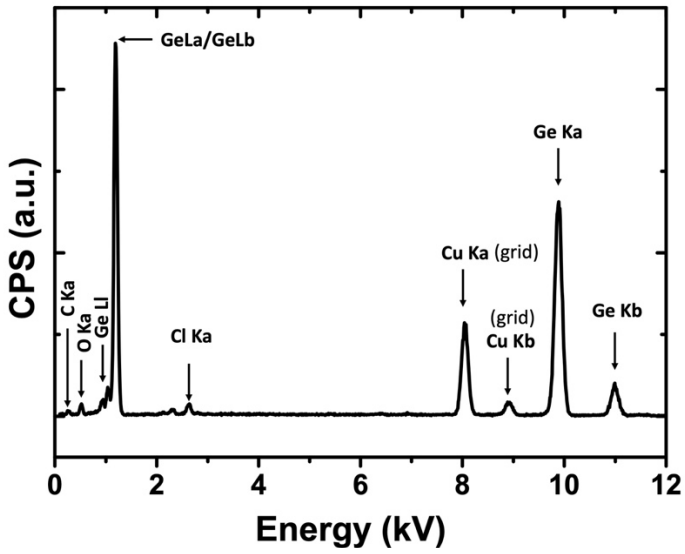

Figure 5.6. EDX spectrum of $[GeH_2]_n$, measured at an area with a vacuum background on a holey carbon grid.

To confirm the bonding environment further, we performed Fourier-transform infrared spectroscopy (FTIR), Raman spectroscopy, and X-ray photoelectron spectroscopy (XPS) on the $[GeH_2]_n$ nanostructures (Figure 5.7 and 5.10). FTIR performed on the freshly synthesized $[GeH_2]_n$ by both methods show intense Ge–H_2 stretching and bending modes at ca. 2042–2046, 776, and 831 cm^{-1}, respectively.[70] Additional O–H stretching and bending at ~3370 and 1630 cm^{-1} can be assigned to free water adsorbed between these nanostructures.[200,242] To verify further that water will not oxidize the $[GeH_2]_n$, especially in Method 1, we also measured the FTIR for $(Ca(OH)_2GeH_2)_n$, freshly purified $[GeH_2]_n$ without drying, and $[GeH_2]_n$ that had been stored in the dark at room temperature (Figure 5.7), and we observed that all the spectra show intense Ge–H_2 stretching and bending vibrations.

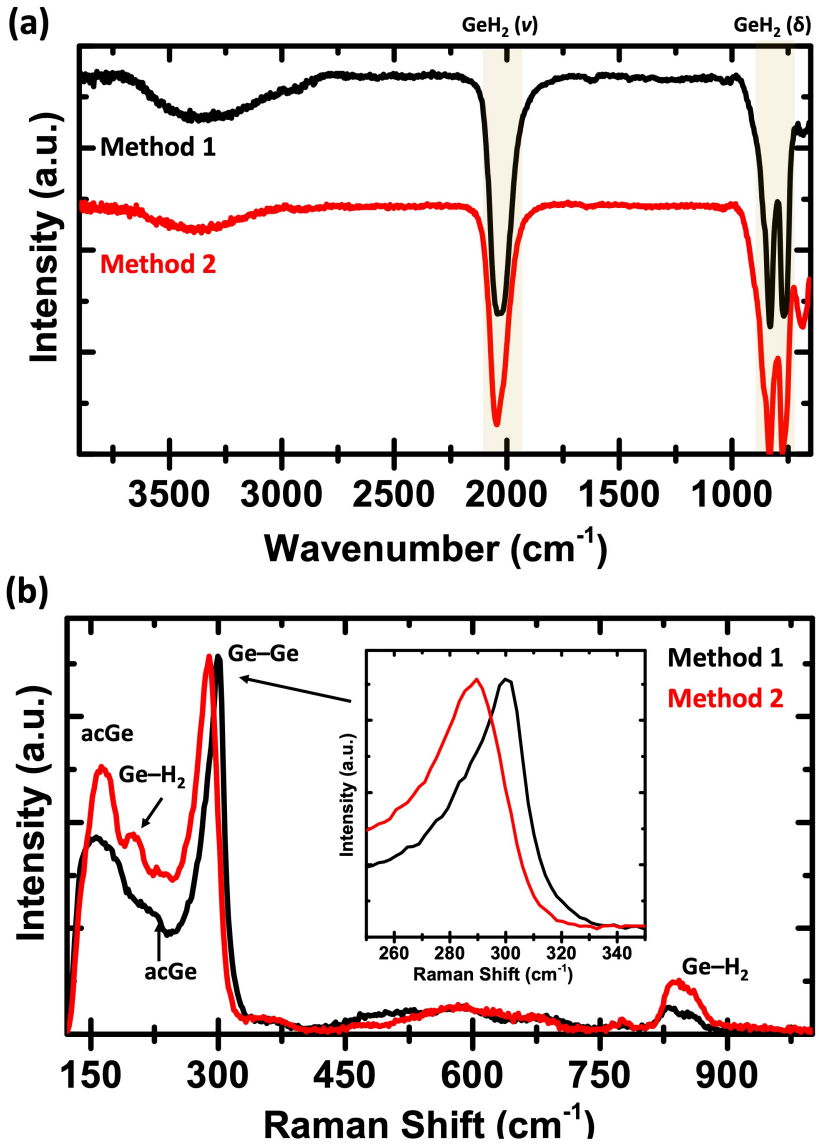

Figure 5.7. (a) FTIR and (b) Raman spectroscopy of $[GeH_2]_n$ synthesized by Method 1 and 2, with inset highlighting the Ge–Ge peak center.

For $[Ca(OH)_2GeH_2]_n$, an additional sharp characteristic $Ca(OH)_2$ stretching vibration at 3645 cm^{-1} was observed;[276] it was completely eliminated in the purified wet $[GeH_2]_n$. The intense free water peaks again were diminished upon drying (Figure 5.8).

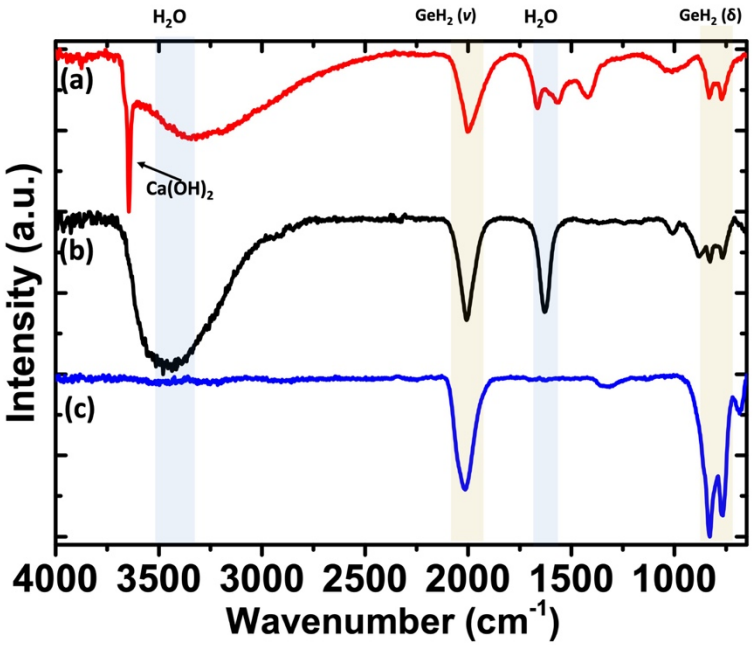

Figure 5.8. FTIR spectra of $[GeH_2]_n$ prepared by Method 1 at different stages: (a) $(Ca(OH)_2GeH_2)_n$, (b) wet $[GeH_2]_n$ with adsorbed H_2O, and (c) slightly decomposed $[GeH_2]_n$.

From Raman spectroscopy, the main Ge–Ge optical vibration occurs at 300 and 289 cm^{-1} for $[GeH_2]_n$ prepared by Method 1 and 2, respectively. Additional Ge–H_2 vibrations can be observed at 180 and 820 cm^{-1}. For $[GeH_2]_n$ prepared by Method 2, this red-shift was compared with bulk Ge crystal (300 cm^{-1}) [277,278] results from a disorder-induced activation of phonon density, as described by Weinstein and Cardona,[279] which agrees with the observation from TEM analysis. In addition to optical phonons, acoustic-like Ge (acGe) peaks at ~160–170 cm^{-1} and ~225 cm^{-1} were observed, contributed by the vibration of $[GeH_2]_n$ strands.[279,280] The more intense and blue-shifted acGe peaks were observed for $[GeH_2]_n$ prepared by Method 2 due to the closer spacing between the $[GeH_2]_n$ strands.

XPS measurements, which can probe the elemental composition as well as the oxidation states of Ge at the surface (i.e., a few nm), were performed for precursor CaGe after argon cleaning and for synthesized $[GeH_2]_n$ by Method 1 before and after

argon cleaning. All spectra were calibrated to adventitious carbon at a binding energy (BE) of 284.8 eV.[120,253] Survey spectra also were provided and compared with a freshly etched clean Ge(111) wafer to help identify emissions from Ca (Figure 5.9), where both the Ca 2p and 3s peaks are overlapped heavily with Ge emissions. In the survey scans, all spectra show strong Ge emissions and a trace C 1s signal from adventitious carbon. Additional intense Ca 3s and O 1s emissions were observed in the CaGe sample after argon cleaning, which suggests mild oxidation by fast deintercalation with water.

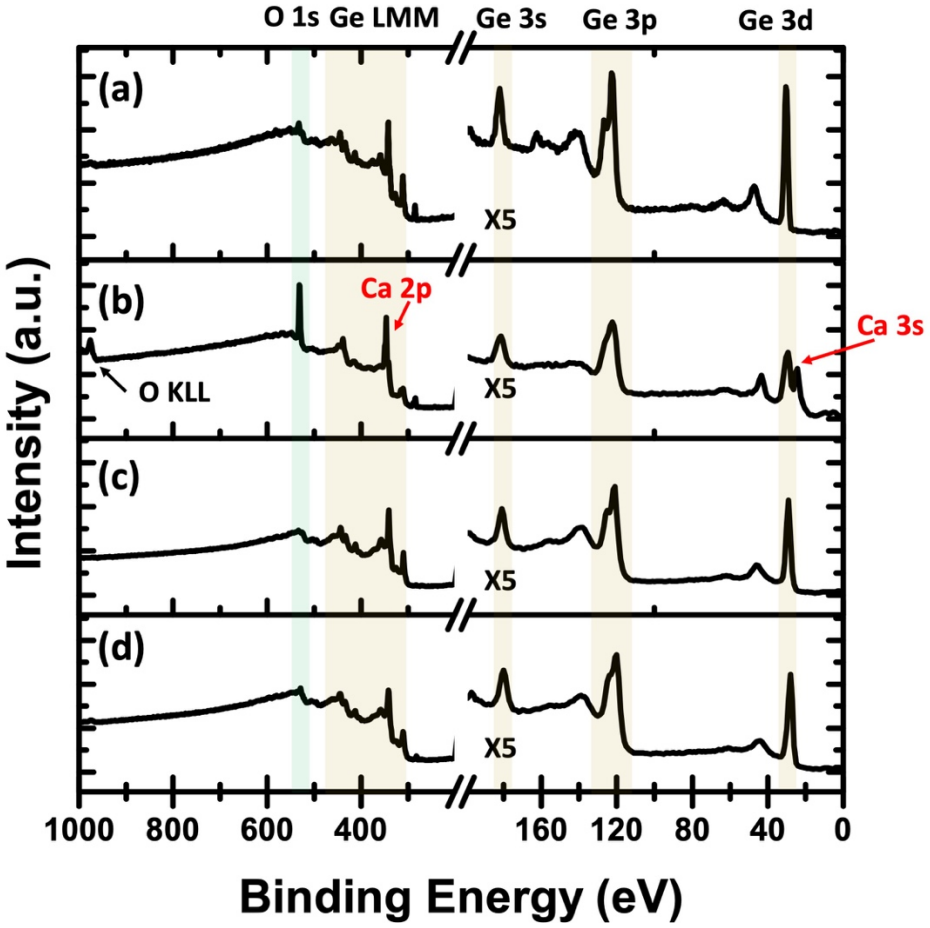

Figure 5.9. Survey XP spectra of (a) clean Ge (111) wafer, (b) CaGe after Ar cleaning, (c) $[GeH_2]_n$ with residual CaGe after etching, and (d) $[GeH_2]_n$ before Ar cleaning.

High-resolution XP spectra of the Ge 3d region were fitted to the Ge 3d5/2 and 3d3/2 spin-orbit couple, with a 0.58 eV difference in BE, where each set was defined by the same colour set (Figure 5.10). In the CaGe sample, a Ge^{-} component was deconvoluted, centred at 28.62 eV, significantly lower than the reference elemental Ge (29.45 eV), but comparable to Ge (–1) in $CaGe_2$.[200] Although the Ge in CaGe has an official oxidation state of (–2), we believe that a higher BE is related strongly to the fast deintercalation reaction at surface level, which can be supported by some of the Ca^{2+} in the form of $CaCO_3$. An additional Ge–O (31.1 eV) emission[245,281] and a Ge–Ge emission were contributed by GeH_2 (+2, 30.07 eV).

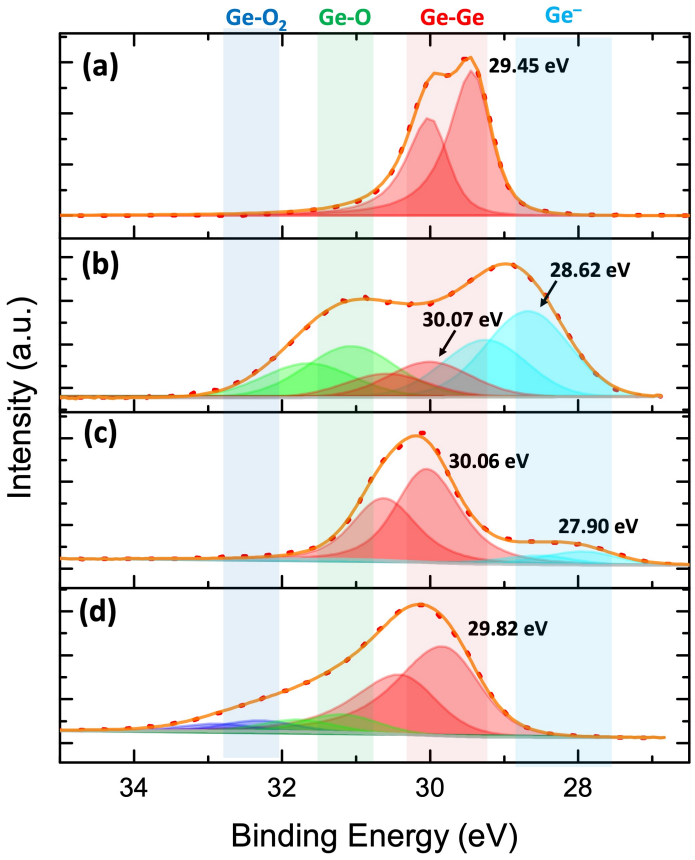

Figure 5.10. High resolution XP spectra of Ge 3d region, (a) clean Ge (111) wafer, (b) CaGe after Ar cleaning, (c) $[GeH_2]_n$ with residual CaGe after Ar cleaning, and (d) $[GeH_2]_n$ before Ar cleaning.

Before argon cleaning, the $[GeH_2]_n$ shows a strong emission at 29.82 eV, slightly higher than the reference Ge (0) due to more electronegative hydride-termination.[282] In addition, minor Ge–O (31.1 eV) and Ge–O_2 (32.5 eV) peaks suggest that slight oxidation and dehydrogenation occurred at the surface. After argon cleaning, all the emissions associated with Ge–O were removed completely, and the Ge–Ge emission contributed by GeH_2 has a BE of 30.06 eV. Interestingly, although Ca emissions were not observed in the survey spectrum, a residual peak centred at 27.90 eV can be assigned only as Ge (–2) from residual CaGe in the center that was not deintercalated.

Diffuse reflectance absorption (DRA) was performed to evaluate the optical band gap of $[GeH_2]_n$ prepared by Method 1 and 2, with an optical bandgap measured as 2.31 and 2.70 eV, respectively (Figure 5.11). Wei and Xiao Cheng previously had performed a first-principle calculation on polygermanes with H– or Ph– substituents and concluded that the band-edge states are contributed mainly by the skeletal Ge atomic orbitals, and the bandgap for $(GePh_2)_n$, can reduce from 2.13 eV to 1.131 eV when a tensile strain is present.[87]

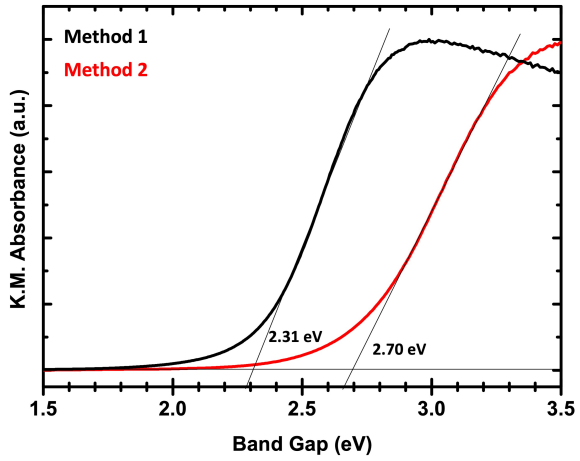

Figure 5.11. DRA plot of $[GeH_2]_n$ prepared by Method 1 (black) and 2 (red), with optical band gap measured 2.31 eV and 2.70 eV, respectively.

Since $[GeH_2]_n$ synthesized by both methods originated from CaGe with a pre-existing Ge–Ge skeleton, especially by Method 1, it is plausible that the band gap difference is a consequence of tensile strain. Urbach tails were observed to the lower energy level and were larger for $[GeH_2]_n$ prepared by Method 2 due to the lack of long-range order;[5,70] this is consistent with TEM and Raman results.

5. 4. 3 Stability Test

Similar to previous methods, we also noticed that $[GeH_2]_n$ prepared by Method 2 is not stable at ambient condition when dry.[109] A small scale explosion, with a visible flame and loud sound, was observed with ≥ ca. 0.25 g dry powder, yielding a black crystalline Ge powder. A smaller-scale explosion or micro-explosion with <1 mg material also can be trigged using an anti-static gun or a 1.99 mW laser power. Surprisingly, $[GeH_2]_n$ prepared by Method 1 is easy to handle at dry ambient conditions even at a larger scale (i.e., ≥ 2.0 g). Upon a 1.99–3.98 mW laser exposure for 60 s, it only results in the decomposition, and no explosive decomposition was observed (Figure 5.12).

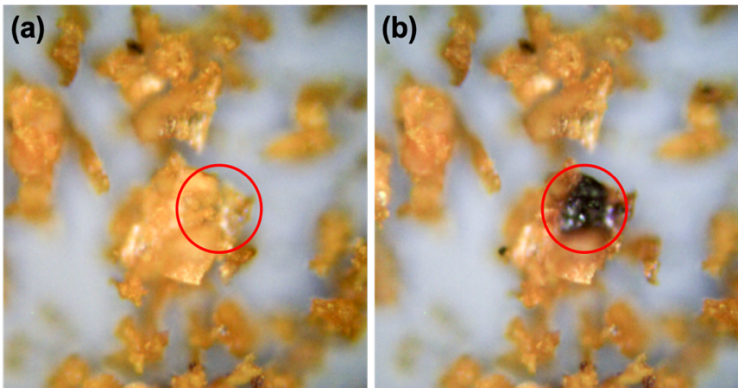

Figure 5.12. Photograph obtained from optical microscopy equipped on a Raman spectrometer at a magnification of 20X. $[GeH_2]_n$ prepared by Method 1 (a) before and (b) after a 50% laser power (1.99 mW) exposure for 60 s.

Raman spectra of exploded product from Method 2 and decomposed product from Method 1 were measured (Figure 5.13). Compared to the original $[GeH_2]_n$, these decomposed materials show a primary Ge–Ge peak, with a minor acGe peak, similar to crystalline Ge powder, suggesting a more ordered Ge–Ge framework.

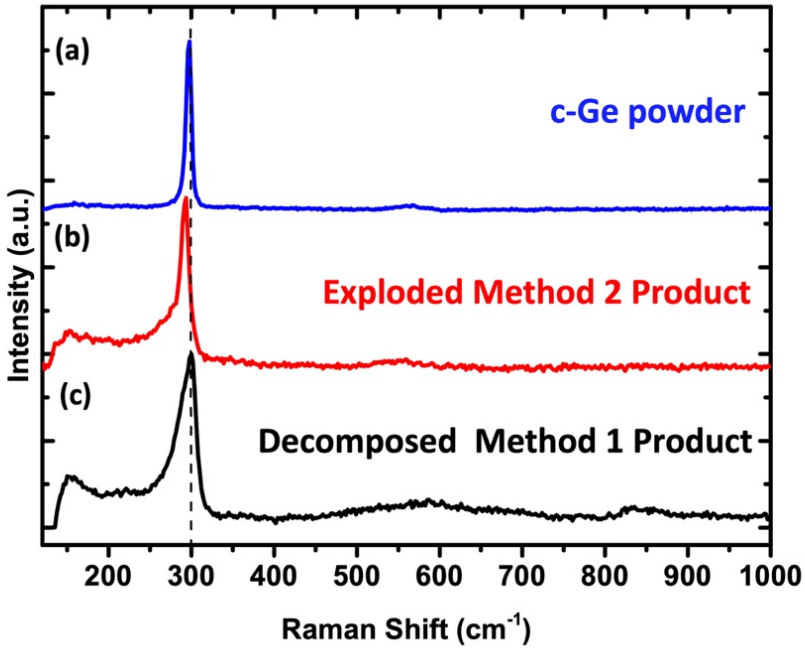

Figure 5.13. Raman spectra of (a) crystalline Ge powder as a reference, (b) exploded residual from $[GeH_2]_n$ produced by Method 2, and (c) a rescan of decomposed product from $[GeH_2]_n$ produced by Method 1 after a 50% laser power (1.99 mW) exposure for 60 s.

Thermal stability of $[GeH_2]_n$ prepared by Method 1 was evaluated via FTIR, Raman spectroscopy and DRA after curing at 75 – 200 °C in a dark Ar environment for four hours (Figure 5.14b-d). The colours of the resulting samples shifted from golden to brown and eventually turned into black, with a luster. FTIR and Raman spectra for samples cured at below 120 °C (magenta line) show a negligible difference. Above 120 °C (magenta line), all Ge–H_2 bending modes were diminished, and a broad Ge–O–Ge stretching mode was detected in FTIR.

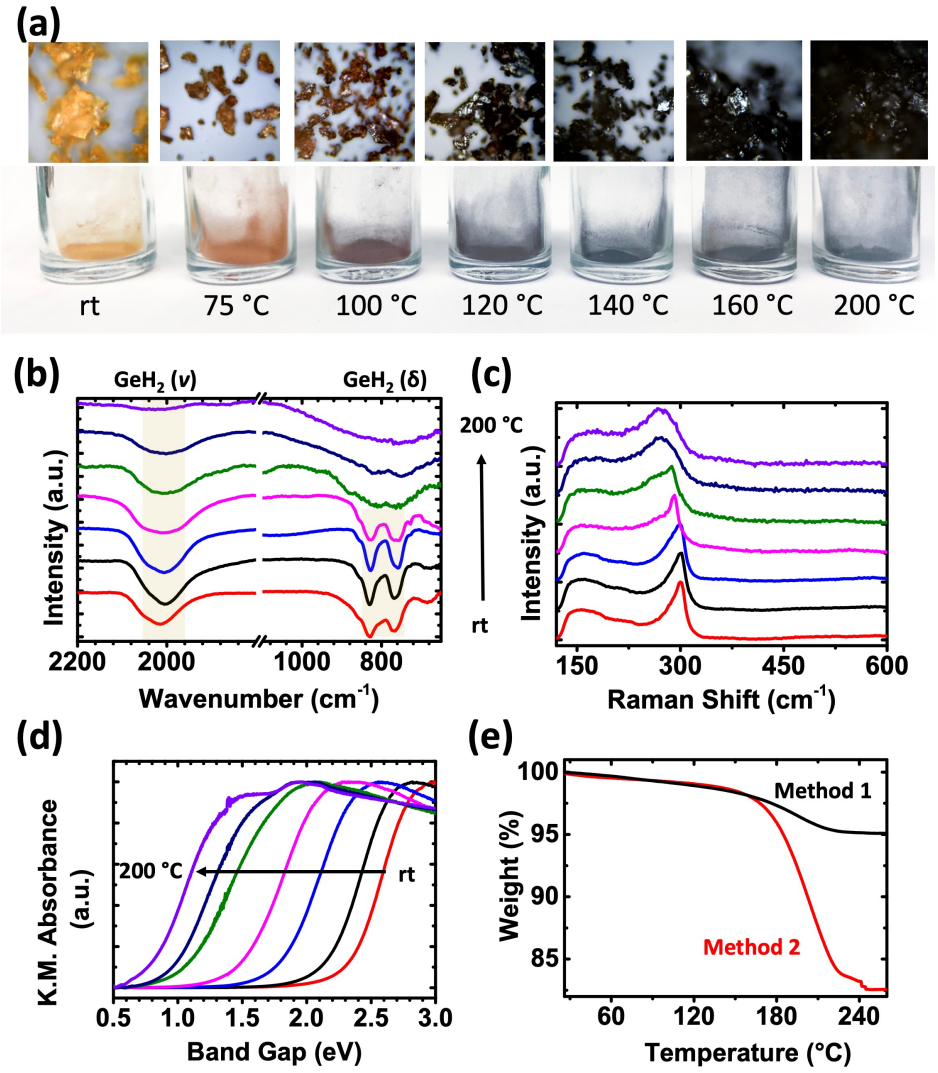

Figure 5.14. Thermal stability measurements. (a) Optical photographs of $[GeH_2]_n$ prepared by Method 1 after curing at the indicated temperature and their (b) FTIR spectra, (c) Raman spectra, and (d) absorption spectra. (e) TGA of $[GeH_2]_n$ prepared by both methods.

Raman spectra also indicate that the transition started at 120 °C, where the Ge–Ge red shifted due to disorder, and the peaks broadened at the higher temperature. Both FTIR and Raman suggest that curing at above 120 °C accelerates the dehydrogenative reaction, resulting in a disturbed Ge–Ge skeleton. The optical bandgap was decreased gradually from 2.31 eV to 1.50 eV at 120 °C, with an increase of the Urbach tail. Upon curing at 140 °C (green line), the band gap suddenly dropped

to 1.06 eV, which is comparable with an amorphous hydrogenated germanium film (1.1 eV),[283] and continuously reduced to 0.73 eV for a sample cured at 200 °C. For samples cured at higher than 140 °C, the Urbach tails reduced, suggesting a more ordered structure. TGA was performed for $[GeH_2]_n$ prepared by both methods (Figure 5.14e), where a slow 2% weight loss at a temperature before 150 °C was attributed to the loss of ~0.75 equivalent hydrogens in $[GeH_2]_n$. This temperature is lower than that of germanane (200–250 °C)[70,200] because of the higher accessibility of the hydrogen source, and the remaining hydrogen is single bonded to Ge, as evidenced by FTIR. The second weigh loss between 180 °C and 220 °C is steeper and about 3% and16 % for $[GeH_2]_n$ prepared by Method 1 and 2, respectively. A 16% weight loss is close to a magnitude higher than the possible hydrogen coverage in $[GeH_2]_n$, which indicates that some Ge segments (i.e., Ge_xH_{2x+2}) were decoupled from the skeleton.[107] By assuming that all the leaving groups are simple germane (GeH_4), the 16% weight loss can be calculated as ca. 0.24 equivalents of hydrogen in $[GeH_2]_n$. It suggests that most of the residual Ge–H decompose into Ge and GeH_4 at the higher temperature (Method 2), where Ge–Ge skeletons break down. On the other hand, for $[GeH_2]_n$ prepared by Method 1, the 3% weight loss was estimated to be a combination of H_2 loss (ca. 0.2 equivalents) and GeH_4 loss (ca. 0.02 equivalents).

5. 4. 4 Side-Group Substitution

Finally, we demonstrated that side group substitution is possible on $[GeH_2]_n$ via a thermal hydrogermylation reaction with unsaturated bonds (i.e., 1-dodecene), and the reactions were evaluated by the diminishing of Ge–H stretching in FTIR (Figure 5.15), with morphologies characterized by TEM (Figure 5.16 and 5.17). Spectra of all the synthesized $(Ge(C_{12}H_{25})_2)_n$, show the expected features of a dodecyl group, without the unsaturated features (i.e., C–H sp2 stretching and C=C vibrations)

of 1-dodecene. Residual Ge−H features at ca. 830 cm^{-1} and ca. 2010 cm^{-1} were observed for samples functionalized without sonication, while these features were diminished completely in sonicated samples prepared by both methods.

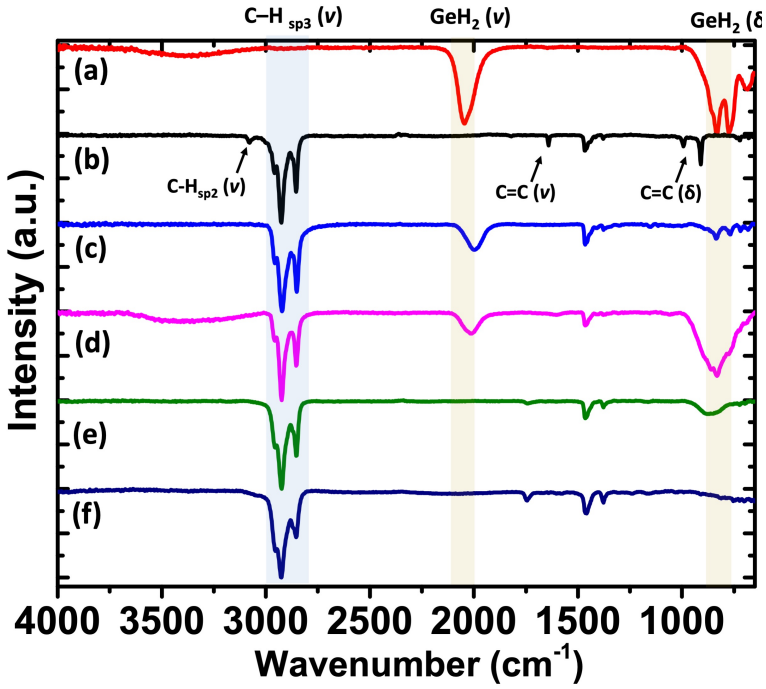

Figure 5.15. FTIR spectra of (a) $[GeH_2]_n$ prepared by Method 1, (b) neat 1-dodecene, $[Ge(C_{12}H_{25})_2]_n$ prepared without sonication from (c) Method 1 and (d) Method 2, and $[Ge(C_{12}H_{25})_2]_n$ prepared with sonication from (e) Method 1 and (f) Method 2.

This difference of Ge–H stretching in IR spectra was revealed by TEM analysis. When the $[GeH_2]_n$ fine powders are not disturbed/exfoliated via sonication, the close distances between these strands will prevent the diffusion of substituents and further functionalization, which leads to a similar linear assembly or randomly agglomerated morphologies as $[GeH_2]_n$ prepared by Method 1 (Figure 5.16 a-d) and Method 2 (Figure 5.17 a and b), respectively.

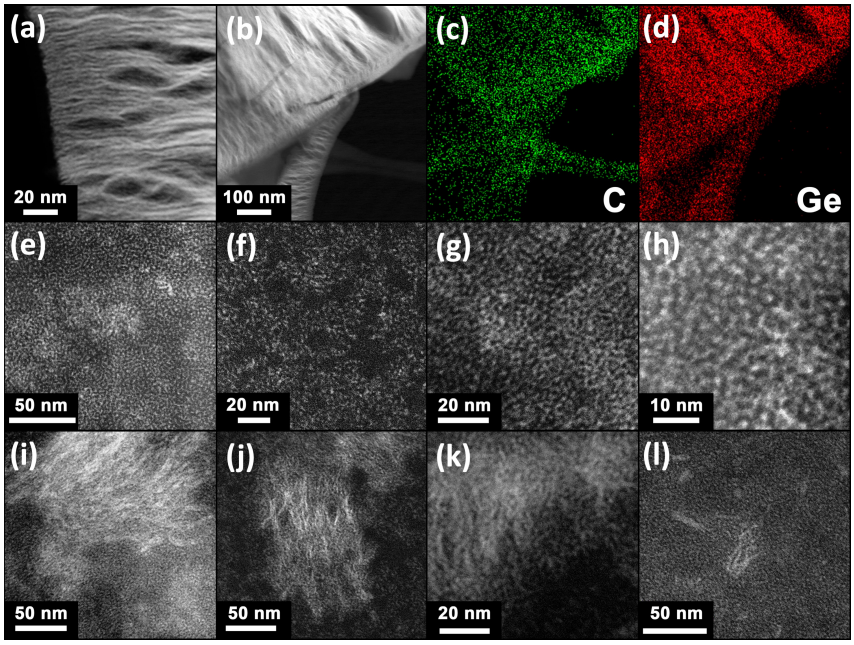

Figure 5.16. HAADF-STEM images of $[Ge(C_{12}H_{25})_2]_n$ prepared from Method 1 (a-d) without sonication: (a) high-resolution image, (b) low-resolution image, (c) C Kα mapping at area (b), and (d) Ge Kα mapping at area (b); (e-h) the assembly of free-standing $[Ge(C_{12}H_{25})_2]_n$ at different magnification; (i-l) exfoliation process and break down of large Ge–Ge strands.

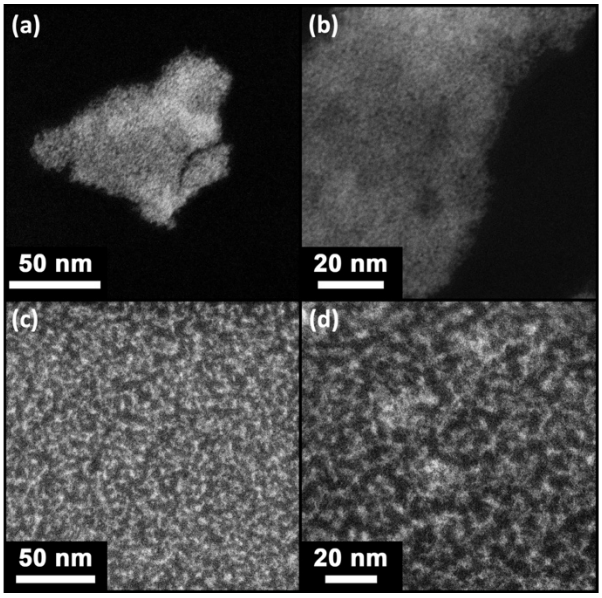

Figure 5.17. HAADF-STEM images of $[Ge(C_{12}H_{25})_2]_n$ prepared from Method 2 (a,b) without sonication: (a) low-resolution image, (b) high-resolution image; (c, d) the assembly of freestanding $[Ge(C_{12}H_{25})_2]_n$ at different magnification.

Although structurally similar, further EDX mapping confirmed that the C signal is comparable with the underlying carbon grid and that it overlapped well with the Ge signal. Furthermore, the EDX spectrum (Figure 5.18) also confirms strong C and Ge signals, with trace O, measured at an area without a grid support.

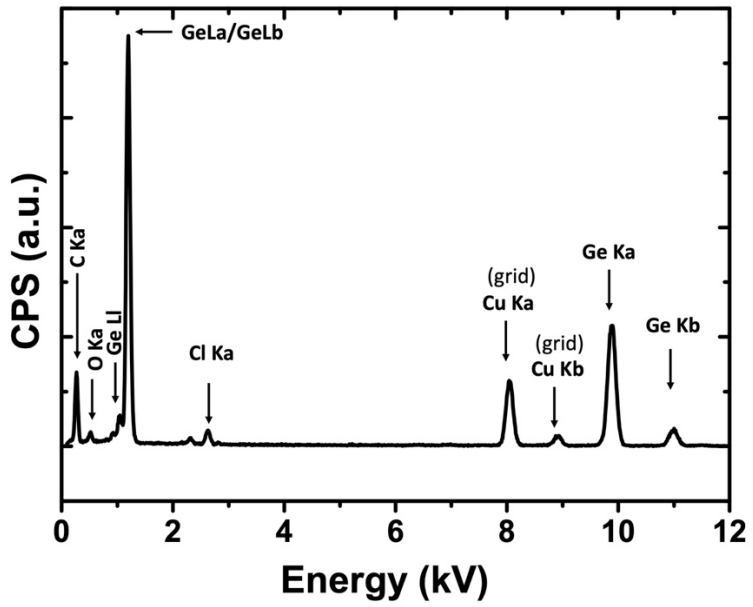

Figure 5.18. EDX spectrum of $[Ge(C_{12}H_{25})_2]_n$ prepared from Method 1, measured at an area with a vacuum background on a holey carbon grid.

Once the polygermane strands were exfoliated fully and functionalized, we noticed improved organic solvent compatibility in that they remain in suspension for months. Upon drying, HAADF-STEM images for both methods (Figure 5.16i-h, Figure 5.17c and d) show that a uniformly distributed self-assembly-like pattern formed on the ultra-thin carbon grid. We further analyzed the non-fully exfoliated Ge–Ge strands (Figure 5.16i-l) and noticed that the $[GeH_2]_n$ does not remain as a single linear strand. Instead, large fibres will decouple directly into smaller pieces with a similar width; this explains the narrow distribution for the pattern sizes.

Unfortunately, it is challenging to study the fine structure of these materials as

images were blurred due to ligand coverage, and an attempt at sample cleaning would alter their morphologies (Figure 5.19). This will be the basis of future investigations.

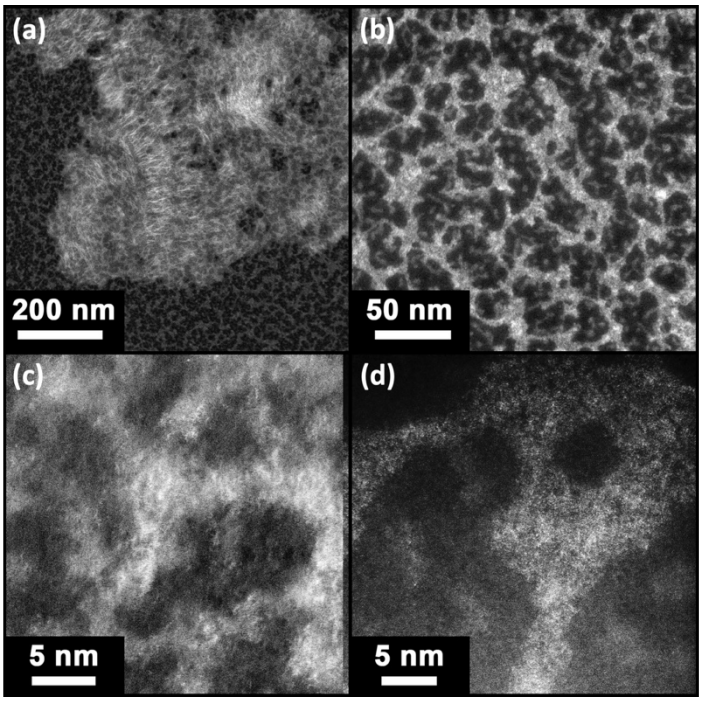

Figure 5.19. HAADF-STEM images of $[Ge(C_{12}H_{25})_2]_n$ prepared from Method 1 after plasma cleaning: (a) residual large strands and (b) free-standing assembly after harsh cleaning; (c,d) high magnification images of the free-standing assembly after (c) gentle cleaning and (d) harsh cleaning.

5.5 Conclusions

In summary, we have prepared a stable form of polydihydrogermane that retains linear fabric nanostructure after deintercalation. XRD shows that it has a larger interstrand distance compared with polydihydrogermane prepared in previous reports, which leads to a red-shift in the transverse acoustic vibration in Raman spectroscopy. Thermal stability measurements reveal that this stable form only proceeds the dehydrogenation reaction slowly, with trace GeH_x decomposition byproducts due to a stronger Ge–Ge bond, compared with the traditional method. Lastly, we showed that

both forms of polydihydrogermane can be modified via a hydrogermylation reaction, offering the opportunity for various functional catenated polygermanes.

Chapter 6

Thesis Summary and Outlook

6.1 Summary of Chapters

Group 14 nanostructures have shown glamorous applications due to their optical and electronic properties. Surface functionalization is an essential aspect of nanostructure design and preparation that imparts stability, processability, and functionality. Compared to the well-established protocols on the functionalization of Si surfaces, the modification of Ge surfaces is still under development. The aim of the research outlined in this Thesis was to explore Zintl phase precursors for germanium nanomaterials and tailor the surface chemistry of Ge-based 1D and 2D nanomaterials and the potential hybrids. The work presented in Chapters 2, 3, and 4 presents the synthesis of Ge NSs and surface functionalization via hydrogermylation and dehydrocoucpling reactions, while Chapter 5 investigated the improved method for the synthesis of poly(dihydrogermanes) and ligand substitution via a hydrogermylation reaction.

Chapter 1 gives a brief introduction to the basic principles of Group 14 nanostructure synthesis, functionalization, and potential Zintl phase precursors. The Chapter starts with a few general methods for the preparation of Si/Ge nanostructures with various morphologies, from 0D QDs, 1D nanorods/wires, to 2D nanosheeets, and briefly discusses their size and shape control. The synthesis strategies of 1D polysilanes/polygermanes are introduced, with the main categories being Wurtz-type coupling, electrochemical reduction, and dehydrocoupling. Next, the surface functionalization methods on the flat Si and Ge wafer surfaces, porous surfaces, and nanostructure surfaces are summarized, including various hydrosilylation/

hydrogermylation methods, Grignard and organolithium reagents, dehydrocoupling reactions, amination and thiolation reactions, and topotactic transformations using Zintl phases precursors. Following this, the concept of Zintl phases, a few useful examples of Ge-containing Zintl phases, and the compounds presented in the Ca–Ge phase diagram are deliberated. Finally, the exfoliation methods of deintercalated Zintl phase subunits held by vdW forces into individual nanostructures are introduced.

Chapter 2 presents the synthesis of the high crystalline $CaGe_2$ Zintl precursor and germanane $(Ge_6H_6)_n$ from the subsequent deintercalation reaction. Compared to the previously reported methods that require a specific dynamic reactive epitaxy instrument or a week-long temperature profile, the use of a compact arc furnace instead greatly reduces the synthesis time to less than an hour, with yields over the grams scale. PXRD and SEM were carried out to characterize the crystal structure and morphologies of both $CaGe_2$ and $(Ge_6H_6)_n$, confirming the layered network. The composition of materials was analyzed further using FTIR, XPS, and Raman spectroscopic techniques. As inferred by the formula $(Ge_6H_6)_n$, Ge—Ge and Ge—H are the major vibration modes, with a binding energy of Ge 3d slight higher than that of the elemental form due to the electronegativity difference resulting from hydride-termination. Upon liquid phase exfoliation, $(Ge_6H_6)_n$ nanosheets can be observed directly under TEM, with its crystal retained, as evidenced by SAED.

Chapter 3 describes the hydrogermylation chemistry to produce Ge—C bonds by simple heating or radical initiation of the reaction of hydride-terminated Ge nanosheets with alkenes. Upon reaction, the Ge—H bonds were consumed and intense alkyl vibration modes were observed in FTIR spectra. The surface coverage of the ligand was estimated using the model derived from the overlayer coverage calculation on the wafer surface. After the hydrogermylation reaction, the Ge–Ge network shows an intact crystalline structure confirmed by SAED or HRTEM. The

thickness was probed using AFM for each functionalized NS monolayer, revealing a significant increase compared to the original hydride-terminated NS. While germanane surfaces oxidize under ambient conditions, alkyl-terminated Ge NSs are thermally stable up to >475 °C.

Chapter 4 introduces the heteroatom dehydrocoupling reaction between Si—H and Ge—H bonds to form a Si—Ge bond by simple thermal heating. This facile reaction can couple both primary hydridosilanes, $H_3SiC_{18}H_{37}$ and $H_3Si(CH_2)_2(CF_2)_6CF_3$, and tertiary hydridosilanes, $HSi(Me)(C_{18}H_{37})$ and $HSi(CH_{17})_3$, onto the Ge NSs surface. FTIR, Raman, XPS, and EDX mapping were carried out to confirm the organosilane-termination, where addition of Si signals are distributed uniformly on the Ge NSs. Substitution levels of Ge–H on the starting Ge NSs surface by organosilanes were quantified using an XPS emission signal, whose average value is close to 25%. Hydride-terminated Si QDs with various average sizes (3–64 nm) also were coupled onto the Ge NSs surface. With successful coupling, the characteristic bright red PL of 3 nm Si QDs was quenched, while PL remains in the physical mixture.

Chapter 5 presents the synthesis, stability test, and ligand substitution of poly(dihydrogermanes) prepared from the CaGe Zintl precursor. Topotactic deintercalation of CaGe in concentrated HCl at low temperature or in a water-mediated solvent at room temperature can produce poly(dihydrogermanes) with a similar composition. The Ge—Ge bond length, interstrand distance, stability, and HOMO–LUMO gap of poly(dihydrogermanes) prepared via the two methods are divergent, as evidenced in Raman spectra, pXRD pattern, and DRA analysis. TGA revealed that poly(dihydrogermane) prepared by the two methods also have different decomposition processes and products. The Ge—H bonds on the Ge–Ge backbone were an excellent platform for ligand substitution. An example of thermal

hydrogermylation reaction to produce poly(didodecylgermane) was provided.

6.2 Future Work

6. 2. 1 Other Hydrogermylation Methods on the Ge Surface or Backbone

As briefly introduced in Chapter 1, limited methods of surface functionalization have been established on the germanium nanostructures, and there even fewer in the case of nanosheets and polygermane. Hydrogermylation, as a counterpart of hydrosilylation reaction, is explored far less. Several potentially viable methods, including etchant-assisted, plasmon-assisted, Lewis-acid catalyzed, photochemical, and transition metal-mediated hydrogermylation, need to be explored. In Chapter 3, the examples of thermally-induced and AIBN radical-initiated hydrogermylation are demonstrated. We also have used XeF_2 as an etchant or 4-decylbenzene diazonium tetrafluoroborate (4-DDB) as a radical initiator to assist hydrogermylation reaction on Ge NSs surfaces (Figure 6.1).

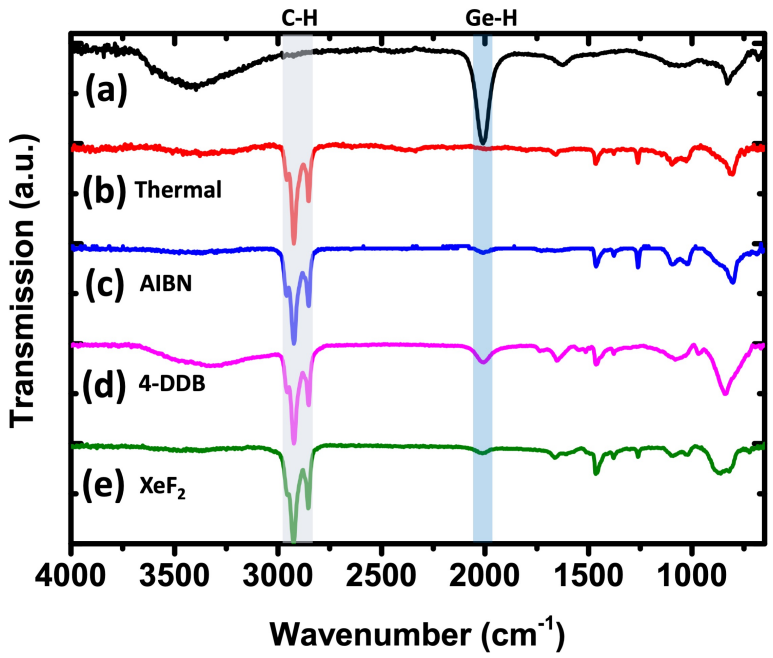

Figure 6.1. FTIR spectra of (a) germanane and (b-e) dodecyl-terminated Ge NSs using the indicated

methods: (b) thermal, (c) AIBN, (d) 4-decylphenyl diazonium tetrafluoroborate, and (e) XeF_2.

After functionalization, similar to other hydrogermylation methods, FTIR spectra show the concomitant appearance of ν(C—H) features at 2852 cm^{-1} and the loss of ν(Ge—H) at 2001 cm^{-1} and ν(C=C) at 3078 cm^{-1}. One of the major advantages of hydrogermylation using a 4-DDB or XeF_2 reagent at room temperature is that it offers the opportunity of volatile ligand substitution (i.e., ethylene),[187] further diversifying the functional groups on Ge surfaces or backbones. The reaction of Ge–H with alkene containing other functional groups, such as Cl, Br, F, C_{60}, Ph, or unsaturated monomers, are promising future directions.

6. 2. 2 Amination and Thiolation on the Ge Surface or Backbone

The study and development of methods for the functionalization of Ge-based nanostructures coupled with heteroatoms is still in its infancy. Amination and thiolation are two simple methods that have been established on other Si and Ge based nanostructures for introducing Si/Ge—N and Si/Ge—S bonds.[48,111,154,202] An amination reaction on 3 nm Si QDs surface was explored previously, where the PL wavelength of the functionalized Si QDs was altered greatly due to the introduction of a new surface state.[112] From our preliminary data, amination and thiolation reactions occur at temperatures lower than 80 °C in neat amine, thiol, or in an appropriate solvent (i.e., THF, toluene). In fact, the fully exfoliated $[GeH_2]_n$ will change colour instantly from yellow/orange to deep red/orange upon the addition of alkylamines at room temperature. After amination or thiolation on Ge NSs or polygermane, FTIR spectra show the ν(C—H) features at 2852 cm^{-1} from alkylamine and alkylthiol and the loss of Ge—H, N—H, and S—H related features (Figure 6.2). With the wide range of commercially available amines and thiols, it is possible to create a library of functionalities on Ge-based nanostructures via Ge—S and Ge—N bonds.

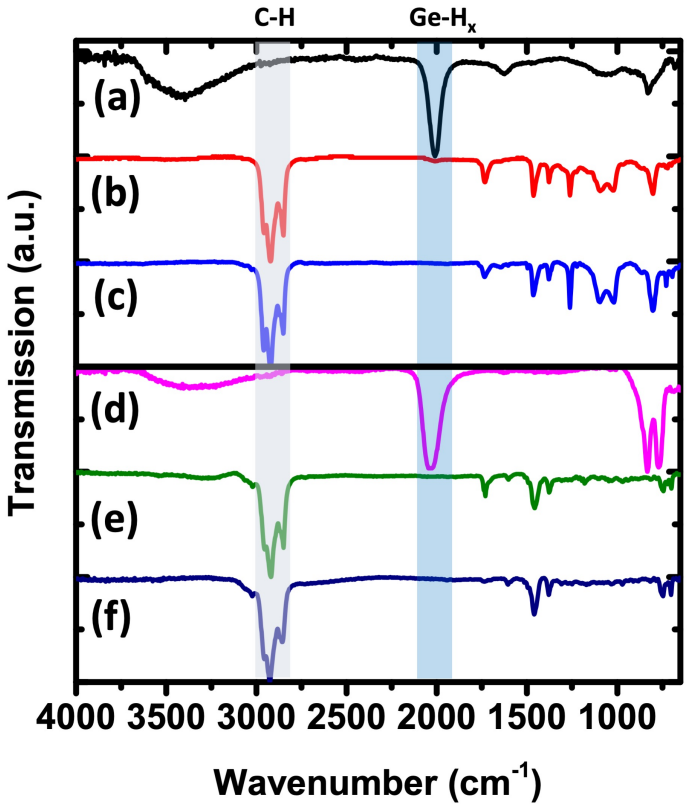

Figure 6.2. FTIR spectra of (a) germanane, (b) hexanethiol-functionalized Ge NSs, (c) hexaneamine-functionalized Ge NSs, (d) poly(dihydrogermane), (e) hexanethiol-substituted polygermane, and (f) hexaneamine-substituted polygermane.

6. 2. 3 Ketyl-radical Mediated Dehydrogenative Coupling Reaction on the Ge NSs Surface or Polygermane Backbone

A dehydrocoupling reaction between Ge–H and Si–H is another approach of introducing heteroatom bonding. As described in Chapter 4, this reaction can be done by heating homogenously mixed H-GeNSs and hydriosilanes at 100 °C for 48 h. We noticed that this reaction can be catalyzed by adding a ketyl radical at room temperature. A ketyl group, $R_2C^{-}O\bullet$, is the product of the 1-electron reduction of a ketone. The sodium benzophenone ketyl is prepared usually by the reaction of benzophenone and excess sodium metal in THF.[284] It has a characteristic deep blue or purple colour and often is used to test solvent dryness in the glovebox. Moreover,

addition of a ketyl radical into hydridosilanes or H–Ge NS solutions will lead to the diminishing of its colour. This process can be observed gradually during exfoliation of germanane flakes, helping in understanding the reaction mechanism. Octadecylsilane and (tridecafluoro-1,1,2,2-tetrahydrooctyl)silane were utilized to evaluate the dehydrocoupling reaction on Ge NSs. FTIR spectra show the ν(C—H) features at 2852 cm^{-1} and/or ν(C—F) features at ~1250 cm^{-1}, with the loss of Ge—H and Si—H bond related features (Figure 6.3). No benzophenone related vibrations (i.e., aryl and C=O) were observed.

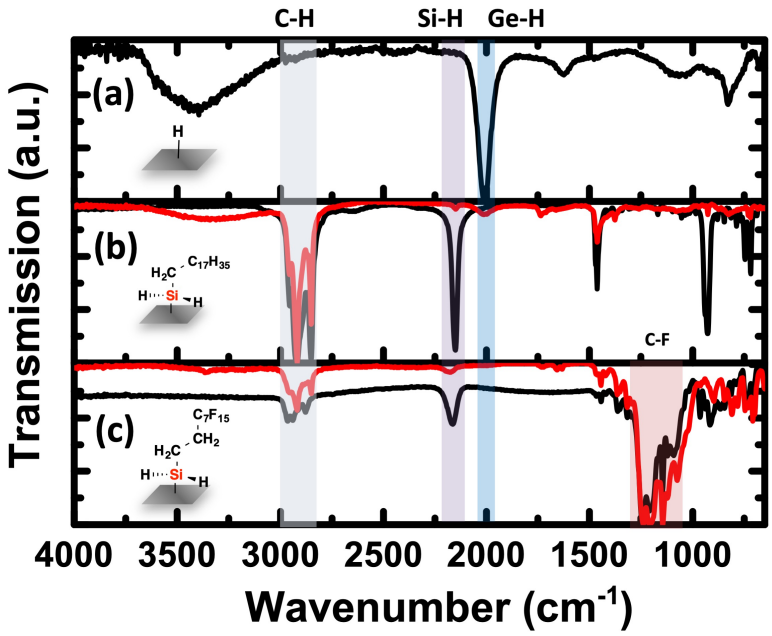

Figure 6.3. FTIR spectra of (a) germanane, (b) octadecylsilane, and (c) (tridecafluoro-1,1,2,2-tetrahydrooctyl)silane functionalized Ge NSs. Red spectra are neat silane ligand.

Energy dispersive X-ray mapping of (tridecafluoro-1,1,2,2-tetrahydrooctyl)silane functionalized Ge NSs were measured under high angle annular dark-field (HAADF) scanning mode (Figure 6.4). Regions with a high-contrast in HAADF images consisted primarily of Ge, F, Si and C elements, as evidenced by spatial overlapping of their Kα X-ray mapping.

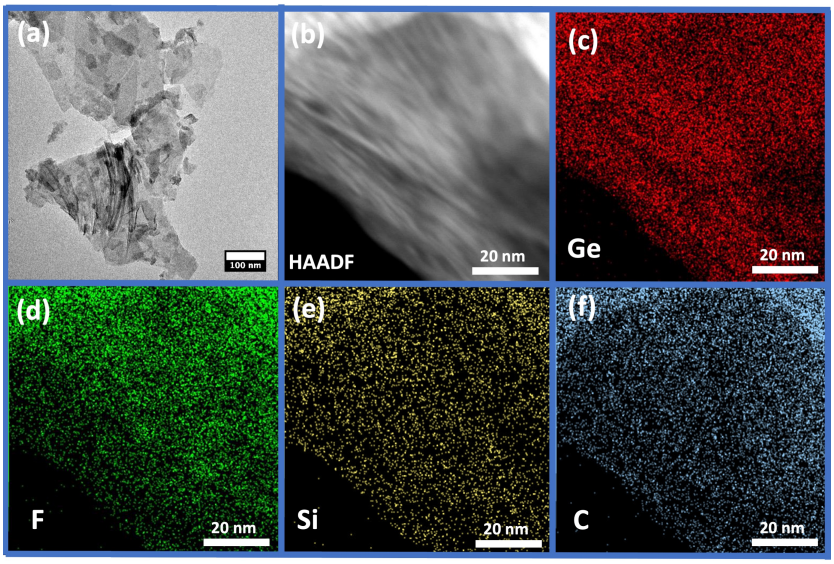

Figure 6.4. (a) Bright-field TEM image and (b–f) HAADF-STEM images with indicated elemental mapping of (tridecafluoro-1,1,2,2-tetrahydrooctyl)silane-terminated Ge NSs.

For a better understanding of the completion of reaction, four different reaction sequences were attempted: (a) adding a ketyl-silane mixture into exfoliated H-GeNSs, (b) adding a ketyl radical into the homogenously H-GeNSs/silane mixture, (c) adding silane into the homogenously H-GeNSs/radical mixture, and (d) a one-pot mixture of H-GeNSs, silane, and ketyl radical before exfoliation (Figure 6.5). The FTIR spectrum shows nearly complete loss of *ν*(Si—H) for sequence (a), suggesting that the ketyl radical could activate the hydridosilanes. Sequences (b) and (c) show almost identical spectra, in which not all the Si—H bonds are consumed. Additional features of non-exfoliated germanane small flakes were presented in sequence (d). The results from these sequences are, however, not enough to understand the catalytic mechanism. In future work, a rigorous systematic study of the reaction mechanism is inevitable. It is also plausible to extend the ketyl radical dehydrocoupling reaction to other Ge/Si-based nanostructures.

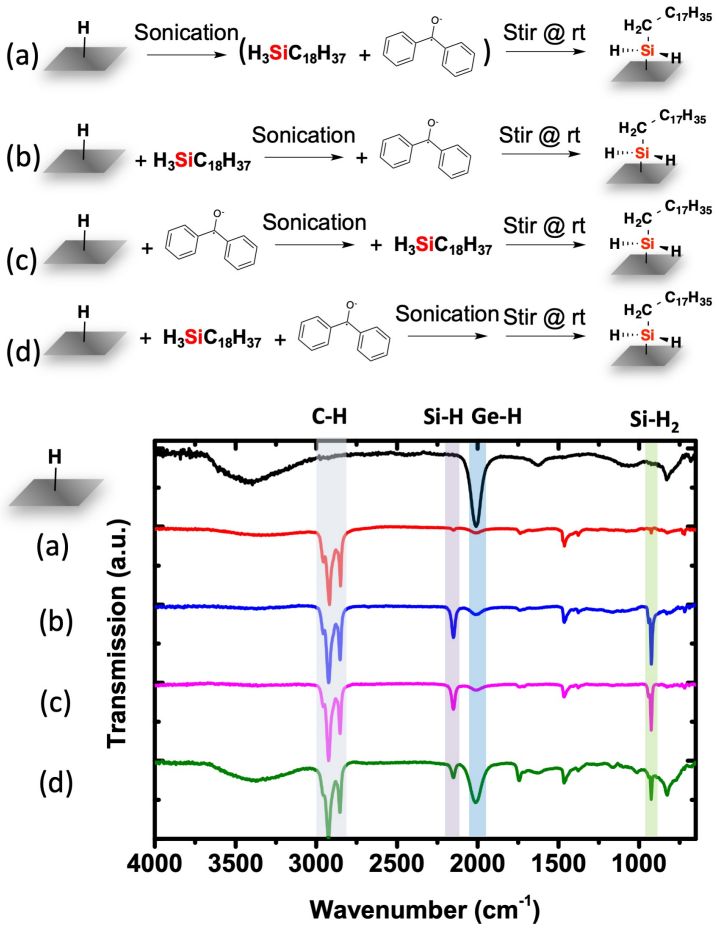

Figure 6.5. A schematic illustration of dehydrocoupling reaction sequences (top) and their FTIR spectra (bottom).

6. 2. 4 Create Silica or Silica-Based Hybrid Patterns Using Focus Ion Beam Lithography

Recently, helium ion microscopy (HIM), a powerful tool in high-resolution imaging with enhanced depth of field and short De Broglie wavelength, has been developed into a platform that provides high-resolution nanostructure fabrication by milling, etching, deposition, and lithographic patterning in resists.[285–287] Hydrogen silisesquioxane (HSQ) as a precursor material in Si QDs synthesis used in the Veinot lab is also an important resist layer in electron beam lithography (EBL).[288] Therefore, it may be a suitable resist material for focused ion beam-based (i.e., HIM) lithography.

In order to develop nano/micropatterns, a uniform thin film of resist material with known thickness is required. To address this, 0.05 mL of HSQ in methyl isobutyl ketone (MIBK) at various concentrations (from 15 wt% to 0.15 wt%) were spin coated onto freshly cleaned Si wafers at a speed of 3000 rpm (Figure 6.6). The thin film thicknesses were confirmed using cross-section SEM, with average values of 500 nm (15 wt%), 200 nm (7.5 wt%), 50 nm (3.0 wt%), and 20 nm (1.5 wt%). The resulting film prepared from the 0.15 wt% HSQ solution was too thin to distinguish the thickness under cross-section SEM. Instead, only Z-contrast was observed on the Si substrate where the thin film was peeled off (Figure 6.6 g and h). In addition to a pure HSQ solution, a mixture of HSQ and 3 nm diameter Si QDs also was prepared using the same procedure, aiming for the development of hybrid nano/micropatterns.

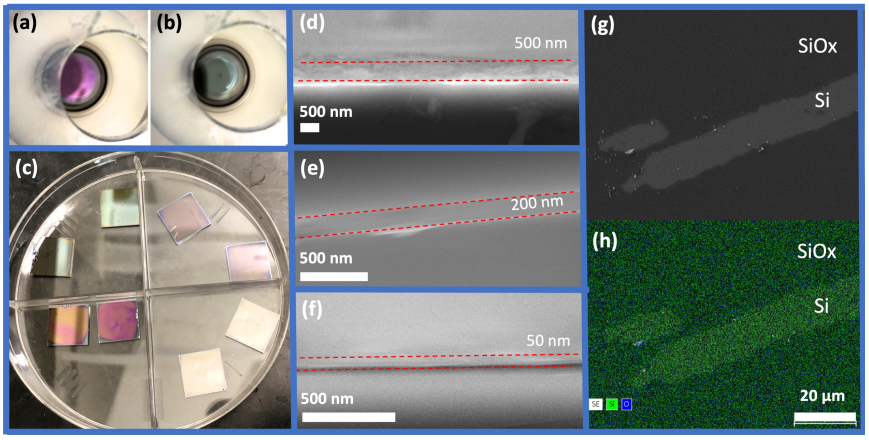

Figure 6.6. Optical images (a, b) of spin coating a HSQ layer at different concentrations, and (c) the resulting thin films. (d–f) Cross-section SEM images of prepared thin films using concentrations of (d) 15 wt%, (e) 7.5 wt%, and (f) 3.0 wt%. (g–h) SEM image and EDS mapping of 0.15 wt% HSQ deposited thin film.

The nano/micropatterns were designed and developed on Zeiss Orion HIM equipped with a NanoPatterning and Visualization Engine (NPVE) software package. All the patterns were developed on the 200 nm HSQ or HSQ/Si QDs mixture coated Si wafer. According to a known publication, the stopping power of 15 keV He^+ in

HSQ is 43 eV $nm^{-1}ion^{-1}$, corresponding to 0.066 mC/cm^2.[289] For each designed pattern, the dose-to-print value was set to 0.050–0.10 mC/cm^2, with 2 nm probe resolution. On average, when a 40 μm diameter aperture was applied, a 50 × 50 μm^2 sized pattern takes ~2 min to complete.

After the exposure, the samples were developed in an aqueous mixture of 1 wt% NaOH and 4 wt% NaCl for 1 min at room temperature and rinsed with deionized water for 30 s (Figure 6.7). Only the sufficiently crosslinked HSQ remained attached on the Si substrate, and the substrate appeared similar to that before coating. Stains remained on the HSQ/Si QDs mixture-coated surface, which might be due to the inhomogeneous mixing of Si QDs in toluene with HSQ in MIBK.

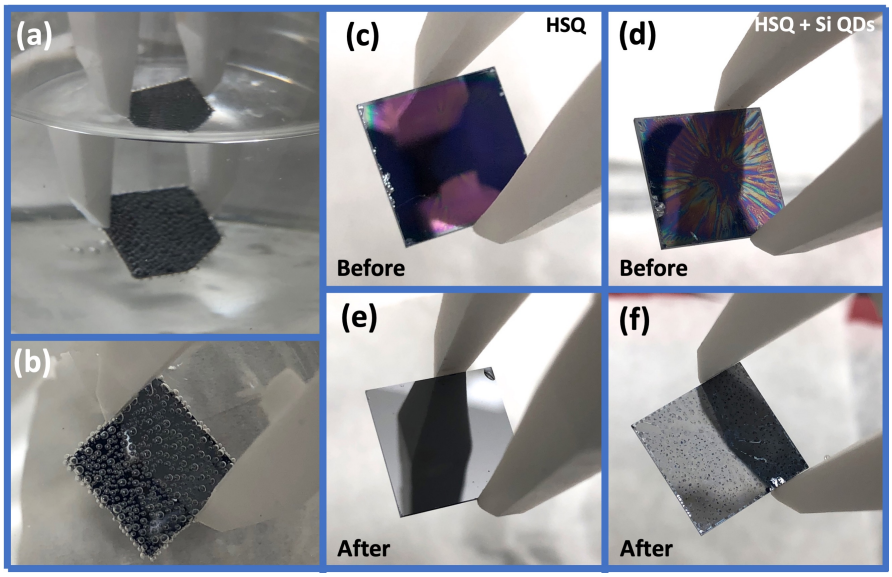

Figure 6.7. Optical images of a thin film in a salty developer (a and b), exposed HSQ thin film (c–f), and mixed HSQ with Si QDs thin film before (c,d) and after (e,f) development.

Smooth flat surfaces with curved edges were observed under SEM for all the created patterns (Figure 6.8). This is due to the crosslinking of HSQ occurring first at the flat layer surface and then He^+ diffusing in a cone-like interactive volume. At a

dose of 0.050 mC/cm^2, the special resolution was determined to be near 200 nm (i.e., densely packed patterns will merge together, as shown in Figure 6.8c and j). Smaller doses could lead to smaller structures with higher special resolution. These patterns did not reach the substrate so that they could be removed from the substrate during developing (Figure 6.8.d). The patterns developed from pure HSQ are made of SiO_2, as confirmed by EDX elemental mapping and spectrum. When HSQ was mixed with Si QDs, the background is contaminated, but the pattern developing was not affected.

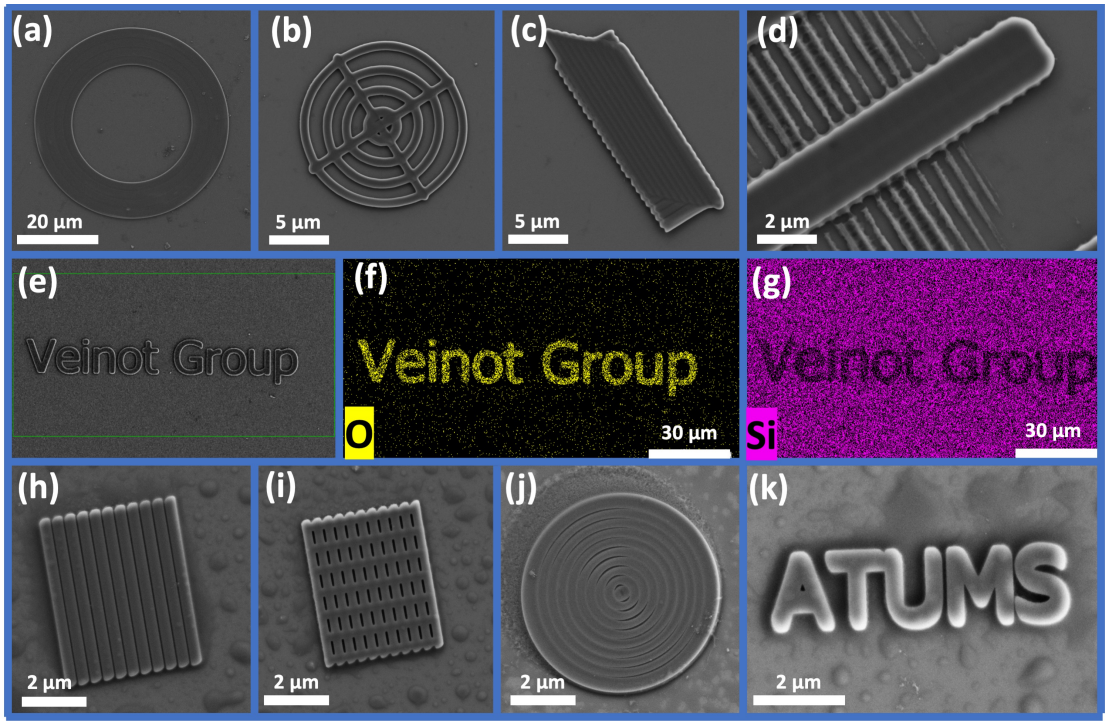

Figure 6.8. SEM images of developed nano/micropatterns, using (a–g) pure HSQ resist and (h–k) HSQ/Si QDs mixed resist. (f and g) O and Si elemental mapping of (e).

In future work, many directions, such as more delicate nano/micropatterns designing, pattern transferring, homogenous blending of resist material, the combination of cross-linking lithography and He^+/Ga^+ ion milling, post-patterning functionalization, and opto-device fabrication, still need to be further explored.

Bibliography

(1) Ye, Q.; Tsu, R.; Nicollian, E. H. Resonant Tunneling via Microcrystalline-Silicon Quantum Confinement. *Phys. Rev. B* **1991**, *44* (4), 1806–1811.

(2) Huang, J.; Zhang, L.; Chen, B.; Ji, N.; Chen, F.; Zhang, Y.; Zhang, Z. Nanocomposites of Size-Controlled Gold Nanoparticles and Graphene Oxide: Formation and Applications in SERS and Catalysis. *Nanoscale* **2010**, *2* (12), 2733–2738.

(3) Eustis, S.; El-Sayed, M. A. Why Gold Nanoparticles are More Precious than Pretty Gold: Noble Metal Surface Plasmon Resonance and Its Enhancement of the Radiative and Nonradiative Properties of Nanocrystals of Different Shapes. *Chem. Soc. Rev.* **2006**, *35* (3), 209–217.

(4) Paciotti, G. F.; Kingston, D. G. I.; Tamarkin, L. Colloidal Gold Nanoparticles: A Novel Nanoparticle Platform for Developing Multifunctional Tumor-Targeted Drug Delivery Vectors. *Drug Dev. Res.* **2006**, *67* (1), 47–54.

(5) Fujiki, M.; Kato, M.; Kawamoto, Y.; Kwak, G. Green-and-Red Photoluminescence from Si–Si and Ge–Ge Bonded Network Homopolymers and Copolymers. *Polym. Chem.* **2011**, *2* (4), 914–922.

(6) Qian, C.; Sun, W.; Wang, L.; Chen, C.; Liao, K.; Wang, W.; Jia, J.; Hatton, B. D.; Casillas, G.; Kurylowicz, M.; Yip, C. M.; Mastronardi, M. L.; Ozin, G. A. Non-Wettable, Oxidation-Stable, Brightly Luminescent, Perfluorodecyl-Capped Silicon Nanocrystal Film. *J. Am. Chem. Soc.* **2014**, *136* (45), 15849–15852.

(7) Somers, R. C.; Bawendi, M. G.; Nocera, D. G. CdSe Nanocrystal Based Chem-/Bio- Sensors. *Chem. Soc. Rev.* **2007**, *36* (4), 579–591.

(8) Peng, F.; Su, Y.; Zhong, Y.; Fan, C.; Lee, S.-T.; He, Y. Silicon Nanomaterials Platform for Bioimaging, Biosensing, and Cancer Therapy. *Acc. Chem. Res.* **2014**, *47* (2), 612–623.

(9) Manzeli, S.; Ovchinnikov, D.; Pasquier, D.; Yazyev, O. V.; Kis, A. 2D

Transition Metal Dichalcogenides. *Nat. Rev. Mater.* **2017**, *2* (8), 17033.

(10) Dean, C. R.; Young, A. F.; Meric, I.; Lee, C.; Wang, L.; Sorgenfrei, S.; Watanabe, K.; Taniguchi, T.; Kim, P.; Shepard, K. L.; Hone, J. Boron Nitride Substrates for High-Quality Graphene Electronics. *Nat. Nanotechnol.* **2010**, *5* (10), 722–726.

(11) Withers, F.; Del Pozo-Zamudio, O.; Mishchenko, A.; Rooney, A. P.; Gholinia, A.; Watanabe, K.; Taniguchi, T.; Haigh, S. J.; Geim, A. K.; Tartakovskii, A. I.; Novoselov, K. S. Light-Emitting Diodes by Band-Structure Engineering in van Der Waals Heterostructures. *Nat. Mater.* **2015**, *14* (3), 301–306.

(12) Radisavljevic, B.; Radenovic, A.; Brivio, J.; Giacometti, V.; Kis, A. Single-Layer MoS_2 Transistors. *Nat. Nanotechnol.* **2011**, *6* (3), 147–150.

(13) Islam, M. A.; Purkait, T. K.; Veinot, J. G. C. Chloride Surface Terminated Silicon Nanocrystal Mediated Synthesis of Poly(3-Hexylthiophene). *J. Am. Chem. Soc.* **2014**, *136* (43), 15130–15133.

(14) Iqbal, M.; Purkait, T. K.; Goss, G. G.; Bolton, J. R.; Gamal El-Din, M.; Veinot, J. G. C. Application of Engineered Si Nanoparticles in Light-Induced Advanced Oxidation Remediation of a Water-Borne Model Contaminant. *ACS Nano* **2016**, *10* (5), 5405–5412.

(15) Michel, J.; Liu, J.; Kimerling, L. C. High-Performance Ge-on-Si Photodetectors. *Nat. Photonics* **2010**, *4* (8), 527–534.

(16) Walters, R. J.; Bourianoff, G. I.; Atwater, H. A. Field-Effect Electroluminescence in Silicon Nanocrystals. *Nat. Mater.* **2005**, *4* (2), 143–146.

(17) Yongping Ding; Ying Dong; Bapat, A.; Nowak, J. D.; Carter, C. B.; Kortshagen, U. R.; Campbell, S. A. Single Nanoparticle Semiconductor Devices. *IEEE Trans. Electron Devices* **2006**, *53* (10), 2525–2531.

(18) Law, D. C.; King, R. R.; Yoon, H.; Archer, M. J.; Boca, A.; Fetzer, C. M.; Mesropian, S.; Isshiki, T.; Haddad, M.; Edmondson, K. M.; Bhusari, D.; Yen, J.; Sherif, R. A.; Atwater, H. A.; Karam, N. H. Future Technology Pathways of Terrestrial III–V Multijunction Solar Cells for Concentrator Photovoltaic

Systems. *Sol. Energy Mater. Sol. Cells* **2010**, *94* (8), 1314–1318.

(19) Stelzner, T.; Pietsch, M.; Andrä, G.; Falk, F.; Ose, E.; Christiansen, S. Silicon Nanowire-Based Solar Cells. *Nanotechnology* **2008**, *19* (29), 295203.

(20) Perez-Wurfl, I.; Hao, X.; Gentle, A.; Kim, D.-H.; Conibeer, G.; Green, Martin. A. Si Nanocrystal P-i-n Diodes Fabricated on Quartz Substrates for Third Generation Solar Cell Applications. *Appl. Phys. Lett.* **2009**, *95* (15), 153506.

(21) Aghajamali, M.; Xie, H.; Javadi, M.; Kalisvaart, W. P.; Buriak, J. M.; Veinot, J. G. C. Size and Surface Effects of Silicon Nanocrystals in Graphene Aerogel Composite Anodes for Lithium Ion Batteries. *Chem. Mater.* **2018**, *30* (21), 7782–7792.

(22) McVey, B. F. P.; Tilley, R. D. Solution Synthesis, Optical Properties, and Bioimaging Applications of Silicon Nanocrystals. *Acc. Chem. Res.* **2014**, *47* (10), 3045–3051.

(23) Robidillo, C. J. T.; Islam, M. A.; Aghajamali, M.; Faramus, A.; Sinelnikov, R.; Zhang, X.; Boekhoven, J.; Veinot, J. G. C. Functional Bioinorganic Hybrids from Enzymes and Luminescent Silicon-Based Nanoparticles. *Langmuir* **2018**, *34* (22), 6556–6569.

(24) Gonzalez, C. M.; Veinot, J. G. C. Silicon Nanocrystals for the Development of Sensing Platforms. *J. Mater. Chem. C* **2016**, *4* (22), 4836–4846.

(25) Clark, R. J.; Aghajamali, M.; Gonzalez, C. M.; Hadidi, L.; Islam, M. A.; Javadi, M.; Mobarok, M. H.; Purkait, T. K.; Robidillo, C. J. T.; Sinelnikov, R.; Thiessen, A. N.; Washington, J.; Yu, H.; Veinot, J. G. C. From Hydrogen Silsesquioxane to Functionalized Silicon Nanocrystals. *Chem. Mater.* **2017**, *29* (1), 80–89.

(26) Yang, Z.; Dobbie, A. R.; Cui, K.; Veinot, J. G. C. A Convenient Method for Preparing Alkyl-Functionalized Silicon Nanocubes. *J. Am. Chem. Soc.* **2012**, *134* (34), 13958–13961.

(27) Heitsch, A. T.; Hessel, C. M.; Akhavan, V. A.; Korgel, B. A. Colloidal Silicon Nanorod Synthesis. *Nano Lett.* **2009**, *9* (8), 3042–3047.

(28) Javadi, M.; Picard, D.; Sinelnikov, R.; Narreto, M. A.; Hegmann, F. A.; Veinot, J. G. C. Synthesis and Surface Functionalization of Hydride-Terminated Ge Nanocrystals Obtained from the Thermal Treatment of $Ge(OH)_2$. *Langmuir* **2017**. *33* (35), 8757–8765.

(29) Wang; Huang; Ren. Synthesis of Germanium Nanocubes by a Low-Temperature Inverse Micelle Solvothermal Technique. *Langmuir* **2005**, *21* (2), 751–754.

(30) Chockla, A. M.; Harris, J. T.; Korgel, B. A. Colloidal Synthesis of Germanium Nanorods. *Chem. Mater.* **2011**, *23* (7), 1964–1970.

(31) Wen, B.; Huang, Y.; J. Boland, J. A Simple Solvothermal Route to Controlled Diameter Germanium Nanowires. *J. Mater. Chem.* **2008**, *18* (17), 2011–2015.

(32) Nogales, E.; Montone, A.; Cardellini, F.; ndez, B. M.; Piqueras, J. Visible Cathodoluminescence from Mechanically Milled Germanium. *Semicond. Sci. Technol.* **2002**, *17* (12), 1267–1271.

(33) Švrček, V.; Rehspringer, J.-L.; Gaffet, E.; Slaoui, A.; Muller, J.-C. Unaggregated Silicon Nanocrystals Obtained by Ball Milling. *J. Cryst. Growth* **2005**, *275* (3), 589–597.

(34) Shen, T. D.; Koch, C. C.; McCormick, T. L.; Nemanich, R. J.; Huang, J. Y.; Huang, J. G. The Structure and Property Characteristics of Amorphous/Nanocrystalline Silicon Produced by Ball Milling. *J. Mater. Res.* **1995**, *10* (1), 139–148.

(35) Poffo, C. M.; Lima, J. C. de; Souza, S. M.; Trichês, D. M.; Grandi, T. A.; Biasi, R. S. de. Structural, Thermal and Optical Study of Nanocrystalline Silicon Produced by Ball Milling. *J. Raman Spectrosc.* **2010**, *41* (12), 1606–1609.

(36) Giri, P. K. Strain Analysis on Freestanding Germanium Nanocrystals. *J. Phys. Appl. Phys.* **2009**, *42* (24), 245402.

(37) Mayeri, D.; Phillips, B. L.; Augustine, M. P.; Kauzlarich, S. M. NMR Study of the Synthesis of Alkyl-Terminated Silicon Nanoparticles from the Reaction of $SiCl_4$ with the Zintl Salt, NaSi. *Chem. Mater.* **2001**, *13* (3), 765–770.

(38) Taylor, B. R.; Kauzlarich, S. M.; Delgado, G. R.; Lee, H. W. H. Solution Synthesis and Characterization of Quantum Confined Ge Nanoparticles. *Chem. Mater.* **1999**, *11* (9), 2493–2500.

(39) Pettigrew, K. A.; Liu, Q.; Power, P. P.; Kauzlarich, S. M. Solution Synthesis of Alkyl- and Alkyl/Alkoxy-Capped Silicon Nanoparticles via Oxidation of Mg_2Si. *Chem. Mater.* **2003**, *15* (21), 4005–4011.

(40) Chiu, H. W.; Kauzlarich, S. M. Investigation of Reaction Conditions for Optimal Germanium Nanoparticle Production by a Simple Reduction Route. *Chem. Mater.* **2006**, *18* (4), 1023–1028.

(41) Prabakar, S.; Shiohara, A.; Hanada, S.; Fujioka, K.; Yamamoto, K.; Tilley, R. D. Size Controlled Synthesis of Germanium Nanocrystals by Hydride Reducing Agents and Their Biological Applications. *Chem. Mater.* **2010**, *22* (2), 482–486.

(42) Mastronardi, M. L.; Hennrich, F.; Henderson, E. J.; Maier-Flaig, F.; Blum, C.; Reichenbach, J.; Lemmer, U.; Kübel, C.; Wang, D.; Kappes, M. M.; Ozin, G. A. Preparation of Monodisperse Silicon Nanocrystals Using Density Gradient Ultracentrifugation. *J. Am. Chem. Soc.* **2011**, *133* (31), 11928–11931.

(43) Mastronardi, M. L.; Maier-Flaig, F.; Faulkner, D.; Henderson, E. J.; Kübel, C.; Lemmer, U.; Ozin, G. A. Size-Dependent Absolute Quantum Yields for Size-Separated Colloidally-Stable Silicon Nanocrystals. *Nano Lett.* **2012**, *12* (1), 337–342.

(44) Hossain, M. A.; Javadi, M.; Yu, H.; Thiessen, A. N.; Ikpo, N.;Oliynyk, A. O.; Veinot, J. G. C. Dehydrocoupling – an Alternative Approach to Functionalizing Germanium Nanoparticle Surfaces. *Nanoscale* **2020**, *12* (11), 6271–6278.

(45) Vaughn, D. D.; Bondi, J. F.; Schaak, R. E. Colloidal Synthesis of Air-Stable Crystalline Germanium Nanoparticles with Tunable Sizes and Shapes. *Chem. Mater.* **2010**, *22* (22), 6103–6108.

(46) Yu, Y.; Lu, X.; Guillaussier, A.; Voggu, V. R.; Pineros, W.; de la Mata, M.; Arbiol, J.; Smilgies, D.-M.; Truskett, T. M.; Korgel, B. A. Orientationally Ordered Silicon Nanocrystal Cuboctahedra in Superlattices. *Nano Lett.* **2016**,

16 (12), 7814–7821.

(47) Holmes, J. D.; Johnston, K. P.; Doty, R. C.; Korgel, B. A. Control of Thickness and Orientation of Solution-Grown Silicon Nanowires. *Science* **2000**, *287* (5457), 1471–1473.

(48) Holmberg, V. C.; Korgel, B. A. Corrosion Resistance of Thiol- and Alkene-Passivated Germanium Nanowires. *Chem. Mater.* **2010**, *22* (12), 3698–3703.

(49) Yang, Z.; C. Veinot, J. G. Size-Controlled Template Synthesis of Metal-Free Germanium Nanowires. *J. Mater. Chem.* **2011**, *21* (41), 16505–16509.

(50) Wu, X.; Kulkarni, J. S.; Collins, G.; Petkov, N.; Almécija, D.; Boland, J. J.; Erts, D.; Holmes, J. D. Synthesis and Electrical and Mechanical Properties of Silicon and Germanium Nanowires. *Chem. Mater.* **2008**, *20* (19), 5954–5967.

(51) Reparaz, J. S.; Peica, N.; Kirste, R.; Goñi, A. R.; Wagner, M. R.; Callsen, G.; Alonso, M. I.; Garriga, M.; Marcus, I. C.; Ronda, A.; I Berbezier; Maultzsch, J.; Thomsen, C.; Hoffmann, A. Probing Local Strain and Composition in Ge Nanowires by Means of Tip-Enhanced Raman Scattering. *Nanotechnology* **2013**, *24* (18), 185704.

(52) Geim, A. K.; Novoselov, K. S. The Rise of Graphene. *Nat. Mater.* **2007**, *6* (3), 183–191.

(53) Geim, A. K. Graphene: Status and Prospects. *Science* **2009**, *324* (5934), 1530–1534.

(54) Duong, D. L.; Yun, S. J.; Lee, Y. H. Van Der Waals Layered Materials: Opportunities and Challenges. *ACS Nano* **2017**, *11* (12), 11803–11830.

(55) Geim, A. K.; Grigorieva, I. V. Van Der Waals Heterostructures. *Nature* **2013**, *499* (7459), 419–425.

(56) Matthes, L.; Pulci, O.; Bechstedt, F. Massive Dirac Quasiparticles in the Optical Absorbance of Graphene, Silicene, Germanene, and Tinene. *J. Phys. Condens. Matter* **2013**, *25* (39), 395305.

(57) Kara, A.; Enriquez, H.; Seitsonen, A. P.; Lew Yan Voon, L. C.; Vizzini, S.; Aufray, B.; Oughaddou, H. A Review on Silicene — New Candidate for Electronics. *Surf. Sci. Rep.* **2012**, *67* (1), 1–18.

(58) Lalmi, B.; Oughaddou, H.; Enriquez, H.; Kara, A.; Vizzini, S.; Ealet, B.; Aufray, B. Epitaxial Growth of a Silicene Sheet. *Appl. Phys. Lett.* **2010**, *97* (22), 223109.

(59) Enriquez, H.; Vizzini, S.; Kara, A.; Lalmi, B.; Oughaddou, H. Silicene Structures on Silver Surfaces. *J. Phys. Condens. Matter* **2012**, *24* (31), 314211.

(60) Lin, C.-L.; Arafune, R.; Kawahara, K.; Tsukahara, N.; Minamitani, E.; Kim, Y.; Takagi, N.; Kawai, M. Structure of Silicene Grown on Ag(111). *Appl. Phys. Express* **2012**, *5* (4), 045802.

(61) Fleurence, A.; Friedlein, R.; Ozaki, T.; Kawai, H.; Wang, Y.; Yamada-Takamura, Y. Experimental Evidence for Epitaxial Silicene on Diboride Thin Films. *Phys. Rev. Lett.* **2012**, *108* (24), 245501.

(62) Aizawa, T.; Suehara, S.; Otani, S. Silicene on Zirconium Carbide (111). *J. Phys. Chem. C* **2014**, *118* (40), 23049–23057.

(63) Chiappe, D.; Scalise, E.; Cinquanta, E.; Grazianetti, C.; Broek, B. van den; Fanciulli, M.; Houssa, M.; Molle, A. Two-Dimensional Si Nanosheets with Local Hexagonal Structure on a MoS_2 Surface. *Adv. Mater.* **2014**, *26* (13), 2096–2101.

(64) Meng, L.; Wang, Y.; Zhang, L.; Du, S.; Wu, R.; Li, L.; Zhang, Y.; Li, G.; Zhou, H.; Hofer, W. A.; Gao, H.-J. Buckled Silicene Formation on Ir(111). *Nano Lett.* **2013**, *13* (2), 685–690.

(65) Yuhara, J.; Shimazu, H.; Ito, K.; Ohta, A.; Araidai, M.; Kurosawa, M.; Nakatake, M.; Le Lay, G. Germanene Epitaxial Growth by Segregation through Ag(111) Thin Films on Ge(111). *ACS Nano* **2018**, *12* (11), 11632–11637.

(66) Dávila, M. E.; Xian, L.; Cahangirov, S.; Rubio, A.; Lay, G. L. Germanene: A Novel Two-Dimensional Germanium Allotrope Akin to Graphene and

Silicene. *New J. Phys.* **2014**, *16* (9), 095002.

(67) Li, L.; Lu, S.; Pan, J.; Qin, Z.; Wang, Y.; Wang, Y.; Cao, G.; Du, S.; Gao, H.-J. Buckled Germanene Formation on Pt(111). *Adv. Mater.* **2014**, *26* (28), 4820–4824.

(68) Tao, L.; Cinquanta, E.; Chiappe, D.; Grazianetti, C.; Fanciulli, M.; Dubey, M.; Molle, A.; Akinwande, D. Silicene Field-Effect Transistors Operating at Room Temperature. *Nat. Nanotechnol.* **2015**, *10* (3), 227–231.

(69) Qiu, J.; Fu, H.; Xu, Y.; Zhou, Q.; Meng, S.; Li, H.; Chen, L.; Wu, K. From Silicene to Half-Silicane by Hydrogenation. *ACS Nano* **2015**, *9* (11), 11192–11199.

(70) Bianco, E.; Butler, S.; Jiang, S.; Restrepo, O. D.; Windl, W.; Goldberger, J. E. Stability and Exfoliation of Germanane: A Germanium Graphane Analogue. *ACS Nano* **2013**, *7* (5), 4414–4421.

(71) Vogg, G.; Brandt, M. S.; Stutzmann, M. Polygermyne—A Prototype System for Layered Germanium Polymers. *Adv. Mater.* **2000**, *12* (17), 1278–1281.

(72) Helbich, T.; Lyuleeva, A.; Ludwig, T.; Scherf, L. M.; Fässler, T. F.; Lugli, P.; Rieger, B. One-Step Synthesis of Photoluminescent Covalent Polymeric Nanocomposites from 2D Silicon Nanosheets. *Adv. Funct. Mater.* **2016**, *26* (37), 6711–6718.

(73) Dahn, J. R.; Way, B. M.; Fuller, E.; Tse, J. S. Structure of Siloxene and Layered Polysilane (Si_6H_6). *Phys. Rev. B* **1993**, *48* (24), 17872–17877.

(74) Vogg, G.; Zamanzadeh-Hanebuth, N.; Brandt, M. S.; Stutzmann, M.; Albrecht, M. Preparation and Characterization of Epitaxial $CaSi_2$ and Siloxene Layers on Silicon. *Monatshefte Für Chem. Chem. Mon.* **1999**, *130* (1), 79–87.

(75) Vogg, G.; Brandt, M. S.; Stutzmann, M.; Albrecht, M. From $CaSi_2$ to Siloxene: Epitaxial Silicide and Sheet Polymer Films on Silicon. *J. Cryst. Growth* **1999**, *203* (4), 570–581.

(76) Pinchuk, I. V.; Odenthal, P. M.; Ahmed, A. S.; Amamou, W.; Goldberger, J. E.; Kawakami, R. K. Epitaxial Co-Deposition Growth of $CaGe_2$ Films by

Molecular Beam Epitaxy for Large Area Germanane. *J. Mater. Res.* **2014**, *29* (3), 410–416.

(77) Madhushankar, B. N.; Kaverzin, A.; Giousis, T.; Potsi, G.; Gournis, D.; Rudolf, P.; Blake, G. R.; Wal, C. H. van der; Wees, B. J. van. Electronic Properties of Germanane Field-Effect Transistors. *2D Mater.* **2017**, *4* (2), 021009.

(78) Amamou, W.; Odenthal, P. M.; Bushong, E. J.; O'Hara, D. J.; Luo, Y. K.; Baren, J. van; Pinchuk, I.; Wu, Y.; Ahmed, A. S.; Katoch, J.; Bockrath, M. W.; Tom, H. W. K.; Goldberger, J. E.; Kawakami, R. K. Large Area Epitaxial Germanane for Electronic Devices. *2D Mater.* **2015**, *2* (3), 035012.

(79) Lyuleeva, A.; Holzmüller, P.; Helbich, T.; Stutzmann, M.; S. Brandt, M.; Becherer, M.; Lugli, P.; Rieger, B. Charge Transfer Doping in Functionalized Silicon Nanosheets/P3HT Hybrid Material for Applications in Electrolyte-Gated Field-Effect Transistors. *J. Mater. Chem. C* **2018**, *6* (27), 7343-7352.

(80) Serino, A. C.; Ko, J. S.; Yeung, M. T.; Schwartz, J. J.; Kang, C. B.; Tolbert, S. H.; Kaner, R. B.; Dunn, B. S.; Weiss, P. S. Lithium-Ion Insertion Properties of Solution-Exfoliated Germanane. *ACS Nano* **2017**, *11* (8), 7995–8001.

(81) Trout, A. H.; Wang, Y.; Esser, B. D.; Jiang, S.; Goldberger, J. E.; Windl, W.; McComb, D. W. Identification of Turbostratic Twisting in Germanane. *J. Mater. Chem. C* **2019**, *7* (32), 10092–10097.

(82) Cultrara, N. D.; Arguilla, M. Q.; Jiang, S.; Sun, C.; Scudder, M. R.; Ross, R. D.; Goldberger, J. E. Group-13 and Group-15 Doping of Germanane. *Beilstein J. Nanotechnol.* **2017**, *8* (1), 1642–1648.

(83) Foucher, D. Catenated Germanium and Tin Oligomers and Polymers. In *Main Group Strategies towards Functional Hybrid Materials*; John Wiley & Sons, Ltd, 2018; pp 209–236.

(84) Weinert, C. S. Germanium: Organometallic Chemistry. In *Encyclopedia of Inorganic and Bioinorganic Chemistry*; American Cancer Society, 2015; pp 1–18.

(85) Mochida, K.; Chiba, H. Synthesis, Absorption Characteristics and Some Reactions of Polygermanes. *J. Organomet. Chem.* **1994**, *473* (1), 45–54.

(86) Schepers, T.; Michl, J. Optimized ladder C and ladder H models for sigma conjugation: chain segmentation in polysilanes. *J. Phys. Org. Chem.* **2002**, *15* (8), 490–498.

(87) Fa, W.; Zeng, X. C. Polygermanes: Bandgap Engineering via Tensile Strain and Side-Chain Substitution. *Chem. Commun.* **2014**, *50* (65), 9126–9129.

(88) Okano, M.; Toriumi, T.; Hamano, H. Electrochemical Synthesis of Germane–Germane and Germane–Silane Copolymers. *Electrochimica Acta* **1999**, *44* (20), 3475–3482.

(89) Amadoruge, M. L.; Gardinier, J. R.; Weinert, C. S. Substituent Effects in Linear Organogermanium Catenates. *Organometallics* **2008**, *27* (15), 3753–3760.

(90) Klingensmith, K. A.; Downing, J. W.; Miller, R. D.; Michl, Josef. Electronic Excitation in Poly(Di-n-Hexylsilane). *J. Am. Chem. Soc.* **1986**, *108* (23), 7438–7439.

(91) Kipping, F. S.; Sands, J. E. XCII1.-Organic Derivatives of Silicon. Part X X V. Saturated and Unsaturated Siliconhydrocarbons, Si_4Ph_8. *J. Chem. Soc., Trans* **1921**, *119* (0), 830–847.

(92) Koe, J.; Fujiki, M. Chapter 6 - Polysilanes. In *Organosilicon Compounds*; Lee, V. Ya., Ed.; Academic Press, 2017; pp 219–300.

(93) Koe, J. Contemporary Polysilane Synthesis and Functionalisation. *Polym. Int.* **2009**, *58* (3), 255–260.

(94) Marro, E. A.; Klausen, R. S. Conjugated Polymers Inspired by Crystalline Silicon. *Chem. Mater.* **2019**, *31* (7), 2202–2211.

(95) Miller, R. D.; Michl, J. Polysilane High Polymers. *Chem. Rev.* **1989**, *89* (6), 1359–1410.

(96) Miller, R. D. Polysilanes—A New Look at Some Old Materials. *Angew. Chem. Int. Ed. Engl.* **1989**, *28* (12), 1733–1740.

(97) Shono, T.; Kashimura, S.; Murase, H. Electroreductive Synthesis of Polygermane and Germane–Silane Copolymer. *J. Chem. Soc. Chem. Commun.* **1992**, No. 12, 896–897.

(98) Okano, M.; Takeda, K.; Toriumi, T.; Hamano, H. Electrochemical Synthesis of Polygermanes. *Electrochimica Acta* **1998**, *44* (4), 659–666.

(99) Amadoruge, M. L.; Weinert, C. S. Singly Bonded Catenated Germanes: Eighty Years of Progress. *Chem. Rev.* **2008**, *108* (10), 4253–4294.

(100) Aitken, C.; Harrod, J. F.; Malek, A.; Samuel, E. Oligomerization of Phenylgermanes by Catalytic Dehydrocoupling. *J. Organomet. Chem.* **1988**, *349* (3), 285–291.

(101) Choi, N.; Tanaka, M. Zirconocene-Catalyzed Dehydrogenative Coupling of Phenylgermane and Properties of the Resulting Partially Network Polyphenylgermanes. *J. Organomet. Chem.* **1998**, *564* (1), 81–84.

(102) Katz, S. M.; Reichl, J. A.; Berry, D. H. Catalytic Synthesis of Poly(Arylmethylgermanes) by Demethanative Coupling: A Mild Route to σ-Conjugated Polymers. *J. Am. Chem. Soc.* **1998**, *120* (38), 9844–9849.

(103) Reichl, J. A.; Popoff, C. M.; Gallagher, L. A.; Remsen, E. E.; Berry, D. H. Ruthenium-Catalyzed Demethanative Coupling of $HGeMe_3$: A High Yield Route to Polygermanes. *J. Am. Chem. Soc.* **1996**, *118* (39), 9430–9431.

(104) Masuda, T.; Matsuki, Y.; Shimoda, T. Characterization of Polydihydrosilane by SEC-MALLS and Viscometry. *Polymer* **2012**, *53* (14), 2973–2978.

(105) Masuda, T.; Matsuki, Y.; Shimoda, T. Pyrolytic Transformation from Polydihydrosilane to Hydrogenated Amorphous Silicon Film. *Thin Solid Films* **2012**, *520* (21), 6603–6607.

(106) Masuda, T.; Matsuki, Y.; Shimoda, T. Stability of Polydihydrosilane Liquid Films on Solid Substrates. *Thin Solid Films* **2012**, *520* (15), 5091–5096.

(107) Chambreau, S. D.; Zhang, J. GeH_x (X=0–3) and Ge_nH_x (N=2–7) in Flash Pyrolysis of GeH_4. *Chem. Phys. Lett.* **2002**, *351* (3), 171–177.

(108) Royen, P.; Schwarz, R. Beiträge Zur Chemie Des Germaniums. XIV. Mitteilung. Die Eigenschaften Des Polygermens $(GeH_2)_x$. *Z. Für Anorg. Allg. Chem.* **1933**, *215* (3–4), 295–309.

(109) Royen, P.; Rocktäschel, C. Zur Kenntnis niedere Hydride des Siliciums und Germaniums. *Z. Für Anorg. Allg. Chem.* **1966**, *346* (5–6), 279–289.

(110) Dasog, M.; De los Reyes, G. B.; Titova, L. V.; Hegmann, F. A.; Veinot, J. G. C. Size vs Surface: Tuning the Photoluminescence of Freestanding Silicon Nanocrystals Across the Visible Spectrum via Surface Groups. *ACS Nano* **2014**, *8* (9), 9636–9648.

(111) Dasog, M.; Kehrle, J.; Rieger, B.; Veinot, J. G. C. Silicon Nanocrystals and Silicon-Polymer Hybrids: Synthesis, Surface Engineering, and Applications. *Angew. Chem. Int. Ed.* **2016**, *55* (7), 2322–2339.

(112) Sinelnikov, R.; Dasog, M.; Beamish, J.; Meldrum, A.; Veinot, J. G. C. Revisiting an Ongoing Debate: What Role Do Surface Groups Play in Silicon Nanocrystal Photoluminescence? *ACS Photonics* **2017**, *4* (8), 1920–1929.

(113) Guo, Y.; Rowland, C. E.; Schaller, R. D.; Vela, J. Near-Infrared Photoluminescence Enhancement in Ge/CdS and Ge/ZnS Core/Shell Nanocrystals: Utilizing IV/II–VI Semiconductor Epitaxy. *ACS Nano* **2014**, *8* (8), 8334–8343.

(114) Guo, Y.-J.; Yang, F.; Zhang, L.; Pi, J.; Cai, J.-Y.; Yang, P.-H. Facile Synthesis of Multifunctional Germanium Nanoparticles as a Carrier of Quercetin to Achieve Enhanced Biological Activity. *Chem. – Asian J.* **2014**, *9* (8), 2272–2280.

(115) Dasog, M.; De los Reyes, G. B.; Titova, L. V.; Hegmann, F. A.; Veinot, J. G. C. Size vs Surface: Tuning the Photoluminescence of Freestanding Silicon Nanocrystals Across the Visible Spectrum via Surface Groups. *ACS Nano* **2014**, *8* (9), 9636–9648.

(116) Yin, H.; Cai, H.-H.; Cai, J.-Y.; Teng, J.-W.; Yang, P. Facile Solution Routes for the Syntheses of Water-Dispersable Germanium Nanoparticles and Their Biological Applications. *Mater. Lett.* **2013**, *109*, 108–111.

(117) Javadi, M.; Purkait, T.; Hadidi, L.; Washington, J.; Veinot, J. G. C. Synthesis and Properties of Covalently Linked Photoluminescent Magnetic Magnetite Nanoparticle-Silicon Nanocrystal Hybrids. *MRS Adv.* **2016**, *1* (33), 2321–2329.

(118) Robidillo, C. J. T.; Wandelt, S.; Dalangin, R.; Zhang, L.; Yu, H.; Meldrum, A.; Campbell, R. E.; Veinot, J. G. C. Ratiometric Detection of Nerve Agents by Coupling Complementary Properties of Silicon-Based Quantum Dots and Green Fluorescent Protein. *ACS Appl. Mater. Interfaces* **2019**, *11* (36), 33478–33488.

(119) Lu, X.; Korgel, B. A.; Johnston, K. P. High Yield of Germanium Nanocrystals Synthesized from Germanium Diiodide in Solution. *Chem. Mater.* **2005**, *17* (25), 6479–6485.

(120) Thiessen, A. N.; Ha, M.; Hooper, R. W.; Yu, H.; Oliynyk, A. O.; Veinot, J. G. C.; Michaelis, V. K. Silicon Nanoparticles: Are They Crystalline from the Core to the Surface? *Chem. Mater.* **2019**, *31* (3), 678–688.

(121) Wei, W.; Dai, Y.; Huang, B.; Jacob, T. Many-Body Effects in Silicene, Silicane, Germanene and Germanane. *Phys. Chem. Chem. Phys.* **2013**, *15* (22), 8789–8794.

(122) B. Huey, W. L.; E. Goldberger, J. Covalent Functionalization of Two-Dimensional Group 14 Graphane Analogues. *Chem. Soc. Rev.* **2018**, *47* (16), 6201–6223.

(123) Kovacs, G. T. A.; Maluf, N. I.; Petersen, K. E. Bulk Micromachining of Silicon. *Proc. IEEE* **1998**, *86* (8), 1536–1551.

(124) Choi, K.; Buriak, J. M. Hydrogermylation of Alkenes and Alkynes on Hydride-Terminated Ge(100) Surfaces. *Langmuir* **2000**, *16* (20), 7737–7741.

(125) Li, Y.-H.; Buriak, J. M. Dehydrogenative Silane Coupling on Silicon Surfaces via Early Transition Metal Catalysis. *Inorg. Chem.* **2006**, *45* (3), 1096–1102.

(126) Buriak, J. M. Organometallic Chemistry on Silicon and Germanium Surfaces. *Chem. Rev.* **2002**, *102* (5), 1271–1308.

(127) Loscutoff, P. W.; Bent, S. F. REACTIVITY OF THE GERMANIUM

SURFACE: Chemical Passivation and Functionalization. *Annu. Rev. Phys. Chem.* **2006**, *57* (1), 467–495.

(128) Linford, M. R.; Chidsey, C. E. D. Alkyl Monolayers Covalently Bonded to Silicon Surfaces. *J. Am. Chem. Soc.* **1993**, *115* (26), 12631–12632.

(129) Linford, M. R.; Fenter, P.; Eisenberger, P. M.; Chidsey, C. E. D. Alkyl Monolayers on Silicon Prepared from 1-Alkenes and Hydrogen-Terminated Silicon. *J. Am. Chem. Soc.* **1995**, *117* (11), 3145–3155.

(130) Wang, D.; Buriak, J. M. Trapping Silicon Surface-Based Radicals. *Langmuir* **2006**, *22* (14), 6214–6221.

(131) Sung, M. M.; Kluth, G. J.; Yauw, O. W.; Maboudian, R. Thermal Behavior of Alkyl Monolayers on Silicon Surfaces. *Langmuir* **1997**, *13* (23), 6164–6168.

(132) Boukherroub, R.; Petit, A.; Loupy, A.; Chazalviel, J.-N.; Ozanam, F. Microwave-Assisted Chemical Functionalization of Hydrogen-Terminated Porous Silicon Surfaces. *J. Phys. Chem. B* **2003**, *107* (48), 13459–13462.

(133) Petit, A.; Delmotte, M.; Loupy, A.; Chazalviel, J.-N.; Ozanam, F.; Boukherroub, R. Microwave Effects on Chemical Functionalization of Hydrogen-Terminated Porous Silicon Nanostructures. *J. Phys. Chem. C* **2008**, *112* (42), 16622–16628.

(134) Wang, X.; Ruther, R. E.; Streifer, J. A.; Hamers, R. J. UV-Induced Grafting of Alkenes to Silicon Surfaces: Photoemission versus Excitons. *J. Am. Chem. Soc.* **2010**, *132* (12), 4048–4049.

(135) Stewart, M. P.; Buriak, J. M. Photopatterned Hydrosilylation on Porous Silicon. *Angew. Chem. Int. Ed.* **1998**, *37* (23), 3257–3260.

(136) Eves, B. J.; Lopinski, G. P. Formation of Organic Monolayers on Silicon via Gas-Phase Photochemical Reactions. *Langmuir* **2006**, *22* (7), 3180–3185.

(137) Sieval, A. B.; van den Hout, B.; Zuilhof, H.; Sudhölter, E. J. R. Molecular Modeling of Alkyl Monolayers on the Si(111) Surface. *Langmuir* **2000**, *16* (7), 2987–2990.

(138) Sieval, A. B.; van den Hout, B.; Zuilhof, H.; Sudhölter, E. J. R. Molecular Modeling of Covalently Attached Alkyl Monolayers on the Hydrogen-Terminated Si(111) Surface. *Langmuir* **2001**, *17* (7), 2172–2181.

(139) Sun, Q.-Y.; de Smet, L. C. P. M.; van Lagen, B.; Giesbers, M.; Thüne, P. C.; van Engelenburg, J.; de Wolf, F. A.; Zuilhof, H.; Sudhölter, E. J. R. Covalently Attached Monolayers on Crystalline Hydrogen-Terminated Silicon: Extremely Mild Attachment by Visible Light. *J. Am. Chem. Soc.* **2005**, *127* (8), 2514–2523.

(140) Rijksen, B.; Pujari, S. P.; Scheres, L.; van Rijn, C. J. M.; Baio, J. E.; Weidner, T.; Zuilhof, H. Hexadecadienyl Monolayers on Hydrogen-Terminated Si(111): Faster Monolayer Formation and Improved Surface Coverage Using the Enyne Moiety. *Langmuir* **2012**, *28* (16), 6577–6588.

(141) Stewart, M. P.; Buriak, J. M. Exciton-Mediated Hydrosilylation on Photoluminescent Nanocrystalline Silicon. *J. Am. Chem. Soc.* **2001**, *123* (32), 7821–7830.

(142) Sugimura, H.; Mo, S.; Yamashiro, K.; Ichii, T.; Murase, K. Photochemical Assembly of Gold Nanoparticle Arrays Covalently Attached to Silicon Surface Assisted by Localized Plasmon in the Nanoparticles. *J. Phys. Chem. C* **2013**, *117* (6), 2480–2485.

(143) Wu, J.-L.; Chen, F.-C.; Hsiao, Y.-S.; Chien, F.-C.; Chen, P.; Kuo, C.-H.; Huang, M. H.; Hsu, C.-S. Surface Plasmonic Effects of Metallic Nanoparticles on the Performance of Polymer Bulk Heterojunction Solar Cells. *ACS Nano* **2011**, *5* (2), 959–967.

(144) Buriak, J. M. Illuminating Silicon Surface Hydrosilylation: An Unexpected Plurality of Mechanisms. *Chem. Mater.* **2014**, *26* (1), 763–772.

(145) Okubo, T.; Tsuchiya, H.; Sadakata, M.; Yasuda, T.; Tanaka, K. An Organic Functional Group Introduced to Si(111) via Silicon–carbon Bond: A Liquid-Phase Approach. *Appl. Surf. Sci.* **2001**, *171* (3), 252–256.

(146) Bansal, A.; Li, X.; Lauermann, I.; Lewis, N. S.; Yi, S. I.; Weinberg, W. H. Alkylation of Si Surfaces Using a Two-Step Halogenation/Grignard Route. *J. Am. Chem. Soc.* **1996**, *118* (30), 7225–7226.

(147) Zhu, X.-Y.; Boiadjiev, V.; Mulder, J. A.; Hsung, R. P.; Major, R. C. Molecular Assemblies on Silicon Surfaces via Si−O Linkages. *Langmuir* **2000**, *16* (17), 6766–6772.

(148) He, J.; Patitsas, S. N.; Preston, K. F.; Wolkow, R. A.; Wayner, D. D. M. Covalent Bonding of Thiophenes to Si(111) by a Halogenation/Thienylation Route1Issued as NRCC Publ. No. 40854.1. *Chem. Phys. Lett.* **1998**, *286* (5), 508–514.

(149) Cullen, G. W.; Amick, J. A.; Gerlich, D. The Stabilization of Germanium Surfaces by Ethylation: I . Chemical Treatment. *J. Electrochem. Soc.* **1962**, *109* (2), 124.

(150) Lu, Z. H. Air‐stable Cl‐terminated Ge(111). *Appl. Phys. Lett.* **1996**, *68* (4), 520–522.

(151) Royea, W. J.; Juang, A.; Lewis, N. S. Preparation of Air-Stable, Low Recombination Velocity Si(111) Surfaces through Alkyl Termination. *Appl. Phys. Lett.* **2000**, *77* (13), 1988–1990.

(152) Cullen, G. W.; Amick, J. A.; Gerlich, D. The Stabilization of Germanium Surfaces by Ethylation I . Chemical Treatment. *J. Electrochem. Soc.* **1962**, *109* (2), 124–127.

(153) Knapp, D.; Brunschwig, B. S.; Lewis, N. S. Chemical, Electronic, and Electrical Properties of Alkylated Ge(111) Surfaces. *J. Phys. Chem. C* **2010**, *114* (28), 12300–12307.

(154) Hu, M.; Liu, F.; Buriak, J. M. Expanding the Repertoire of Molecular Linkages to Silicon: Si–S, Si–Se, and Si–Te Bonds. *ACS Appl. Mater. Interfaces* **2016**, *8* (17), 11091–11099.

(155) Chang, S.-S.; Hummel, R. E. Comparison of Photoluminescence Behavior of Porous Germanium and Spark-Processed Ge. *J. Lumin.* **2000**, *86* (1), 33–38.

(156) Cheul Choi, H.; M. Buriak, J. Preparation and Functionalization of Hydride Terminated Porous Germanium. *Chem. Commun.* **2000**, *0* (17), 1669–1670.

(157) Bateman, J. E.; Eagling, R. D.; Worrall, D. R.; Horrocks, B. R.; Houlton, A.

Alkylation of Porous Silicon by Direct Reaction with Alkenes and Alkynes. *Angew. Chem. Int. Ed.* **1998**, *37* (19), 2683–2685.

(158) Boukherroub, R.; Morin, S.; Wayner, D. D. M.; Bensebaa, F.; Sproule, G. I.; Baribeau, J.-M.; Lockwood, D. J. Ideal Passivation of Luminescent Porous Silicon by Thermal, Noncatalytic Reaction with Alkenes and Aldehydes. *Chem. Mater.* **2001**, *13* (6), 2002–2011.

(159) Buriak, J. M.; Allen, M. J. Lewis Acid Mediated Functionalization of Porous Silicon with Substituted Alkenes and Alkynes. *J. Am. Chem. Soc.* **1998**, *120* (6), 1339–1340.

(160) Buriak, J. M.; Stewart, M. P.; Geders, T. W.; Allen, M. J.; Choi, H. C.; Smith, J.; Raftery, D.; Canham, L. T. Lewis Acid Mediated Hydrosilylation on Porous Silicon Surfaces. *J. Am. Chem. Soc.* **1999**, *121* (49), 11491–11502.

(161) Lewis, L. N. On the Mechanism of Metal Colloid Catalyzed Hydrosilylation: Proposed Explanations for Electronic Effects and Oxygen Cocatalysis. *J. Am. Chem. Soc.* **1990**, *112* (16), 5998–6004.

(162) Holland, J. M.; Stewart, M. P.; Allen, M. J.; Buriak, J. M. Metal Mediated Reactions on Porous Silicon Surfaces. *J. Solid State Chem.* **1999**, *147* (1), 251–258.

(163) Sudo, T.; Asao, N.; Gevorgyan, V.; Yamamoto, Y. Lewis Acid Catalyzed Highly Regio- and Stereocontrolled Trans-Hydrosilylation of Alkynes and Allenes. *J. Org. Chem.* **1999**, *64* (7), 2494–2499.

(164) Huck, L. A.; Buriak, J. M. Toward a Mechanistic Understanding of Exciton-Mediated Hydrosilylation on Nanocrystalline Silicon. *J. Am. Chem. Soc.* **2012**, *134* (1), 489–497.

(165) Kim, D.; Joo, J.; Pan, Y.; Boarino, A.; Jun, Y. W.; Ahn, K. H.; Arkles, B.; Sailor, M. J. Thermally Induced Silane Dehydrocoupling on Silicon Nanostructures. *Angew. Chem. Int. Ed.* **2016**, *55* (22), 6423–6427.

(166) Kim, N. Y.; Laibinis, P. E. Improved Polypyrrole/Silicon Junctions by Surfacial Modification of Hydrogen-Terminated Silicon Using Organolithium Reagents. *J. Am. Chem. Soc.* **1999**, *121* (30), 7162–7163.

(167) Song, J. H.; Sailor, M. J. Functionalization of Nanocrystalline Porous Silicon Surfaces with Aryllithium Reagents: Formation of Silicon−Carbon Bonds by Cleavage of Silicon−Silicon Bonds. *J. Am. Chem. Soc.* **1998**, *120* (10), 2376–2381.

(168) Kim, N. Y.; Laibinis, P. E. Derivatization of Porous Silicon by Grignard Reagents at Room Temperature. *J. Am. Chem. Soc.* **1998**, *120* (18), 4516–4517.

(169) Höhlein, I. M. D.; Angı, A.; Sinelnikov, R.; Veinot, J. G. C.; Rieger, B. Functionalization of Hydride-Terminated Photoluminescent Silicon Nanocrystals with Organolithium Reagents. *Chem. – Eur. J.* **2015**, *21* (7), 2755–2758.

(170) Yang, Z.; Gonzalez, C. M.; Purkait, T. K.; Iqbal, M.; Meldrum, A.; Veinot, J. G. C. Radical Initiated Hydrosilylation on Silicon Nanocrystal Surfaces: An Evaluation of Functional Group Tolerance and Mechanistic Study. *Langmuir* **2015**, *31* (38), 10540–10548.

(171) Yang, Z.; Iqbal, M.; Dobbie, A. R.; Veinot, J. G. C. Surface-Induced Alkene Oligomerization: Does Thermal Hydrosilylation Really Lead to Monolayer Protected Silicon Nanocrystals? *J. Am. Chem. Soc.* **2013**, *135* (46), 17595–17601.

(172) Höhlein, I. M. D.; Kehrle, J.; Helbich, T.; Yang, Z.; Veinot, J. G. C.; Rieger, B. Diazonium Salts as Grafting Agents and Efficient Radical-Hydrosilylation Initiators for Freestanding Photoluminescent Silicon Nanocrystals. *Chem. - Eur. J.* **2014**, *20* (15), 4212–4216.

(173) Helbich, T.; J. Kloberg, M.; Sinelnikov, R.; Lyuleeva, A.; C. Veinot, J. G.; Rieger, B. Diaryliodonium Salts as Hydrosilylation Initiators for the Surface Functionalization of Silicon Nanomaterials and Their Collaborative Effect as Ring Opening Polymerization Initiators. *Nanoscale* **2017**, *9* (23), 7739–7744.

(174) Tilley, R. D.; Warner, J. H.; Yamamoto, K.; Matsui, I.; Fujimori, H. Micro-Emulsion Synthesis of Monodisperse Surface Stabilized Silicon Nanocrystals. *Chem. Commun.* **2005**, No. 14, 1833–1835.

(175) Tilley, R. D.; Yamamoto, K. The Microemulsion Synthesis of Hydrophobic and Hydrophilic Silicon Nanocrystals. *Adv. Mater.* **2006**, *18* (15), 2053–2056.

(176) Purkait, T. K.; Iqbal, M.; Wahl, M. H.; Gottschling, K.; Gonzalez, C. M.; Islam, M. A.; Veinot, J. G. C. Borane-Catalyzed Room-Temperature Hydrosilylation of Alkenes/Alkynes on Silicon Nanocrystal Surfaces. *J. Am. Chem. Soc.* **2014**, *136* (52), 17914–17917.

(177) Thiessen, A. N.; Purkait, T. K.; Faramus, A.; Veinot, J. G. C. Lewis Acid Protection: A Method Toward Synthesizing Phase Transferable Luminescent Silicon Nanocrystals. *Phys. Status Solidi A.* **2018**. *215* (7), 1700620.

(178) Kelly, J. A.; Shukaliak, A. M.; Fleischauer, M. D.; Veinot, J. G. C. Size-Dependent Reactivity in Hydrosilylation of Silicon Nanocrystals. *J. Am. Chem. Soc.* **2011**, *133* (24), 9564–9571.

(179) Hua, F.; Swihart, M. T.; Ruckenstein, E. Efficient Surface Grafting of Luminescent Silicon Quantum Dots by Photoinitiated Hydrosilylation. *Langmuir* **2005**, *21* (13), 6054–6062.

(180) Yang, Z.; Wahl, M. H.; Veinot, J. G. C. Size-Independent Organosilane Functionalization of Silicon Nanocrystals Using Wilkinson's Catalyst. *Can. J. Chem.* **2014**, *92* (10), 951–957.

(181) Angı, A.; Sinelnikov, R.; Meldrum, A.; C. Veinot, J. G.; Balberg, I.; Azulay, D.; Millo, O.; Rieger, B. Photoluminescence through In-Gap States in Phenylacetylene Functionalized Silicon Nanocrystals. *Nanoscale* **2016**, *8* (15), 7849–7853.

(182) Höhlein, I. M. D.; Angı, A.; Sinelnikov, R.; Veinot, J. G. C.; Rieger, B. Functionalization of Hydride-Terminated Photoluminescent Silicon Nanocrystals with Organolithium Reagents. *Chem. – Eur. J.* **2015**, *21* (7), 2755–2758.

(183) Fok, E.; Shih, M.; Meldrum, A.; Veinot, J. G. C. Preparation of Alkyl-Surface Functionalized Germanium Quantum Dots via Thermally Initiated Hydrogermylation. *Chem. Commun.* **2004**, 4, 386–387.

(184) Yu, Y.; Rowland, C. E.; Schaller, R. D.; Korgel, B. A. Synthesis and Ligand Exchange of Thiol-Capped Silicon Nanocrystals. *Langmuir* **2015**, *31* (24), 6886–6893.

(185) Holmberg, V. C.; Korgel, B. A. Corrosion Resistance of Thiol- and Alkene-Passivated Germanium Nanowires. *Chem. Mater.* **2010**, *22* (12), 3698–3703.

(186) Ii, D. D. V.; E. Schaak, R. Synthesis, Properties and Applications of Colloidal Germanium and Germanium-Based Nanomaterials. *Chem. Soc. Rev.* **2013**, *42* (7), 2861–2879.

(187) Mobarok, M. H.; Purkait, T. K.; Islam, M. A.; Miskolzie, M.; Veinot, J. G. C. Instantaneous Functionalization of Chemically Etched Silicon Nanocrystal Surfaces. *Angew. Chem.* Int. Ed. **2017**, *129* (22), 6169–6173.

(188) Li, X.; He, Y.; Swihart, M. T. Surface Functionalization of Silicon Nanoparticles Produced by Laser-Driven Pyrolysis of Silane Followed by HF−HNO_3 Etching. *Langmuir* **2004**, *20* (11), 4720–4727.

(189) Li, S.; Silvers, S. J.; El-Shall, M. S. Surface Oxidation and Luminescence Properties of Weblike Agglomeration of Silicon Nanocrystals Produced by a Laser Vaporization−Controlled Condensation Technique. *J. Phys. Chem. B* **1997**, *101* (10), 1794–1802.

(190) Dasog, M.; Bader, K.; Veinot, J. G. C. Influence of Halides on the Optical Properties of Silicon Quantum Dots. *Chem. Mater.* **2015**, *27* (4), 1153–1156.

(191) Restrepo, O. D.; Krymowski, K. E.; Goldberger, J.; Windl, W. A First Principles Method to Simulate Electron Mobilities in 2D Materials. *New J. Phys.* **2014**, *16* (10), 105009.

(192) Ottaviani, G.; Canali, C.; Nava, F.; Mayer, J. W. Hole Drift Velocity in High‐purity Ge between 8 and 220 ° K. *J. Appl. Phys.* **1973**, *44* (6), 2917–2918.

(193) Chen, Q.; Liang, L.; Potsi, G.; Wan, P.; Lu, J.; Giousis, T.; Thomou, E.; Gournis, D.; Rudolf, P.; Ye, J. Highly Conductive Metallic State and Strong Spin–Orbit Interaction in Annealed Germanane. *Nano Lett.* **2019**, *19* (3), 1520–1526.

(194) Chen, J.-H.; Jang, C.; Xiao, S.; Ishigami, M.; Fuhrer, M. S. Intrinsic and Extrinsic Performance Limits of Graphene Devices on SiO_2. *Nat. Nanotechnol.* **2008**, *3* (4), 206–209.

(195) Helbich, T.; Lyuleeva, A.; Höhlein, I. M. D.; Marx, P.; Scherf, L. M.; Kehrle, J.; Fässler, T. F.; Lugli, P.; Rieger, B. Radical-Induced Hydrosilylation Reactions for the Functionalization of Two-Dimensional Hydride Terminated Silicon Nanosheets. *Chem. - Eur. J.* **2016**, *22* (18), 6194–6198.

(196) Restrepo, O. D.; Mishra, R.; Goldberger, J. E.; Windl, W. Tunable Gaps and Enhanced Mobilities in Strain-Engineered Silicane. *J. Appl. Phys.* **2014**, *115* (3), 033711.

(197) Lyuleeva, A.; Helbich, T.; Rieger, B.; Lugli, P. Polymer-Silicon Nanosheet Composites: Bridging the Way to Optoelectronic Applications. *J. Phys. Appl. Phys.* **2017**, *50* (13), 135106.

(198) Nakano, H.; Nakano, M.; Nakanishi, K.; Tanaka, D.; Sugiyama, Y.; Ikuno, T.; Okamoto, H.; Ohta, T. Preparation of Alkyl-Modified Silicon Nanosheets by Hydrosilylation of Layered Polysilane (Si_6H_6). *J. Am. Chem. Soc.* **2012**, *134* (12), 5452–5455.

(199) Helbich, T.; Lyuleeva, A.; Marx, P.; Scherf, L. M.; Purkait, T. K.; Fässler, T. F.; Lugli, P.; Veinot, J. G. C.; Rieger, B. Lewis Acid Induced Functionalization of Photoluminescent 2D Silicon Nanosheets for the Fabrication of Functional Hybrid Films. *Adv. Funct. Mater.* **2017**, *27* (21), 1606764.

(200) Yu, H.; Helbich, T.; Scherf, L. M.; Chen, J.; Cui, K.; Fässler, T. F.; Rieger, B.; Veinot, J. G. C. Radical-Initiated and Thermally Induced Hydrogermylation of Alkenes on the Surfaces of Germanium Nanosheets. *Chem. Mater.* **2018**, *30* (7), 2274–2280.

(201) Sugiyama, Y.; Okamoto, H.; Mitsuoka, T.; Morikawa, T.; Nakanishi, K.; Ohta, T.; Nakano, H. Synthesis and Optical Properties of Monolayer Organosilicon Nanosheets. *J. Am. Chem. Soc.* **2010**, *132* (17), 5946–5947.

(202) Okamoto, H.; Sugiyama, Y.; Nakanishi, K.; Ohta, T.; Mitsuoka, T.; Nakano, H. Surface Modification of Layered Polysilane with N-Alkylamines, α,ω-Diaminoalkanes, and ω-Aminocarboxylic Acids. *Chem. Mater.* **2015**, *27* (4), 1292–1298.

(203) Ohshita, J.; Yamamoto, K.; Tanaka, D.; Nakashima, M.; Kunugi, Y.; Ohashi,

M.; Nakano, H. Preparation and Photocurrent Generation of Silicon Nanosheets with Aromatic Substituents on the Surface. *J. Phys. Chem. C* **2016**, *120* (20), 10991–10996.

(204) Bonitz, E. Lepidoide, VI: Ein Neuer Weg Zur Herstellung von Aktivem Silicium Oder Siliciummonochlorid. *Chem. Ber.* **1961**, *94* (1), 220–225.

(205) Liu, J.; Yang, Y.; Lyu, P.; Nachtigall, P.; Xu, Y. Few-Layer Silicene Nanosheets with Superior Lithium-Storage Properties. *Adv. Mater.* **2018**, *30* (26), 1800838.

(206) Ohashi, M.; Shirai, S.; Nakano, H. Direct Chemical Synthesis of Benzyl-Modified Silicane from Calcium Disilicide. *Chem. Mater.* **2019**, *31* (13), 4720–4725.

(207) Jiang, S.; Butler, S.; Bianco, E.; Restrepo, O. D.; Windl, W.; Goldberger, J. E. Improving the Stability and Optical Properties of Germanane via One-Step Covalent Methyl-Termination. *Nat. Commun.* **2014**, *5*, 3389.

(208) Jiang, S.; Arguilla, M. Q.; Cultrara, N. D.; Goldberger, J. E. Improved Topotactic Reactions for Maximizing Organic Coverage of Methyl Germanane. *Chem. Mater.* **2016**, *28* (13), 4735–4740.

(209) Asel, T. J.; Huey, W. L. B.; Noesges, B.; Molotokaite, E.; Chien, S.-C.; Wang, Y.; Barnum, A.; McPherson, C.; Jiang, S.; Shields, S.; D'Andrea, C.; Windl, W.; Cinquanta, E.; Brillson, L. J.; Goldberger, J. E. Influence of Surface Chemistry on Water Absorption in Functionalized Germanane. *Chem. Mater.* **2020**, *32* (4), 1537–1544.

(210) Jiang, S.; Krymowski, K.; Asel, T.; Arguilla, M. Q.; Cultrara, N. D.; Yanchenko, E.; Yang, X.; Brillson, L. J.; Windl, W.; Goldberger, J. E. Tailoring the Electronic Structure of Covalently Functionalized Germanane via the Interplay of Ligand Strain and Electronegativity. *Chem. Mater.* **2016**, *28* (21), 8071–8077.

(211) Uhlig, W. Zur synthese funktionel substituierter polysilane mittels trifluormethansulfonsäure. *J. Organomet. Chem.* **1991**, *402* (3), C45–C49.

(212) Nesper, R. The Zintl-Klemm Concept – A Historical Survey. *Z. Für Anorg.*

Allg. Chem. **2014**, *640* (14), 2639–2648.

(213) Kauzlarich, S. M. Zintl Compounds. In *Encyclopedia of Inorganic Chemistry*; American Cancer Society, 2006.

(214) Beekman, M.; Kauzlarich, S. M.; Doherty, L.; Nolas, G. S. Zintl Phases as Reactive Precursors for Synthesis of Novel Silicon and Germanium-Based Materials. *Materials* **2019**, *12* (7).

(215) Schäfer, H.; Eisenmann, B.; Müller, W. Zintl Phases: Transitions between Metallic and Ionic Bonding. *Angew. Chem. Int. Ed. Engl.* **1973**, *12* (9), 694–712.

(216) Zaikina, J. V.; Muthuswamy, E.; Lilova, K. I.; Gibbs, Z. M.; Zeilinger, M.; Snyder, G. J.; Fässler, T. F.; Navrotsky, A.; Kauzlarich, S. M. Thermochemistry, Morphology, and Optical Characterization of Germanium Allotropes. *Chem. Mater.* **2014**, *26* (10), 3263–3271.

(217) Geier, S.; Jung, R.; Peters, K.; A. Gasteiger, H.; Fattakhova-Rohlfing, D.; F. Fässler, T. A Wet-Chemical Route for Macroporous Inverse Opal Ge Anodes for Lithium Ion Batteries with High Capacity Retention. *Sustain. Energy Fuels* **2018**, *2* (1), 85–90.

(218) Bentlohner, M. M.; Waibel, M.; Zeller, P.; Sarkar, K.; Müller‐Buschbaum, P.; Fattakhova‐Rohlfing, D.; Fässler, T. F. Zintl Clusters as Wet-Chemical Precursors for Germanium Nanomorphologies with Tunable Composition. *Angew. Chem. Int. Ed.* **2016**, *55* (7), 2441–2445.

(219) Armatas, G. S.; Kanatzidis, M. G. Mesostructured Germanium with Cubic Pore Symmetry. *Nature* **2006**, *441* (7097), 1122–1125.

(220) Sun, D.; Riley, A. E.; Cadby, A. J.; Richman, E. K.; Korlann, S. D.; Tolbert, S. H. Hexagonal Nanoporous Germanium through Surfactant-Driven Self-Assembly of Zintl Clusters. *Nature* **2006**, *441* (7097), 1126–1130.

(221) Armatas, G. S.; Kanatzidis, M. G. Hexagonal Mesoporous Germanium. *Science* **2006**, *313* (5788), 817–820.

(222) Palenzona, A.; Manfrinetti, P.; Fornasini, M. L. The Phase Diagram of the

Ca–Ge System. *J. Alloys Compd.* **2002**, *345* (1), 144–147.

(223) Okamoto, H. Ca-Ge (Calcium-Germanium). *J. Phase Equilibria Diffus.* **2013**, *34* (2), 172–173.

(224) Djaballah, Y.; Pasturel, A.; Belgacem-Bouzida, A. Thermodynamic Assessment of the Calcium–Germanium System. *J. Alloys Compd.* **2010**, *497* (1), 74–79.

(225) Eckerlin, P.; Meyer, H. J.; Wölfel, E. Die Kristallstruktur von CaSn und CaGe. *Z. Anorg. Allg. Chem.* **1955**, *281* (5–6), 322–328.

(226) Tobash, P. H.; Bobev, S. Synthesis, Structure and Electronic Structure of a New Polymorph of $CaGe_2$. *J. Solid State Chem.* **2007**, *180* (5), 1575–1581.

(227) Vogg, G.; Brandt, M. S.; Stutzmann, M.; Genchev, I.; Bergmaier, A.; Görgens, L.; Dollinger, G. Epitaxial $CaGe_2$ Films on Germanium. *J. Cryst. Growth* **2000**, *212* (1–2), 148–154.

(228) Cultrara, N. D.; Wang, Y.; Arguilla, M. Q.; Scudder, M. R.; Jiang, S.; Windl, W.; Bobev, S.; Goldberger, J. E. Synthesis of 1T, 2H, and 6R Germanane Polytypes. *Chem. Mater.* **2018**, *30* (4), 1335–1343.

(229) Yaokawa, R.; Nagoya, A.; Mukai, K.; Nakano, H. Crystal Structures and Thermodynamic Stabilities of Two New $CaGe_2$ Polymorphs. *Acta Mater.* **2018**, *151*, 347–355.

(230) Nicolosi, V.; Chhowalla, M.; Kanatzidis, M. G.; Strano, M. S.; Coleman, J. N. Liquid Exfoliation of Layered Materials. *Science* **2013**, *340* (6139), 1226419.

(231) Nakamura, D.; Nakano, H. Liquid-Phase Exfoliation of Germanane Based on Hansen Solubility Parameters. *Chem. Mater.* **2018**, *30* (15), 5333–5338.

(232) Okamoto, H.; Sugiyama, Y.; Nakano, H. Synthesis and Modification of Silicon Nanosheets and Other Silicon Nanomaterials. *Chem. – Eur. J.* **2011**, *17* (36), 9864–9887.

(233) Lopez-Sanchez, O.; Lembke, D.; Kayci, M.; Radenovic, A.; Kis, A. Ultrasensitive Photodetectors Based on Monolayer MoS_2. *Nat. Nanotechnol.*

2013, *8* (7), 497–501.

(234) Lee, C.; Wei, X.; Kysar, J. W.; Hone, J. Measurement of the Elastic Properties and Intrinsic Strength of Monolayer Graphene. *Science* **2008**, *321* (5887), 385–388.

(235) Vogt, P.; De Padova, P.; Quaresima, C.; Avila, J.; Frantzeskakis, E.; Asensio, M. C.; Resta, A.; Ealet, B.; Le Lay, G. Silicene: Compelling Experimental Evidence for Graphenelike Two-Dimensional Silicon. *Phys. Rev. Lett.* **2012**, *108* (15), 155501.

(236) Wöhler, F. Ueber Verbindungen Des Siliciums Mit Sauerstoff Und Wasserstoff. *Justus Liebigs Ann. Chem.* **1863**, *127* (3), 257–274.

(237) Balendhran, S.; Walia, S.; Nili, H.; Sriram, S.; Bhaskaran, M. Elemental Analogues of Graphene: Silicene, Germanene, Stanene, and Phosphorene. *Small* **2015**, *11* (6), 640–652.

(238) Cahangirov, S.; Topsakal, M.; Aktürk, E.; Şahin, H.; Ciraci, S. Two- and One-Dimensional Honeycomb Structures of Silicon and Germanium. *Phys. Rev. Lett.* **2009**, *102* (23), 236804.

(239) Helbich, T.; Lyuleeva, A.; Höhlein, I. M. D.; Marx, P.; Scherf, L. M.; Kehrle, J.; Fässler, T. F.; Lugli, P.; Rieger, B. Radical-Induced Hydrosilylation Reactions for the Functionalization of Two-Dimensional Hydride Terminated Silicon Nanosheets. *Chem. – Eur. J.* **2016**, *22* (18), 6194–6198.

(240) Grimme, S. Semiempirical GGA-Type Density Functional Constructed with a Long-Range Dispersion Correction. *J. Comput. Chem.* **2006**, *27* (15), 1787–1799.

(241) Paton, K. R.; Varrla, E.; Backes, C.; Smith, R. J.; Khan, U.; O'Neill, A.; Boland, C.; Lotya, M.; Istrate, O. M.; King, P.; Higgins, T.; Barwich, S.; May, P.; Puczkarski, P.; Ahmed, I.; Moebius, M.; Pettersson, H.; Long, E.; Coelho, J.; O'Brien, S. E.; McGuire, E. K.; Sanchez, B. M.; Duesberg, G. S.; McEvoy, N.; Pennycook, T. J.; Downing, C.; Crossley, A.; Nicolosi, V.; Coleman, J. N. Scalable Production of Large Quantities of Defect-Free Few-Layer Graphene by Shear Exfoliation in Liquids. *Nat. Mater.* **2014**, *13* (6), 624–630.

(242) Chen, L.; He, X.; Liu, H.; Qian, L.; Kim, S. H. Water Adsorption on Hydrophilic and Hydrophobic Surfaces of Silicon. *J. Phys. Chem. C* **2018**, *122* (21), 11385–11391.

(243) Miller, D. J.; Biesinger, M. C.; McIntyre, N. S. Interactions of CO2 and CO at Fractional Atmosphere Pressures with Iron and Iron Oxide Surfaces: One Possible Mechanism for Surface Contamination? *Surf. Interface Anal.* **2002**, *33* (4), 299–305.

(244) Boehm, H. P. Surface Oxides on Carbon and Their Analysis: A Critical Assessment. *Carbon* **2002**, *40* (2), 145–149.

(245) Prabhakaran, K.; Ogino, T. Oxidation of Ge(100) and Ge(111) Surfaces: An UPS and XPS Study. *Surf. Sci.* **1995**, *325* (3), 263–271.

(246) Bodlaki, D.; Yamamoto, H.; Waldeck, D. H.; Borguet, E. Ambient Stability of Chemically Passivated Germanium Interfaces. *Surf. Sci.* **2003**, *543* (1), 63–74.

(247) Okamoto, H.; Kumai, Y.; Sugiyama, Y.; Mitsuoka, T.; Nakanishi, K.; Ohta, T.; Nozaki, H.; Yamaguchi, S.; Shirai, S.; Nakano, H. Silicon Nanosheets and Their Self-Assembled Regular Stacking Structure. *J. Am. Chem. Soc.* **2010**, *132* (8), 2710–2718.

(248) D. Höhlein, I. M.; L. Werz, P. D.; C. Veinot, J. G.; Rieger, B. Photoluminescent Silicon Nanocrystal-Polymer Hybrid Materials via Surface Initiated Reversible Addition–Fragmentation Chain Transfer (RAFT) Polymerization. *Nanoscale* **2015**, *7* (17), 7811–7818.

(249) Hernandez, Y.; Nicolosi, V.; Lotya, M.; Blighe, F. M.; Sun, Z.; De, S.; McGovern, I. T.; Holland, B.; Byrne, M.; Gun'Ko, Y. K.; Boland, J. J.; Niraj, P.; Duesberg, G.; Krishnamurthy, S.; Goodhue, R.; Hutchison, J.; Scardaci, V.; Ferrari, A. C.; Coleman, J. N. High-Yield Production of Graphene by Liquid-Phase Exfoliation of Graphite. *Nat. Nanotechnol.* **2008**, *3* (9), 563–568.

(250) Meyer, J. C.; Geim, A. K.; Katsnelson, M. I.; Novoselov, K. S.; Obergfell, D.; Roth, S.; Girit, C.; Zettl, A. On the Roughness of Single- and Bi-Layer Graphene Membranes. *Solid State Commun.* **2007**, *143* (1–2), 101–109.

(251) Horiuchi, S.; Gotou, T.; Fujiwara, M.; Sotoaka, R.; Hirata, M.; Kimoto, K.; Asaka, T.; Yokosawa, T.; Matsui, Y.; Watanabe, K.; Sekita, M. Carbon Nanofilm with a New Structure and Property. *Jpn. J. Appl. Phys.* **2003**, *42* (9A), L1073.

(252) Ramakrishna Matte, H. S. S.; Gomathi, A.; Manna, A. K.; Late, D. J.; Datta, R.; Pati, S. K.; Rao, C. N. R. MoS_2 and WS_2 Analogues of Graphene. *Angew. Chem. Int. Ed.* **2010**, *49* (24), 4059–4062.

(253) Plymale, N. T.; Dasog, M.; Brunschwig, B. S.; Lewis, N. S. A Mechanistic Study of the Oxidative Reaction of Hydrogen-Terminated Si(111) Surfaces with Liquid Methanol. *J. Phys. Chem. C* **2017**, *121* (8), 4270–4282.

(254) Webb, L. J.; Nemanick, E. J.; Biteen, J. S.; Knapp, D. W.; Michalak, D. J.; Traub, M. C.; Chan, A. S. Y.; Brunschwig, B. S.; Lewis, N. S. High-Resolution X-Ray Photoelectron Spectroscopic Studies of Alkylated Silicon(111) Surfaces. *J. Phys. Chem. B* **2005**, *109* (9), 3930–3937.

(255) Szajman, J.; Jenkin, J. G.; Liesegang, J.; Leckey, R. C. G. Electron Mean Free Paths in Ge in the Range 70–1400 EV. *J. Electron Spectrosc. Relat. Phenom.* **1978**, *14* (1), 41–48.

(256) Wallart, X.; Henry de Villeneuve, C.; Allongue, P. Truly Quantitative XPS Characterization of Organic Monolayers on Silicon: Study of Alkyl and Alkoxy Monolayers on H−Si(111). *J. Am. Chem. Soc.* **2005**, *127* (21), 7871–7878.

(257) Sieval, A. B.; van den Hout, B.; Zuilhof, H.; Sudhölter, E. J. R. Molecular Modeling of Covalently Attached Alkyl Monolayers on the Hydrogen-Terminated Si(111) Surface. *Langmuir* **2001**, *17* (7), 2172–2181.

(258) Chen, R.; Bent, S. F. Highly Stable Monolayer Resists for Atomic Layer Deposition on Germanium and Silicon. *Chem. Mater.* **2006**, *18* (16), 3733–3741.

(259) Sharp, I. D.; Schoell, S. J.; Hoeb, M.; Brandt, M. S.; Stutzmann, M. Electronic Properties of Self-Assembled Alkyl Monolayers on Ge Surfaces. *Appl. Phys. Lett.* **2008**, *92* (22), 223306.

(260) Sturala, J.; Luxa, J.; Matějková, S.; Sofer, Z.; Pumera, M. Germanane Synthesis with Simultaneous Covalent Functionalization: Towards Highly Functionalized Fluorescent Germananes. *Nanoscale* **2019**, *11* (41), 19327–19333.

(261) Spencer, M. D.; Shelby, Q. D.; Girolami, G. S. Titanium-Catalyzed Dehydrocoupling of Silanes: Direct Conversion of Primary Monosilanes to Titanium(0) Oligosilane Complexes with Agostic α-Si-H···Ti Interactions. *J. Am. Chem. Soc.* **2007**, *129* (7), 1860–1861.

(262) Tessier, C. A.; Kennedy, V. O.; Zarate, E. A. Silane Dehydrocoupling Reactions Catalyzed by the Late Transition Metals. In *Inorganic and Organometallic Oligomers and Polymers*; Harrod, J. F., Laine, R. M., Eds.; Springer Netherlands: Dordrecht, 1991; pp 13–22.

(263) Itoh, M.; Mitsuzuka, M.; Utsumi, T.; Iwata, K.; Inoue, K. Dehydrogenative Coupling Reactions between Hydrosilanes and Monosubstituted Alkynes Catalyzed by Solid Bases. *J. Organomet. Chem.* **1994**, *476* (2), c30–c31.

(264) Mooney, P. M.; Dacol, F. H.; Tsang, J. C.; Chu, J. O. Raman Scattering Analysis of Relaxed GexSi1−x Alloy Layers. *Appl. Phys. Lett.* **1993**, *62* (17), 2069–2071.

(265) Persans, P. D.; Ruppert, A. F.; Abeles, B.; Tiedje, T. Raman Scattering Study of Amorphous Si-Ge Interfaces. *Phys. Rev. B* **1985**, *32* (8), 5558–5560.

(266) Alonso, M. I.; Winer, K. Raman Spectra of C-$Si_{1-X}Ge_x$ Alloys. *Phys. Rev. B* **1989**, *39* (14), 10056–10062.

(267) McFeely, F. R.; Morar, J. F.; Himpsel, F. J. Soft X-Ray Photoemission Study of the Silicon-Fluorine Etching Reaction. *Surf. Sci.* **1986**, *165* (1), 277–287.

(268) Dietrich, P. M.; Glamsch, S.; Ehlert, C.; Lippitz, A.; Kulak, N.; Unger, W. E. S. Synchrotron-Radiation XPS Analysis of Ultra-Thin Silane Films: Specifying the Organic Silicon. *Appl. Surf. Sci.* **2016**, *363*, 406–411.

(269) Dietrich, P. M.; Streeck, C.; Glamsch, S.; Ehlert, C.; Lippitz, A.; Nutsch, A.; Kulak, N.; Beckhoff, B.; Unger, W. E. S. Quantification of Silane Molecules on Oxidized Silicon: Are There Options for a Traceable and Absolute

Determination? *Anal. Chem.* **2015**, *87* (19), 10117–10124.

(270) Arrigo, A.; Mazzaro, R.; Romano, F.; Bergamini, G.; Ceroni, P. Photoinduced Electron-Transfer Quenching of Luminescent Silicon Nanocrystals as a Way To Estimate the Position of the Conduction and Valence Bands by Marcus Theory. *Chem. Mater.* **2016**, *28* (18), 6664–6671.

(271) Kodaira, T.; Watanabe, A.; Ito, O.; Matsuda, M.; Tokura, S.; Kira, M.; Nagano, S.-S.; Mochida, K. Third-Order Nonlinear Optical Properties of Thin Films of Organogermane Homopolymers and Organogermane-Organosilane Copolymers*. *Adv. Mater.* **1995**, *7* (11), 917–919.

(272) Watanabe, A.; Ito, O.; Mochida, K. Photoinduced Electron Transfer from Polygermane to C60 Studied by Laser Flash Photolysis. *Organometallics* **1995**, *14* (9), 4281–4285.

(273) Zaitsev, K. V.; Lam, K.; Zhanabil, Z.; Suleimen, Y.; Kharcheva, A. V.; Tafeenko, V. A.; Oprunenko, Y. F.; Poleshchuk, O. Kh.; Lermontova, E. Kh.; Churakov, A. V. Oligogermanes Containing Only Electron-Withdrawing Substituents: Synthesis and Properties. *Organometallics* **2017**, *36* (2), 298–309.

(274) Motonaga, M.; Nakashima, H.; Katz, S.; Berry, D. H.; Imase, T.; Kawauchi, S.; Watanabe, J.; Fujiki, M.; Koe, J. R. The First Optically Active Polygermanes: Preferential Screw Sense Helicity of Enantiopure Chiral-Substituted Aryl Polygermanes and Comparison with Analogous Polysilanes. *J. Organomet. Chem.* **2003**, *685* (1), 44–50.

(275) Huo, Y.; Berry, D. H. Synthesis and Properties of Hybrid Organic−Inorganic Materials Containing Covalently Bonded Luminescent Polygermanes. *Chem. Mater.* **2005**, *17* (1), 157–163.

(276) Kalinkin, A. M.; Kalinkina, E. V.; Zalkind, O. A.; Makarova, T. I. Chemical Interaction of Calcium Oxide and Calcium Hydroxide with CO2 during Mechanical Activation. *Inorg. Mater.* **2005**, *41* (10), 1073–1079.

(277) Parker, J. H. Raman Scattering by Silicon and Germanium. *Phys. Rev.* **1967**, *155* (3), 712–714.

(278) Alfaro-Calderón. P.; Cruz-Irisson. M.; Wang-Chen. C. Theory of Raman Scattering by Phonons in Germanium Nanostructures. *Nanoscale Res Lett.* **2008**, *3* (2), 55–59.

(279) Weinstein, B. A.; Cardona, M. Second-Order Raman Spectrum of Germanium. *Phys. Rev. B* **1973**, *7* (6), 2545–2551.

(280) Perova, T. S.; Kasper, E.; Oehme, M.; Cherevkov, S.; Schulze, J. Features of Polarized Raman Spectra for Homogeneous and Non-Homogeneous Compressively Strained $Ge_{1-y}Sn_y$ Alloys. *J. Raman Spectrosc.* **2017**, *48* (7), 993–1001.

(281) Deegan, T.; Hughes, G. An X-Ray Photoelectron Spectroscopy Study of the HF Etching of Native Oxides on Ge(111) and Ge(100) Surfaces. *Appl. Surf. Sci.* **1998**, *123–124*, 66–70.

(282) Park, S. W.; Kaufman-Osborn, T.; Kim, H.; Siddiqui, S.; Sahu, B.; Yoshida, N.; Brandt, A.; Kummel, A. C. Combined Wet and Dry Cleaning of SiGe(001). *J. Vac. Sci. Technol. A* **2015**, *33* (4), 041403.

(283) Donovan, T. M.; Spicer, W. E.; Bennett, J. M. Evidence for A Sharp Absorption Edge in Amorphous Ge. *Phys. Rev. Lett.* **1969**, *22* (20), 1058–1061.

(284) Inoue, R.; Yamaguchi, M.; Murakami, Y.; Okano, K.; Mori, A. Revisiting of Benzophenone Ketyl Still: Use of a Sodium Dispersion for the Preparation of Anhydrous Solvents. *ACS Omega* **2018**, *3* (10), 12703–12706.

(285) Sidorkin, V.; van Veldhoven, E.; van der Drift, E.; Alkemade, P.; Salemink, H.; Maas, D. Sub-10-Nm Nanolithography with a Scanning Helium Beam. *J. Vac. Sci. Technol. B Microelectron. Nanometer Struct. Process. Meas. Phenom.* **2009**, *27* (4), L18–L20.

(286) Sarriugarte, P.; Schnell, M.; Chuvilin, A.; Hillenbrand, R. Polarization-Resolved Near-Field Characterization of Nanoscale Infrared Modes in Transmission Lines Fabricated by Gallium and Helium Ion Beam Milling. *ACS Photonics* **2014**, *1* (7), 604–611.

(287) Kollmann, H.; Piao, X.; Esmann, M.; Becker, S. F.; Hou, D.; Huynh, C.;

Kautschor, L.-O.; Bösker, G.; Vieker, H.; Beyer, A.; Gölzhäuser, A.; Park, N.; Vogelgesang, R.; Silies, M.; Lienau, C. Toward Plasmonics with Nanometer Precision: Nonlinear Optics of Helium-Ion Milled Gold Nanoantennas. *Nano Lett.* **2014**, *14* (8), 4778–4784.

(288) Häffner, M.; Haug, A.; Heeren, A.; Fleischer, M.; Peisert, H.; Chassé, T.; Kern, D. P. Influence of Temperature on HSQ Electron-Beam Lithography. *J. Vac. Sci. Technol. B Microelectron. Nanometer Struct. Process. Meas. Phenom.* **2007**, *25* (6), 2045–2048.

(289) Cai, J.; Zhu, Z.; Alkemade, P. F. A.; Veldhoven, E. van; Wang, Q.; Ge, H.; Rodrigues, S. P.; Cai, W.; Li, W.-D. 3D Volumetric Energy Deposition of Focused Helium Ion Beam Lithography: Visualization, Modeling, and Applications in Nanofabrication. *Adv. Mater. Interfaces* **2018**, *5* (12), 1800203.